NMR DIFFUSION MEASUREMENTS OF COMPARTMENTALIZED AND MULTICOMPONENT BIOLOGICAL SYSTEMS

Studies of Tropoelastin, the Self Association of N-Methylacetamide, and q-Space Analysis of Real and Model Cell Suspensions

---

A thesis submitted for the degree of Doctor of Philosophy
by David Gabriel Regan
BSc (Hons)

August 2002

School of Molecular and Microbial Biosciences
University of Sydney
NSW 2006
Australia

Abstract

Molecular diffusion is an inherent feature of all fluid systems. The processes and interactions that characterize these systems are in some way dependent upon the mobility of the component molecules. Pulsed field-gradient spin-echo nuclear magnetic resonance (PGSE NMR) is a powerful tool for the study of molecular diffusion; for heterogeneous systems, such as those typically found in biology, this technique is unsurpassed in the diversity of systems that yield to its probing. The aim of the work presented in this thesis was to use an integrated NMR-based approach, in conjunction with computer modeling, for the study of molecular diffusion in compartmentalized and multicomponent biological systems.

Erythrocyte suspensions provided an ideal experimental system for the study of compartmentalized diffusion in cells. Water exchanges rapidly between the intra- and extracellular regions and, as the major constituent of the cell, provides a strong and predominant proton NMR signal. In addition, the cells are known to align in the strong static magnetic field of the spectrometer. As a consequence of these two properties, the signal intensity from a suitably designed series of PGSE NMR experiments exhibits a series of maxima and minima when graphed as a function of the magnitude of the spatial wave number vector $\mathbf{q}$. The apparently periodic phenomenon is mathematically analogous to optical diffraction and interference and is referred to here as diffusion-coherence. It is the characterization of this phenomenon, with the aid of computer-based models, which was the focus of a major section of the work described herein.

Two quite distinct molecular systems formed the basis of the work in which I investigated diffusion in multicomponent systems. Both systems involved molecules that undergo self-association such that at equilibrium a population distribution of different oligomeric species is present. The first of these was tropoelastin, the monomeric subunit of elastin, which under certain conditions aggregates to form a coacervate. The second system was N-methylacetamide (NMA) which also undergoes extensive self-association. NMA oligomers have previously been studied as peptide analogues due to the presence in the monomer of a peptide linkage. In this work the aim was to use PGSE NMR diffusion measurements, in a manner that is in many ways analogous to analytical ultracentrifugation, to obtain estimates of hydrodynamic and thermodynamic parameters. Computer modeling was also used extensively in this section of work for the interpretation of the experimental data.

Main References

This thesis is based on the following papers which are ordered according to publication date and will be referred to in the text by their corresponding Roman numeral. The author's role in each paper is outlined in italics below each reference:

I. Torres A.M., Taurins A.T., Regan D.G., Chapman B.E., Kuchel P.W. (1999) Assignment of coherence features in NMR q-space plots to particular diffusion modes in erythrocyte suspensions. *J. Magn. Reson.* **138**, 135-143.

   ➢ *design, development, and application of computer models used to assist in the assignment of coherence features; analysis and interpretation of simulation data; involvement in the analysis and interpretation of experimental data and in all discussions of ideas presented in the paper*

II. Regan D.G., Kuchel P.W. (2000) Mean residence time of molecules diffusing in a cell bounded by a semi-permeable membrane: Monte Carlo simulations and an expression relating membrane transition probability to permeability. *Eur. Biophys. J.* **29**, 221-227.

   ➢ *design, development, and application of computer models; analysis and interpretation of data; development of theory relating membrane transition probability to permeability in collaboration with co-author*

III. Kuchel P.W., Durrant C.J., Chapman B.E., Jarrett P.S., Regan D.G. (2000) Evidence of red cell alignment in the magnetic field of an NMR spectrometer based on the diffusion tensor of water. *J. Magn. Reson.* **145**, 291-301.

   ➢ *direct involvement at all levels of project including: design and implementation of PGSE NMR experiments, discussion of ideas; development and formulation of theory; development of computer-based mathematical methods for data analysis*

IV. Toonkool P., Regan D.G., Kuchel P.W., Morris M.B., Weiss A.S. (2001) Thermodynamic and hydrodynamic properties of human tropoelastin: analytical ultracentrifuge and pulsed field-gradient spin-echo NMR studies. *J. Biol. Chem.* **276**, 28042-28050.

> *design, development and application of computer models used in testing hypotheses; design and implementation of PGSE NMR experiments; analysis and interpretation of diffusion and simulation data; involvement in all discussion of ideas relating to the project*

V. Regan D.G., Kuchel P.W. (2002) Simulations of molecular diffusion in lattices of cells: insights for NMR of red blood cells. *Biophys. J.* **83**, 161-171.

> *design, development and application of computer models; design and implementation of PGSE NMR experiments; analysis and interpretation of experimental and simulation data; formulation of theory in collaboration with co-author*

VI. Regan D.G., Kuchel P.W. (2002) Simulations of NMR-detected diffusion in suspensions of red cells: the 'signatures' in q-space plots of various lattice arrangements. *Eur. Biophys. J.*, (in press**)**.

> *design, development and application of computer models; analysis and interpretation of simulation data; formulation of theory in collaboration with co-author*

VII. Regan D.G., Chapman B.E., Kuchel P.W. (2002) PGSE NMR Diffusion study of the self-association of N-methylacetamide in carbon tetrachloride. *Magn. Reson. Chem.*, (in press**)**.

> *design, development and application of computer models; design and implementation of PGSE NMR experiments; analysis and interpretation of experimental data; formulation of theory in collaboration with co-authors*

Preface

Here I describe the investigation of diffusion in compartmentalized and heterogeneous systems. The work entailed combining the experimental results from pulsed field-gradient spin-echo nuclear magnetic resonance (PGSE NMR) experiments with those obtained with computer simulations of the systems under investigation.

Erythrocyte (red blood cell; RBC) suspensions provided the cellular model for the study of diffusion in compartmentalized systems and computer models were developed to simulate these samples. Simulations were also performed on a more idealized system in which the cells were oblate-spheroids. Both systems were simulated in the context of PGSE NMR experiments. Central to this work were the concepts of q-space and diffusion-coherence. We have shown that diffusion-coherence phenomena can be interpreted, by means of q-space analysis, to provide unique information about cell suspensions. This information includes cell dimensions and spacing, membrane transport rates, and the geometrical arrangement of cells in the suspension. The computer models assisted in the assignment of coherence features to particular modes of diffusion (Paper I), and were used to explore and interpret some of the many complex 'signatures' present in q-space data (Papers V and VI). They were also used to develop a theory which relates membrane transition probability to membrane permeability in the context of the simulations (Paper II).

The diffusion tensor is a useful indicator of diffusion anisotropy in heterogeneous systems and in this work we showed that it provided additional confirmation of erythrocyte alignment in the static magnetic field of the NMR spectrometer (Paper III). Furthermore, it contains information relating to the arrangement of cells in the suspension (Paper VI).

Two quite different multicomponent systems were studied using PGSE NMR diffusion measurements. The first of these was tropoelastin, the monomeric subunit that is cross-linked in elastic fibers, which forms a coacervate under certain condition of temperature, pH, and salt concentration. This work was carried out to provide complementary data to those obtained using analytical ultracentrifugation and which suggested that soluble tropoelastin existed as two distinct isoforms (Paper IV). Computer modeling was again used to test this theory against various possible overall protein conformations.

The second multicomponent system that was studied was *N*-methylacetamide (NMA) in carbon tetrachloride. NMA is known to self-associate through the formation of hydrogen bonds in a manner that is both temperature and concentration dependent. The aim of the work was to use PGSE NMR to extend the temperature and concentration range beyond that available to analytical ultracentrifugation, for estimating hydrodynamic and thermodynamic parameters of multicomponent systems. A computer model was developed around the Kirkwood-Riseman theory of macromolecular diffusion, and was used in conjunction with PGSE NMR diffusion measurements to estimate equilibrium constants and oligomer population distributions (as a function of NMA concentration) on the basis of an attenuative model of indefinite self-association (Paper VII).

An historical perspective and a general outline of the studies described in Papers I-VII is given in the Introduction (page vii). Sections 1-6 cover topics central to these papers and provide more in-depth background information than is supplied by them. Sections 7 and 8 contain summaries of the results obtained and the conclusions drawn from them, respectively. Finally, it is noted that this, like all scientific endeavors, is work in progress and Section 9, Future Directions, sets out what I believe to be the important steps that should be taken to advance the areas of research dealt with in this thesis. Indeed, some of this work is already underway and data have already been obtained which will appear in future publications but are beyond the scope of the present treatise.

Contents

Introduction

There are few processes more fundamental to physical and biological systems than those by which molecules are transported, leading to interactions with each other and with various components of their environment. Two primary underlying mechanisms of molecular transport are diffusion and locally coherent flow. In living systems, molecular diffusion is a major factor in determining the rates at which life-sustaining processes occur in and around cells. The study of diffusional behavior in biological systems, and the development of methods to measure and characterize it, are therefore of central importance in Biological Chemistry.

While a number of methods are available for measuring self-diffusion coefficients (see footnote 1 on page 1 for a definition of "self-diffusion"), pulsed field-gradient spin-echo nuclear magnetic resonance (PGSE NMR) has become the method of choice for this type of measurement in biological systems. The reasons for this include: the non-invasive nature of the technique; the ability to measure molecular displacements on the micrometre distance scale, which is the scale of cells and organelles; the wide range of temperatures and pressures over which measurements can be made; and the ability to make measurements on systems under both equilibrium and non-equilibrium conditions. In addition to self-diffusion coefficients, the study of diffusional behavior by PGSE NMR can provide structural information about tissues, and thermodynamic and kinetic parameters of reactions and interactions. The diffusional properties of tissues can be exploited in diffusion-weighted magnetic resonance imaging (DT MRI) to give improved image contrast over traditional MRI; both of these techniques are based on the application of pulsed magnetic field-gradients.

From an historical perspective it was Hahn (1950) in his seminal paper on spin-echoes who first pointed out that the echo amplitude from this simple experiment would be attenuated by molecular diffusion through fluctuations in the local magnetic field. Carr and Purcell (1954) followed up on this observation with a formal treatment of the effects of molecular diffusion on the amplitude of spin-echo signals, and suggested a variation of Hahn's spin-echo experiment involving radio frequency (rf) pulses of different duration to more accurately measure transverse relaxation times (T_2) in the presence of locally inhomogeneous magnetic fields. In this paper they also

demonstrated that the method could be used directly to measure molecular self-diffusion; and an estimate of the self-diffusion coefficient of water at 25ºC was obtained that was in close agreement with previous non-NMR determinations. The first suggestion of the pulsed field-gradient method appeared in a paper by McCall, Douglas, and Anderson (1963) and the experiment was later effectively demonstrated by Stejskal and Tanner (1965). An important development in this paper was the derivation of the exact dependence of the amplitude of the spin-echo signal on the self-diffusion coefficient, for magnetic field-gradient pulses of finite duration. This formulation was encapsulated in a more general propagator formalism which was able to account for restricted and otherwise anisotropic diffusion (Stejskal 1965).

These ground-breaking papers showed that magnetic field gradients could be used to encode spatial information in the phase of spin magnetization in order to measure positional displacement. Yet more than two decades passed from the time of Hahn's original spin-echo experiment until the realization and demonstration by Lauterbur (1973), and independently Mansfield and Grannell (1973), that this spatial encoding could be used to obtain structural information from heterogeneous systems. These two papers presented quite different approaches to the study of structure in solids but the analogy to optical diffraction suggested by Mansfield and Grannell is of particular relevance to the work on cell suspensions described in this thesis. The measurement of positional displacement by NMR as a probe of structure and compartmentation is now well established and has been extensively described in the context of NMR diffraction (Callaghan et al. 1991; Callaghan et al. 1992) and in more general terms using the diffusion propagator representation (Kärger and Heink 1983; Cory and Garroway 1990; Mitra et al. 1992).

Kuchel, Coy, and Stilbs (1997) were the first to demonstrate that this approach could be applied to cell suspensions which can also be thought of as being compartmentalized. They showed that diffraction-like effects from PGSE NMR experiments on erythrocyte suspensions could be observed in so-called "q-space plots" and that the features of these plots contained information relating to cell dimensions and the rate of water exchange across the membrane. Furthermore, the shape of the q-space plot was dependent on the direction in which diffusion was measured providing evidence of alignment of the cells in the suspension. In paper I, we used Monte Carlo random walk simulations of diffusion in erythrocyte

suspensions that I developed, in conjunction with PGSE NMR data, to show that various features of the q-space plots could be assigned to different modes of diffusion. In Paper II, I extended this work to show the relationship between membrane permeability and certain parameters used in the Monte Carlo approach, and to show that it is the combination of the diffusion coefficient and the dimensions of the enclosing compartment that determine the mean residence time (MRT) of the diffusant in the compartment. The work described in Papers V and VI investigated the effects of changing cell geometry, packing density, and packing arrangement on the shape of the q-space plot, as well as presenting methods for analysis and interpretation of the data.

Modern triple-axis NMR diffusion probes, which enable the measurement of diffusion in any combination of the x-, y-, and z- Cartesian directions, facilitate the study of diffusion anisotropy which can be expressed in terms of a 3×3 diffusion tensor. In Paper III this method is used to provide further evidence that erythrocytes align in the magnetic field of the spectrometer; and a method is presented, which employs the symbolic algebra package *Mathematica*, for analyzing the experimental data and construction of the diffusion tensor. Diffusion tensor analysis is also used as a method of analyzing the simulation data presented in Papers V and VI.

In addition to compartmentalized systems, this thesis presents the results of investigations I have conducted on multicomponent systems. These systems are heterogeneous in a different sense, because although the diffusion of the individual components is essentially isotropic, the components differ amongst themselves, either spanning a range of molecular weights or existing as different conformational isomers. The two systems studied were: N-methylacetamide (NMA, Paper VII), which is known to self-associate in solution (Klotz and Franzen 1962; Albers et al. 1971; Howlett et al. 1973); and tropoelastin (Paper IV), which also associates under physiological conditions (Vrhovski et al. 1997; Vrhovski and Weiss 1998), but was studied here to test the hypothesis that in its soluble form it exists as two distinct conformational isomers.

These studies combined computer modeling, based on the Kirkwood-Riseman theory of macromolecular diffusion (Kirkwood 1967), with PGSE NMR diffusion data to test various models of self-association and polymer conformation. They also relied heavily on the fact that diffusion measurements made using PGSE NMR yield weight-

average diffusion coefficients and in the fast-exchange regime, ensemble averaging occurs (Callaghan and Pinder 1983). Diffusion measurement on proteins by PGSE NMR are typically more difficult than for small molecules due to slow diffusion and short transverse (T_2) relaxation times (Haner and Schleich 1989). While tropoelastin is not typical in this respect, careful experimental design was required to make accurate diffusion measurements.

This section of my work demonstrates, I believe, that NMR can be used very fruitfully in a manner that is similar in many ways to the use of analytical ultracentrifugation for the study of multicomponent systems. It has the advantage of not being subject to some of the limitations imposed by that method on elements of experimental design, such as temperature range, duration of experiments, and ease of preparation of samples.

1   Diffusion in Biological Systems

Underlying the enormous molecular complexity of living organisms and their behavioral processes is the process of diffusion by which the participating molecules migrate in solution and encounter one another. The growth in interest in this process has stemmed largely from the increase in the number and power of available techniques for measuring diffusion, and the increasingly important role of NMR imaging in biomedicine. All of the work described in this thesis focused on the measurement of diffusion by NMR, and the interpretation of the experimental data, for particular biological or model-biological systems. This section provides a brief overview of the theory of diffusion, and describes the methods used for its measurement by NMR, including the interpretation of experimental data. In addition, the characteristics of the systems which were investigated and the motivation for studying them are outlined.

1.1 General Diffusion Theory

Translational molecular diffusion refers to the random migration of molecules that arises from motion due to thermal energy. In the case of self-diffusion[1] the net force acting on an ensemble of molecules is zero and the process is consequently macroscopically not immediately apparent. In 1828 Brown first noted the macroscopic manifestation of this process as the irregular motion of tiny pollen grains on the surface of water, giving rise to the term "Brownian" motion which refers to the observable manifestation of diffusion but not to the underlying physical process.

Fick (1855) recognized the analogy between the transfer of heat by conduction due to random molecular motion and the process of diffusion. He formulated the hypothesis that the rate of transfer of a diffusing substance through unit area of section is proportional to the concentration gradient measured normal to the section, i.e.,

$$J = -D\frac{\partial C}{\partial x},$$

(1.1)

---

[1] Self-diffusion is defined as being diffusion in a system which contains only two distinguishable (e.g., by isotopic labeling, nuclear magnetic dipole vector orientation, etc) forms of the same chemical species (Tyrrell and Harris 1984)

where J is rate of transfer per unit area (flux), C is the concentration of the diffusant, x is the distance coordinate measured normal to the section, and D is the self-diffusion coefficient. This equation, known as Fick's first law, is only valid for isotropic media in which structural and diffusional properties are the same in all directions (Crank 1975). For anisotropic diffusion the more general differential equation of diffusion, known as Fick's second law, applies:

$$\frac{\partial C}{\partial t} = D\nabla^2 C ; \qquad (1.2)$$

where ∇^2 is the second order spatial derivative or Laplacian.

Einstein (1905; 1956) explained the phenomenon of Brownian motion in terms of the bombardment of the observable particles by microscopic particles in the liquid obeying a Maxwellian velocity distribution. He derived the relationship, now referred to as the Einstein diffusion equation, which relates the mean-square of the displacement s of the particle in time t to the self-diffusion coefficient. For unbounded diffusion in three dimensions the equation is;

$$\langle s^2 \rangle = 6Dt . \qquad (1.3)$$

This relationship can be derived in a number of ways but perhaps the simplest is the random walk method which forms the basis of many of the simulations described in this thesis (Papers I, II, V, and VI). While Eq. 1.3 is valid for isotropic unbounded (on the scale of s) diffusion at infinite dilution, more complicated expressions are required when these criteria are not met (Crank 1975; Waldeck et al. 1997). Bounded diffusion is discussed briefly in Section 1.2.

The translational self-diffusion coefficient for uncharged particles at infinite dilution is related to the bulk viscosity of the medium by the Einstein-Smoluchowsky equation (Tanford 1961):

$$D = \frac{kT}{f} , \qquad (1.4)$$

where f is the hydrodynamic frictional coefficient of the diffusant, k is Boltzmann's constant, and T is the absolute temperaturre. For a hard sphere having a hydrodynamic radius (called the Stokes radius) r_h, moving in laminar flow in a medium of viscosity η, the value of f is given by:

$$f = 6\pi\eta r_{\mathrm{h}}. \hspace{4cm} (1.5)$$

Equations 1.3, 1.4, and 1.5 form the basis for calculating intrinsic self-diffusion coefficients in the computer models described in Papers I, II, and IV-VII.

1.2 Bounded Diffusion

Bounded or restricted diffusion refers to a class of anisotropic systems in which diffusion is impeded by the presence of impermeable or semi-permeable barriers which are separated by distances of the order of s (see Eq. 1.3). In these systems, the experimentally determined values of the self-diffusion coefficient appear to be diffusion-time dependent taking a maximum value at short observation times and reaching a limiting value of zero for long observation times (Tanner and Stejskal 1968). This is due to the diffusant being reflected multiple times off the restricting barriers such that the net displacement over the time of the experiment is less than would be the case in the absence of the barriers. Self-diffusion coefficients measured under conditions of restriction are therefore referred to as 'apparent' self-diffusion coefficients and as 'intrinsic' self-diffusion coefficients in the absence of restriction.

PGSE NMR (see Section 1.3), which is capable of resolving displacements on the micrometre scale, is a particularly useful technique for probing restricted diffusion and has been used extensively, for example, in studying diffusion behavior in microporous solids (Kärger et al. 1994; Callaghan 1996) and in erythrocyte suspensions (Tanner 1983; Kuchel et al. 1997). The diffusion of water in erythrocyte suspensions, the subject of Papers I-III, V and VI, is of particular interest because water exchanges across the cell membrane (see Section 3.5) between the intra- and extracellular regions and its diffusional behavior in each region is distinct (see Section 1.7.1).

The value of the apparent self-diffusion coefficient reflects the mathematical form of the 'propagator' for the system i.e., the conditional probability that a molecule initially at a position $\mathbf{r}_0$ will be found at a position $\mathbf{r}$ after a time interval Δ (Kärger and Heink 1983). The propagator, in effect, contains all the relevant information regarding the translational properties of the system, on a microscopic scale. However, for all but a few limiting cases (Crank 1975; Coy and Callaghan 1994; Kuchel and Durrant 1999), an analytical representation of the propagator for heterogeneous systems is mathematically intractable and for this reason a Monte Carlo random walk

approach was adopted in the work described here for studying diffusion in cell suspensions (see Section 5).

1.3 PGSE NMR Measurement of Diffusion

PGSE NMR has become the method of choice for measuring molecular diffusion. It is particularly appropriate for the study of transport processes in biological systems (Waldeck et al. 1997) because it is non-invasive and is able to resolve molecular displacements in the range 0.01-100 μm, the distance-scale of organelles and cells. In addition to measuring transport processes in biological systems, the method is also useful for measuring thermodynamic binding constants (Lennon et al. 1994) and both of these applications have been exploited in the work described herein. The methods for measuring molecular diffusion by NMR have been comprehensively reviewed (Stilbs 1987; Kärger et al. 1988) and so only a brief overview is given here.

The basis of NMR diffusion measurements is the Hahn spin-echo experiment (Hahn 1950). The original experiment, which employed a steady gradient, has been superseded by pulsed-gradient methods (Stejskal and Tanner 1965) which, along with higher gradient magnitudes, extend the range of measurable self-diffusion coefficients. The general principles of both methods, however, are the same.

If we consider a sample of NMR-sensitive nuclei in a homogeneous magnetic field $\mathbf{B}_0$, the frequency ω of their precession is given by the Larmor equation:

$$\boldsymbol{\omega} = -\gamma \mathbf{B}_0 ; \qquad\qquad (1.6)$$

where γ is the nuclear magnetogyric ratio. If a magnetic field-gradient is then superimposed upon the sample, the nuclei will experience a shift in precessional phase which depends on their position in the sample; in other words, the spatial position of a nuclear ensemble (spin isochromat) in the sample is "encoded" in the phase of its nuclear magnetization vector. It is this principle that forms the basis of the PGSE method for measuring molecular diffusion.

The standard PGSE pulse sequence is illustrated in Fig. 1.1A. According to this scheme the static magnetic field is aligned along the z-axis and the exciting radio frequency (rf) field is applied along the x-axis in the rotating frame of reference. As a result of the first $\pi/2$ (90º) rf pulse, the net magnetization vector is nutated into the x-y plane and lies along the y-axis. A linear field gradient pulse of duration δ and

magnitude g is then superimposed on $\mathbf{B}_0$ to bring about the positional encoding described above. The second π rf pulse is applied after a time τ, which is sufficient for all phase coherence, macroscopically averaged across the sample, to be lost, and all magnetization that is in the x-y plane is nutated 180º around the x-axis. The second field-gradient pulse is then applied for a duration δ such that the two gradient pulses are separated by a time interval Δ. For nuclear spins that have remained motionless during Δ, this second field-gradient pulse had the effect of reversing the precessional phase shift induced by the first field-gradient pulse, refocusing is said to occur in that phase coherence is restored and an unattenuated echo signal is induced in the receiver coil of the spectrometer. If, on the other hand, diffusional displacement has occurred during Δ, refocusing is incomplete resulting in attenuation of the echo signal. The degree of attenuation with respect to the signal acquired when g is equal to zero is therefore a measure of the dynamic displacement. This relationship is expressed in the following equation (Stejskal and Tanner 1965):

$$E = \ln\left[\frac{A_g}{A_0}\right] = -\left(\gamma\delta g\right)^2 D\left(\Delta - \frac{\delta}{3}\right); \qquad (1.7)$$

where E is the natural logarithm of the relative signal intensity, A_0 is the amplitude of the signal when $g = 0$, and A_g is the amplitude when $g \neq 0$.

For isotropic diffusion, the self-diffusion coefficient can be obtained by calculating the slope of the regression line for a plot of relative signal intensity as a function of the Stejskal-Tanner parameter b (so-called Stejskal-Tanner plot) given by:

$$b = -(\gamma\delta g)^2\left(\Delta - \frac{\delta}{3}\right). \qquad (1.8)$$

In cases where the sample is polydisperse with respect to the observed species, the self-diffusion coefficient yielded by PGSE NMR will be a weight-average self-diffusion coefficient (Callaghan and Pinder 1983) as discussed in Section 1.7.2. If the components giving rise to the polydispersity are in rapid exchange on the NMR time-scale, ensemble averaging occurs and the Stejskal-Tanner plot will be linear. If the exchange is not rapid, the Stejskal-Tanner plot will be the result of a sum of exponentials arising from the signal traces of the discrete components and will be curvilinear. In this latter case the self-diffusion coefficient can not be simply obtained from the slope of the curve.

1.4 Pulse Sequences

The standard spin-echo (SE) NMR pulse sequence for measuring diffusion (90º - τ - 180º - τ – acquire) has been described in Section 1.3 above and is illustrated in 1.1A. This pulse sequence is generally applicable for diffusion measurements on small molecules where the rate constant for transverse relaxation ($1/T_2$) is comparable to that of longitudinal relaxation constant ($1/T_1$), and in the absence of convection. More elaborate pulse sequences must be employed for studying the diffusion of large molecules where T_2 is usually much less than T_1, and when convection is present.[2] The effects due to convection are usually more apparent for large molecules having smaller self-diffusion coefficients because the signal attenuation due to convective flow is large in comparison to that due to diffusion for a given magnitude of field-gradient.

In the PGSE-based stimulated-echo (STE) technique (Hahn 1950; Stilbs 1987; Kärger et al. 1988) a three-pulse sequence is used, as is illustrated in Fig. 1.1B. The advantage of this method is that in the entire interval between the second and third $\pi/2$ pulses, the NMR signal is dampened by longitudinal rather than transverse relaxation. This allows for the measurement of smaller self-diffusion coefficients associated with large molecules where T_1 often greatly exceeds T_2. However, because only one-half of the equilibrium magnetization contributes to the stimulated-echo (Tanner and Stejskal 1968), the amplitude of the acquired echo will be at most 50% of the original magnetization. The lower limit of self-diffusion coefficient that can be measured using this method depends both on the system under investigation and the sensitivity of the spectrometer (Kärger et al. 1988).

Convection currents may arise in samples of low viscosity when heating or cooling of the sample is not homogeneous over its entire length. Sample heating or cooling in the NMR spectrometer is generally achieved by using a stream of temperature-regulated air fed in through the bottom of the probe. When the sample is being heated from below by air at a temperature which is above that of room air convective flow results from temperature gradients over the length of the sample. The extent and rate of dissipation or persistence of these temperature gradients depends on the viscosity of

---

[2] The 'rule of thumb' adopted in the work described in this thesis was that in the absence of convection and for values of Δ less than about 40 ms, the standard SE pulse sequence is appropriate.

the sample, the efficiency of heat transfer, sample geometry, gas flow rate, and probe design.

If the conventional PGSE sequences described above are used to measure diffusion in the presence of convection, the measured values will be artefactually high (Goux et al. 1990). When raising the temperature of samples it is therefore necessary to take measures to either minimize convection[3] or to compensate for it so that such artefacts are obviated. Double-SE (Callaghan 1991; Callaghan and Xia 1991) and double-STE (Jerschow and Müller 1997) pulse sequences have been developed to compensate for convection, and these are illustrated in Figs 1.1C and 1.1D, respectively. The pulse sequences rely on the convection being able to be approximated by constant laminar flow during the diffusion measuring interval, thus allowing for the cancellation, by refocusing, of resulting coherent phase shifts[4]; they are not suitable for compensating for turbulent flow. The double-SE/STE pulse sequences are the equivalent to two identical standard SE/STE sequences applied in succession, leading to a doubling of the attenuation of the echo signal in comparison with the single SE for a given magnitude and duration of field-gradient pulses. Consequently, in calculating the self-diffusion coefficient from the Stejskal-Tanner plot (see Section 1.3) Eqs 1.7 and 1.8 become:

$$E = \ln\left[\frac{A_{\mathrm{g}}}{A_0}\right] = -2\left(\gamma\delta g\right)^2 D\left(\Delta - \frac{\delta}{3}\right); \qquad (1.9)$$

$$b = -2\left(\gamma\delta g\right)^2\left[\Delta - \frac{\delta}{3}\right]. \qquad (1.10)$$

---

[3] It is difficult to eliminate convection altogether but it is usually possible to minimize its effects by using sample rotation (while I have not used this method I have some reservations regarding its effectiveness), special sample cells and transverse gradients (Lounila et al. 1996; Jerschow and Müller 1997; Esturau et al. 2001).

[4] An explanation for these phase shifts as well as the underlying principle of the double spin-echo to compensate for them was first suggested by Carr and Purcell (1954).
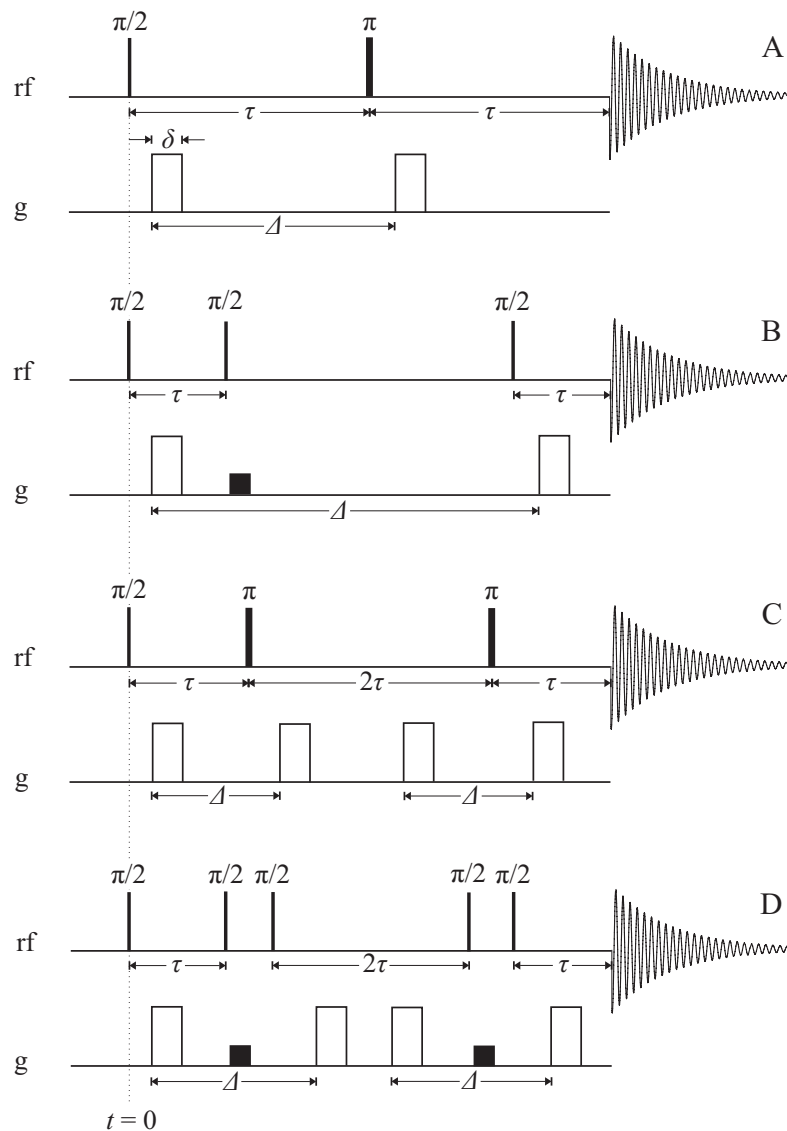
Figure 1.1. PGSE NMR pulse sequences used for measuring molecular diffusion. Radio frequency (rf) pulses are depicted as solid bars and magnetic field-gradient pulses are depicted as open rectangles below the rf pulses. The solid rectangles represent homospoil pulses used to remove any residual magnetization remaining in the x-y plane during the storage period of the STE pulse sequences. The intervals between rf pulses during which the magnetization is in the *x-y* plane are given in terms of τ. The duration of the gradient pulses is denoted by δ. The time intervals separating pairs of gradient pulses are denoted by Δ. The FIDs are purely illustrative and are not drawn to scale either in time or in amplitude. The pulse sequences are all drawn to be of equivalent total duration to give an indication of the relative magnetization evolution times but in practice other considerations will determine this. The vertical dotted line depicts the start (t = 0) of the excitation of the nuclear population by the pulse sequence. A) Standard PGSE pulse sequence. B) PGSE-based STE pulse sequence. C) Standard PGSE pulse sequence with convection compensation. D) PGSE-based STE pulse sequence with convection compensation.

1.5 Diffusion Coherence and q-Space

In physical optics, two light sources derived from a single source and bearing a constant phase relationship are said to be coherent. Optical interference and diffraction patterns arise as a result of overlapping waves arriving at a particular point in space in phase coherence or non-coherence.

Phase coherence also occurs for nuclear magnetic spins in a magnetic field-gradient. If the field-gradient is linear, coherence occurs when the distance separating the spins, in the direction of the field, is of a specific value as determined by the strength of the field-gradient. If the spins are homogeneously dispersed in the field-gradient the sum of these coherences will be zero. However, if the sample is heterogeneous such that the spins are restricted to compartments or otherwise obstructed, an effect that is mathematically analogous to interference/diffraction can be observed as a result of local phase coherences (Callaghan et al. 1991; Mitra and Sen 1992).

In an erythrocyte suspension, solute and solvent molecules diffuse in two distinct regions: intracellular diffusion is bounded by the plasma membrane, but these membranes also impede extracellular diffusion. Kuchel at al. (1997) showed that diffusion-coherence effects are manifest in PGSE NMR data as a result of this compartmentalization. Two distinct effects are observed: diffusion interference is due to the displacement of spins between adjacent interstitial "pores" formed by the closely packed cells and is known as "pore-hopping"; and diffusion-diffraction, which is due to spins diffusing within the restricted confines of the cell and can be described mathematically in terms of the autocorrelation or "shape" function of the cell.

The diffusion-coherence phenomenon described above can be visualized by plotting the signal intensities from a PGSE NMR experiment as a function of the wave number vector **q** in a *q*-space plot, where the magnitude of **q** is given by:

$$q = (2\pi)^{-1} \gamma \delta g . \qquad (1.11)$$

q-Space refers to the reciprocal space, in the Fourier transform sense, of spin displacement. Diffusion-interference is manifested as a shoulder in the initial part of the attenuation curve and diffusion-diffraction as a subsequent series of maxima and minima (see Fig. 1.2). Paper I deals with the assignment of these features to the

particular modes of diffusion as described above and shows that the *q*-values corresponding to maxima and minima in the *q*-space plot can be reciprocally related to cell dimensions and cell spacing.
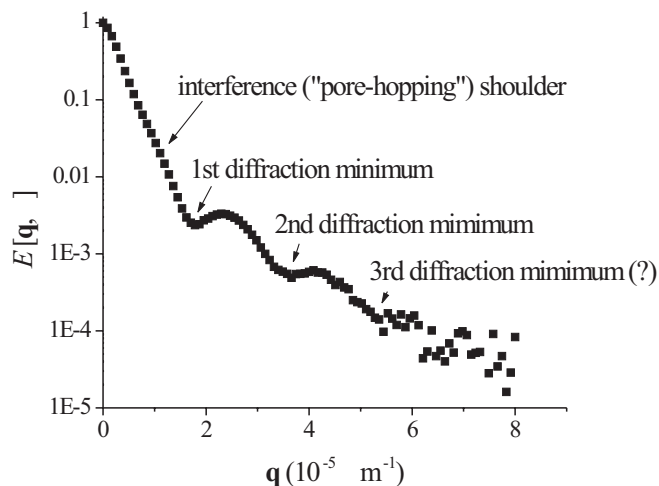
Figure 1.2. A typical *q*-space plot derived from a sample of human erythrocytes with the pore-hopping shoulder and the first two diffusion-diffraction minima labeled accordingly. A third putative diffusion-diffraction minimum is labeled with a question mark to indicate uncertainty as to its position. The *q*-values corresponding to the pore-hopping shoulder and diffusion-diffraction minima bear a simple inverse relationship with the spacing between extracellular pores (and consequently the cells) and the projection of the mean dimension of the cells, in the direction of the applied magnetic field-gradient, respectively.

1.6 Diffusion Tensors

When diffusion is anisotropic, the value of the self-diffusion coefficient can not be expressed as a single scalar value. Somehow account must be taken of the behavior of the diffusant in all directions in the reference frame. The diffusion anisotropy that is present in heterogeneous systems can be expressed as a 3×3 array of values known as a diffusion tensor. In ordered systems such as some biological tissues the elements of the tensor provide information about the orientation of the local structures causing the anisotropy. Techniques such as diffusion-tensor magnetic resonance imaging (DT MRI) are based on this principle (Basser et al. 1994).

With modern NMR triple-axis gradient probes, which allow the measurement of diffusion along any combination of the *x*-, *y*-, and *z*- Cartesian axes, it is possible to construct a diffusion tensor from PGSE NMR data. Paper III demonstrates how this is

done and provides additional confirmation of the alignment of erythrocytes in the magnetic field of the spectrometer. Furthermore, a simplified method is described for facilitating the analysis of diffusion tensor data. This paper provides a thorough theoretical background to diffusion tensors in the PGSE NMR context hence no further treatment of the topic is given here.

1.7 Diffusion in Heterogeneous Systems

The term 'heterogeneous systems' in the context of this thesis refers to those in which diffusion is anisotropic, due to the presence of impeding barriers, or in which the observed species is present in a number of isoforms or aggregation states. PGSE NMR is a particularly powerful tool for studying these types of systems for a number of reasons: it is non-invasive; molecular displacements in the micrometre range can be observed; measurements can be made over a wide range of temperatures and pressures; in a single experiment it is possible to measure the diffusion of multiple species; the signal-to-noise ratio can be improved by repeating the identical experiment a large number of times when the system is at equilibrium, but the method may also be applied to non-equilibrium systems.

The heterogeneous systems investigated here fall into two main categories: compartmentalized systems represented by cell suspensions (Papers I-III, V, and VI); and multicomponent or polydisperse systems represented by tropoelastin (see Section 4.1) and N-methylacetmide (NMA: see Section 4.2). The following sections provide a brief outline of these types of systems in the context of PGSE NMR diffusion measurements.

1.7.1 Compartmentalized Systems – Erythrocyte Suspensions

Erythrocyte suspensions provided the biological model of a compartmentalized system for the diffusion studies described in Papers I-III, V, and VI. Kuchel et al. (1997) first showed that diffusion-diffraction effects were manifest in PGSE q-space data (see Section 1.5) from water in erythrocyte suspensions and the work described in subsequent papers involved the characterization of these effects, with the aid of computer models, and the development of methods of data analysis and interpretation.

 In an erythrocyte suspension, there are two types of compartment between which water is able to exchange via the semi-permeable plasma membrane of the cells (see Section 3.5). The erythrocytes themselves constitute one type of compartment and,

ignoring exchange, can be viewed as a system of isolated pores. Conversely the extracellular space, which constitutes the second type of compartment, can be seen as a network of interconnected pores created in the suspension by the closely packed cells; the pores become better defined and their geometric centers become closer as the packing density of the cells is increased. Water is able to move relatively freely between the interconnected extracellular pores, between the intra- and extracellular pores via the plasma membrane, and between cells via the plasma membrane and the extracellular spaces.

The features observed in q-space plots from erythrocyte suspensions result from the superposition of the coherences that arise from first- and higher-order displacements of the types just described (diffusion-interference), and the coherences due to diffusion-diffraction of water inside the cells. The degree to which higher order effects will be significant, e.g., the diffusion between next-nearest neighbor pores, will depend on the timescale in which they occur and the observation time of the experiment. In order to observe diffusion-diffraction effects, intracellular diffusion must be restricted on the time scale of the experiment. By derivation from Eq. 1.3 (for the two dimensional case) we can state that this will occur when $\varDelta \gg a^2/2D$, where a is the mean dimension of the cell in the direction in which diffusion is being measured.

For water in an erythrocyte suspension, the features of the q-space plot will generally be dominated by those arising from the diffusion-diffraction of water inside the cells. This is because the extracellular water, which is less restricted and has a larger intrinsic self-diffusion coefficient due to the lower viscosity of the medium, has a larger apparent self-diffusion coefficient and consequently the PGSE signal is more highly attenuated than that of the intracellular water at a given magnitude of magnetic field-gradient.

1.7.2 Multicomponent Systems – NMA and Tropoelastin

Two quite different multicomponent systems were studied here using PGSE NMR. NMA, the subject of Paper VII, is a small molecule that self-associates in solution and has been extensively studied as a peptide analogue. Tropoelastin, the subject of Paper IV, is a biological macromolecule involved in the formation of elastic fibers; it associates in solution under physiological conditions and in its soluble form is

proposed to exist as two conformationally distinct isomers. Both these systems can be considered to be polydisperse because under the appropriate conditions the species whose diffusional properties are of interest occur in a variety of aggregation or conformation states. The properties, biochemistry, and self-association behavior of these molecules are discussed in Section 4. Following is a brief outline of the implications of making diffusion measurements on polydisperse systems.

For a polydisperse solution consisting of discrete species which are not in exchange (or are in slow exchange on the NMR timescale) and which have a range of molecular weights, the Stejskal-Tanner plot of the PGSE data will be multi-exponential, the sum of the single-exponential decays of signals for each of the individual species. It is known that while methods such as Laplace transformation can be used to extract solutions for the individual self-diffusion coefficients from multi-exponential data, it is difficult to obtain a unique solution. If, however, the species are in rapid exchange on the NMR timescale, ensemble averaging results in a single-exponential dependence of signal intensity on b and a single apparent self-diffusion coefficient representing the weight-average self-diffusion coefficient (D_w) can be estimated (Callaghan and Pinder 1983). In either case, the degree of polysdispersity is expressed as the ratio M_w/M_n, where M_w is the weight-average molecular weight and M_n is the number average molecular weight (Tanford 1961).

While NMA solutions fall into the rapid-exchange category described in the previous paragraph, tropoelastin poses a different sort of problem. In its aggregated state, known as a coacervate (see Section 4.1), the protein becomes insoluble and forms a dense viscous phase in the bottom of the sample tube. This phase separation and the broad signal from the aggregated protein make accurate measurement of the self-diffusion coefficient using PGSE NMR impossible. In its soluble form, however, it is proposed that tropoelastin exists as two conformational isomers (see Paper IV). These two isomers have the same molecular weight but different sedimentation coefficients and presumably, therefore, different diffusion coefficients.

One of the challenges of the work described in Paper IV was to predict, from PGSE diffusion measurements of soluble tropoelastin, whether the two isomers were in the slow- or fast-exchange regime. While slow exchange for a two-species system was expected to give rise to a bi-exponential dependence of signal intensity on b, rapid exchange would result in a mono-exponential dependence due to ensemble averaging.

However, because the two species are conformational isomers, the differences in their self-diffusion coefficients were expected to be very small, due only to differences in their frictional coefficients. Computer modeling was therefore undertaken to determine whether it would be possible to distinguish between the two possibilities, slow or fast exchange, on the basis of the Stejskal-Tanner plots, for a binary system in which the difference in diffusion coefficient is (very) small.

1.8 Kirkwood-Riseman Theory of Macromolecular Diffusion

Equations 1.4 and 1.5 (Einstein-Smoluchowsky and Stokes equations, respectively) can be used in combination to calculate the self-diffusion coefficient of particles which have, or are treatable as having, hard-sphere geometry. These equations were insufficient, however, for estimating the self-diffusion coefficients for tropoelastin and NMA oligomers (Papers IV and VII, respectively) if their structures were assumed to be linearly extended. Kirkwood and Riseman developed a theory, based on statistical mechanical and hydrodynamic principles, which enables the calculation of frictional and self-diffusion coefficient values for macromolecules that are composed of identical subunits.[5] The theory provides a formulation for calculation of these values for molecules having either rod-like (Riseman and Kirkwood 1951) or flexible-chain characteristics (Kirkwood and Riseman 1948; Kirkwood 1949). Previously, formulations which approximated extended molecules as ellipsoidal bodies gave results that were only consistent with experimentally obtained data over a limited range of molecular weights.

The flexible chain model is based on fluid flow through a linear polymer consisting of identical subunits numbered from $-n$ to n and connected by $2n$ bonds of length b_1. The configuration of the polymer is specified by a set of coordinates which implicitly specifies the angles between successive pairs of bonds. The degree of polymerization, Z, is equal to M/M_0 where M and M_0 are the polymer molecular-weight and monomer molecular-weight, respectively. The final result which is relevant to the work described in this thesis is the derivation of formulae for a frictional scaling factor (λ),

---

[5] This theory, in its entirety, as well as more general statistical mechanical theory on irreversible processes in solutions of macromolecules upon which, in turn, this theory is based, can be found in the edited compilation entitled *John Gamble Kirkwood Collected Works. Macromolecules* (Kirkwood 1967).

which effectively scales Eq. 1.4 for a flexible polymer, and the self-diffusion coefficient:

$$\lambda = \frac{\zeta}{\left(6\pi^3\right)^{1/2}\eta_0 b_1}\,;\qquad(1.12)$$

$$D = \left[1 + \left(8\lambda/3\right)Z^{1/2}\right]\left(kT/Z\zeta\right),\qquad(1.13)$$

where ζ is the frictional coefficient of the monomeric subunit; η_0 is the viscosity of the solvent; b_1 is the bond-length; k is the Boltzmann constant; and T is the absolute temperature.

The prescription of the rod-like polymer model is essentially the same as that for flexible-chain polymers except that the bond angle between successive bond vectors is zero. The following formulae are derived for λ and D.

$$\lambda = \frac{\zeta}{6\pi\eta_0 b_1}\,;\qquad(1.14)$$

$$D = \frac{kT}{Z\zeta}2\lambda\left\{\log Z - \left[1 - \left(1/2\lambda\right)\right]\right\}.\qquad(1.15)$$

In the work described in Papers IV and VII, three models were tested: flexible chain and rod-like models as described above; and a model whereby the polymer was treated as a sphere whose volume was based on its molecular weight and partial specific volume (Waldeck et al. 1997). For tropoelastin, the monomer in the flexible-chain and rod-like models was a single amino acid residue, while for NMA oligomers the monomer was a single NMA molecule.

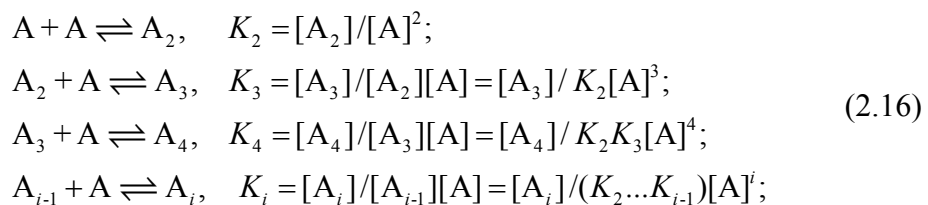## 2   Models of Indefinite Self-Association

Many of the important studies that have been conducted on the self-association of NMA (see Paper VII) have based their analysis and interpretation of data on the assumption of an indefinitely self-associating system (Albers et al. 1971; Howlett et al. 1973). The importance of these types of systems in biology and a description of NMA self-association are given in Section 4.

Three models of indefinite self-association were tested against experimental PGSE NMR diffusion data for NMA in the work described in Paper VII: an isodesmic model according to which the equilibrium constant for dimer formation and for higher orders

of association are equal; a semi-isodesmic model where the dimerization and higher order association constants are not equal; and an attenuative model in which successive equilibrium constants are attenuated by an amount that is proportional to the order of association. Following is a general mathematical description of indefinite self-association and its application to the isodesmic, semi-isodesmic, and attenuative models.[6]

2.1 General Formulation

The equilibria in an indefinite self-association of a solute A can be represented in terms of the molar concentrations (indicated by square brackets) of the species involved (A, A_2, A_3 … A_i), and the respective equilibrium constants (K_2, K_3 … K_i):

$$
\begin{aligned}
A + A &\rightleftharpoons A_2, \quad K_2 = [A_2]/[A]^2; \\
A_2 + A &\rightleftharpoons A_3, \quad K_3 = [A_3]/[A_2][A] = [A_3]/K_2[A]^3; \\
A_3 + A &\rightleftharpoons A_4, \quad K_4 = [A_4]/[A_3][A] = [A_4]/K_2K_3[A]^4; \\
A_{i-1} + A &\rightleftharpoons A_i, \quad K_i = [A_i]/[A_{i-1}][A] = [A_i]/(K_2...K_{i-1})[A]^i;
\end{aligned}
\tag{2.16}
$$

where $i = 2,…,\infty$. The total molar concentration C_T of solute A in all its forms can be expressed as:

$$
\begin{aligned}
C_T &= [A] + 2[A_2] + 3[A_3] + 4[A_4]... \\
&= [A](1 + 2K_2[A] + 3K_2K_3[A]^2 + 4K_2K_3K_4[A]^3 + ...).
\end{aligned}
\tag{2.17}
$$

The mole fraction of monomer α, and the weight fraction of higher order oligomers $α_i$ are given by, respectively:

$$
α = [A]/C_T = 1/(1 + 2K_2[A] + 3K_2K_3[A]^2 + 4K_2K_3K_4[A]^3 + ...); \tag{2.18}
$$

$$
α_2 = 2[A_2]/C_T, \quad α_3 = 3[A_3]/C_T, \quad α_4 = 4[A_4]/C_T, \quad α_i = 2[A_i]/C_T. \tag{2.19}
$$

All $α_i$ can, of course, be expressed in terms of α and the equilibrium constants. It must be stressed that the above formulation is only applicable to an indefinite association and not to one where the association is "capped" at a certain order of oligomerization.

---

[6] A full derivation of all the equations in this chapter can be found in the review of indefinite self-association models by Martin (1996).

2.2 Isodesmic

In an isodesmic self-association all equilibrium constants are equal:

$$K_E = K_2 = K_3 = K_4 = ... = K_i.$$ (2.20)

Once again $i = 2,...,\infty$. By defining two dimensionless variables, $x = K_E[A]$ and $L = K_E C_T$, an expression can be derived for the mole fraction of monomer:

$$\alpha = [A]/C_T = x/L = (1-x)^2 = (1-\alpha L)^2 ;$$ (2.21)

which yields

$$\alpha = \frac{2L+1-\sqrt{4L+1}}{2L^2}.$$ (2.22)

As already mentioned above, the weight fractions of higher-order oligomers can be expressed in terms of α and the equilibrium constants, in this case simply K_E.

2.3 Semi-Isodesmic

In a semi-isodesmic self-association the equilibrium constant for dimerization differs from that for higher order oligomerization. Here we define the ratio $\rho = K_2 / K_E$ and Eq. 2.20 becomes:

$$K_E = K_2 / \rho = K_3 = K_4 = ... = K_i.$$ (2.23)

When $\rho > 1$, dimerization is favored over higher order oligomerization. This may occur when there is steric interference or electrostatic repulsion between solute molecules. Conversely, $\rho < 1$ implies that dimer formation is less favorable than higher order oligomers; and the involvement of a nucleation process is characterized by $\rho << 1$. Clearly, when $\rho = 1$, we have an isodesmic self-association. For the semi-isodesmic self-association it can be shown that:

$$\alpha = (1-x)^2 /(1-x(2-x)(1-\rho));$$ (2.24)

which reduces to Eq. 2.21 when $\rho = 1$. With $x = \alpha L$ from Eq. 2.21, Eq. 2.24 becomes:

$$\alpha^3 L^2(\rho-1) + \alpha^2 L(L-2(\rho-1)) - \alpha(2L+1) + 1 = 0.$$ (2.25)

For both the isodesmic and semi-isodesmic schemes, the weight fraction of higher order oligomers is given by (remembering that for the isodesmic model $\rho = 1$):

$$\alpha_i = \rho i [\mathrm{A}]^i K_{\mathrm{E}}^{i-1} / C_{\mathrm{T}} = \rho i \alpha x^{i-1} = \rho i \alpha^i L^{i-1}, \quad i \geq 2 \,. \tag{2.26}$$

2.4 Attenuative

A full description of the attenuative model is given in Paper VII but the formulation is presented here in brief for completeness. This model of self-association requires successive equilibrium constants to be attenuated according to $K_{\mathrm{A}i} = K_{\mathrm{A}} / i$ so that:

$$K_2 = \tau K_{\mathrm{A}} / 2, \quad K_3 = K_{\mathrm{A}} / 3, \quad K_4 = K_{\mathrm{A}} / 4, ..., K_{\mathrm{A}i} = K_{\mathrm{A}} / i \,. \tag{2.27}$$

The ratio $\tau = 2K_2 / K_{\mathrm{A}}$ is specified and is analogous to ρ in the previous section; in this case a value of $\tau > 2/3$ favors dimer formation. By defining the two dimensionless variables $x = K_{\mathrm{A}}[\mathrm{A}]$ and $L = K_{\mathrm{A}} C_{\mathrm{T}}$ it can be shown that:

$$\alpha = x / L = 1 / (1 + \tau (\mathrm{e}^x - 1)) \,, \tag{2.28}$$

which must be solved numerically; and

$$\alpha_i = \tau \alpha x^{i-1} / (i-1)! = \tau \alpha^i L^{i-1} / (i-1)!, \quad i \geq 2 \,. \tag{2.29}$$
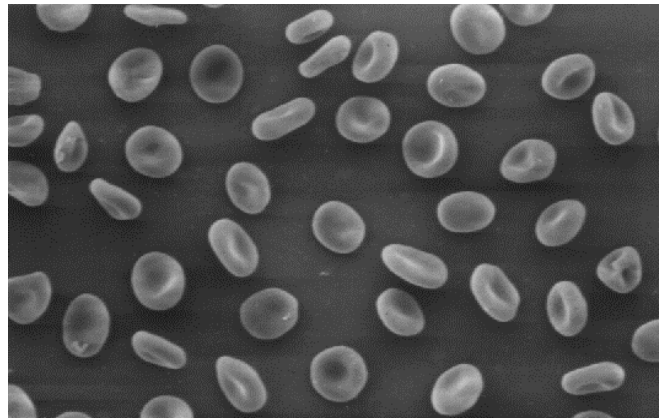
3   Biology of Human Erythrocytes

Much of the work described in this thesis involved the experimental analysis and simulation of diffusion of water in suspensions of erythrocytes and erythrocyte-shaped cells. Experiments and modeling were conducted at a biophysical level but it seemed relevant to provide some general background on the biology of these important cells, because the work was intended to illuminate aspects of their cell biology. In addition, an outline of erythrocyte function and cytology relevant to this study is given.

3.1 General Features

The human erythrocyte is a disc-shaped cell which is concave on its two main faces (Fig. 3.1).[7] There are about 25 trillion in the human body and the primary function of these cells is the delivery of oxygen from the lungs to body tissues and the removal of carbon dioxide from the tissues to the lungs, where it is exhaled. This gas transfer is achieved by means of the heme-containing hemoglobin which occupies ~30% of the cell volume. It is the iron containing heme group which gives the erythrocyte its red

---

[7] Erythrocyte shape is discussed in more detail in section 3.3

color and hence the common name "red cell". The mature erythrocyte has no organelles or nucleus and consequently relies on its endogenous store of already produced proteins and enzymes to maintain cellular function and homeostasis.

Figure 3.1. Scanning electron micrograph of human erythrocytes showing their biconcave disc shape. After correction for shrinkage artefacts that arise from fixing the cells, the mean diameter of the whole population was ~8 μm.

Homeostasis also depends to a large extent on the concentration of solutes in the blood plasma (this is the non-cellular part of the blood consisting of ~90% water, ~7% protein, and ~3% electrolytes, amino acids, glucose and other nutrients, various hormones, metabolic "wastes", and traces of other organic and inorganic compounds). Under normal circumstances the plasma is isotonic to the intracellular fluid and a zero osmotic pressure gradient exists across the plasma membrane. If the plasma becomes hypertonic, water leaves the cell and it will crenate. Conversely, the cell will swell and burst (hemolyse) if the plasma becomes hypotonic. Water transport is discussed in greater detail in Section 3.5.

In the fetus erythrocyte production (erythropoiesis) occurs progressively in the yolk sac, liver, and spleen, before moving to the bone marrow cavities. After birth, erythrocytes are produced primarily in the red marrow of the long bones where they are derived from committed stem cells called hemocytoblasts. Hemocytoblasts differentiate into common myeloid progenitor cells, some of which differentiate into erythroblasts which begin synthesizing hemoglobin. Still in the bone marrow, the erythroblast loses its nucleus becoming a reticulocyte which enters the blood stream, continuing to synthesize hemoglobin. After 1 or 2 days the reticulocyte will have lost its endoplasmic reticulum, mitochondria, and ribosomes, becoming a mature erythrocyte.

After 80 to 120 days in the blood stream, largely due to the absence of the machinery required to replace enzymes and proteins, the plasma membrane begins to leak ions and the cell loses its integrity. As the aged cell passes through the narrow capillaries of the liver, spleen, and reticuloendothelial system, it ruptures and the remnants are phagocytosed by macrophages. The production and destruction of erythrocytes is maintained at an equal rate which is controlled mainly by the hormone erythropoietin from the kidney, which operates in a negative feedback mode.

More extensive information regarding erythrocyte biology can be found in the following references: Dacie and Lewis (1975); Grimes (1980); and Carola et al. (1992).

3.2 Human Erythrocyte Metabolism

The human erythrocyte is a highly specialized but metabolically simple cell whose main function is to facilitate the transport of oxygen throughout the body. Because organelles are absent, metabolic activity consists primarily of the glycolytic and pentose phosphate pathways (Grimes 1980). It is by means of these two pathways that ATP and reducing equivalents are produced thus maintaining cellular function.

Glucose enters the cell rapidly by facilitated diffusion which is independent of metabolism. The glucose transporter, also known as GLUT1, is a 55-kD membrane glycoprotein which constitutes 3-5% of the erythrocyte's membrane proteins (Silverman 1991; Gould and Holman 1993). Normal erythrocytes have no deposits of glycogen, and while the enzymes required for its synthesis and breakdown are present, the activity of glycogen synthetase is so low that no accumulation takes place.

Glycolysis is fuelled by environmental supplies of glucose. Normally, more than 95% of the glucose passes through the Embden-Meyerhof pathway (EMP) with the remainder passing via the pentose phosphate pathway (PPP). The EMP in erythrocytes is distinguished by the presence of the enzymes for the production and hydrolysis of 2,3-bisphosphoglycerate (2,3-BPG) whose high concentration in these cells is crucial in their oxygen transporting role. The flux of glucose through the EMP, whose enzymes are all located in the cytoplasm maintains the levels of glycolytic intermediates the most important of which are 2,3-BPG, adenosine triphosphate (ATP), and nicotinamide adenine dinucleotide (NAD^+). 2,3-BPG is important in the

modulation of the half maximal position of the oxygen dissociation curve, ATP is the primary energy intermediate of the cell, and NAD^+ is the coenzyme for glyceraldehyde-3-phosphate dehydrogenase (GADP) and lactate dehydrogenase (LDH).

The PPP maintains levels of reduced nicotinamide adenine dinucleotide phosphate (NADPH) and provides ribose 5-phosphate (R5P) for ATP synthesis. Reduced glutathione, NADH and NADPH provide the cell with reducing potential that reverses various oxidative reactions. The other important intermediate of the PPP, R5P, is involved in limited purine metabolism (in nucleated cells it is involved in nucleic acid metabolism). This cyclic pathway, which is often referred to as a shunt, leads from glucose 6-phosphate (G6P) and produces glyceraldehyde-3-phosphate (GA3P) and fructose 6-phosphate (F6P), which are intermediates in the EMP.

A comprehensive mathematical model of human erythrocyte metabolism based on detailed enzyme kinetic equations has been developed by Mulquiney et al. (Mulquiney et al. 1999; Mulquiney and Kuchel 1999a, b) and will soon appear in a book by Mulquiney and Kuchel entitled "Modeling Metabolism with *Mathematica*: Incorporating a Detailed Analysis of Human Erythrocyte Metabolism" to be Published by CRC Press, Boca Raton, FL.

3.3 Erythrocyte Shape

The shape of the red blood cell is a key element in much of the work presented in this thesis. Indeed Paper V is largely concerned with the differences that are observed in features of *q*-space plots from suspensions of erythrocytes, when compared with suspensions of cells having oblate spheroid shape. The following sections provide a brief description of erythrocyte shape, the changes that occur in various pathologies, and the mathematical description of the erythrocyte shape that is used in the simulations described in Papers I, II, V, and VI.

3.3.1 General Description

Normal human erythrocytes have the shape of a biconcave disc (or discocyte; Fig. 3.1) with a main diameter of ~8 μm, a maximum thickness of ~2 μm, a thickness in the central dimpled region of ~1 μm (See Paper V, Fig. 2 for a two dimensional representation), and a mean volume of ~86 fL. The surface area of the cell is in the range 130-160 μm^2 (Dacie and Lewis 1975; Grimes 1980). The biconcave-disc shape

provides a larger surface area to volume ratio than would be the case for a flat disc or a sphere and this ensures more efficient gas exchange. The cell can also undergo reversible changes in shape which do not result in a change in volume or surface area; these are called isochoric changes. The flexibility of the plasma membrane enables the cell to flow easily through narrow capillaries half its main diameter. Cell shape is maintained by a balance of intra- and extracellular forces and appears to be controlled by ATP-dependent phosphorylation of components of the cytoskeletal scaffolding (Marikovsky 1996).

3.3.2 Shape Change and Pathology

As described above, the plasticity of the erythrocyte enables it to flow readily through narrow capillaries (Section 3.3.1), and shape changes may also be brought about by experimentally manipulating the pH and osmolality of the suspension medium (Section 3.1). The shape of the cell may also change in response to alterations in metabolism that affect the ATP concentration (Nakao et al. 1960; Nakao et al. 1961; Weed et al. 1969; Marikovsky et al. 1985; Marikovsky 1996), or as a manifestation of various pathologies such as hereditary stomatocytosis and megaloblastic anemia (Bessis et al. 1973; Dacie and Lewis 1975; Grimes 1980; Torres et al. 1998).

In hypotonic media (200-250 mOsmol kg^{-1}), erythrocytes swell but maintain their disc shape, whereas in hypertonic media (400-600 mOsmol kg^{-1}) the cells become flattened discs. Furthermore, if the cells are incubated under conditions in which ATP is depleted they undergo a disc-to-sphere transformation which sees them first become crenated (spiky) discs, then crenated spheres (echinocytes) and finally smooth spheres (spherocytes).

It has been shown that these changes in cell shape can be detected using NMR q-space analysis as described in Section 1.5. (Torres et al. 1998) and that this method provides an adjunct to conventional methods for diagnosing erythrocyte shape and functional abnormalities. Two such abnormalities mentioned above are: hereditary stomatocytosis, which is a rare form of hemolytic anemia in which the central biconcave region appears slit-like, and the cells are thicker and of smaller diameter due to increased water content as a result of defective cell volume regulation; and megaloblastic anemia which results from vitamin B_{12} deficiency and manifests itself

in greater polydispersity of cell sizes, and increased cell volume with maintenance of general discoidal features (Dacie and Lewis 1975; Grimes 1980).

3.3.3 Mathematical Representation

Kuchel and Fackerell (1999) formulated an equation in Cartesian coordinates which relates the three major shape-defining measurements of the human erythrocyte (see Section 3.1 above) to three of the parameters of a curvilinear disc-cyclide coordinate system (Moon and Spencer 1988). This formulation provides a realistic representation of the shape of the erythrocyte surface and is thus the one that was used in the simulations described in this thesis. The main equation and the equations for the three parameters are given in Paper VI.

3.4 Erythrocytes and Magnetic Fields

A unique characteristic of normal oxygenated erythrocytes, and one which strongly influenced the design of computer models used in this study, as well as the results obtained from simulations and NMR experiments, is their propensity to align in a strong (>1 T) magnetic field, such that their disc planes are parallel with the direction of the field. This was first demonstrated (in non-NMR experiments) by Higashi et al. (1993) and has since been confirmed both by q-space analysis (Kuchel et al. 1997) and diffusion tensor analysis (Paper III).

The phenomenon can be explained by considering the diamagnetic anisotropy of the phospholipids in the membrane. In normal oxygenated erythrocytes both the hemoglobin and the membrane lipids are diamagnetic. Field theory indicates that the most energetically favorable conformation for a diamagnetic biconcave disc-shaped body in a magnetic field is one in which the disc planes are aligned perpendicular to the direction of the magnetic field. However, the manner in which the lipids are "stacked" in the membrane (perpendicular to the plane of the membrane) gives rise to magnetic anisotropy that dominates over the diamagnetism of the hemoglobin in the biconcave body and causes the cell to be aligned with its disc planes parallel to the direction of the field.

Conversely, if the hemoglobin is converted to a paramagnetic form (methemoglobin)[8] the effect of the difference in magnetic susceptibility between the paramagnetic interior and the extracellular environment of the cell dominates over the diamagnetic effect of the membrane lipids. Thus the most energetically favorable conformation is attained when the disc planes are aligned perpendicular to the direction of the magnetic field.

3.5 Water Transport

On of the main features of biological membranes, and one that inspired the concept of the semi-permeable membrane, is that water is able to pass freely through them while most ions cannot. The active erythrocyte consists of ~70% by mass of water and the unique properties of this molecule make it ideally suited to the primary biological role it plays as the dispersion medium of the cell. The osmotic behavior of living cells has thus been a major focus of study. Indeed the subject of transport of water across the erythrocyte membrane is central to this thesis. Papers I-III, V, and VI deal with the diffusion of water in cell suspensions and a recurring theme in all of these studies is the rate at which water crosses the membrane. A discussion of water transport across the erythrocyte membrane is thus warranted.

3.5.1 Water Channels

The primary mechanism of water transport across the mammalian cell membrane is by passive diffusion facilitated by a member of the family of membrane proteins known as water channels or aquaporins[9] (Verkman et al. 1996; Borgnia et al. 1999; Heymann and Engel 1999; Verkman and Mitra 2000). In human erythrocytes, water

---

[8] This can be achieved by suspending the cells in medium containing NO_2^- at a concentration equimolar to that of the hemoglobin subunits in the sample. The addition of NO_2^- causes the autocatalytic oxidation of Fe(II) in the hemoglobin to Fe(III) rendering them paramagnetic (Jung and Spolaczyck 1983; Kosaka et al. 1983). Higashi et al. (1996) have reported that gluteraldehyde-fixed cells align in the magnetic field with their disc planes perpendicular to the direction of the field and have attributed this to the paramagnetism of the membrane-bound hemoglobin.

[9] A small amount of water diffuses unaided through the bilayer (Benga et al. 1990; Haines 1994) and transport is also known to occur through certain membrane transport proteins such as the glucose transporter (Fishchbarg et al. 1990), and through the anion channel in erythrocytes (Solomon et al. 1983). Most recently, facilitated water transport via the urea transporter UT-B has been reported, and while this transporter is present in much smaller numbers than AQP1, a comparable single channel water permeability is suggested (Yang and Verkman 2002).

transport is mediated by aquaporin 1 (AQP1) also known as CHIP28 (channel-forming integral protein, 28 kDa). This protein is a homotetramer with each individual monomer consisting of six membrane-spanning α-helices and constituting an independent aqueous pore (Cheng et al. 1997; Walz et al. 1997).

AQP1 channels allow the bidirectional passage of water across the membrane while the passage of ions including protons is highly energetically not favored. This selectivity, which is not present in all members of the aquaporin family, is achieved through a combination of steric and solute binding properties of the channel, while the amphipathic nature of the channel is a key factor in facilitating rapid transport (Murata et al. 2000; Sui et al. 2001).

Water transport across the erythrocyte membrane is inhibited by mercurial reagents such as *p*-chloromercuribenzene sulfonate (PCMBS) that bind non-specifically to the sulfhydryl groups (SH) of proteins (Benga et al. 1986). Recently, it was shown that 8-bromo-adenosine 3',5'-monophoshate (forskolin) increases membrane permeability to water via AQP1 and triggers a cationic conductance (Yool et al. 1996)

3.5.2 Membrane Permeability and Water Exchange

The permeability coefficient of the plasma membrane with respect to a particular solute can be defined as the rate with which the solute moves across the membrane and consequently has units of m s^{-1}. The driving force for this movement is the chemical potential difference, and the net flux occurs in the direction of decreasing potential (Stein 1986). In the erythrocyte, it is the osmotic gradient (set up by primary active transport of ions) which drives the transport of water across the plasma membrane, and the permeability to water is determined primarily by the number of water channels present per unit surface area of membrane and the permeability of the individual channels.[10] At 25ºC, the permeability of the erythrocyte plasma membrane to water is ~4.3 × 10^{-5} m s^{-1} (Benga et al. 2000).

The mean residence time (MRT) of solute and solvent molecules in a cell is a function of the permeability of the membrane (with respect to the solute or solvent), the self-diffusion coefficient of the solute or solvent, and the dimensions of the cell. The MRT

---

[10] There are 40,000-50,000 AQP1 channels present per erythrocytes (Cho et al. 1999), and the mean surface area of the cell is ~140 μm^2 (Dacie and Lewis 1975), therefore the channel density is ~280-350 μm^{-2}

for water in an erythrocyte is ~10 ms (Benga et al. 2000). I show in Paper II that the permeability of the membrane is the main factor in determining the MRT for a particular solute when its self-diffusion coefficient is above a particular threshold value; below that threshold, the cell dimensions are the main determining factor. I calculated that in the case of the erythrocyte, when the solute is water, this threshold occurs at a self-diffusion coefficient of ~1.25×10^{-10} m s^{-1} (see Paper II, Table 2). This value is well below the value of 6-8 $\times 10^{-10}$ m s^{-1} for the measured self-diffusion coefficient of water inside erythrocytes (Tanner 1983) suggesting that the MRT is primarily a function of the membrane permeability.

A number of methods have been developed for measuring membrane water permeability in cells. These include light scattering and confocal and fluorescence microscopy (Verkman 2000), and NMR (Herbst and Goldstein 1989; Kirk 1990). NMR methods can be loosely categorized as doping or non-doping and it is the former that will be briefly discussed here as it is the most widely used for measuring water transport in erythrocytes (Benga 1989). The doping method is an NMR relaxation-time method first introduced by Conlon and Outhred (1972) in which a high concentration (up to 48 mM) of Mn^{++}, which only slowly enter the cells, is added to the suspension medium. This has the effect of greatly enhancing the relaxation rate of the extracellular water-proton signal. As water egresses from the cell into the extracellular fluid, its proton signal is "quenched" by the relaxation agent. Hence from a measurement of the rate at which the intracellular water-proton signal diminishes an estimate of the permeability can be obtained (Benga 1989).

4 Self-Associating Systems

Processes of molecular association and polymerization are both common and important in biological systems. Some examples are the assembly of tubulin molecules into microtubules that form the mitotic spindle and actin molecules into muscle filaments, the linking of amino acids to form peptides and proteins, and the stacking of nucleotide bases in RNA and DNA molecules (Alberts et al. 1994). An understanding of the mechanisms, kinetics and thermodynamics of such processes, and the means by which to measure them is therefore vital if we are to gain a full understanding of the roles these assemblies play in the organism. Two self-associating systems were studied in the work presented here: NMA and tropoelastin; the

following sections provide some background information regarding these two molecules that is not covered in Papers IV and VII which deal with this aspect of my work.[11]

4.1 *Tropoelastin*

Tropoelastin (Fig. 4.1A) is the soluble precursor of elastin which is cross-linked to form elastic fibers. These fibers are an important component of the extracellular matrix of connective tissues in vertebrates because they provide the necessary elasticity and resilience enabling them to deform both repetitively and reversibly (Vrhovski and Weiss 1998). Elastogenesis is a complex process in which tropoelastin has a major role but which also involves numerous other components including microfibrillar proteins, and the enzyme lysyl oxidase which is responsible for initiating elastin cross-linking.

Human tropoelastin, which shares a high degree of sequence homology with tropoelastin from other vertebrate species, contains two major types of structural domain (see Fig. 4.1A): hydrophobic domains which are rich in non-polar amino acids, particularly alanine, glycine, proline, and valine; and hydrophilic domains which are involved in cross-linking and are usually rich in lysine and alanine.

Synthesis of tropoelastin is known to occur in smooth muscle cells, endothelial and microvascular cells, chondrocytes, and fibroblasts. It is delivered to the plasma membrane by secretory vesicles and then to the exterior of the cell where it undergoes little post-translational modification and is not known to be glycosylated. Outside the cell membrane tropoelastin is rapidly incorporated into elastin fibers along with microfibrils which have also been secreted into the extracellular space close to the cell. It is thought that the microfibrils provide a scaffold for the alignment and cross-linking of tropoelastin into elastin and its subsequent deposition.

At physiological temperatures, tropoelastin undergoes a process of intermolecular interaction or 'coacervation' (Urry and Long 1977; Vrhovski et al. 1997).[12] This process can be observed *in vitro* where at low temperatures aqueous solutions of

---

[11] See Section 1.7.2 which puts this work into the context of PGSE NMR and diffusion.

[12] Coacervation is described as "The separation into two liquid phases in colloidal systems. The phase more concentrated in colloid component is the coacervate, and the other phase is the equilibrium solution." in the IUPAC Compendium of Chemical Terminology (McNaught and Wilkinson 1997).

tropoelastin appear completely clear, but on raising the temperature to around 37ºC the solution becomes cloudy and eventually separates into a dense viscous phase and an aqueous phase. The interaction that gives rise to coacervation is primarily between oligopeptide repeats present in the hydrophobic domains of the protein (Urry 1988). It is thought that coacervation constitutes a vital step in the formation of elastic fibers by aligning them for subsequent cross-linking.

While this process of coacervation is what originally attracted our attention, it was the proposal that soluble tropoelastin exits as two distinct conformational isomers that I investigated from a diffusion viewpoint in Paper IV. All the information contained in this section, as well as secondary references, can be found in the comprehensive review on the biochemistry of tropoelastin by Vrhovski and Weiss (1998).
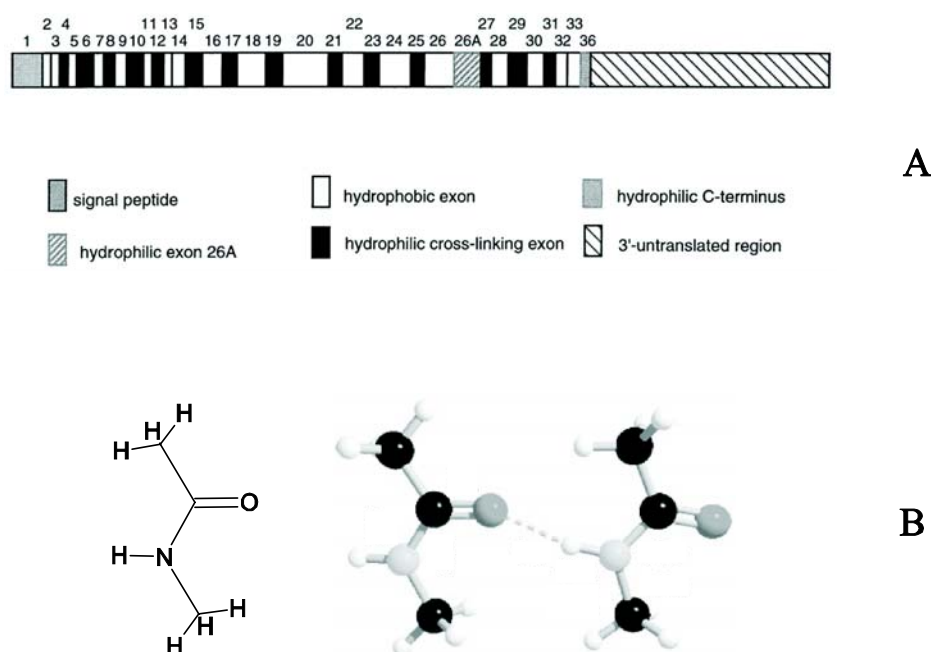
Figure 4.1. Self-associating molecules. A) cDNA structure of tropoelastin adapted from Vrhovski and Weiss (1998). The diagram illustrates the alternating hydrophobic and cross-linking domains involved in coacervation and elastin formation, respectively. B) *Ab initio* calculated dimer of *N*-methylacetamide (NMA) adapted from Huelsekopf (2001), showing the hydrogen bonding scheme. Oligomer formation is thought to be a linear extension of this scheme. The labeled structure of NMA shows the location of the atoms (carbon atoms are not labeled) with the dashed rectangle indicating the peptide group within the molecule.

4.2 N-*Methylacetamide*

N-methyl acetamide (NMA) is the smallest molecule to contain an amide group (-NHCO-, see Fig. 4.1B). This group is the basic repeat unit of peptides and proteins and consequently NMA has been used extensively as a model for investigating many aspects of their structure. The spatial structure of NMA dictates that the amide group has a trans configuration (Schweitzer-Stenner et al. 1998). The molecule also has two complementary hydrogen-bonding sites: the amide proton acts as a proton donor; and the carbonyl oxygen acts as a proton acceptor. These features in combination enable the formation of linear hydrogen-bonded oligomers through multi-step head-to-tail association (Longsworth 1966; Klotz and Farnham 1968; Albers et al. 1971; Howlett et al. 1973; Pralat et al. 1983; Schweitzer-Stenner et al. 1998). This process is also of central importance to biological macromolecules because peptide and protein structures are thought to be partially stabilized by hydrogen bonds between amide protons and carbonyl oxygens. Because of its simple structure and the repetitiveness of its association oligomers NMA has also been a popular choice as a model for applying *ab initio* methods to the calculation of spectroscopic and structural properties (Huelsekopf and Ludwig 2001).

Despite the large number of studies that have been conducted on NMA association in solution, the published values of thermodynamic parameters are hugely divergent and there is almost no conclusive information about the structure of the oligomers formed in this process. The aim of the work described on Paper VII was to combine PGSE NMR measurements of NMA diffusion with computer modeling as an alternative approach for probing structure and for the estimation of relevant thermodynamic parameters (see also Sections 1.7.2 and 1.8). Paper VII also contains a more extensive list of references than is provided here.

5 Monte Carlo Simulations

Fick's second law (see Eq. 1.2) is often referred to simply as the diffusion equation because of its general applicability. In the context of PGSE NMR the translational diffusion phenomena pertaining to a particular system are best expressed in terms of the propagator (see Section 1.2) which satisfies this equation for the boundary conditions that define the system. While analytical solutions to the diffusion equation can be derived for isotropic and relatively simple anisotropic systems (Mitra and Sen

1992; Coy and Callaghan 1994; Barzykin et al. 1995; Callaghan 1995; Kuchel et al. 1996; Kuchel and Durrant 1999), the problem is often mathematically intractable for systems with more complicated boundary conditions. Indeed, for all practical purposes, this is the case for the systems involving suspensions of biconcave disc- and oblate spheroid-shaped cells that are the subject of Papers I, V, and VI.[13] The complexity of these systems lies in their compartmentalization, which is further complicated by exchange between the compartments, and the relative complexity of the cell geometry.

When an analytical solution to the diffusion equation for a particular system is not available, alternative approaches must be sought for a mathematical representation of the system. The process of molecular diffusion for a single particle can be represented as a "random walk" in which it is possible to calculate the mean-square distance traveled in a given interval of time but in which it is impossible to predict the direction in which the particle will move. Diffusion of the bulk fluid, therefore, may be represented as an ensemble of random walk "trajectories" characterized by a mean-square displacement and a displacement profile which will be determined by the boundary conditions of the system. In an isotropic system the mean-square displacement for an ensemble can be calculated from the Einstein equation (Eq. 1.3) and the displacement profile will be a Gaussian centered on $\overline{s}$; but for an anisotropic system this will not be the case. The random walk and the boundaries then constitute a way of representing the average propagator (Kärger and Heink 1983) for the system, in the absence of an analytical solution.

The random walk is the main element of a Monte Carlo simulation of diffusion, so-named because of the use of random number generators for assigning the direction the particle will move in at each 'jump' in the trajectory. This method is enormously flexible in that as long as the geometry of the system can be defined, the need to analytically solve the diffusion equation is obviated. This is the method that was used for simulating diffusion in suspensions of cells in the work described in Papers I, V, and VI and for isolated enclosures in Paper II.

---

[13] Jiang et al. (2001) published an analytical model for the interpretation of PGSE NMR data of water diffusion in a suspension of cells. The model makes a number of simplifying assumptions and approximations and I believe that it is not generally applicable to arbitrary cell geometries and lattice arrangements.

The Monte Carlo methods used in Papers I, II, V, and VI for simulating diffusion are described in those papers. Paper VI in particular provides extensive detail of these methods and the algorithms developed for their implementation; therefore they are not discussed further in this section. However the subject of membrane permeability in the Monte Carlo context warrants discussion as it is the subject of Paper II and a crucial element of the computer models. When initially I set out to estimate the mean residence times (MRT) for water in enclosures of various geometries using Monte Carlo simulations I found what appeared to be a dependence of the membrane permeability on the jump-length chosen for the simulation. In the original model, the permeability of the membrane was determined by a specified transition probability in accordance with which transition across the membrane would occur. The value for this parameter was chosen to yield a mean residence time for erythrocyte-shaped cells of ~10 ms as found experimentally (Benga et al. 2000). However, this value was set independently of the jump-length and when that parameter was varied I found that the MRT also changed. This led to the development of an expression, described in Paper II, which relates membrane transition probability (tp), jump-length (jl), membrane permeability (P_d), and the self-diffusion coefficient:

$$P_d = \frac{D\,tp}{jl}\,.$$

(5.30)

The significance of this is that the membrane transition probability was determined in the simulations as a function of the values assigned to D and P_d which were generally chosen to reflect the physiological values, and the value of jl. The latter value was assigned pragmatically on the basis of system geometry to be no greater than one fifth of the smallest distance separating barriers (Piton et al. 1994).

6   Methods

The methods and procedures used in the work presented in Papers I-VII, are described in those papers and these descriptions are not repeated here. However, the following list constitutes a summary of the primary methods used, with reference to the specific paper/s in which they appear:

❖ *Preparation of erythrocyte suspensions for PGSE NMR*. Papers I and III contain precise prescriptions for the preparation of the erythrocyte suspensions used in the experiments. In paper VII, in which experiments on erythrocyte

suspensions are also described, the reader is referred to the paper by Kuchel et al. (1997) in which the standard method is given.

❖ *PGSE NMR*. The general PGSE method for measuring diffusion is described in Section 1.3 and the various pulse sequences used are described in Section 1.4. The standard pulse sequence (Fig. 1.1A) was used in Papers I, III, and V, while the standard convection compensated sequence (Figs 1.1C) was used in Paper VII. In paper IV, STE pulse sequences, with and without convection compensation, were used (Figs 1.1B, D), in addition to the standard sequence. In all these papers the PGSE parameters used are specified.

❖ *Monte Carlo Simulations*. Papers I, II, V, and VI, all describe studies which made extensive use of Monte Carlo simulations of diffusion. Each paper contains a general description of this method and specifies the parameters used to obtain the data. Paper VI provides a particularly comprehensive description of the procedures and algorithms used to simulate diffusion and of the design of the model-cell suspension.

❖ *Data presentation and analysis, and algorithm development*. Numerous methods were used for visualizing data, q-space plots for example, and for analyzing and fitting data. Linear and non-linear regression procedures, most commonly used to calculate diffusion coefficients from Stejskal-Tanner data, were routinely performed using the technical graphing package Origin (Microcal, MA, USA). The Matlab (The MathWorks, MA, USA) 'nlinfit' and 'fzero' functions were used to perform the non-linear least-squares fitting of NMA diffusion data in Paper VII. Matlab was also used to perform the diffusion tensor, Fourier transform, and 1st and 2nd derivative analyses described in Papers V and VI. *Mathematica* (Wolfram Research, IL, USA) was used for the analysis of PGSE NMR diffusion data and the construction of diffusion tensors in the work described in Paper III, and an analogous Matlab program was used to perform the same task on simulation data in Papers V and VI. Matlab and *Mathematica* were both used extensively for the development, prototyping, and testing of algorithms used in the Monte Carlo simulations of diffusion in cell suspensions.

7 Summary of Results

Papers I-VII, which form the body of work discussed in this thesis, were numbered according to the chronological order of their publication. This sequence, however, does not reflect the manner in which the work evolved. The following summary, therefore, aims to present a synthesis of the major findings contained herein in their logical rather than chronological order.

The major discovery leading to much of the work and subsequent findings described in this thesis was the paper by Kuchel et al. reporting the diffusion-diffraction of water in erythrocyte suspensions. By combining the results obtained from simulations of diffusion in erythrocyte suspensions with those obtained from PGSE NMR experiments on real suspensions, my co-workers and I were able to show that coherence features in the q-space plots could be assigned to different modes of diffusion, i.e., diffusion-diffraction of intracellular water and diffusion-interference due to pore-hopping of extracellular water.

The next major development in my work was the derivation of the relationship which related the membrane transition probability, used in the Monte Carlo simulations to specify the rate of membrane transport, and the membrane permeability. This enabled me to show that for a cell of given dimensions, there exists a threshold for the diffusion coefficient below which the MRT of the diffusant in the cell increases sharply but above which the MRT remains relatively constant, determined by the permeability of the membrane.

These studies laid the groundwork for further work in which I sought to characterize the coherence features manifest in q-space plots from cell suspensions under various conditions. This was achieved largely with the aid of computer simulations which enabled me to vary the packing density and arrangement of the cells, the geometry of the cells, and to turn membrane exchange on and off. The ability to easily modulate these conditions enabled me to show that these changes could be detected in the resulting q-space plots. In the course of these investigations I developed a number of useful methods for the analysis of q-space data. The parallel development of a simplified method for constructing and analyzing diffusion tensors from PGSE diffusion data, in which I participated, provided another useful tool which I used for analyzing diffusion data obtained from PGSE NMR experiments on erythrocyte

suspensions and from simulations. This method also provided additional evidence of the alignment of erythrocytes in the magnetic field of the spectrometer.

The work on NMA and tropoelastin demonstrated that diffusion measurements made by PGSE NMR, in combination with good theoretical and numerical models, can provide great insight into the behavior of these systems, from both hydrodynamic and thermodynamic perspectives. Using this approach I was able to suggest possible models for the association and conformation of NMA oligomers and to test suggested conformational models of tropoelastin. This work also demonstrates the huge potential of PGSE NMR as a tool for studying these types of systems in the absence of many of the limitations presented by more traditional methods for their study such as analytical ultracentrifugation.

8   Concluding Remarks

As stated in the Introduction, PGSE NMR is a powerful tool for the study of molecular diffusion and this is particularly true for heterogeneous and multicomponent systems. Computer models constitute a powerful adjunct as they allow one to easily manipulate the system being studied in ways that may not be readily achieved in the real experimental system. In my doctoral work I have aimed to combine these two techniques in the study of two quite different systems: red blood cell suspensions and the multicomponent systems of tropoelastin and *N*-methylacetamide.

Red blood cell suspensions were studied primarily through the method of q-space analysis which I refined in the course of this work. This method provides an alternative to the analytical-propagator representation of molecular diffusion and provides the equivalent information. It is particularly useful in contexts where there is refractoriness to classical analysis. q-Space analysis, in combination with diffusion tensor analysis, has the potential to provide a detailed picture of molecular displacement on the microscopic scale in compartmentalized systems, and this work presents a portion of that picture.

N-methylacetamide and tropoelastin were studied as representatives of multicomponent systems. Here, PGSE NMR diffusion measurements and computer modeling were again used in combination, but in this case to probe the hydrodynamic and thermodynamic properties of these systems and to test conformational models. While further work is required to confirm the validity of these models, the strategy clearly has general applicability to the study of rapidly self-associating and multicomponent systems.

9   Future Directions

It is less often in Science than in Art that it can be claimed that one has applied the final brush-stroke to the canvas, and in the case of my doctoral research such a claim would be no less misinformed. I note here therefore, and restate what I wrote in the Preface to this thesis, that this is "work in progress". Already, since completing the requisite studies for this undertaking, experiments and simulations have been conducted, by me and others in our group, aimed at extending the scope of the work presented here. Following is a brief account of these projects, and others which I think will provide deeper insights to the sorts of systems that have been discussed.

❖ While the study of water diffusion in erythrocyte suspensions by means of q-space analysis provides information relating to trans-membrane exchange rates, a non-exchanging diffusant is in many ways preferable for obtaining structural information. One example of a compound, whose exchange across the erythrocyte membrane is very slow on the NMR timescale, is hexafluoro-phosphate (PF_6^-) which, due to six highly NMR-sensitive fluorine atoms, provides a strong signal even at relatively low concentrations (20 mM). The primary advantage of this particular compound is the presence in the NMR spectrum of separate peaks for the intracellular and extracellular fractions.

❖ The present models for simulating diffusion in cell suspensions are idealized and have served as canonical systems for exploring the features of q-space plots and the processes that give rise to them. However, q-space plots from real cell suspensions do not exhibit the detail seen in the simulated data, so the next stage in the development of the models will be to incorporate more of the characteristics of the real system. This will involve, for example, randomizing cell size and shape, and orientation of cells in the lattice, to reflect the manner in which these properties are distributed in real cell suspensions. While the lattice representation of the cells in the suspension is a convenient one, it does not reflect the true nature of cell suspensions and alternative approaches will be sought.

❖ In Paper VI, I refer to the different patterns obtained from q-space data due to varying the packing arrangement of the cells as 'signatures'. For some time now I have contemplated applying artificial network analysis to the

recognition of these signatures and I have conducted some preliminary feasibility studies. If successful, this could solve the 'inverse problem' and perhaps provide a one-shot method for the direct estimation of structural and exchange related parameters of cell suspensions from q-space data, in the absence of prior knowledge about the system.

❖ Some work has been conducted on the manipulation of erythrocyte orientation in the spectrometer by combining the effect of an imposed electric field with that of the static magnetic field. Some technical difficulties must be overcome, but the method has the potential to provide an additional tool for widening the scope of q-space studies of erythrocyte suspensions.

❖ While erythrocyte suspensions have provided the ideal biological tissue for q-space studies, due to their relative uniformity in both shape and size, it was always foreseen that this technique would be applied to other tissue systems. This would make q-space analysis a potentially useful, powerful, and perhaps most importantly, non-invasive diagnostic tool for detecting changes in cell morphology and function that occur in many diseases. q-Space MRI is already being used in the imaging of certain tissues but the spectroscopic application has the potential for revealing finer structural information than can be achieved at present by MRI.

❖ The coacervation of tropoelastin is an important process on the synthesis of elastin and elastic fibers. Initial attempts to study this protein in the coacervate state failed due to phase separation in the sample and broad signals. I hope to return to this fascinating system, to solve these problems, and to attempt to shed some light on the process of coacervation of tropoelastin using PGSE NMR methods.

❖ Further work is required in the study of NMA self-association in order to understand better the hydrogen-bonding process by which it occurs. Some work has already been conducted to investigate, by means of PGSE NMR diffusion measurements, the effect of introducing other hydrogen-bonding compounds into the system. By choosing compounds with different combinations of hydrogen-bond donor and hydrogen-bond acceptor sites it is possible to disrupt or to enhance the self-association process in a manner that

is reflected in the measured (apparent) diffusion coefficient. It is anticipated that a better understanding of this process will shed light on other biological polymerization processes in which hydrogen-bonding is important in the stabilizing the resulting structures.

Acknowledgments

First and foremost, I wish to thank my supervisor, Professor Philip Kuchel, for his guidance, encouragement, inspiration, enthusiasm, and friendship throughout the course of this work. I am grateful to have had the opportunity to undertake my candidature as a member of his research group.

I acknowledge with gratitude the help of Dr Bob Chapman on all aspects of the NMR spectroscopy. Dr Bill Bubb is also thanked for help with NMR spectroscopy and for providing a meticulously maintained state-of-the-art NMR facility. Mr Bill Lowe is acknowledged for technical and computing facilities. Members of the Kuchel group, present and past, are thanked for their helpful discussions, advice and friendship throughout my candidature.

I wish to thank the academic and general staff of the School of Molecular and Microbial Biosciences (formerly the Department of Biochemistry) for providing an environment conducive to productive and scholarly scientific research.

Associate Professor Russell Standish, Director of the High Performance Computing Support Unit at the University of New South Wales, is thanked for invaluable help with access to and utilization of the super-computer facilities of the AC3 consortium and the APAC National Facility. The support staff of those facilities are also gratefully acknowledged.

I thank my family: my wife and best friend, Judith, for her unstinting support and encouragement; my children, Ella and Aarin, for providing some 'balance' and healthy distraction; my parents in law, Josie and Ian, without whose support it simply would not have been possible; and my mother, Pam, who laid the foundations for all I have been able to achieve.

The Australian Commonwealth Government is thanked for the financial support provided in the form of a Commonwealth Postgraduate Award and Stipend.

References

Albers, R.J., Swanson, A.B., Kreshek, G.C. (1971) An equilibrium centrifugation study of the self-association of N-methylacetamide in carbon tetrachloride at 25°C. *J. Am. Chem. Soc.* **93**, 7075-7078.

Alberts, B., Bray, D., Lewis, J., Raff, M., Roberts, K., Watson, J.D. (1994) *Molecular Biology of the Cell*, 3rd edn. Garland, NewYork.

Barzykin, A.V., Hayamizu, K., Price, W.S., Tachiya, M. (1995) Pulsed-field-gradient NMR of diffusive transport through a spherical interface into an external medium containing a relaxation agent. *J. Magn. Reson. A* **114**, 39-46.

Basser, P.J., Mattiello, J., LeBihan, D. (1994) MR diffusion tensor spectroscopy and imaging. *Biophys. J.* **66**, 259-267.

Benga, G., Popescu, O., Pop, V.I., Holmes, R.P. (1986) *p*-(Chloromercuri)benzenesulfonate binding by membrane proteins and the inhibition of water transport in human erythrocytes. *Biochemistry* **25**, 1535-1538.

Benga, G. (1989) Water exchange through the erythrocyte membrane. *Int. Rev. Cytol.* **114**, 273-316.

Benga, G., Pop, V.I., Popescu, O., Borza, V. (1990) On measuring the diffusional water permeability of human red blood cells and ghosts by nuclear magnetic resonance. *J. Biochem. Biophys. Methods* **21**, 87-102.

Benga, G., Kuchel, P.W., Chapman, B.E., Cox, G.C., Ghiran, I., Gallagher, C.H. (2000) Comparative cell shape and diffusional water permeability of red blood cells from Indian elephant (*Elephas maximus*) and Man (*Homo sapiens*). *Comp. Haematol. Int.* **10**, 1-8.

Bessis, M., Weed, R.I., Leblond, P.F. (1973) *Red Cell Shape: Physiology, Pathology, Ultrastructure*. Springer-Verlag, New York.

Borgnia, M., Nielson, S., Engel, A., Agre, P. (1999) Cellular and molecular biology of the aquaporin water channels. *Annu. Rev. Biochem.* **68**, 425-458.

Callaghan, P.T., Pinder, D.N. (1983) A pulsed field gradient NMR study of self diffusion in a polydisperse polymer system: dextran in water. *Macromolecules* **16**, 968-973.

Callaghan, P.T. (1991) *Principles of Nuclear Magnetic Resonance Microscopy*. Oxford University Press, Oxford.

Callaghan, P.T., Coy, A., MacGowan, D., Packer, K.J., Zelaya, F.O. (1991) Diffraction-like effects in NMR diffusion studies of fluids in porous solids. *Nature* **351**, 467-469.

Callaghan, P.T., Xia, Y. (1991) Velocity and diffusion imaging in dynamic NMR microscopy. *J. Magn. Reson.* **91**, 326-352.

Callaghan, P.T., Coy, A., Halpin, T.P.J., MacGowan, D., Packer, K.J., Zelaya, F.O. (1992) Diffusion in porous systems and the influence of pore morphology in pulsed gradient spin-echo nuclear magnetic resonance studies. *J. Chem. Phys.* **97**, 651-662.

Callaghan, P.T. (1995) Pulsed-gradient spin-echo NMR for planar, cylindrical, and spherical pores under conditions of wall relaxation. *J. Magn. Reson. A* **113**, 53-59.

Callaghan, P.T. (1996) NMR imaging, NMR diffraction and applications of pulsed gradient spin echoes in porous media. *Magn. Reson. Imaging* **14**, 701-709.

Carola, R., Harley, J.P., Noback, C.R. (1992) *Human Anatomy and Physiology*, 2nd edn. McGraw-Hill, New York.

Carr, H.Y., Purcell, E.M. (1954) Effects of diffusion on free precession in nuclear magnetic resonance experiments. *Phys. Rev.* **94**, 630-638.

Cheng, A., van Hoek, A.N., Yeager, M., Verkman, A.S., Mitra, A.K. (1997) Three-dimensional organization of a human water channel. *Nature* **387**, 627-630.

Cho, M.R., Knowles, D.W., Smith, B.L., Moulds, J.J., Agre, P., Mohandas, N., Golan, D.E. (1999) Membrane dynamics of the water transport protein aquaporin-1 in intact human red cells. *Biophys. J.* **76**, 1136-1144.

Conlon, T., Outhred, R. (1972) Water diffusion permeability of erythrocytes using an NMR technique. *Biochim. Biophys. Acta* **288**, 354-361.

Cory, D.G., Garroway, A.N. (1990) Measurement of translational displacement probabilities by NMR: an indicator of compartmentation. *Magn. Reson. Med.* **14**, 435-444.

Coy, A., Callaghan, P.T. (1994) Pulsed gradient spin echo nuclear magnetic resonance for molecules diffusing between partially reflecting rectangular barriers. *J. Chem. Phys.* **101**, 4599-4609.

Crank, J. (1975) *The Mathematics of Diffusion*. Clarendon Press, Oxford.

Dacie, J.V., Lewis, S.M. (1975) *Practical Haematology*, 5th edn. Churchill Livingstone, London.

Einstein, A. (1905) Über die von der molekularkinetischen Theorie der Wärme geforderte Bewegung von in ruhenden Flüssigkeiten suspendierten Teilchen. *Ann. Physik* **17**, 549-560.

Einstein, A. (1956) *Investigations on the Theory of the Brownian Movement*. Dover, New York.

Esturau, N., Sánchez-Ferrando, F., Gavin, J.A., Roumestand, C., Delsuc, M.-A., Parella, T. (2001) The use of sample rotation for minimizing convection effects in self-diffusion measurements. *J. Magn. Reson.* **153**, 48-55.

Fick, A. (1855) Über Diffusion. *Ann. Physik* **94**, 59.

Fishchbarg, J., Kuang, K.Y., Vera, J.C., Arant, S., Silverstein, S.C., Loike, J., Rosen, O.M. (1990) Glucose transporters serve as water channels. *Proc. Natl. Acad. Sci. U. S. A.* **87**, 3244-3247.

Gould, G.W., Holman, G.D. (1993) The glucose transporter family: structure, function and tissue-specific expression. *Biochem. J.* **15**, 329-341.

Goux, W.J., Verkruyse, L.A., Salter, S.J. (1990) The impact of Rayleigh-Bernard convection on NMR pulsed-field-gradient diffusion measurements. *J. Magn. Reson.* **88**, 609-614.

Grimes, A.J. (1980) *Human Red Cell Metabolism*. Blackwell, Oxford.

Hahn, E.L. (1950) Spin echoes. *Phys. Rev.* **80**, 580-594.

Haines, T.H. (1994) Water transport across biological membranes. *FEBS Lett.* **346**, 115-122.

Haner, R.L., Schleich, T. (1989) Measurement of translational motion by pulse-gradient spin-echo nuclear magnetic resonance. *Methods Enzymol.* **176**, 418-446.

Herbst, M.D., Goldstein, J.H. (1989) A review of water diffusion measurement by NMR in human red blood cells. *Am. J. Physiol.* **256**, C1097-C1104.

Heymann, J.B., Engel, A. (1999) Aquaporins: phylogeny, structure, and physiology of water channels. *News Physiol. Sci.* **14**, 187-193.

Higashi, T., Yamagishi, A., Takeuchi, T., Kawaguchi, N., Sagawa, S., Onishi, S., Date, M. (1993) Orientation of erythrocytes in a strong static magnetic field. *Blood* **82**, 1328-1334.

Higashi, T., Sagawa, S., Ashida, N., Takeuchi, T. (1996) Orientation of gluteraldehyde-fixed erythrocytes in strong static magnetic fields. *Bioelectromagnetics* **17**, 335-338.

Howlett, G.J., Nichol, L.W., Andrews, P.R. (1973) Sedimentation equilibrium studies on indefinitely self-associating systems. N-methylacetamide in carbon tetrachloride. *J. Phys. Chem.* **77**, 2907-2912.

Huelsekopf, M., Ludwig, R. (2001) Correlations between structural, NMR and IR spectroscopic properties of *N*-methylacetamide. *Magn. Reson. Chem.* **39**, S127-S134.

Jerschow, A., Müller, N. (1997) Suppression of convection artifacts in stimulated-echo diffusion experiments. Double-stimulated-echo experiments. *J. Magn. Reson.* **125**, 372-375.

Jiang, P.-C., Yu, T.-Y., Perng, W.-C., Hwang, L.-P. (2001) Pore-to-pore hoppping model for the interpretation of the pulsed gradient spin echo attenuation of water diffusion in cell suspension systems. *Biophys. J.* **80**, 2493-2504.

Jung, F., Spolaczyck, M. (1983) The reaction between nitrite and hemoglobin. *Biomed. Biochim. Acta* **42**, S144-S148.

Kärger, J., Heink, W. (1983) The propagator representation of molecular transport in microporous crystallites. *J. Magn. Reson.* **51**, 1-7.

Kärger, J., Pfeifer, H., Heink, W. (1988) Principles and application of self-diffusion measurements by nuclear magnetic resonance. *Adv. Magn. Reson.* **12**, 1-89.

Kärger, J., Bär, N.-K., Heink, W., Pfeifer, H., Seiffert, G. (1994) On the use of pulsed field gradients in a high-field NMR spectrometer to study restricted diffusion in zeolites. *Z. Naturforsch. A* **50**, 186-190.

Kirk, K. (1990) NMR methods for measuring membrane transport rates. *NMR Biomed.* **3**, 1-16.

Kirkwood, J.G., Riseman, J. (1948) The intrinsic viscosities and diffusion constants of flexible macromolecules in solution. *J. Chem. Phys.* **16**, 565-573.

Kirkwood, J.G. (1949) The statistical mechanical theory of irreversible processes in solutions of flexible macromolecules. *Recl. Trav. Chim.* **68**, 649-660.

Kirkwood, J.G. (1967) *John Gamble Kirkwood Collected Works. Macromolecules.* Gordon and Breach, New York.

Klotz, I.M., Franzen, J.S. (1962) Hydrogen bonds between model peptide groups in solution. *J. Am. Chem. Soc.* **84**, 3461-3466.

Klotz, I.M., Farnham, S.B. (1968) Stability of an amide-hydrogen bond in an apolar environment. *Biochemistry* **7**, 3879-3882.

Kosaka, H., Tyuma, I., Imaizumi, K. (1983) Mechanism of autocatalytic oxidation of oxyhemoglobin by nitrite. *Biomed. Biochim. Acta* **42**, S144-S148.

Kuchel, P.W., Lennon, A.J., Durrant, C. (1996) Analytical solutions and simulations for spin-echo measurements of diffusion of spins in a sphere with surface and bulk relaxation. *J. Magn. Reson. B* **112**, 1-17.

Kuchel, P.W., Coy, A., Stilbs, P. (1997) NMR "diffusion-diffraction" of water revealing alignment of erythrocytes in a magnetic field and their dimensions and membrane transport characteristics. *Magn. Reson. Med.* **37**, 637-643.

Kuchel, P.W., Durrant, C. (1999) Permeability coefficients from NMR q-space data: models with unevenly spaced semi-permeable parallel membranes. *J. Magn. Reson.* **139**, 258-272.

Kuchel, P.W., Fackerell, E.D. (1999) Parametric-equation representation of biconcave erythrocytes. *Bull. Math. Biol.* **61**, 209-220.

Lauterbur, P.C. (1973) Image formation by induced local interactions. Examples employing nuclear magnetic resonance. *Nature* **242**, 190 -191.

Lennon, A.J., Scott, N.R., Chapman, B.E., Kuchel, P.W. (1994) Hemoglobin affinity for 2,3-bisphosphoglycerate in solutions and intact erythrocytes: studies using pulsed-field gradient nuclear magnetic resonance and Monte Carlo simulations. *Biophys. J.* **67**, 2096-2109.

Longsworth, L.G. (1966) The diffusion of hydrogen bonding solutes in carbon tetrachloride. *J. Colloid Interface Sci.* **22**, 3-11.

Lounila, J., Oikarinen, K., Ingman, P., Jokisaari, J. (1996) Effects of thermal convection on NMR and their elimination by sample rotation. *J. Magn. Reson. A* **118**, 50-54.

Mansfield, P., Grannell, P.K. (1973) NMR 'diffraction' in solids? *J. Phys. C: Solid State Phys.* **6**, L422-L426.

Marikovsky, Y., Weinstein, R.S., Skutelsky, E., Danon, D. (1985) Changes of cell shape and surface charge topology in ATP-depleted human red blood cells. *Mech. Ageing Dev.* **29**, 309-316.

Marikovsky, Y. (1996) The cytoskeleton in ATP-depleted erythrocytes: the effect of shape transformation. *Mech. Ageing Dev.* **16**, 137-144.

Martin, R.B. (1996) Comparisons of indefinite self-association models. *Chem. Rev.* **96**, 3043-3064.

McCall, D.W., Douglass, D.C., Anderson, E.W. (1963) Self-diffusion studies by means of nuclear magnetic resonance spin-echo techniques. *Ber. Bunsen-Ges. Phys. Chem.* **67**, 336-340.

McNaught, A.D., Wilkinson, A. (1997) *Compendium of Chemical Terminology: Gold Book*, 2nd edn. Blackwell, Oxford.

Mitra, P.P., Sen, P.N. (1992) Effects of microgeometry and surface relaxation on NMR pulsed-field-gradient experiments: simple pore geometries. *Phys. Rev. B* **45**, 143-156.

Mitra, P.P., Sen, P.N., Schartz, L.M., Le Doussal, P. (1992) Diffusion propagator as a probe of the structure of porous media. *Phys. Rev. Lett.* **68**, 3555-3558.

Moon, P., Spencer, D.E. (1988) *Field Theory Handbook. Including Coordinate Systems, Differential Equations and Their Solutions*. Springer-Verlag, Berlin.

Mulquiney, P.J., Bubb, W.A., Kuchel, P.W. (1999) Model of 2,3-bisphosphoglycerate metabolism in the human erythrocyte based on detailed enzyme kinetic equations: *in vivo* kinetic characterization of 2,3-bisphosphoglycerate synthase/phosphatase using ^{13}C and ^{31}P NMR. *Biochem. J.* **342**, 567-580.

Mulquiney, P.J., Kuchel, P.W. (1999a) Model of 2,3-bisphosphoglycerate metabolism in the human erythrocyte based on detailed enzyme kinetic equations: equations and parameter refinement. *Biochem. J.* **342**, 581-596.

Mulquiney, P.J., Kuchel, P.W. (1999b) Model of 2,3-bisphosphoglycerate metabolism in the human erythrocyte based on detailed enzyme kinetic equations: computer simulation and metabolic control analysis. *Biochem. J.* **342**, 597-604.

Murata, K., Mitsuoka, K., Hirai, T., Walz, T., Agre, P., Heymann, J.B., Engel, A., Fujiyoshi, Y. (2000) Structural determinants of water permeation through aquaporin-1. *Nature* **407**, 599-605.

Nakao, M., Nakao, T., Yamazoe, S. (1960) Adenosine triphosphate and maintenance of shape of human red cells. *Nature* **187**, 945-946.

Nakao, M., Nakao, T., Yamazoe, S., Yoshikawa, H. (1961) Adenosine triphosphate and shape of erythrocytes. *J. Biochem. (Tokyo).* **49**, 487-492.

Piton, M.C., Lennon, A.J., Chapman, B.E., Kuchel, P.W. (1994) Diffusion of solvent in swollen latex particles. *J. Colloid Interface Sci.* **166**, 437-443.

Pralat, K., Jadzyn, J., Balanicka, S. (1983) Dielectric properties and molecular structure of amide solutions. 1. *N*-methylacetamide in carbon tetrachloride. *J. Phys. Chem.* **87**, 1385-1390.

Riseman, J., Kirkwood, J.G. (1951) The intrinsic viscosity, translational and rotatory diffusion constants of rod-like macromolecules in solution. *J. Chem. Phys.* **18**, 512-516.

Schweitzer-Stenner, R., Sieler, G., Mirkin, N.G., Krimm, S. (1998) Intermolecular coupling in liquid and crystalline states of *trans-N*-methylacetamide investigated by polarized Raman and FT-IR spectroscopies. *J. Phys. Chem. A* **102**, 118-127.

Silverman, M. (1991) Structure and function of hexose transporters. *Annu. Rev. Biochem.* **60**, 757-794.

Solomon, A.K., Chasan, B., Dix, J.A., Lukacovic, M.F., Toon, M.R., Verkman, A.S. (1983) The aqueous pore of the red cell membrane: band 3 as a channel for anions, cations, nonelectrolytes, and water. *Ann. N. Y. Acad. Sci.* **414**, 97-124.

Stein, D. (1986) *Transport and Diffusion across Cell Membranes.* Academic Press, Orlando, FL.

Stejskal, E.O. (1965) Use of spin echoes in a pulsed magnetic-field gradient to study anisotropic, restricted diffusion and flow. *J. Chem. Phys.* **43**, 3597-3602.

Stejskal, E.O., Tanner, J.E. (1965) Spin diffusion measurements: spin echoes in the presence of a time-dependent field gradient. *J. Chem. Phys.* **42**, 288-292.

Stilbs, P. (1987) Fourier transform pulsed-gradient spin-echo studies of molecular diffusion. *Prog. Nucl. Magn. Reson. Spectrosc.* **19**, 1-45.

Sui, H., Han, B.-G., Lee, J.K., Walian, P., Jap, B.K. (2001) Structural basis of water-specific transport through the AQP1 water channel. *Nature* **414**, 872-878.

Tanford, C. (1961) *Physical Chemistry of Macromolecules*. John Wiley & Sons, New York.

Tanner, J.E., Stejskal, E.O. (1968) Restricted self-diffusion of protons in colloidal systems by the pulsed-gradient, spin-echo method. *J. Chem. Phys.* **49**, 1768-1777.

Tanner, J.E. (1983) Intracellular diffusion of water. *Arch. Biochem. Biophys.* **224**, 416-428.

Torres, A.M., Michniewicz, R.J., Chapman, B.E., Young, G.A.R., Kuchel, P.W. (1998) Characterisation of erythrocyte shapes and sizes by NMR diffusion-diffraction of water: correlations with electron micrographs. *Magn. Reson. Imaging* **16**, 423-434.

Tyrrell, H.J.V., Harris, K.R. (1984) *Diffusion in Liquids*. Butterworths, London.

Urry, D.W., Long, M.M. (1977) On the conformation, coacervation and function of polymeric models of elastin. *Adv. Exp. Med. Biol.* **79**, 685-714.

Urry, D.W. (1988) Entropic elastic processes in protein mechanisms. I. Elastic structures due to an inverse temperature transition and elasticity due to internal chain dynamics. *J. Protein Chem.* **7**, 1-34.

Verkman, A.S., Van Hoek, A.N., Ma, T., Frigeri, A., Skach, W.R., Mitra, A., Tamarappoo, B.K., Farinas, J. (1996) Water transport across mammalian cell membranes. *Am. J. Physiol.* **270**, C12-C30.

Verkman, A.S. (2000) Water permeability measurement in living cells and complex tissues. *J. Membr. Biol.* **173**, 73-87.

Verkman, A.S., Mitra, A.K. (2000) Structure and function of aquaporin water channels. *Am. J. Physiol. Renal Physiol.* **278**, F13-F28.

Vrhovski, B., Jensen, S.A., Weiss, A.S. (1997) Coacervation characteristics of recombinant human tropoelastin. *Eur. J. Biochem.* **250**, 92-98.

Vrhovski, B., Weiss, A.S. (1998) Biochemistry of tropoelastin. *Eur. J. Biochem.* **258**, 1-18.

Waldeck, R.A., Kuchel, P.W., Lennon, A.J., Chapman, B.E. (1997) NMR diffusion measurements to characterise membrane transport and solute binding. *Prog. Nucl. Magn. Reson. Spectrosc.* **30**, 39-68.

Walz, T., Hirai, T., Murata, K., Heymann, J.B., Mitsuoka, K., Fujiyoshi, Y., Smith, B.L., Agre, P., Engel, A. (1997) The three-dimensional structure of aquaporin-1. *Nature* **387**, 624-626.

Weed, R.I., LaCelle, P.L., Merill, E.W. (1969) Metabolic dependence of red cell deformability. *J. Clin. Invest.* **48**, 795-809.

Yang, B., Verkman, A.S. (2002) Analysis of double knockout mice lacking aquaporin-1 and urea transporter UT-B: evidence for UT-B facilitated water transport in erythrocytes. *J. Biol. Chem.*, (in press).

Yool, A.J., Stamer, D.W., Regan, J.W. (1996) Forskolin stimulation of water and cation permeability in aquaporin1 water channels. *Science* **273**, 1216-1218.

Papers I-VII

I. Torres A.M., Taurins A.T., Regan D.G., Chapman B.E., Kuchel P.W. (1999) Assignment of coherence features in NMR q-space plots to particular diffusion modes in erythrocyte suspensions. *J. Magn. Reson.* **138**, 135-143.

II. Regan D.G., Kuchel P.W. (2000) Mean residence time of molecules diffusing in a cell bounded by a semi-permeable membrane: Monte Carlo simulations and an expression relating membrane transition probability to permeability. *Eur. Biophys. J.* **29**, 221-227.

III. Kuchel P.W., Durrant C.J., Chapman B.E., Jarrett P.S., Regan D.G. (2000) Evidence of red cell alignment in the magnetic field of an NMR spectrometer based on the diffusion tensor of water. *J. Magn. Reson.* **145**, 291-301.

IV. Toonkool P., Regan D.G., Kuchel P.W., Morris M.B., Weiss A.S. (2001) Thermodynamic and hydrodynamic properties of human tropoelastin: analytical ultracentrifuge and pulsed field-gradient spin-echo NMR studies. *J. Biol. Chem.* **276**, 28042-28050.

V. Regan D.G., Kuchel P.W. (2002) Simulations of molecular diffusion in lattices of cells: insights for NMR of red blood cells. *Biophys. J.* **83**, 161-171.

VI. Regan D.G., Kuchel P.W. (2002) Simulations of NMR-detected diffusion in suspensions of red cells: the 'signatures' in q-space plots of various lattice arrangements. *Eur. Biophys. J.*, (in press**)**.

VII. Regan D.G., Chapman B.E., Kuchel P.W. (2002) PGSE NMR Diffusion study of the self-association of *N*-methylacetamide in carbon tetrachloride. *Magn. Reson. Chem.*, (in press**)**.

PAPER I

Assignment of Coherence Features in NMR *q*-Space Plots to Particular Diffusion Modes in Erythrocyte Suspensions

Allan M. Torres, Andrew T. Taurins, David G. Regan, Bogdan E. Chapman, and Philip W. Kuchel[1]

Department of Biochemistry, University of Sydney, Sydney, New South Wales, 2006, Australia

NMR *q*-space plots derived from water diffusing inside and around erythrocytes in a suspension display reproducible and characteristic coherence features. The aim of the present work was to determine which water population gives rise to the respective features. The central experimental strategy was to use choline and choline phosphate which are virtually membrane impermeant on the time scale of the experiment; the former was incorporated into erythrocytes by a lysis-resealing method and the latter was simply added to the suspensions. Dimethyl sulfoxide, which readily but more slowly exchanges across the cell membranes than water, also yielded *q*-space plots which were similar to those of water, but the differences were able to be accounted for on the basis of its slower transmembrane exchange rate. Random walk simulations using a Monte Carlo procedure, together with a model of an array of biconcave discocytes, helped verify the interpretations of the assignment of the features of the plots to molecules diffusing in the two regions. In addition, the simulations revealed how the presence or absence of transmembrane exchange affects the form of *q*-space plots. © 1999 Academic Press

Key Words: diffusion diffraction; NMR *q*-space; erythrocytes; random walk simulation; Monte Carlo.

INTRODUCTION

When the pulsed field gradient spin-echo (PFGSE) experiment is carried out on a suspension of diamagnetic erythrocytes, the plot of the logarithm of the normalized signal intensity, $\log_{10}(E[q, \Delta])$, *versus* the scaled magnitude of the gradient pulses q ($q = (2\pi)^{-1}\gamma g\delta$, where γ is the nuclear magnetogyric ratio, g is the magnitude of the field gradient pulses, and δ is the duration of each of the gradient pulses) displays "coherence" peaks (*1, 2*). The analogy between *q*-space plots derived from PFGSE experiments and diffraction patterns of physical optics was an important insight presented in 1990 (*3*). The experiment employing the ^{1}H NMR water signal has been shown to be capable of characterizing erythrocyte sizes and shapes in normal and disease states. Thus *q*-space analysis of erythrocyte suspensions is potentially useful as a diagnostic tool in hematology since it provides rela-

tively unbiased estimates of population-mean cell dimensions and shapes in a sample (*2*).

Figure 1 shows a typical *q*-space plot of the water signal from a 0.30-hematocrit (Ht, volume fraction of the sample that is cells) suspension of metabolically active human erythrocytes. It is evident that the plot is characterized by a monotonic decline that is "embellished" with an inflection and several maxima and minima. These reproducible features in the declining curve provide more "specificity" in the subsequent estimates of lengths and distances than are typically available from multiple exponential analysis, or interpretation of the Gaussian-like curves that arise, for example, from yeast cells because of their size heterogeneity (*3*). From earlier experimental and theoretical work on randomly packed beds of polymer spheres (*4–6*) and glass spheres (*7*), it was predicted that some of the coherence features in *q*-space plots from erythrocyte suspensions would arise from water diffusing in the interstices between the cells. This coherence effect has been interpreted physically by using a simplified model referred to as "pore-hopping," and it bears an analogy with the two-slit interference experiment of physical optics (*8*). On the other hand, theoretical consideration has been given to spins constrained to move inside isolated (*not* interconnected) lacunae. These systems also display coherences in *q*-space plots, but the physical interpretation is that this is analogous to the single-slit diffraction effect of optics (*3, 9–11*). These two simple analogies with coherences in optics apply strictly only when the PFGSE experiment is carried out with the duration of the gradient pulses, δ, being negligible relative to the time interval, Δ, between them [viz., the short gradient pulse (SGP) approximation]. Also, the time over which the diffusion is measured, Δ, must be sufficiently large to ensure multiple interactions of the spins with the limiting barriers that are separated by the distance a; specifically, $\Delta \gg a^2/2D$, where D is the diffusion coefficient. Under these conditions the NMR signal intensity, $E[q, \Delta]$, is the power 2 spectrum (Fourier transform) of the autocorrelation function of the diffusion-restricting compartment(s) (*3, 9, 12, 13*).

Thus, since water is diffusing both inside and outside cells in a suspension, a *q*-space plot will be the superposi-

[1] To whom correspondence should be addressed. Fax: (+61-2) 9351 4726. E-mail: p.kuchel@biochem.usyd.edu.au.

tion of the interference and diffraction effects noted above. In addition, in a cell suspension, exchange of water across the membranes will lead to a "mixing" of the two effects that will complicate the interpretation of the data. On the other hand, because the effects are mixed this might form the basis of a new means of measuring the rate of exchange across the membrane. Indeed, in a recent theoretical study of spin exchange out of spheres, it was shown that the positions of minima in q-space plots move to larger q values if the membrane permeability is increased (14). This phenomenon was observed experimentally in the earlier q-space study of human erythrocytes (1).

Therefore, the aim of the present work was to assign the various features of q-space plots from water, and other molecules, in erythrocyte suspensions to diffusing populations inside and outside the cells. We used molecular species, in addition to water, that were confined to either the outside or the inside of the cells, hence allowing separation of the interference and diffraction effects, and also eliminating the mixing of them due to transmembrane exchange. In our earlier studies (1, 2), we attributed the first diffraction peak, which appears as a "shoulder" near $q \sim 1.0 \times 10^5$ m^{-1}, to the pore-hopping phenomenon; this was verified in a more direct way in the present work. This interference peak was found to be more pronounced in lower hematocrit samples (Ht < 0.50) in which the relative amount of extracellular water was significantly higher. The second peak with $q_{max} \sim 2.2 \times 10^5$ m^{-1}, on the other hand, was ascribed to water diffusing inside the cells.

The reciprocal of the q position of the diffusion-interference *maximum* is inversely related to the mean distance between the interstitial water-filled cavities that exist between the cells in the suspension. These cavities are often referred to as "pores." The q positions of the diffusion-diffraction *minima* (q_{min}) are inversely related to the main dimension of the intracellular compartment, viewed in the direction of the field gradient pulses. Exact mathematical expressions derived with the SGP approximation, which relate signal intensity $E[q, \Delta]$ with the dimensions of simple compartments, have been presented by Callaghan; these include expressions for spherical, planar, and cylindrical lacunae (10). Such expressions do not exist for the biconcave disc of the mammalian erythrocyte, but numerical calculations using the expression for a discocyte (15) were done in the course of the present work (see Discussion).

It is also important to note that the rationale behind the peak assignments in the q-space plots from erythrocyte suspensions was based primarily on known erythrocyte dimensions from studies using microscopy (1, 2). No experimental results until now have been shown to separate and convincingly identify the two types of coherence peaks. Therefore, it was considered important to study each type of curve separated from the other.

MATERIALS AND METHODS

Sample Preparation

Blood was obtained from healthy human donors by venipuncture in the cubital fossa. The cells were centrifugally washed (3000 $\times$ g, 5 min) three times in cold saline solution (154 mM NaCl, 10 mM glucose, pH 7.4, 290 mOsmol kg^{-1}, 4°C) and the buffy coat was removed by aspiration. Bubbling with CO was performed prior to the second wash in order to transform the hemoglobin into a stable low-spin diamagnetic state. All solutions used in the sample preparation contained 10 mM glucose. Samples for NMR studies were dispensed in two ways depending on the amount of sample: for small samples, ~180 μL of cell suspension was dispensed into 5-mm-o.d. susceptibility-matched microtubes (BMS-005B, Shigemi, Tokyo, Japan). For larger samples, ~600 μL of cell suspension was dispensed into a flat-bottom Wilmad insert tube made to go inside a 10-mm NMR tube (516-I-10, Wilmad, Buena, NJ). A Teflon vortex plug was inserted onto the top of the sample and the insert tube was in turn placed in the 10-mm-o.d. tube containing ~1.0 mL CCl$_4$. The latter was used to avoid air–glass interfaces near the cell sample and thus minimized static local magnetic field gradients due to large differences in magnetic susceptibility.

Choline loading of the cells was achieved as follows by hypotonic hemolysis and resealing: 10 mL of washed cell pellet was mixed with 90 mL of hypotonic choline solution (45 mM choline chloride, 5 mM sodium phosphate buffer, pH 7.2) so that the final osmolality was ~130 mOsmol kg^{-1}. This resulted in breaching the cell membranes, thus allowing choline to enter the cells. The suspension was incubated for 5 min at 0°C, and then 100 mL of hypertonic "resealing" solution (206 mM LiCl, 10 mM CaCl$_2$, 8 mM MgCl$_2$, 4 mM adenosine, 480 mOsmol kg^{-1}) was added. The resulting mixture was allowed to stand at 37°C for 1 h. Lithium chloride was used in the incubation medium to restrict the efflux of intracellular choline (16) while CaCl$_2$ and MgCl$_2$ were added to maintain the biconcave shape of the cells. However, light microscopy showed that the mean cell shape after resealing was not perfectly biconcave but either spherical or stomatocytic. Approximately 1 mL of the pelleted resealed cells was centrifugally washed three times with ^{2}H$_2$O containing 154 mM lithium chloride. The hematocrit of the resulting suspension was adjusted, as required, prior to the NMR experiment.

The introduction of choline phosphate and dimethyl sulfoxide (DMSO) into the cell suspensions was much simpler. This was done by centrifugally washing 1 mL of pelleted cells three times with 2 mL of the requisite solutions constituted in ^{2}H$_2$O. The solutions that were used were 72.5 mM choline phosphate, and 4–7% (v/v) DMSO. The phosphate group on choline phosphate prevents this compound from entering the cells while DMSO is known to enter the cells freely.

NMR Spectroscopy

PFGSE NMR experiments were performed on a Bruker AMX 400 wide-bore spectrometer equipped with a gradient probe capable of delivering a maximum gradient of $\sim 10\ T\ m^{-1}$ in the direction of B_0. In all experiments, the standard PFGSE pulse sequence and phase cycles were used (1, 2). The probe temperature was set to 298 K. In a typical experiment, the duration of the $\pi/2$ pulse was 22 μs; that of the two gradient pulses, δ, was 2 ms; the time interval between the gradient pulses was 20 or 40 ms; the relaxation delay between transients was 3 s; and the number of transients per spectrum was 16 or 32. The field gradient was incremented in 32 or 96 steps to obtain a maximum value of $\sim 9.6\ Tm^{-1}$.

The acquired data consisted of 1k of complex points spanning a spectral width of 1 or 2 kHz. No zero-filling of the data was used, and a line-broadening factor of 5–20 Hz was used with exponential multiplication of the data prior to its Fourier transformation. A Matlab program (1) was used to process and analyze the data; the relevant spectral peaks were automatically integrated and scaled to the largest peak in the series by this program.

Monte Carlo Simulations

Diffusion in the context of a PFGSE experiment was simulated by performing a three-dimensional random walk for an ensemble of noninteracting point molecules (water). This so-called Monte Carlo method followed procedures described previously for simulating q-space plots for samples composed of molecules diffusing in restricting geometries (17). Various new algorithms were designed and verified using Mathematica (18) to account for the particular geometry describing a biconcave disc. The simulation code was written in "C", and simulations were executed on either a Silicon Graphics workstation or a Pentium PC.

Simulation parameters were chosen to mimic as closely as possible a sample of erythrocytes at a packing density of 0.50 in isotonic solution. The main cell diameter was 8 μm, maximum thickness 2.12 μm, and thickness at the central "dimple" 1 μm, yielding a cell volume of $8.6 \times 10^{-17}\ m^3$. Each cell was assumed to occupy the center of a hexagonal prism, and periodic boundary conditions were applied, thus simplifying the study to a single "reference cell" centered on the Cartesian origin (17, 19). The diffusion coefficient both inside and outside the cells was set to the same value of $2.0 \times 10^{-9}\ m^2\ s^{-1}$. (The same value was used to minimize the number of different parameter values employed in the simulations.) In real cellular systems these values differ, but since the diffusion time was chosen to be relatively long, the condition $\Delta \gg a^2/2D$ would still have been met even if the diffusion coefficient for inside the cells was less than half of that for the molecules outside. The simulated field gradient was incremented in 96 steps, from an initial value of 0.0 to a maximum of 9.41 T m^{-1}. The set of simulated echo intensities for all gradients in any one simula-
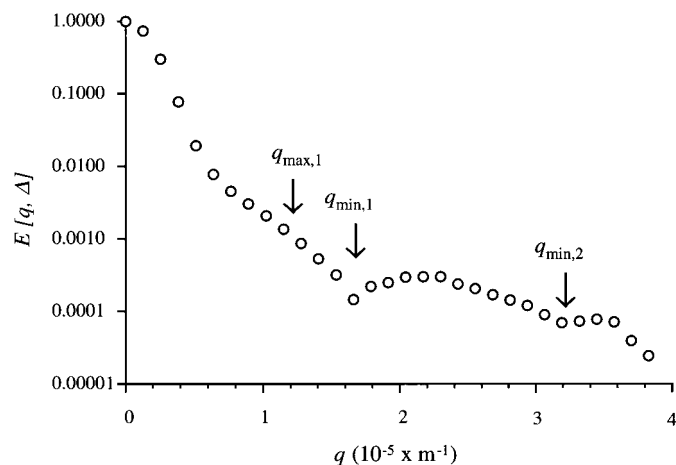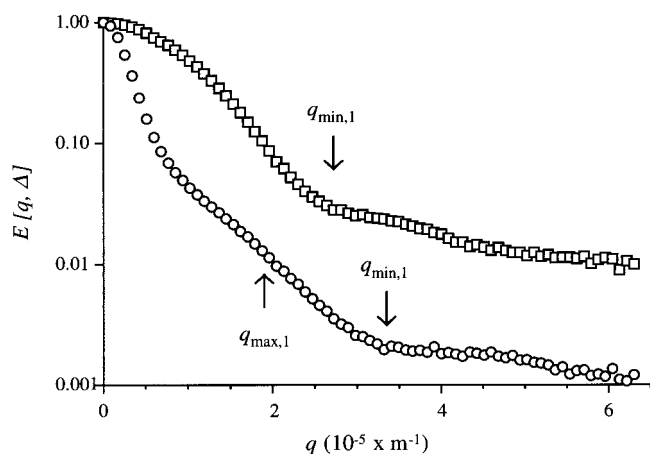

FIG. 1. ^{1}H NMR q-space plot of water in a suspension of fresh human erythrocytes with a hematocrit (Ht, fraction of the sample volume that is cells) of 0.30, at 298 K. The field gradient **g**, for this and all other experiments reported here, was applied in the direction of B_0, namely the z axis. The assignments of diffusion modes to the various features of the curves are extracellular diffusion-interference ("pore-hopping") shoulder at $q_{max,1}$ and intracellular diffusion-diffraction minima at $q_{min,1}$ and $q_{min,2}$. The q positions of the interference and diffraction features are inversely related to the mean cell diameter, bearing in mind that the cells would have been aligned with their disc planes parallel to B_0 (1).

tion was normalized to the maximum echo intensity produced when the gradient was zero. An "ensemble" consisted of 10×10^6 point molecules whose individual trajectories were studied. Each point molecule was assigned a random starting point and performed a random walk trajectory during the total diffusion time given by Δ (20 ms) + δ (2ms). During this time the molecule performed 3300 three-dimensional random jumps of length 28.28 μm, as determined by the Einstein equation for self-diffusion in *each* of the three dimensions, namely jump length = $(2\ D\ \text{jump time})^{1/2}$ (17, 19). The membrane transition probability was determined by trial simulations to ensure that the mean residence time for any point molecule inside the biconcave disc would be of the order of ~ 10 ms, in accordance with experimental values (20). The accumulated phase shifts of the magnetization (dipole moment per unit volume) for all point molecules, during the total diffusion time, were summed and averaged, and the echo intensity was then calculated for all gradient values and stored in an array. From this array of values the q-space plot was generated.

RESULTS

q-Space Plots from $^{1}H_2O$ in Suspensions of Erythrocytes

Figure 1 shows a typical ^{1}H NMR q-space plot obtained from the signal of water diffusing in a slightly hypotonic suspension of metabolically active human erythrocytes. The fact that the curve is not "monotonically strictly decreasing" is evident. The features of the curve are similar to those reported

FIG. 2. ^{1}H NMR q-space plots of water ($\bigcirc$) and choline ($\square$) in a 0.70-Ht suspension of resealed erythrocytes loaded with choline, at 298 K. The water curve is very different from that in Fig. 1 because the resealed cells were no longer biconcave discs but rather were a mixture of stomatocytes and spherocytes. The minima in the choline curve resulted from intracellular diffusion diffraction only. The difference between the two plots is due to the absence of extracellular interference diffraction (pore hopping) and transmembrane exchange, with the choline.

previously (*1*, *2*), but as a result of the higher values of field gradients now available, a higher order coherence was routinely observed. The shoulder centered at $\sim1.2 \times 10^5$ m^{-1} (denoted $q_{max,1}$) was previously inferred to be due to pore hopping (*1*, *2*); and the two minima at $\sim1.6 \times 10^5$ and $\sim3.2 \times 10^5$ m^{-1} are denoted $q_{min,1}$ and $q_{min,2}$, respectively. The physical bases of these three coherence features were addressed experimentally, as follows.

Choline and ^1H_2O q-Space Plots and Intracellular Diffusion Diffraction

Figure 2 shows the q-space plots for choline and water (residual ^{1}H^{2}HO) proton signals in a 0.70-Ht suspension of resealed erythrocytes. In the experiment, the duration of the spin-echo time, 2τ, was set to 40 ms compared with our commonly used value of 20–30 ms when water diffusion is studied (*1*, *2*). This allowed for the fact that the diffusion coefficient of choline is significantly smaller than that of water. Comparison of the q-space plots from water in Figs. 1 and 2 clearly shows that the positions of the maxima and minima in the two curves were not the same. This difference implied an alteration of cell shape between the fresh erythrocytes used for Fig. 1 and the resealed cells used for Fig. 2. Light microscopic examination of the resealed cells showed that they were not strictly biconcave but rather were a mixture of distorted discs and spheres.

A typical q-space plot from water in a suspension of *spherical* erythrocytes, akin to those obtained in a previous study (*2*), is shown in Fig. 3. Examination of this plot reveals a distinct similarity to the profile obtained for water in the resealed cells
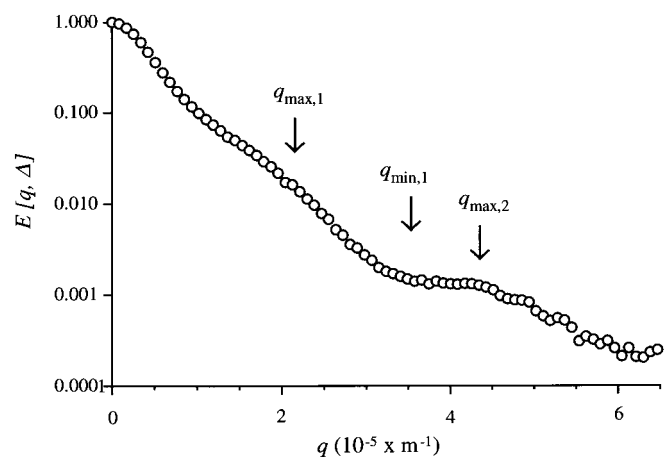

FIG. 3. High-resolution ^{1}H NMR q-space plot of water in a 0.62-Ht suspension of spherical erythrocytes, at 310 K. The curve is notably similar to that of water in the suspension of resealed cells shown in Fig. 2.

(Fig. 2). In both cases the first maximum (more correctly an "inflection," or a maximum in the first derivative) is at $\sim2 \times 10^5$ m^{-1} ($q_{max,1}$) while the minimum ($q_{min,1}$) after the first maximum is at $\sim3.4 \times 10^5$ m^{-1}. In the choline data $q_{min,1}$ is at $\sim2.8 \times 10^5$ m^{-1} while the next maximum is at $\sim3.5 \times 10^5$ m^{-1}. In our previous work (*2*) we attributed the first maximum in the water data (Fig. 3) to diffusion interference, while the second maximum (Fig. 3, $q_{max,2}$) was attributed to intracellular diffusion diffraction. On the other hand $q_{max,2}$ is not clearly delineated in Fig. 2 (see Discussion).

Choline Phosphate and ^1H_2O

Figure 4 shows the q-space plots of choline phosphate and water in a suspension of fresh red blood cells of Ht = 0.60.
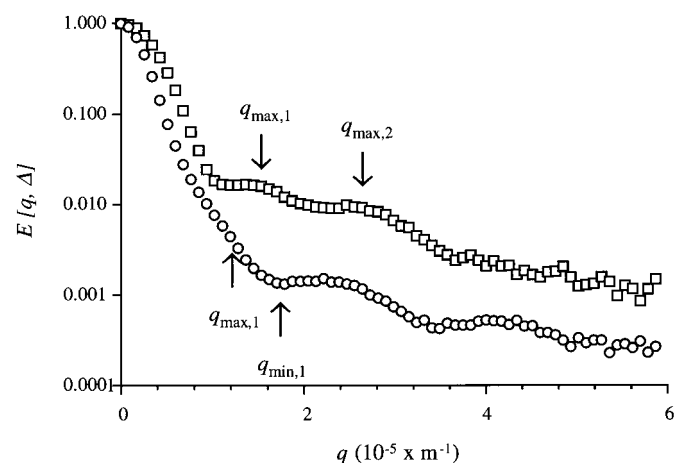
FIG. 4. ^{1}H NMR q-space plots of water ($\bigcirc$) and choline phosphate ($\square$) in a 0.60-Ht suspension of fresh erythrocytes, which had been washed in 72.5 mM choline phosphate, at 298 K. The peaks in the curve ($q_{max,1}$ and $q_{max,2}$), which are indicated by arrows, resulted from interference diffraction (pore hopping) only, since the choline phosphate was located exclusively extracellularly.
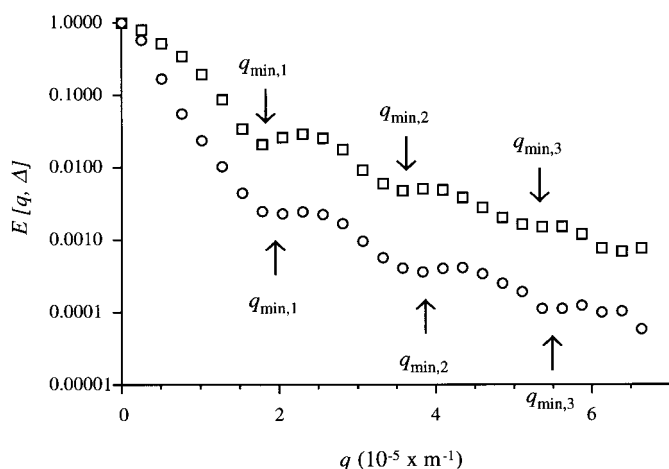
FIG. 5. ^{1}H NMR q-space plots of water (○) and DMSO (□) in a 0.60-Ht suspension of fresh erythrocytes that had been washed with 4% (v/v) DMSO, at 310 K. The DMSO curve is notably similar to the water curve, indicating that DMSO molecules were present inside and outside the cells. However, the signal attenuation of the DMSO was substantially less than that of water for a given q value.

Unlike the choline experiment (Fig. 2), in which the erythrocytes were primarily spherocytes (including some distorted discocytes), the cells in this case were all discocytes. This uniform cell shape was reflected in the form of the water q-space plot which was very similar to that from the metabolically active cells used for Fig. 1. For Fig. 4, the spin-echo time, 2τ, was set to 40 ms to enable a longer diffusion time, thus allowing for the smaller diffusion coefficient of choline phosphate. A large proportion of the water (60%) was located in the intracellular region (exchange notwithstanding) but the choline phosphate was only in the extracellular region; hence its diffusion would have been less restricted than if it were inside the cells. The apparent diffusion coefficient for each species was estimated from the initial slope of the data, when the $\log_{10}(E[q, \Delta])$ was plotted as a function of the Stejskal–Tanner parameter, $\gamma^2 g^2 \delta^2(\Delta - \delta/3)$; the respective values were 3.1×10^{-10} and 6.9×10^{-10} m^2 s^{-1} for choline phosphate and water.

DMSO q-Space Plots

Figure 5 shows q-space plots from DMSO and water in a 0.60-Ht erythrocyte suspension. A notable difference in the two plots is that the DMSO curve is higher, for all q values, than the water curve. Besides this difference, it is evident that the DMSO curve is similar in overall form to that of water; the q positions of the maxima and minima are basically the same but shifted (slightly) to the left. Specifically, common q_{min} values are at $\sim 1.8 \times 10^5$, 3.7×10^5, and 5.4×10^5 m^{-1}.

It was initially anticipated that the diffusion-interference effect would also be manifest in the DMSO curve; however, it was not discernible in any of the experiments.
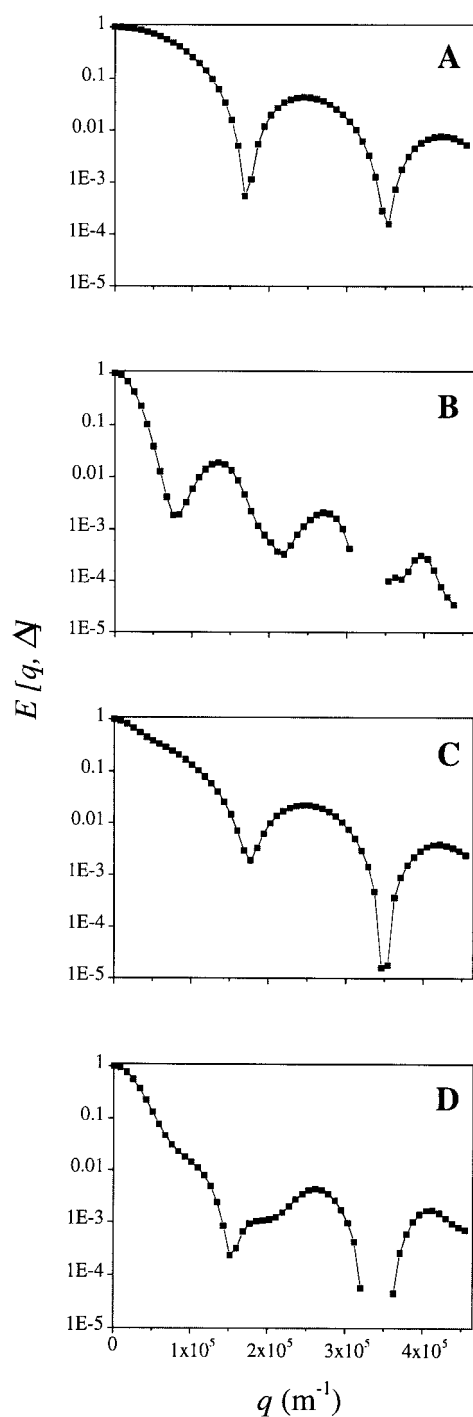
Simulations of q-Space Plots

Figure 6A shows the particular geometrical arrangement of model erythrocytes used for the computer simulation of NMR diffusion-coherence phenomena. The cells were assumed to occupy the centers of regular hexagonal prisms arranged with their faces in the two-dimensional crystallographic space group $p3$; and the corresponding sides were arranged as linear $p1$. Figure 6B shows two simulated erythrocytes with their axis of rotational symmetry orthogonal to $\mathbf{B}_0$.

Figure 7 shows the results of computer simulations in which the erythrocytes were assumed to occupy 50% of the sample volume, and the point water molecules were allowed to undergo random walks under four different conditions. Figure 7A shows the q-space plot for a system in which the water molecules were confined to diffuse in the intracellular compartments only and they were not allowed to undergo exchange across the membrane. Thus, there were no contributions to the signal from extracellular water. The q_{min} values were at 166,710 and 351,981 m^{-1}. The reciprocals of these values are 6.00 and 2.84 μm, respectively. The main diameter of the virtual erythrocyte was set to 8 μm; thus the scaling factors that
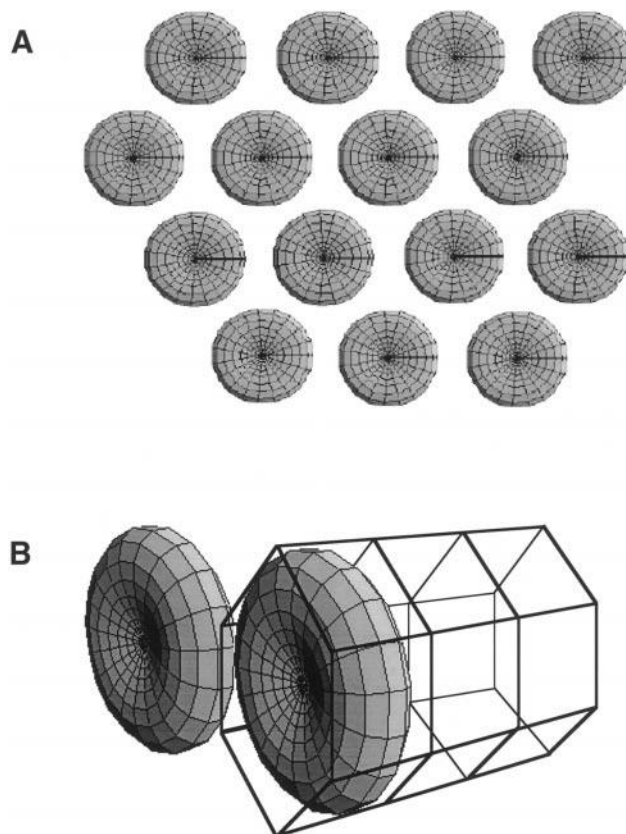
FIG. 6. (A) Schematic representation of a section of one layer of the array of discocytes used in the Monte Carlo random walk simulation of diffusion in a suspension of erythrocytes. (B) A detailed view of a discocyte and one of its neighbors in a "unit cell" in the space-filling hexagonal-prism three-dimensional tessellation, used in modeling a q-space experiment.

FIG. 7. Simulated q-space plots for molecules diffusing outside and inside cells, of the shape and spatial organization shown in Fig. 6. (A) Data obtained when the NMR-detected molecules were restricted exclusively to the intracellular compartment; this gave rise to the diffusion-diffraction effect in the q-space plot. (B) Simulation with the detected molecules diffusing exclusively in the extracellular region; this gave rise to the diffusion-interference effect. (The discontinuity in this curve, and the two below, was due to negative values of $E[q, \Delta]$, which can arise with the present type of finite system, and for which the logarithm is physically meaningless.) (C) Data from the situation in which the detected molecules diffused in both the intra- and extracellular regions; the curve was shown to be the sum of the two curves in A and B. (D)

relate the position of each diffusion-diffraction minimum to the main cell diameter (d) were calculated to be 1.333 and 2.82, respectively; thus $d = 1.333/q_{min,1}$ for the first minimum, and $d = 2.82/q_{min,2}$ for the second (or $d = 2 \times 1.41/q_{min,2}$).

The Bessel function relationships that describe q-space plots for diffusion in transverse cylinders and spheres are not strictly periodic (10). This is also the case for the model erythrocyte since the scaling factor for the second minimum was not an integral multiple of that for the first.

Figure 7B shows the coherences that arose when water was confined to diffuse in the extracellular region and was not allowed to exchange across the cell membranes. In this case the signal attenuation was much more rapid and the first minimum occurred at a much smaller q value (80,869 m^{-1}) than in Fig. 7A. However, by analogy with pore hopping around closely packed spheres of uniform size (4), a simple relationship exists between the main cell diameter and the position of the first two maxima. Thus $q_{max,1} = 132,904$ and $q_{max,2} = 268,460$ m^{-1} and therefore the "rules" that relate the positions of the maxima to the cell diameter are $d = 1.063/q_{max,1}$ and $d = 2 \times 1.073/q_{max,2}$, respectively.

Figure 7C shows the q-space plot obtained when water was allowed to diffuse in both the intra- and extracellular spaces, but without transmembrane exchange. This curve was directly superimposable on the one that resulted from the simple addition of the data in the two panels above it; this outcome was a useful verification of the simulation program. (Note that the data sets were weighted according to the relative volumes inside and outside the cell in its "virtual" hexagonal prism; in the case of an Ht of 0.50 the relative weighting was 1:1.) The two notable features of the q-space curve in Fig. 7C are that the first interference peak, evident in Fig. 7B, is only manifest as a poorly defined shoulder, and the diffraction minima evident in Fig. 7A are in almost identical positions in Fig.7C. This outcome indicates that at Ht = 0.5 the diffusion-diffraction signal dominates over that of diffusion interference.

Finally, Fig. 7D shows a simulated q-space plot for a system identical to that of Fig. 7C but here the membrane was "made" permeable to the water such that exchange across the membrane occurred. The probability of a point molecule crossing the membrane on encountering it, whether impacting it from

The same situation as in C but with exchange allowed across the cell membrane. Parameters used in the simulations: Erythrocytes, equation as given by (15); main diameter, 8.0 μm; center thickness, 1.0 μm; maximum thickness, 2.0 μm; volume and surface area calculated on the basis of the previous three values, 86 fL and 126 μm^2, respectively. Hexagonal unit cell: orientation as depicted in Fig. 6, with side length of the regular hexagon adjusted to give the requisite Ht value. Monte Carlo random walk: jump length less than 0.2 of the minimum distance between the cell surface and the wall of the prism; periodic boundary conditions applied at the hexagonal-prism walls (thus simulating an infinite array using just one unit cell and its contents); and the total number of trajectories for each simulation, 10×10^6. In D the "transition probability" of a molecule, when encountering the cell membrane, of passing through it was set to 0.01.

the outside or the inside, was set to a value (0.01) so that the intracellular mean residence lifetime for a point molecule matched that observed experimentally for human erythrocytes, at 37°C (20). There are three notable features: (1) there is a much greater extent of signal attenuation than for corresponding q values in Fig. 7C; (2) the diffusion-interference shoulder is better delineated; and (3) the values of $q_{min,1}$ (152,127 m^{-1}) are less than either of those in Fig. 7A (166,710 m^{-1}) or 7C (176,322 m^{-1}); this was also true, although less clearly defined, for the $q_{min,2}$ values.

DISCUSSION

General

In this investigation of q-space plots from erythrocyte suspensions several probe substances were used, namely choline, choline phosphate, and DMSO; these were used in order to discriminate between the features of diffusion interference and diffusion diffraction. Choline was entrapped in erythrocytes by hypotonic hemolysis and resealing, while choline phosphate was added to the suspensions without it entering the cells. By observing the proton signals from choline or choline phosphate in a PFGSE experiment, q-space plots showing only intracellular diffusion diffraction from choline, or the diffusion-interference effect from extracellular choline phosphate, were observed (Figs. 2 and 4, respectively). In addition, DMSO was added to erythrocyte suspensions as a control experiment (Fig. 2); DMSO enters the cell freely and therefore should show both coherence effects. However, the diffusion-interference shoulder was not "resolved" and so the plot was dominated by signal from the intracellular molecules.

Choline q-Space Plots and Intracellular Diffusion Diffraction

The hypotonic-lysis method used for rapidly incorporating choline into the cells caused marked changes in cell shape when the cells became resealed. These changes were clearly observable under the light microscope. As a result of these morphological changes it was not possible to correlate the features of the q-space plots of resealed cells (Fig. 2) with those of *fresh* erythrocytes (Fig. 1). The features of the q-space plots of choline and water shown in Fig. 2 did, however, provide important information regarding the diffusion of these two species in a cell suspension. First, signal attenuation at a given q value was considerably less for choline than for water. In free solution it would be expected that the water signal would be attenuated more rapidly than that of choline because water, being a smaller molecule, has a higher diffusion coefficient. In the case of restricted diffusion, differences in the rate of diffusion will not result in significantly different extents of attenuation as long as the condition $\Delta \gg a^2/2D$ (where a is the effective cell diameter) is maintained for both species. In the experiment this condition was maintained, but while cho-

line was restricted to diffuse solely within the intracellular compartments water was free to exchange across the membranes and hence to diffuse larger distances in the time Δ. The greater attenuation of the water signal can therefore be interpreted as being due, in part, to the larger mean diffusion distance available to it. A second contributing factor is that water in the extracellular region diffuses in a less viscous medium so its "intrinsic" as well as its "apparent" diffusion coefficient will be greater than that for either water or choline inside the cells.

Another significant difference in the water and choline q-space plots in Fig. 2 was the positions of the diffusion-diffraction peaks. This difference was very important because it enabled discrimination between the extracellular diffusion-interference and the intracellular diffusion-diffraction phenomena, which was the main aim of the investigation. The peak maximum at ~2.0×10^5 m^{-1} in the water curve was clearly absent in the choline curve. Thus the first peak (shoulder) present in the water curve was able to be assigned to an effect of water diffusing in the space between the cells, namely "pore hopping." In other words, the phenomenon occurs only with molecules that diffuse outside the cells. By the same reasoning, the peak ($q_{max,1}$, in Fig. 2) which appears in the choline curve at ~3.5×10^5 m^{-1} was readily ascribed to intracellular diffusion diffraction. Therefore, this experiment discriminated between the diffusion-interference and diffusion-diffraction effects in the q-space plots.

Diffusion-diffraction patterns in q-space plots, where rapid transmembrane exchange is present, should lead to estimates of apparent cell dimensions that are smaller than if exchange were not present (14). Therefore, q_{min} values for water were expected to be lower in comparison with those for choline. However, under the conditions used for Fig. 2 this was not readily discernible. Since only intracellular diffusion diffraction was manifest in the choline curve, the peak minimum ($q_{min,1}$ in Fig. 2) at ~2.8×10^5 m^{-1} should be considered the "relevant" $q_{min,1}$ and not the ambiguous one for water located at ~3.4×10^5 m^{-1}. The interpretation of this result is that the first interference peak for water (see Fig. 7B) is partly superimposed on the first diffraction "valley" (see Fig. 7A), thus displacing the position of the overall minimum. At first sight this displacement might be expected to be to the right, but rapid transmembrane exchange suppresses the interference effect and displaces the first (and subsequent) minimum in the overall q-space curve to the *left*. Comparing Figs. 7C and D readily demonstrates this outcome.

In a previous study (2) the spherical cell diameter was calculated to be $1/2.0 \times 10^5$ m^{-1} = 5.0 μm, based on the pore hopping interpretation for water diffusion outside the cells, and $1.46/3.2 \times 10^5$ m^{-1} = 4.6 μm based on the $q_{min,1}^d$ of the intracellular diffraction peak. The cell diameter estimated from $q_{min,1}$ of the choline curve was $1.46/2.8 \times 10^5$ m^{-1} = 5.2 μm, which was significantly different from the corresponding value (4.6 μm) derived from the water curve. The basis of this

difference lies in the matters discussed in the previous paragraph.

These results clearly show that the presence of both diffusion-interference and diffusion-diffraction peaks can potentially complicate the inference of compartment sizes from q-space plots of water if the first diffraction and interference peaks are used. A more accurate estimate of cell diameter comes about if the diffusion-interference effect is minimized and this can be achieved by using a high hematocrit. Alternatively, if the signal-to-noise is sufficiently high the higher order diffraction peaks (and minima) can be used as then the interference pattern makes an insignificant contribution to the overall q-space signal. The remaining complication to the interpretation of the data is the extent to which the transmembrane exchange causes a shift in the diffraction minima. The extent of this effect can be judged from the data in Fig. 5.

Choline Phosphate and Extracellular Diffusion Interference

It is instructive to compare the curve for choline phosphate in Fig. 4 with that for choline in Fig 2: the choline phosphate signal declines more steeply, over the first few q values up to 2.0×10^5 m^{-1}. However, choline phosphate, being a larger molecule, has a smaller intrinsic diffusion coefficient than choline, so the greater signal attenuation of choline phosphate cannot be ascribed to a larger intrinsic diffusion coefficient. The proposed reason for the more rapid attenuation of the signal is that the motion of choline phosphate is less restricted, as a result of it only being in the extracellular space.

It can also be seen in Fig. 4 that $q_{max,1}$ for choline phosphate (upper curve) and $q_{max,1}$ for water (lower curve) do not coincide. Specifically, there are two major coherence peaks in the choline phosphate plot that are centered at ~1.5×10^5 m^{-1} ($q_{max,1}$) and ~2.6×10^5 m^{-1} ($q_{max,2}$), while for water there is a shoulder at ~1.2×10^5 m^{-1} and a peak at ~2.3×10^5 m^{-1}. Since the choline phosphate molecules were confined to the outside of the cells, the two maxima can be ascribed only to the diffusion-interference phenomenon. The position of the water peaks at a lower value of q can be attributed to the fact that water exchanges between the inside and the outside of the cells (1, 14). In effect this makes the available mean diffusion distance of the outside water larger because of access to the inside of the cells. The effect is well illustrated by comparing the q position of the first peak in Fig. 7B and the shoulder in Fig, 7D.

The diffusion-interference peak at ~1.2×10^5 m^{-1} (shoulder, $q_{max,1}$ in Figs. 1 and 4) was not evident with high hematocrit samples of discocytes. This is in contrast with the shoulder seen with *spherical* erythrocytes where it was *pronounced* (see Figs 2 and 3).

In Fig. 4 the shoulder on the water curve, to a first approximation, implies a cell diameter of 8.3 μm; this value was arrived at by assuming that the cells approximate flat cylinders with their axis of rotational symmetry orthogonal to $\mathbf{B}_0$ and for this arrangement the diameter is given by $1.23/q_{max,1}$ (1, 2). By

the same reasoning, the first choline phosphate peak corresponds to a mean cell diameter of 6.7 μm. The difference between the two values is, again, ascribable to the effect of the transmembrane exchange of water (1, 14). This matter is discussed next.

DMSO q-Space Plots

In Fig. 5 the close similarity of the forms of the q-space plots from DMSO and water, and the fact that DMSO is known to permeate the cell membrane, suggests that the DMSO coherences also arise from the same phenomena as for water. However, DMSO permeation through cell membranes is slow on the NMR time scale so it would be expected that the diffusion-diffraction minima would be at (slightly) smaller values of q, and this is indeed evident in Fig. 5. The differences in q_{min} values give an indication of the possible magnitude of errors in estimates of mean cell diameter when the probe molecule is in rapid exchange across the cell membranes. The positions of the second- and third-order diffusion-diffraction peaks are much less affected by underlying diffusion-interference peaks (see Fig. 7 and discussion below) so a comparison of the $q_{min,2}$ and $q_{min,3}$ values (notwithstanding lower signal-to-noise) would give a more accurate impression of the effects of transmembrane exchange on estimates of cell diameter.

The q-space plot of the DMSO data in Fig. 5 is similar to the simulated data in Fig. 7C while the water data are more like the simulated data in Fig. 7D; this is consistent with the relative rates of transmembrane exchange of the two molecules. Furthermore it is clear from Fig. 7C that if there is no (or slow) transmembrane exchange that the first diffusion-interference peak is much less well defined and this is seen with the DMSO data in Fig. 5.

Simulations of Cellular System Showing Diffusion Coherence

In order to check the physical interpretations of the features of the q-space plots, numerical simulations of diffusion, modeled as a three-dimensional random walk in an array of semi-permeable discocytes (Fig. 6), were shown to be valuable (Fig. 7). The ability to modulate transmembrane exchange between completely "on" and completely "off" states enabled the independent study of the diffraction and interference effects. Where point molecules were confined exclusively to the extracellular region the effects were able to be identified as interference effects. When point molecules were confined exclusively to the intracellular region the effects could be assigned to diffusion diffraction. When exchange was turned on the combined effects of diffusion interference and diffusion diffraction were observed. Therefore, in all cases the features of the q-space plots could be related to the main cell diameter.

It is also worth noting that the signal from the diffusion-interference phenomenon was substantially weaker than that from diffusion diffraction. Therefore, when both phenomena were in operation the combined q-space curve was dominated

by the latter (Figs. 7A and 7B), and this result is consistent with the experimental results (Figs. 1, 4, and 5).

The simple scalar relationships between the values of q_{max} and cell diameter, in the diffusion-interference data, only apply at higher packing densities of the cells, around Ht = 0.50 (Fig. 7B). (However, at Ht values above $\sim$0.7 the small fraction of extracellular water implies a smaller interference signal.) By analogy, in a bed of randomly packed spheres of equal diameter, the pores are separated by a mean distance that is closely approximated by the diameter of a sphere (10). However, if the spheres are dispersed (and stay suspended by "density matching" with the solvent) then clearly the distances between the centers of the pores will be greater than the diameter of the spheres. Thus in q-space analysis, the position of q_{max} does not correspond simply to the reciprocal of the sphere diameter for dilute suspensions; the same would be true for erythrocytes in a dilute suspension. In addition, it is expected that the packing geometry will impact upon the features of q-space plots from arrays of cells; the extent of this variation warrants further study.

CONCLUSIONS

Since the q-space plots of water in erythrocyte suspensions display both intracellular and extracellular coherences, while the choline curve (Fig. 2) shows only intracellular diffraction, it can be concluded that the presence of the interference peak in the water curve partially obscures its diffraction coherence(s) (compare Figs. 7A and 7B). It was expected that the water curve would also display a peak at q_{max} $\sim$3.5 $\times$ 10^5 m^{-1} as was the case with choline (Fig. 2, upper curve), but this was absent. This absence is concluded to have been caused by the dominant overlapping diffraction peak (see Fig. 7C). Also, there was a minimum in the choline curve (Fig. 2) at $\sim$2.8 $\times$ 10^5 m^{-1} which was not present in the water curve. This difference can be attributed to the presence of its interference peak at q $\sim$1.8 $\times$ 10^5 m^{-1}. The minimum in the water curve at $q_{min,1}$ $\sim$2.8 $\times$ 10^5 m^{-1} was therefore concluded to have been caused by diffusion interference since it was absent in the case of choline which only gave diffusion-diffraction effects.

Factors that affect the distinctness of the features of q-space plots have been considered in earlier work on "artificial" ($12, 13$) and cellular systems (2). In the case of cell suspensions, the diffraction effects are also "blurred" by heterogeneity of cell shapes and sizes ($2, 3$). For cells such as erythrocytes, which have only one axis of rotational symmetry, orientation with their axis orthogonal to $\mathbf{B}_0$ clearly creates a favorable situation for observing diffusion-coherence effects ($1, 2$), as also reported herein. Physical and chemical (metabolic) factors that affect the uniformity of this orientation across the entire cell population will also degrade the distinctness of the coherence patterns.

Finally, assignment of the features of q-space plots from erythrocyte suspensions by direct experimental means and consistency of Monte Carlo simulations with inferences drawn from these data pave the way for more quantitative interpretations of such data from other forms of erythrocytes, and more complex cell types and arrays.

REFERENCES

1. P. W. Kuchel, A. Coy, and P. Stilbs, *Magn. Reson. Med.* **37,** 637 (1997).
2. A. M. Torres, R. J. Michniewicz, B. E. Chapman, G. A. R. Young, and P. W. Kuchel, *Magn. Reson. Imaging* **16,** 423 (1998).
3. D. Cory and A. N. Garroway, *Magn. Reson. Med.* **14,** 435 (1990).
4. P. T. Callaghan, A. Coy, D. Macgowan, K. J. Packer, and F. O. Zelaya, *Nature* **351,** 467 (1991).
5. P. T. Callaghan, A. Coy, T. P. J. Halpin, D. Macgowan, K. J. Packer, and F. O. Zelaya, *J. Chem. Phys.* **97,** 651 (1992).
6. P. P. Mitra and P. N. Sen, *Phys. Rev. B* **45,** 143 (1992).
7. A. J. Lennon, "A Pulsed Field Gradient NMR and Random-Walk Simulation Study of Diffusion in Heterogeneous Systems," Ph.D. dissertation, Department of Biochemistry, University of Sydney (1995).
8. F. A. Jenkins and H. E. White, "Fundamentals of Optics," 3rd Ed., McGraw–Hill, New York (1957).
9. P. T. Callaghan, "Principles of Magnetic Resonance Microscopy," Oxford Univ. Press, Oxford (1991).
10. P. T. Callaghan, *J. Magn. Reson. A* **113,** 53 (1995).
11. P. T. Callaghan, *Magn. Reson. Imaging* **14,** 701 (1995).
12. P. T Callaghan and A. Coy, *in* "Nuclear Magnetic Resonance Probes of Molecular Dynamics" (R. Tycko, Ed.), Kluwer, Amsterdam (1994).
13. M. Appel, G. Fleischer, D. Geschke, J. Kärger, and M. Winkler, *J. Magn. Reson. A* **122,** 248 (1996).
14. A. V. Barzykin, K. Hayamizu, W. S. Price, and M. Tachiya, *J. Magn. Reson. A* **114,** 39 (1995).
15. P. W. Kuchel and E. D. Fackerell, *Bull. Math. Biol.,* in press (1999).
16. G. R. Beilharz, C. R. Middlehurst, P. W. Kuchel, G. E. Hunt, and G. F. S. Johnson, *Aust. J. Exp. Biol. Med. Sci.* **64,** 271 (1986).
17. A. J. Lennon and P. W. Kuchel, *J. Magn. Reson. A* **111,** 208 (1994).
18. S. Wolfram, "The Mathematica Book," Version 3, Cambridge Univ. Press, Cambridge (1996).
19. A. J. Lennon and P. W. Kuchel, *J. Magn. Reson. A* **107,** 229 (1994).
20. Gh. Benga, V. I. Pop, O. Popescu, and V. Borza, *J. Biochem. Biophys. Methods* **21,** 87 (1990).

PAPER II

ARTICLE

David G. Regan · Philip W. Kuchel

Mean residence time of molecules diffusing in a cell bounded by a semi-permeable membrane: Monte Carlo simulations and an expression relating membrane transition probability to permeability

Abstract The rapid exchange of water across erythrocyte membranes is readily measured using an NMR method that entails doping a suspension of cells with a moderately high concentration of Mn^{2+} and measuring the rate of transverse relaxation of the nuclear magnetisation. Analysis of the data yields an estimate of the rate constant for membrane transport, from which the membrane permeability can be determined. It is assumed in the analysis that the efflux rate of the water is solely a function of the rate of membrane permeation and that the time it takes for intracellular water molecules to diffuse to the membrane is relatively insignificant. The limits of this assumption were explored by using random-walk simulations of diffusion in cells modelled as parallel planes, spheres, and biconcave discs. The rate of membrane transport was specified in terms of a transition probability but it was not initially clear what the relationship should be between this parameter and the diffusional membrane permeability P_d. This relationship was derived and used to show that the mean residence time for a water molecule is determined by P_d when the diffusion coefficient is above a certain threshold value; it is determined by the distance to the membrane below that value.

Key words Membrane permeability · Parallel planes · Sphere · Biconcave disc · Bounded diffusion

Introduction

Molecular diffusion is a key process in facilitating chemical interactions in biological systems (e.g., Waldeck et al. 1997). The molecules in a cell are immersed in an aqueous medium and random motions that correspond to thermal energy fluctuations lead to molecular migration through the cell. This motion satisfies the proximity requirements for molecular interactions and may, in certain cases, constitute the rate-limiting step in these interactions.

In cellular systems, diffusion-mediated processes are constrained by three main parameters: (1) the intrinsic rate of diffusion (characterised by the diffusion coefficient D) in the intracellular medium; (2) the geometrical shape and dimensions of the cell; and (3) the rate of exchange of the molecular species across the cell membrane. Two of these parameters, diffusion coefficient and membrane exchange rate constant, are incorporated in a property of the cell membrane which is referred to as the permeability, that is denoted by P_d (Stein 1986). Thus, the permeability with respect to a particular molecule will be a function of both the rate of diffusion to the membrane and the rate of exchange across it.

The average length of time that a molecule spends inside a cell before exiting is referred to as the mean residence time (MRT); it is a function of the permeability of the cell membrane with respect to that molecule, and the geometrical form and dimensions of the cell. If the mean time taken for a class of molecule to diffuse across the interior of a cell is comparable to the experimentally measured MRT, then it can be inferred that the membrane does little to impede the efflux from the cell. On the other hand, if the MRT is much greater than this diffusion time, then the inference can be made that the permeability of the membrane is what controls the efflux.

The challenges of the work described here were threefold: (1) to develop a model of molecular diffusion in cells in order to simulate experimental data used in estimating the MRT of water in red blood cells (RBC); (2) to derive a mathematical expression relating membrane transition probability (see Methods) and P_d; and (3) to use the data from the simulations, in conjunction with the permeability expression, to calculate the parameter ranges, for various geometries (parallel planes,

D.G. Regan · P.W. Kuchel (✉)
Department of Biochemistry, University of Sydney,
NSW 2006, Australia
e-mail: p.kuchel@biochem.usyd.edu.au

spheres, and biconcave discs), that determine whether the MRT is dominated by membrane permeability or the cell dimensions. The motivation for the second of these goals arose from the initial finding that MRT, as predicted by computer simulations of membrane-bounded diffusion, depended on the jump length (see Methods) chosen in the simulations.

The computer simulations employed a random walk technique, based on a Monte Carlo method, to simulate the diffusion of water inside a virtual cell that could be described by a mathematical expression in three Cartesian dimensions (e.g., Lennon and Kuchel 1994a, b; Lennon et al. 1994). The predicted MRT values were compared with those calculated from NMR relaxation data obtained using the so-called manganese-doping method (Benga et al. 1990, 1992, 1993).

Theory

Random walk simulations of diffusion

The Monte Carlo random walk procedures used in this work have been described previously (Lennon and Kuchel 1994a, b; Lennon et al. 1994) and specific details of their implementation are given in Methods. However, a general overview of the method is warranted in order to provide a context for the derivation of a mathematical expression for P_d.

Random walks can be implemented in any number of dimensions. In a three-dimensional random walk, a cubic lattice provides a convenient representation of the medium through which a virtual particle (or an ensemble of independent particles) diffuses by jumping from lattice point to lattice point. The distance between adjacent lattice points is the jump length (s) and the time taken to undergo a single jump is the jump time. A single three-dimensional jump is achieved by simultaneously updating the coordinates of the particle by + or – one jump length in the x, y, and z directions (assuming the lattice is aligned with the x-, y-, and z-Cartesian axes). The direction of displacement (+ or –) in each dimension is chosen at random, by means of a random number generator (RNG; specifically, a random binary digit generator). The choice of s and jump time are related to the diffusion coefficient assigned to the virtual particle. The average coordinate after time t for an ensemble of point molecules, starting at the origin and diffusing freely and isotropically, will be zero. However, the mean square displacement, $\langle r^2 \rangle$, for the ensemble in three dimensions is given by the Einstein equation:

$$\langle r^2 \rangle = 6Dt \tag{1}$$

In a system where diffusion is restricted by barriers (bounded diffusion), that may be impermeable or semi-permeable, the apparent (experimentally observed) diffusion coefficient (D_{app}) will be smaller than the intrinsic

diffusion coefficient, i.e., the mean-square displacement in a given time will be smaller than for free diffusion. By considering Eq. (1) it is seen that this effect becomes pronounced when the time interval during which diffusion is observed, τ, is large in comparison with the ratio a^2/D, where a is the separation distance between the barriers. Hence, in the case of a sphere, bounded diffusion will be observed when $\tau \gg \sim a^2/D$, where a is the radius of the sphere.

When diffusion is restricted by a semi-permeable membrane, the simulation of this property is achieved by defining the spatial location of the barrier (namely, $x^2 + y^2 + z^2 = a^2$ for a sphere) and ascribing to it a transition probability (tp) which determines the probability of transition by a virtual particle upon intersection of its trajectory with the barrier. The diffusive permeability coefficient, P_d, for a slice of a membrane of unit area is given by (Stein 1986):

$$P_d = D/\lambda \tag{2}$$

where D is the diffusion coefficient of the diffusant in the membrane and λ is the thickness of the membrane (see Fig. 1). The permeability coefficient has the dimensions $m\ s^{-1}$, which is consistent with the notion that it is a measure of the rate at which a substance crosses the membrane, and it corresponds to the reciprocal of the diffusive resistance. Fick's first law of diffusion specifies that the flux, J_d, through unit area of membrane orthogonal to the flux is equal to the diffusion coefficient of the diffusant multiplied by its concentration gradient in the direction of the flux:

$$J_d = -D(C_2 - C_1)/\lambda = -P_d(C_2 - C_1) \tag{3}$$

Because we do not usually know the effective thickness or how the concentration gradient varies within a biological membrane, the permeability is usually used as an experimentally more convenient measure of flux through the membrane than the diffusion coefficient (Stein 1986).
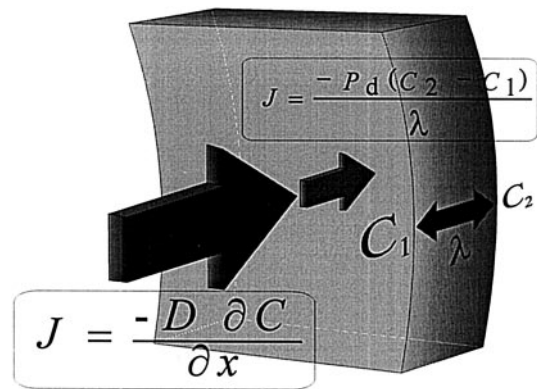
Fig. 1 Schematic representation of flux (J, *large single-headed arrow*) to the membrane and through the membrane (J, *small single-headed arrow*). The concentration difference across the membrane is equal to $C_2 - C_1$, and the membrane thickness is denoted by λ which corresponds to jump length (s) in the context of the Monte Carlo random walk

Relationship between tp and P_d

The transition probability of a membrane is the rate of transfer across the membrane, J_{mem} (represented by the small arrow in Fig. 1), relative to that which would occur in the same region of space in the absence of the membrane, J_{bulk} (the large arrow in Fig. 1); thus:

$$tp = \frac{J_{mem}}{J_{bulk}} = \frac{P_d(C_2 - C_1)}{D\partial C/\partial x} \qquad (4)$$

An individual particle jumps, at each step of its random walk, from its current position at concentration C_1 to its new position at concentration C_2. Because each trajectory is independent of all others, each step is, in effect, a step into an unoccupied volume whose concentration (C_2) is therefore zero; this is true both for diffusion in the bulk medium and for transition across the membrane. While concentration has little physical meaning for a single particle, it is heuristically useful to consider the concentration at C_1 and C_2 as being separated by the distance s, equal to the jump length, and so the partial derivative in the denominator of Eq. (4) can be written as $(C_2 - C_1)/s = -C_1/s$. Equation (4) then simplifies to:

$$tp = \frac{P_d s}{D} \qquad (5)$$

or

$$P_d = \frac{D\,tp}{s} \qquad (6)$$

Thus, s, in effect, represents the membrane thickness as a result of the particular way the membrane boundary is defined. In words, Eq. (6) indicates that a reduction in the transition probability will result in a smaller value for P_d, while a reduction in the thickness of the membrane will result in a larger value. Thus, in a Monte Carlo simulation, the permeability can be kept constant by ensuring that the ratio tp/s is held constant.

Methods

Monte Carlo simulations

The basic procedures and programs employed in simulating bounded molecular diffusion have been described previously (Lennon and Kuchel 1994a, b; Lennon et al. 1994). The original programs, written in C, were modified to allow the calculation of MRT values under prescribed conditions, while various redundancies were eliminated to enable increased computational speed.

Simulations were performed for ensembles of non-interacting point molecules having an intrinsic diffusion coefficient of $D = 2.0 \times 10^{-9}$ m^2 s^{-1}, which is approximately equal to that of water at 20 °C (Mills 1973).

Diffusion was restricted to the region of space enclosed either by parallel planes, a sphere, or a biconcave
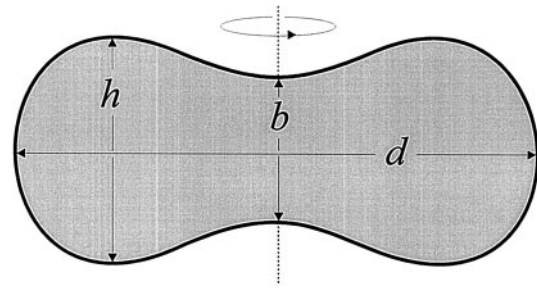
Fig. 2 Two-dimensional representation of a biconcave disc whose shape and dimensions are defined by means of the parameters b, d, and h. Rotation around the axis indicated by the *dotted line* results in a three-dimensional model which approximates the shape of a human red blood cell

disc (Fig. 2). These boundaries were specified as being semi-permeable by assigning them a value of tp, which was invoked upon intersection of a trajectory of a point molecule with the boundary.

The biconcave disc (or discocyte) was represented by a degree-4 equation in Cartesian coordinates (Kuchel and Fackerell 1999). This defines a shape by means of three parameters (see Fig. 2) that closely approximates the shape of a human red blood cell ($b = 1.0 \times 10^{-6}$ m, $h = 2.12 \times 10^{-6}$ m, $d = 8.0 \times 10^{-6}$ m) or of an elephant red blood cell ($b = 1.16 \times 10^{-6}$ m, $h = 2.3 \times 10^{-6}$ m, $d = 9.3 \times 10^{-6}$ m) (Benga et al. 1999).

For diffusion within spherical boundaries, a radius of 5.0×10^{-6} m was chosen. For diffusion bounded by parallel planes, the distance separating the planes was either 1.5×10^{-6} m (a distance which represented approximately the average distance between the flattish surfaces of a human RBC) or 5.0×10^{-6} m.

The diffusion coefficient, tp, and s could also be independently varied, allowing membrane permeability to be manipulated in a number of ways. Comparison of simulation data with analytical results for diffusion between perfectly reflecting parallel planes (Piton et al. 1994) implied that the ratio of the dimension separating the planes to jump length should be at least 5:1 for consistent results and this principle was applied in all simulations.

Calculation of MRT

In order to calculate the MRT for an ensemble of point molecules diffusing in a system bounded by semi-permeable boundaries, each point molecule began its trajectory from a randomly chosen location inside the bounded compartment and was allowed to continue its trajectory until it crossed the membrane. The times spent inside the compartment, prior to membrane transition, were summed and averaged over the entire ensemble consisting of 1000 individual point molecules, to yield an MRT for the particular parameter set.

Results

The original aim of the work was to use Monte Carlo simulations to corroborate MRT data that had been acquired from human RBC, and for other species, using the NMR manganese-doping procedure (Benga et al. 1990, 1992, 1993). Thus, it was necessary to establish the nature of the relationship between tp and P_d, the latter of which can be measured experimentally for real cells. The preliminary simulations revealed an interesting phenomenon: while the predicted MRT was a function of tp as expected (a smaller value of tp resulted in a larger MRT), it was observed that if the jump length was decreased the MRT also decreased. In other words, the MRT appeared to be also dependent on s. This outcome was initially felt to be counterintuitive but the derivation of Eq. (6) revealed the logic of the phenomenon.

Figure 3 shows the results of simulations in which the MRT values were calculated for parallel planes (separation distance, 5×10^{-6} m), a sphere (radius, 5×10^{-6} m), and a biconcave disc (having the dimensions of human RBC; see Methods), with three different values of tp: 0.1, 0.01, and 0.001. The range of jump lengths varied from $s_{min} = 1/5 \times a$ to $s_{max} = 1/10{,}000 \times a$ ($s_{max} = 1/20{,}000 \times a$ in the case of parallel planes), where a was equal to the distance separating the parallel planes, the radius of the sphere, or the dimension b in the biconcave disc (Kuchel and Fackerell 1999; see Fig. 2). Figure 3 shows that the MRT values increased as tp was reduced at any value of s. This was expected since a reduction in tp reduces the number of collisions with the membrane, which on average are required for exit from the cell. However, MRT values also decreased as s was reduced for a given value of tp. Figure 3 also shows that MRT values converged asymptotically to a limiting value as s became small.

Table 1 contains the data used to generate Fig. 3A (parallel planes) and it illustrates the important finding that any two simulations in which tp differed by a factor of, say, 10 yielded approximately the same value of MRT as when s differed by the same proportion for a given tp. Specifically, the MRT equalled 1.154 ms when tp was 0.1 and s was 1×10^{-8} m, and it also equalled 1.156 ms when tp was 0.01 and s was 1×10^{-9} m. Similar results were observed for the sphere and the biconcave disc (data not shown).

Figure 4 shows the relationship between MRT and D, when P_d is held constant. For this series of simulations, D was increased by a factor of two in 11 steps from a minimum of 1.5625×10^{-11} m^2 s^{-1} to a maximum of 1.6×10^{-8} m^2 s^{-1}. P_d was maintained at a constant, predetermined, value by adjusting the value of tp using Eq. (6). Four sets of simulations were conducted using the following boundaries: parallel planes, 1.5×10^{-6} m separation; sphere, 5×10^{-6} m radius; biconcave disc, human RBC dimensions; biconcave disc, elephant RBC dimensions. A P_d of 6.1×10^{-5} m s^{-1} was used for the parallel planes, sphere, and human RBC as
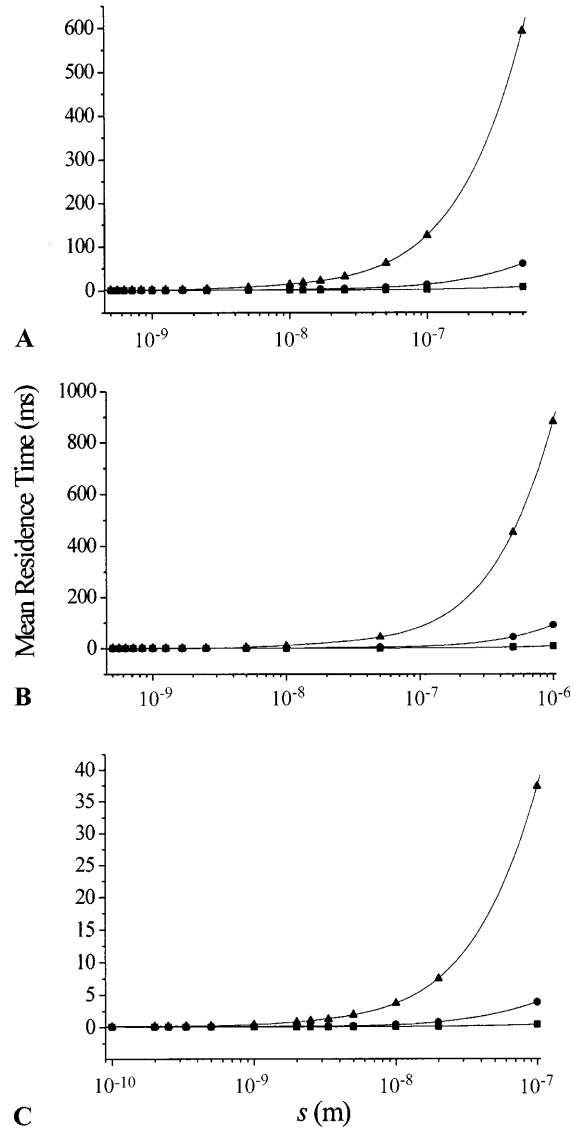
Fig. 3 MRT as a function of jump length (s) for parallel planes (**A**), sphere (**B**), and biconcave disc (**C**) for $tp = 0.1$ (■), $tp = 0.01$ (●), and $tp = 0.001$ (▲). The parallel planes were separated by a distance of 5×10^{-6} m. The radius of the sphere was 5×10^{-6} m. The biconcave disc had the dimensions $b = 1.0 \times 10^{-6}$ m, $d = 8.0 \times 10^{-6}$ m, and $h = 2.12 \times 10^{-6}$ m (see Fig. 2) so as to approximate the size and shape of the human RBC

this value had been determined experimentally for human RBC (Benga et al. 1990). For the elephant RBC, P_d was set to 5.2×10^{-5} m s^{-1}, as was recently determined experimentally (Benga et al. 1999). For Fig. 4A, the MRT values simulated for human RBC were plotted as a function of D (main graph) and as a function of D^{-1} (inset); these transformed data were well represented by a straight line and for purposes of illustration they were fitted using Microcal Origin (Microcal Software, Northampton, Mass., USA). The fitting yielded $MRT_{human\ RBC} = 2.08 \times 10^{-10}/D + 11.87$ ms. On the other hand, the untransformed data clearly revealed that below a particular value of D the MRT increases

Table 1 Mean residence times (MRT) for parallel planes at three values of transition probability and as a function of jump length. The planes were separated by a distance of 5×10^{-6} m. MRT values for individual simulations were calculated by averaging over an ensemble of 1000 independent trajectories of point molecule

s ($10^6 \times$ m)	MRT (ms)		
	$tp = 0.1$	$tp = 0.01$	$tp = 0.001$
0.5	7.363	60.161	591.031
0.1	2.260	13.380	124.461
0.05	1.680	6.987	61.709
0.025	1.317	4.093	31.350
0.0167	1.225	3.184	21.716
0.0125	1.086	2.474	17.800
0.01	1.154	2.391	13.561
0.005	1.078	1.615	7.516
0.0025	1.015	1.293	4.167
0.00167	1.109	1.275	2.978
0.00125	1.012	1.213	2.616
0.001	1.008	1.156	2.491
0.000833	1.071	1.063	2.187
0.000714	1.051	1.069	1.984
0.000625	1.039	1.210	1.876
0.000556	1.012	1.196	1.850
0.0005	1.107	1.171	1.705
0.00025	1.216	1.289	1.558

A

B

Fig. 4A, B MRT as a function of diffusion coefficient (D) at constant permeability. **A** shows the native data for a biconcave disc (human RBC dimensions, main axes) as well as a plot of MRT as a function D^{-1} to which a straight line was fitted (see Methods). **B** shows the linearised data for the sphere (●; radius = 5×10^{-6} m), elephant RBC (▼; $b = 1.16 \times 10^{-6}$ m, $d = 9.3 \times 10^{-6}$ m, $h = 2.3 \times 10^{-6}$ m), human RBC (▲; $b = 1.0 \times 10^{-6}$ m, $d = 8 \times 10^{-6}$ m, $h = 2.12 \times 10^{-6}$ m), and parallel planes (■; separation = 1.5×10^{-6} m)

sharply, whereas above that point (or local domain of values) their values remain almost constant. Figure 4B shows the linearised data from all four sets of simulations yielding the following fits: $MRT_{sphere} = 4.92 \times 10^{-10}/D + 15.81$ ms; $MRT_{elephant\ RBC} = 2.33 \times 10^{-10}/D + 15.76$ ms; $MRT_{parallel\ planes} = 1.85 \times 10^{-10}/D + 12.24$ ms. These results and their associated errors are summarised in Table 2.

The final two columns of Table 2 give the approximate values of D at which the MRT rises exponentially (D_{rise}), and the average value of MRT prior to that rise (MRT_{const}), namely the value of MRT in the region in which it is relatively constant. It should be noted that a difference of a factor of two exists for D between adjacent data points; it will be necessary to subject this region to scrutiny at higher resolution to determine the point of inflexion more accurately. Two additional points warrant noting:

(1) The linear correlation coefficient (r) in each case suggests a strong linear dependency of the trans-

formed data. This is somewhat deceptive, however, since the data points for small values of D^{-1} are densely crowded near the origin and when this portion of the graph is expanded (not shown) the graph appears to be biphasic.

(2) The values in the last column (MRT_{const}) closely correspond to the constant term in the linear equation given in the second column (MRT).

The experimentally determined P_d for human and elephant RBC (Benga et al. 1990, 1999) were calculated

Table 2 Mean residence times for human RBC, elephant RBC, sphere, and parallel planes as a function of D when permeability was kept constant by adjusting tp. The second column (MRT) defines this relationship as approximately linear, as suggested by performing a linear regression on MRT versus D^{-1} data. The third column (SD) is the standard deviation, which provides an indication of the degree to which the actual data deviated from linear, as does the linear correlation coefficient (r) in the fourth column. D_{rise} is the diffusion coefficient below which the MRT began to rise rapidly, and MRT_{const} is the average value of MRT for values of D above that value

	MRT (ms)	SD	r	D_{rise} (m^2 s^{-1})	MRT_{const} (ms)
RBC_{human}	$2.08 \times 10^{-10}/D + 11.87$	0.26	0.998	1.25×10^{-10}	12.08
$RBC_{elephant}$	$2.33 \times 10^{-10}/D + 15.76$	0.81	0.987	1.25×10^{-10}	15.8
Sphere	$4.92 \times 10^{-10}/D + 15.81$	0.58	0.998	5×10^{-10}	16.15
Parallel planes	$1.85 \times 10^{-10}/D + 12.24$	0.29	0.997	1.25×10^{-10}	12.36

from MRT values according to the following formula that interrelates cell volume (V), cell surface area (A), and MRT:

$$P_d = (V/A)(1/MRT) \tag{7}$$

In these calculations, a factor of 0.7 was applied to the V/A ratio to account for the fact that, in real cells, water only occupies ~70% of the total cell volume. Consequently, if the correction factor is eliminated, Eq. (6) predicts MRT for real and elephant RBC of 10.98 ms and 14.23 ms, respectively.

Discussion

Predictions of MRT values made from Monte Carlo random walk simulations of diffusion were compared with previously published results acquired experimentally from RBC. In exploring the validity of the analysis, three model systems were chosen, namely parallel planes, spheres, and biconcave discs. In order for the simulated RBC system to closely correspond to the real one, it was necessary to define the relationship between transition probability (tp) and permeability (P_d).

It initially seemed counter intuitive that a variation in jump length (s) [with its corresponding variation in jump time, via Eq. (1)] should lead to a variation in MRT (Fig. 3). However, once Eq. (6) had been derived, the basis of this phenomenon became apparent. Because a decrease in jump length (s) effectively specifies a decrease in membrane thickness (λ), the result is an increase in P_d [via Eq. (2)]. Conversely, Eq. (6) implies that a decrease in D and/or tp will result in a reduction of P_d. Both of these assertions are consistent with the idea that a reduction in D will increase the time taken for the diffusing molecule to reach the membrane, while a reduction in tp reduces the likelihood of exit once the membrane is reached.

Figure 3 also illustrates that as s becomes very small, such that P_d is high, there is little change in the value of MRT; this is consistent with Eq. (6). Figure 1 also shows that for a biconcave disc whose disc planes are separated by 1–2 μm, the MRT at a particular value of s and tp is much smaller than for parallel planes separated by 5 μm or spheres of radius 5 μm at the same values of s and tp. This observation points to the fact that MRT is not only a function of P_d but also of the geometry and dimensions of the confining region.

From Table 1 it can be seen that for any two simulations at constant D, when the ratios tp/s are equal, the values of MRT obtained are also approximately equal. This underscores the numerical interaction between the parameters that determine the value of P_d, via Eq. (6).

When P_d is constant, MRT remains almost constant for values of D above a certain value (Fig. 4). When D is less than that value, the MRT increases sharply, indicating that the dominant factor in determining MRT is now the time required to diffuse through the average distance to the membrane from a randomly chosen

starting point inside the cell, and not the permeability of the membrane. The inset in Fig. 4A reveals a second finding: an approximately linear relationship exists between MRT and the reciprocal of D and this conformity is better at higher values of D^{-1}. Table 2 also shows that the intercept of the fitted line with the ordinate (i.e., when $D \to \infty$) corresponds to a value of MRT that is approximately equal to the average MRT_{const} value. The threshold occurs at $D \approx 1.25 \times 10^{-10}$ in all cases except for the sphere ($D \approx 5 \times 10^{-10}$), reflecting the fact that for parallel planes, RBC_{human}, and $RBC_{elephant}$ the dimensions are such that the distances between boundaries were in the region of 1–2 μm; for the sphere ($r = 5$ μm) the average distance between boundaries was greater and therefore the threshold below which this factor was the dominant one in determining MRT was higher.

The data in Fig. 4B further illustrate the difference between the sphere and the other shapes with respect to the dependence of MRT on the parameters chosen for the simulations. The values of MRT calculated from parallel planes separated by 1.5 μm closely approximated those for human RBC. The elephant RBC has a greater volume (Benga et al. 1999), so the slightly higher MRT is attributed to a greater separation between the disc planes of the cell. The MRT values of 10.98 ms and 14.23 ms obtained experimentally for real human and elephant RBC, respectively, are in close agreement with those obtained in the Monte Carlo simulations (~12 ms and ~16 ms for human and elephant RBC, respectively, see Table 2).

Finally, it is acknowledged that the models of restricted diffusion used in the simulations involved several fundamental assumptions.

(1) The equation used to describe the RBC is only an approximation of the actual shape (Kuchel and Fackerell 1999); previous work has shown, however, that small departures from real relative dimensions have little effect on the estimated MRT (unpublished data).
(2) Point molecules were assumed to diffuse independently and unimpeded in the entire volume of the cell, whereas in real cells water occupies only ~70% of the cell volume.
(3) For the sake of consistency, the diffusion coefficient was set to 2.0×10^{-9} m^2 s^{-1} for all models; this value is higher than that determined experimentally for diffusion of water inside RBC (~8.0×10^{-10} for human RBC, unpublished data); however, both these values lie well within the region in which MRT is relatively constant (Fig. 4).
(4) The sub-membrane cytoskeleton, the finite thickness of the membrane, and other structural features of cells were absent from the RBC model; these could be incorporated in a more comprehensive model.

Thus, while the model could be refined, even in its present form it illustrates several key factors that influence the MRT of molecules in cells. It also introduces a means of studying the factors that limit the applicability of the data analysis used in the manganese-doping experiments (e.g., Benga et al. 1990).

Conclusions

An expression that relates *tp* and *s* to P_d in a Monte Carlo random walk simulation of diffusion and membrane transport in cells was derived (Eq. 6). The veracity of the equation was established using simulations (Table 1). When the mean distance traversed in the experimentally determined MRT is long relative to the cell dimensions, then it is the value of P_d that will determine the MRT. A quantitative understanding of this result has important implications for the constraints on cell size and MRT that are important in the kinetics of cellular events.

Monte Carlo simulations of diffusion are a potentially useful and sensitive method for determining the MRT for molecular species in cellular and other bounded systems. Future work could include more elaborate models of the cell boundaries that better reflect the complexity of real systems than those used herein.

References

Benga G, Pop VI, Popescu O, Borza V (1990) On measuring the diffusional water permeability of human red blood cells and ghosts by nuclear magnetic resonance. J Biochem Biophys Methods 21: 87–102

Benga Gh, Popescu O, Pop VI, Hodor P, Borza T (1992) Effects on water diffusion of inhibitors affecting various transport processes in human red blood cells. Eur J Cell Biol 59: 219–223

Benga Gh, Chapman BE, Gallagher CH, Agar NS, Kuchel PW (1993) NMR studies of diffusional water permeability of erythrocytes from eight species of marsupial. Comp Biochem Physiol 106A: 515–518

Benga Gh, Kuchel PW, Chapman BE, Cox GC, Ghiran I, Gallagher CH (1999) Comparative cell shape and diffusional water permeability of red blood cells from Indian elephant (*Elephas maximus*) and man (*Homo sapiens*). Comp Haemotol Int (in press)

Kuchel PW, Fackerell ED (1999) Parametric-equation representation of biconcave erythrocytes. Bull Math Biol 61: 209–220

Lennon AJ, Kuchel PW (1994a) Neural networks used to interpret pulsed-gradient restricted diffusion data. J Magn Reson A 107: 229–235

Lennon AJ, Kuchel PW (1994b) Enhancement of the "diffraction-like" effect in NMR diffusion experiments. J Magn Reson A 111: 208–211

Lennon AJ, Scott NR, Chapman BE, Kuchel PW (1994) Hemoglobin affinity for 2,3-bisphosphoglycerate in solutions and intact erythrocytes: studies using pulsed field gradient NMR and Monte Carlo simulations. Biophys J 67: 2096–2109

Mills R (1973) Self-diffusion in normal and heavy water in the range 1–45°. J Phys Chem 77: 685–688

Piton MC, Lennon AJ, Chapman BE, Kuchel PW (1994) Diffusion of solvent in swollen latex particles. J Colloid Interface Sci 166: 437–443

Stein WD (1986) Physical basis of movement across cell membranes. In: Stein WD, Lieb WR (eds) Transport and diffusion across cell membranes. Academic Press, Orlando, pp 173–181

Waldeck AR, Kuchel PW, Lennon AJ, Chapman BE (1997) NMR diffusion measurements to characterise membrane transport and solute binding. Prog NMR Spectrosc 30: 39–68

PAPER III

Evidence of Red Cell Alignment in the Magnetic Field of an NMR Spectrometer Based on the Diffusion Tensor of Water

Philip W. Kuchel,* Christopher J. Durrant,† Bogdan E. Chapman,* Penelope S. Jarrett,* and David G. Regan*

*Department of Biochemistry, and †School of Mathematics and Statistics, University of Sydney, New South Wales 2006, Australia

The alignment of human erythrocytes in aqueous suspensions in the magnetic field B_0 (called the z-direction) of an NMR spectrometer was shown by calculating the diffusion tensor for water in the sample. The diffusion was measured using a pulsed-field-gradient spin-echo NMR method. The extent of diffusion anisotropy for water was exemplified by the values of the apparent diffusion coefficients with erythrocytes of normal shape and volume: for a typical experiment the values for the x-, y-, and z-directions were $(6.88 \pm 0.17) \times 10^{-10}$, $(7.07 \pm 0.17) \times 10^{-10}$, and $(10.20 \pm 0.17) \times 10^{-10}$ m^2 s^{-1}, respectively. Cells in hypo- and hyperosmotic media were also studied and they too showed the anisotropy of the apparent diffusion coefficients but the extents were different. A new method of data analysis was developed using the Standard Add-On Packages in a *Mathematica* program. The experimental findings support evidence of erythrocyte alignment that was previously obtained with a high-field-gradient q-space method. © 2000 Academic Press

Key Words: cell alignment; PGSE NMR; water diffusion; multivariate analysis; erythrocytes; magnetic field effect on cells.

INTRODUCTION

NMR-based evidence that biconcave-shape human erythrocytes in suspension in an aqueous medium become aligned in the magnetic field B_0 of an NMR spectrometer is surprisingly recent. It was provided by the observation of coherence peaks in q-space plots obtained from erythrocytes that were studied with pulsed-field-gradient spin-echo (PGSE) NMR spectroscopy (*1*). A simple mathematical relationship exists between the position of the minima in these q-space plots and the average main diameter of the cells that are aligned with their disc-like faces parallel to B_0 (*2, 3*). The experiments require access to a sample probe that generates very large magnetic field gradients, of the order of 2 to 10 T m^{-1}, and these are not common. Also, the probes usually generate a gradient in only one coordinate direction, parallel to B_0 (i.e., a z-only gradient probe). On the other hand, there is much current interest in diffusion tensor analysis for characterizing the orientation of microstructures in tissues *in vivo* during magnetic resonance imaging (MRI) (*4–9*). The gradient coils for whole body imaging, and their high-resolution NMR counterparts, generate

relatively weak magnetic field gradients that are of the order of 5 to 50 mT m^{-1} (e.g., *6, 8, 10*).

Thus, we set out to determine whether diffusion tensor analysis would provide corroborating evidence of erythrocyte alignment in B_0 using the alternative technology and data processing procedures of diffusion tensor analysis (*4, 5*).

Because biological tissues are ordered on the microscopic scale the diffusion of solutes and water in them is often seen to be anisotropic (*4, 5*). However, this is not an obvious state for cells in a suspension except if they are not spherically symmetrical and experience an aligning force; this situation pertains to the human erythrocyte.

Tissue anisotropy can be expressed in terms of a 3×3 matrix of diffusion coefficients, or a rank two tensor (*4*). The elements of this tensor determined in contemporary MRI investigations are interpreted in terms of the locally ordered orientation of (semi-)impermeable barriers. Thus the location of axon-fiber tracts can be determined in MRI scans of the brain (*9*).

Previous explanations of the method for determining the values of the elements of the diffusion tensor (*4–10*) seemed to us to be unduly complicated; this is especially true now that several well-known computer software packages contain the requisite multivariate regression algorithms and matrix-diagonalization procedures as standard routines. In *Mathematica* (*11*) the functions Regress, NonLinearRegress, and SingularValues perform the essential roles, thus making the implementation of diffusion tensor analysis facile.

Before presenting the experimental results that were analyzed using a program written in *Mathematica*, it is pertinent to give some background theory so that the alternative analytical approach can be set in its correct context.

THEORY

The PGSE Experiment

Consider a PGSE experiment conducted on a sample which is isotropic and in which the diffusion is unbounded. Take a coordinate system with the z-axis in the direction of the polarizing field and let **k** be the unit vector in this direction so that

$B_0 = B_0 \mathbf{k}$. In this experiment the signal characteristics are determined by the gradients imposed on the component of the magnetic field in the direction of $\mathbf{B_0}$. Let this component be $B(x, y, z, t)$. In its simplest implementation the field-gradient pulses are along only one axis, usually the z-axis so that $B(x, y, z, t) = B(z, t)$. The pulses produce a uniform field-gradient $dB/dz = g_z(t)$ so that $B(z, t) = B_0 + g_z(t)z$. The field-gradient pulse is modulated in time, thus it can be written quite generally as $g_z(t) = g_{z,m}p(t)$, where $g_{z,m}$ is the maximum value of the field gradient achieved during the pulse and $p(t)$ is a profile factor. For a rectangular pulse, $p(t) = 1$ during the pulse $0 \le t \le \delta$, and $p(t) = 0$ outside the time of the pulse.

The ratio of the NMR signal intensity obtained with a nonzero field-gradient, relative to that obtained when it is zero, is referred to as the attenuation. The natural logarithm of the attenuation is denoted by R (4, 12):

$$R = \ln\left(\frac{S[g]}{S[0]}\right) = -\gamma^2 P^2 g_{z,m}^2 D, \qquad [1]$$

where γ is the magnetogyric ratio of the detected nucleus, D is the diffusion coefficient of the spin-bearing molecules, and P^2 is a function of the shape profile of the pulses:

$$P^2 = \int_0^{TE/2} \left[\int_0^t p(t')dt' \right]^2 dt$$

$$+ \int_{TE/2}^{TE} \left[\int_0^t p(t')dt' - 2\int_0^{TE/2} p(t')dt' \right]^2 dt, \quad [2]$$

where TE is the spin-echo time. For rectangular pulses, each of duration δ and separated from each other by an interval of Δ, $P^2 = \delta^2(\Delta - \delta/3)$ [12].

The value of D is the negative of the slope of the line that is regressed onto the data pairs (b_i^2, R_i), $i = 1, \ldots, N$, where $b_i^2 = \gamma^2\delta^2(\Delta - \delta/3)g_{z,m,i}^2$ and is referred to as the Stejskal–Tanner parameter (12), and N is the number of different $g_{z,m,i}$ values used in the experiment, with a fixed pulse shape.

Requirement for a Diffusion Tensor

When the sample has barriers such as cell membranes, which are semi-permeable to the diffusant, the apparent (measured) diffusion coefficient is less than that for free diffusion (e.g., 1–5). The value of R (Eq. [1]) varies inversely as a function of the separation distance between the restricting boundaries. Thus for a sample such as a section of brain tissue, where there are bundles of axonal fibers, the apparent diffusion coefficient of water depends on the orientation of the fibers relative to the direction of the magnetic field-gradient pulses. The dependence of D on direction requires D to be treated not as a single scalar quantity but as an array of values that will describe the diffusion behavior in all directions. The mathematical form of D is a second-rank tensor $\mathbf{D}$ with nine elements as is defined here (but it is explained further below):

$$\mathbf{D} = \begin{bmatrix} D_{11} & D_{12} & D_{13} \\ D_{21} & D_{22} & D_{23} \\ D_{31} & D_{32} & D_{33} \end{bmatrix}. \qquad [3]$$

Modern triple-axis NMR gradient probes enable the application of any combination of field-gradient pulses along three Cartesian axes. Thus the directions along which independent gradient pulses can be applied are the x-, y-, and z-axes, represented by the unit vectors $\mathbf{i}$, $\mathbf{j}$, and $\mathbf{k}$, respectively. A pulse directed along the x-axis will produce a uniform field gradient $dB/dx = g_x(t)$ and a pulse along the y-axis will produce a uniform field gradient $dB/dy = g_y(t)$; the case for $g_z(t)$ was discussed above.

Pulsed-Field-Gradient Vectors

Pulses which are applied simultaneously along all three axes produce a combined field-gradient which is the vector sum of the three separate components:

$$\mathbf{g} = \frac{\partial B}{\partial x}\mathbf{i} + \frac{\partial B}{\partial y}\mathbf{j} + \frac{\partial B}{\partial z}\mathbf{k}$$

$$= g_x(t)\mathbf{i} + g_y(t)\mathbf{j} + g_z(t)\mathbf{k}, \qquad [4]$$

where ordinary derivatives are replaced by partial derivatives because the field now varies in all three directions, i.e., $B = B(x, y, z)$. If the pulse profile $p(t)$ is the same in all three directions, we write

$$\mathbf{g} = p(t)(g_{x,m}(t)\mathbf{i} + g_{y,m}(t)\mathbf{j} + g_{z,m}(t)\mathbf{k}). \qquad [5]$$

The vector $\mathbf{g}_m$ is a constant whose magnitude $\|g_m\| = \sqrt{g_{x,m}^2(t) + g_{y,m}^2(t) + g_{z,m}^2(t)}$ is the maximum field-gradient achieved during the pulse and whose direction, represented by the unit vector $\bar{\mathbf{g}}_m = \mathbf{g}_m/\|g_m\|$, is the direction of the pulse.

Generalizing Eq. [1] yields

$$R = \ln\left(\frac{S[\mathbf{g}_m]}{S[0]}\right) = -\gamma^2 P^2\|g_m\|^2 D^e, \qquad [6]$$

where the apparent diffusion coefficient in the direction of $\bar{\mathbf{g}}_m$ is defined to be

$$D^e = \bar{\mathbf{g}}_m^t \mathbf{D} \bar{\mathbf{g}}_m, \qquad [7]$$

where the superscript t denotes the transpose of the matrix. The apparent diffusion coefficient is thus estimated from the experimental measurements by evaluating the following:

$$\Xi_i = \frac{R_i}{-\gamma^2 P^2 \|\mathbf{g}_{m,i}\|^2} = \frac{R_i}{c^2 \|\mathbf{g}_{m,i}\|^2}, \qquad [8]$$

for different $\mathbf{g}_{m,i}$ values.

The Quadratic Form

On physical grounds, the diffusion tensor is expected to be symmetrical, i.e., the diffusion in any given direction is the same if the field-gradient is reversed. In this case $D_{21} = D_{12}$, $D_{31} = D_{13}$, and $D_{32} = D_{23}$. The presence of nonzero off-diagonal elements implies that there are impediments to diffusional motion that are not aligned exactly with the axes chosen for the coordinate system of the laboratory.

The apparent diffusion coefficient, after expansion of the vector–matrix–vector product in Eq. [7], is given by

$$D^e = \bar{g}_x^2 D_{11} + \bar{g}_y^2 D_{22} + \bar{g}_z^2 D_{33} + 2\bar{g}_x\bar{g}_y D_{12}$$
$$+ 2\bar{g}_x\bar{g}_z D_{13} + 2\bar{g}_y\bar{g}_z D_{23}. \qquad [9]$$

This expression is known as the quadratic form because the components of $\bar{g}_i$ occur only in products of degree two (13). Thus, the statistical challenge is to estimate the coefficients of this quadratic form from the experimental data Ξ_i for the various given $\bar{g}_i$.

The variation in the apparent diffusion coefficient in the sample can be represented graphically by an ellipsoid, as in Fig. 1. The direction along which diffusion is measured is experimentally controlled by the appropriate choice of a combination of gradients in the three directions, to produce a gradient in the direction of $\bar{g}_m$. The vector $\mathbf{r}$ in Fig. 1 is drawn in this direction; its tail is located at the origin and its point touches the inner surface of the ellipsoid. The length of $\mathbf{r}$ corresponds to the magnitude of the apparent diffusion coefficient in the direction of the vector.

Regression Analysis

Since the values of six independent elements of the diffusion tensor are to be determined, at least six different gradient directions must be used in the experiment. In addition, since each D_{ij} value was determined in the present experiments from 7, 8, or 16 different values of each of the (at least) six field gradient directions the fitting of the parameters constitutes a typical example of multivariate regression analysis (14, 15). Fitting the elements of the diffusion tensor (Eq. [7]) involves regression of Eq. [9] onto data quadruples that are composed of the three gradient magnitudes and the natural logarithm of the signal intensity, transformed according to the right-hand sides of Eq. [8], to give Ξ_i. The Mathematica function Regress performs the required analysis using the set of fitting functions $\{ \bar{g}_x^2, \bar{g}_y^2, \bar{g}_z^2, 2\bar{g}_x\bar{g}_y, 2\bar{g}_x\bar{g}_z, 2\bar{g}_y\bar{g}_z \}$ that are consistent with the form of Eq. [9]. The output of the analysis includes the 3×3 diffusion tensor $\mathbf{D}$ (see Results).

Statistical bias is expected to be introduced into the esti-
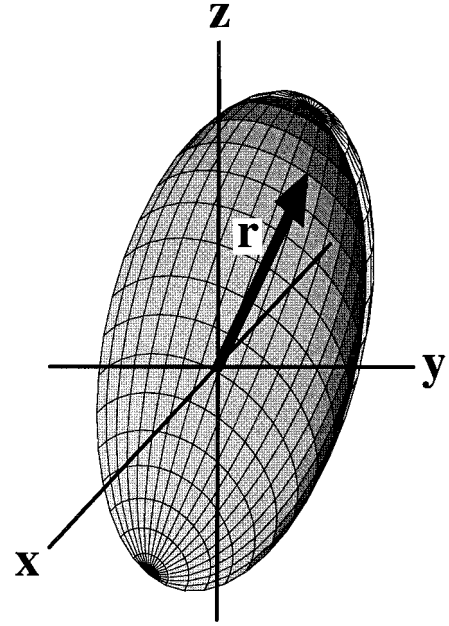
FIG. 1. Diffusion-tensor ellipsoid. The representation of diffusion anisotropy is achieved by assigning values to the three semi-axis lengths of the ellipsoid that are in the ratio of the apparent diffusion coefficients in the x-, y-, and z-directions in the frame of reference of the sample. The laboratory reference frame is represented as the solid lines, and the arrow denotes an arbitrary pulsed-field-gradient vector that arises from a linear combination of the basis gradient vectors $\mathbf{g}_x$, $\mathbf{g}_y$, and $\mathbf{g}_z$.

mates of the elements of $\mathbf{D}$ because of the logarithmic transformation of the original data. However, this bias can be obviated, to a large degree, by using nonlinear regression of the exponential counterpart of Eq. [1] onto the untransformed data. In the present study little difference was found between the estimates of D_{ij} and their uncertainties, obtained with either method (data not shown). Therefore, because of its greater simplicity and the ease of detecting aberrant data from Stejskal–Tanner plots, which ideally are straight lines, the linear regression approach was used thereafter.

Frame Rotation

The nature of the apparent diffusion anisotropy is encapsulated in $\mathbf{D}$ which refers to a Cartesian coordinate system that has axes that are not necessarily aligned with those of the three gradient basis vectors. Therefore, the rotations that are required to bring about the transformation of the experimental frame of reference to that of the sample are achieved with the Euler rotation matrix. This matrix, $\mathbf{E}$, rotates a Cartesian coordinate system through the angles θ, ϕ, and ψ with respect to the original x-, y-, and z-axes of the laboratory frame (specified by the gradient coils). Thus, the transformation of the elements of a vector $\mathbf{y}$ to give the values in the new coordinate system, $\mathbf{y}'$, is described by

$$\mathbf{y}' = \mathbf{E}\mathbf{y}. \qquad [10]$$

Because the diffusion equation (Fick's first law) specifies a linear system of vectors it has the general form

$$\mathbf{y} = \mathbf{D}\mathbf{x}, \qquad [11]$$

by using the *Mathematica* function SingularValues. The values of the rotation angles θ, ϕ, and ψ were obtained by using the expressions for the coefficients of the Euler matrix [using the y-convention of (13); Eq. [15]] and equating them with the corresponding elements in the experimentally determined one.

$$\mathbf{E} = \begin{bmatrix} \cos\phi\cos\theta\cos\psi - \sin\phi\sin\psi & \sin\phi\cos\theta\cos\psi - \cos\phi\sin\psi & -\sin\theta\cos\psi \\ -\cos\phi\cos\theta\sin\psi - \sin\phi\cos\psi & -\sin\phi\cos\theta\sin\psi + \cos\phi\cos\psi & \sin\theta\sin\psi \\ \sin\theta\cos\phi & \sin\theta\sin\phi & \cos\theta \end{bmatrix}. \qquad [15]$$

where $\mathbf{D}$ denotes the experimentally determined diffusion tensor. Under the Euler transformation, Eq. [11] becomes

$$\mathbf{y}' = \mathbf{D}'\mathbf{x}', \qquad [12]$$

where $\mathbf{y}'$ is given by Eq. [10] and $\mathbf{x}' = \mathbf{E}\mathbf{x}$. Hence,

$$\mathbf{E}\mathbf{y} = \mathbf{D}'\mathbf{E}\mathbf{x}, \qquad [13a]$$

or

$$\mathbf{y} = \mathbf{E}^{-1}\mathbf{D}'\mathbf{E}\mathbf{x}. \qquad [13b]$$

Thus,

$$\mathbf{D} = \mathbf{E}^{-1}\mathbf{D}'\mathbf{E}, \qquad [14a]$$

or

$$\mathbf{D}' = \mathbf{E}\mathbf{D}\mathbf{E}^{-1}. \qquad [14b]$$

This is a similarity transform. When E is a rotation matrix, its inverse is equal to its transpose, so

$$\mathbf{D} = \mathbf{E}^{t}\mathbf{D}'\mathbf{E}, \qquad [14c]$$

or

$$\mathbf{D}' = \mathbf{E}\mathbf{D}\mathbf{E}^{t}, \qquad [14d]$$

In words, the product of the Euler matrix, that of the gradient-system diffusion tensor (determined experimentally), and the transpose of the Euler matrix, yield the diffusion tensor $\mathbf{D}'$ in the natural coordinate system of the sample. The latter tensor is a diagonal one. The coefficients of $\mathbf{E}$ are determined by the numerical diagonalization of the experimental diffusion tensor

The natural coordinate system thus formed is the set of principal axes of the ellipsoid and the three elements of the diagonal of $\mathbf{D}'$ are the lengths of the semi-axes in the direction of the three principal axes, such as that drawn in Fig. 1.

EXPERIMENTAL

Erythrocytes. Blood was obtained by venipuncture from the median-cubital vein of the donor (PWK). The cells were washed twice by centrifugation ($3000g$ at $4°C$) in 4 vol of physiological saline (NaCl, 0.9% w/v) containing 10 mM glucose. After the second wash the cell suspension was gassed with CO to convert the hemoglobin to the diamagnetically stable form that is optimal for NMR studies of these cells [e.g., (1)]. To swell the cells, some of the cell pellet was suspended in 4 vol of 121 mM NaCL containing 10 mM glucose, while to shrink the cells, to be more like a flat disc, they were suspended in 242 mM NaCl also containing 10 mM glucose. The suspended cells were then sedimented by centrifugation as before. All cell samples were suspended to give a final hematocrit of ~0.65; this value was chosen because it provided a relatively large extracellular space without allowing significant settling of the cells during the time of the experiment.

NMR samples. A total of 0.5 mL of the erythrocyte suspension was placed in 5-mm-od glass NMR tubes (507-PP, Wilmad, Buena, NJ).

NMR spectrometer. The experiments were conducted on a Bruker DRX-400 spectrometer (Karlsruhe, Germany) with an Oxford Instruments 9.4-T vertical wide-bore magnet (Oxford, UK) with a Bruker TXI 5-mm, ~500 mT m^{-1} x-, y-, and z-axis gradient probe. The sample temperature was controlled at 298 K. PGSE experiments were conducted as described previously (1–3). The pulse-sequence parameters were: duration of field-gradient pulses, $\delta = 2$ ms; time interval between field-gradient pulses, $\Delta = 20$ ms; 90° RF pulse, 12–13 μs; total spin-echo time, TE = 40 ms; 8 transients per spectrum; maximum field-gradient, $g_{r,\text{max}} = 0.5$ T m^{-1}. Routinely 16 spectra were

acquired with a sequential increase in the value of g. The three gradients were calibrated using the known diffusion coefficient of water in an isotropic and unbounded space (*16*).

Data analysis. In each spectrum, the integral of the water resonance was measured using the standard Bruker software (*uxnmr*) where it was normalized with respect to the signal intensity in the first spectrum. Unless the first spectrum was acquired with a small nonzero gradient its phase was substantially different from that of the rest in the series. Therefore, a value of 1 G cm^{-1} was used for the field-gradient magnitude in the first spectrum of each series. The subsequent analysis in a *Mathematica* program followed that described under Theory and in the Appendix.

RESULTS

Erythrocytes in Isotonic Medium

Figure 2A shows a set of ^{1}H PGSE NMR signal intensities obtained from the water in normal-volume human erythrocytes and their extracellular medium. The sample was subjected to a range of values of the following gradients: $\mathbf{g}_x$, $\mathbf{g}_y$, $\mathbf{g}_z$, $\mathbf{g}_{xy}$, $\mathbf{g}_{xz}$, $\mathbf{g}_{yz}$, and $\mathbf{g}_{xyz}$. The composite gradients such as $\mathbf{g}_{xy}$ were generated from the appropriate combination of the basis gradients. The latter were adjusted so that the resultant gradient had the same magnitude as those used in experiments where the basis gradients were applied singly. Fine adjustments to scaling factors for the gradient magnitudes were made during data analysis; these were based on the measurement of the apparent diffusion coefficient of water in all directions and the assumption that it should have the same value in all directions (*16*).

The bottom 16 points (▼) in Fig. 2A were obtained with the field-gradient applied along the z-direction (direction of $\mathbf{B}_0$). The upper set was obtained with the gradient in the x-direction (◆), and these were superimposed upon by those acquired with the field gradient in the y-direction and in the x,y-direction (◇). The next most rapid signal attenuation was obtained with the $\mathbf{g}_{xz}$- and $\mathbf{g}_{yz}$-data. Hence, diffusion in the direction of $\mathbf{g}_z$ was significantly more rapid than in all other directions.

It is also readily seen in Fig. 2A that each data set was not well described by a single straight line. However, a straight line fitted each data set moderately well over the first eight points of each set and even better for the second to the eighth points; the outcome of fitting this truncated sets of the points is shown in Fig. 2B. The four straight lines had significantly different (*t* test) slopes in the order $\mathbf{g}_z$-data > superimposed $\mathbf{g}_{xz}$–$\mathbf{g}_{yz}$-data > $\mathbf{g}_{xyz}$-data > superimposed $\mathbf{g}_x$–$\mathbf{g}_y$–$\mathbf{g}_{xy}$-data. The slopes of the latter three lines were not significantly different and the symbols used for the g_x- and g_y-data in Fig. 2B were superimposed.

Erythrocytes in Hyper- and Hypotonic Media

Experiments, the same as those used for Fig. 2, were carried out on cells that were flattened by the osmotic effect of a
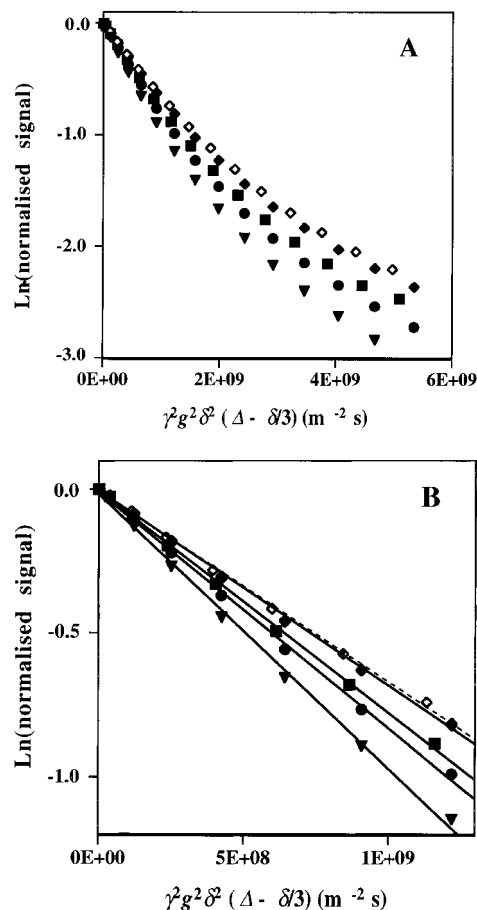
FIG. 2. Signal intensity from water, as a function of the magnitude and direction of the magnetic field-gradient pulses in ^{1}H NMR PGSE experiments conducted on a suspension of normal-volume human erythrocytes, at a hematocrit of 0.65 and temperature of 25°C. The graphs are in the format proposed by Stejskal and Tanner (*12*) and the independent (abscissal) variable is accordingly referred to as the Stejskal–Tanner parameter. Seven data sets were acquired for each of 16 different values of the gradient pulses. A. The gradients and their corresponding data sets are denoted by the symbols: $\mathbf{g}_x$, ◆; $\mathbf{g}_y$, ◆; $\mathbf{g}_z$, ▼; $\mathbf{g}_{xy}$, ◇; $\mathbf{g}_{xz}$, ●; $\mathbf{g}_{yz}$, ●; $\mathbf{g}_{xyz}$, ■. Note that the data for $\mathbf{g}_x$ were superimposed on those of $\mathbf{g}_y$, and similarly for $\mathbf{g}_{xz}$ and $\mathbf{g}_{yz}$. B. A replot of the data in A, but taking only the first eight points and fitting those with a straight line: the symbols are as for A. Each fitted line is clearly associated with a particular data set.

hypertonic saline solution (*2, 17*). The qualitative features of the Stejskal–Tanner plots were the same as in Fig. 2A but the extent of signal attenuation was greater for each of the seven different field-gradient directions (Fig. 3). This effect was quantified when the data were fitted by straight lines to the 2nd to the 8th or the 9th to the 16th points in each set.

When human erythrocytes are placed in hypotonic saline they take on an almost spherical shape while retaining two diametrically opposed indentations (*2, 17*). Not withstanding the more spherical shape of the cells, the two regression lines still revealed a greater apparent diffusion coefficient for the z-direction compared with all others. To avoid overcrowding
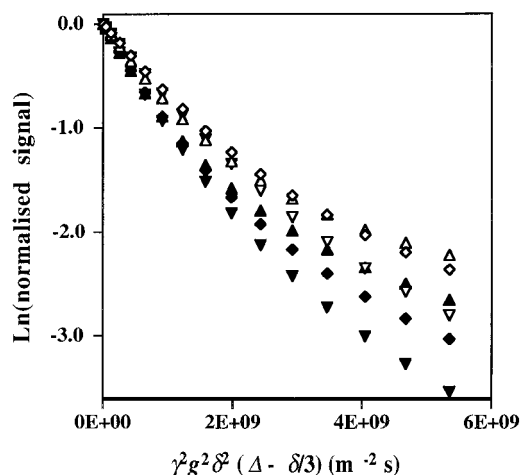
FIG. 3. Stejskal–Tanner plot of the ^{1}H NMR PGSE signal intensity obtained from human erythrocytes of three different average volumes and with the pulsed-field-gradients applied in the x- and z-directions only, for a range of 16 different values. The average volume of the cells, the gradient, and the symbols used were as follows: swollen cells, g_x, $\triangle$; swollen cells, g_z, $\blacktriangle$; normal-volume cells, g_x, $\Diamond$; normal-volume cells, g_z, $\blacklozenge$; shrunken (flattened) cells, g_x, ∇; shrunken cells, g_z, $\blacktriangledown$.

the graph, the data for only the x- and z-directions were presented in Fig. 3.

Diffusion Tensor

The data in Fig. 2A, and the corresponding sets for erythrocytes suspended in hypotonic and hypertonic media, were subjected to quantitative diffusion tensor analysis. This was carried out according to the procedure described under Experimental by using the program presented in the Appendix. Table 1 contains the results of the analysis of the second to eighth points in each Stejskal–Tanner plot; it confirmed in a quantitative way the impression gained from Fig. 2A regarding less restriction of diffusion in the z-direction than all others. For the normal-volume cells the values of D_{11} and D_{22} (average, 6.98×10^{-10} m^2 s^{-1}) were the same within the experimental error and the coefficient of variation was $\sim$2.5%. The error was substantially greater (coefficient of variation $\sim$17%) when the first point was included in the regression, hence its blanking out in all subsequent analyses (see Discussion). The coefficients of variation for the estimates of the three leading-diagonal terms were less for the first half of a data set than for the second half; this is consistent with the appearance of a greater degree of curvature of the plots (Figs. 2A and 3) for larger vales of the Stejskal–Tanner parameter.

In Table 1 the estimate of D_{33} was $10.20 \pm 1.00 \times 10^{-10}$ m^2 s^{-1}, which was more than two standard deviations different from the corresponding D_{11} and D_{22} values. The other elements of the diffusion tensor (the cross-terms) were not significantly different from zero.

For the second to eighth data points in each set, the normal-

volume erythrocytes had a difference between the average of their values of D_{11} and D_{22} and the value of D_{33} of 3.25 $\times$ 10^{-10} m^2 s^{-1}; but for the swollen and flattened cells it was 2.53×10^{-10} and 3.14×10^{-10} m^2 s^{-1}, respectively. The largest difference was with the normal-volume cells. On the other hand, when the last eight point were analyzed (Table 2) the corresponding differences were substantially less, while the largest difference was with the flattened cells. The differences were 1.7 $\times$ 10^{-10}, 1.2 $\times$ 10^{-10}, and 1.9 $\times$ 10^{-10} m^2 s^{-1}, respectively.

Furthermore, Fig. 3 provides graphical representation of the fact that the apparent diffusion coefficient in the x- and z-directions was greatest for the cells in the hypertonic medium, followed by the normovolumic cells, and then the swollen cells.

TABLE 1

Results of the Multivariate Linear Regression Analysis of PGSE ^{1}H NMR Data from Human Erythrocytes That Were Suspended in Isotonic (154 mM), Hypotonic (121 mM), and Hypertonic (242 mM) Saline Solutions

	Parameter ($10^{10} \times$ m^2 s^{-1})	Estimate ($10^{10} \times$ m^2 s^{-1})	SE ($10^{10} \times$ m^2 s^{-1})	Sample frame
Isotonic	x^2 (D_{11})	6.88	0.17	6.80
	y^2 (D_{22})	7.07	0.17	7.16
	z^2 (D_{33})	10.20	0.17	10.20
	$2xy$ (D_{12})	−0.31	0.19	
	$2xz$ (D_{13})	0.16	0.19	
	$2yz$ (D_{23})	0.0009	0.19	
Hypotonic	x^2 (D_{11})	7.99	0.23	8.01
	y^2 (D_{22})	7.50	0.23	7.47
	z^2 (D_{33})	10.27	0.23	10.27
	$2xy$ (D_{12})	−0.20	0.26	
	$2xz$ (D_{13})	0.17	0.25	
	$2yz$ (D_{23})	0.24	0.25	
Hypertonic	x^2 (D_{11})	7.35	0.12	7.43
	y^2 (D_{22})	7.21	0.12	7.11
	z^2 (D_{33})	10.42	0.12	10.43
	$2xy$ (D_{12})	0.30	0.26	
	$2xz$ (D_{13})	0.21	0.26	
	$2yz$ (D_{23})	0.38	0.26	

Note. The 2nd to the 8th points from a total of 16 were used in the analysis; this corresponded to the first linear section of the data set (see Fig. 2B). (It was repeatedly noted, and also in the present data set, that avoidance of using the 1st point in the analysis reduced the coefficient of variation (SE) in the D_{ii} estimates from $\sim$17 to $\sim$3%, hence its omission here.) The basis functions used in the regression of the quadratic form (Eq. [9]) onto the data are those listed in the first column together with the corresponding element of the diffusion tensor (Eq. [3]). The second column contains the estimates of the values of the elements; most notable are the first three values that correspond to the diffusion coefficients in the x-, y-, and z-directions. The SE column contains the standard errors of the parameter estimates that is a standard output of the *Mathematica* function (see Appendix). The right-hand column contains the elements of the diagonalized matrix and these values correspond to the diffusion coefficients in the x-, y-, and z-directions, respectively, in the frame of reference of the sample.

TABLE 2
**Results of the Multivariate Linear Regression Analysis
of the Second Set of Eight Points in Each Data Set**

	Parameter $(10^{10} \times m^2\ s^{-1})$	Estimate $(10^{10} \times m^2\ s^{-1})$	SE $(10^{10} \times m^2\ s^{-1})$	Sample frame
Isotonic	$x^2\ (D_{11})$	5.62	0.30	5.66
	$y^2\ (D_{22})$	5.46	0.30	5.41
	$z^2\ (D_{33})$	7.27	0.30	7.72
	$2xy\ (D_{12})$	−0.18	0.33	
	$2xz\ (D_{13})$	0.13	0.33	
	$2yz\ (D_{23})$	0.16	0.33	
Hypotonic	$x^2\ (D_{11})$	5.60	0.38	5.59
	$y^2\ (D_{22})$	5.30	0.38	5.29
	$z^2\ (D_{33})$	6.69	0.38	6.70
	$2xy\ (D_{12})$	−0.19	0.42	
	$2xz\ (D_{13})$	0.17	0.42	
	$2yz\ (D_{23})$	0.20	0.42	
Hypertonic	$x^2\ (D_{11})$	6.22	0.27	6.19
	$y^2\ (D_{22})$	6.30	0.27	6.29
	$z^2\ (D_{33})$	8.14	0.27	8.17
	$2xy\ (D_{12})$	−0.04	0.60	
	$2xz\ (D_{13})$	0.28	0.59	
	$2yz\ (D_{23})$	0.37	0.59	

Note. The meaning of each column in the table is the same as for Table 1.

DISCUSSION

Two Major Diffusion Domains

The experimental data in Figs. 2 and 3 showed that diffusion of water was less restricted in the z-direction than in all others. The superposition of the g_x–g_y–g_{xy}-data showed that there was no preferred ordering of the cells when projected onto the x,y-plane.

The diagonal element of $\mathbf{D}$ (Tables 1 and 2) with the largest value, D_{33}, corresponding to the apparent diffusion coefficient for water that was both inside and outside the cells in the suspension of normal-volume erythrocytes in the z-direction, was $(10.2 \pm 1.00) \times 10^{-10}\ m^2\ s^{-1}$; but this value is substantially less than $\sim 2 \times 10^{-9}\ m^2\ s^{-1}$ expected for water in an isotropic unbounded saline solution (*16*). This is clear evidence that the diffusion of water was impeded in the erythrocyte suspensions. Furthermore, the general nonconformity of the data sets shown in Fig. 2A with straight lines implies that the water was undergoing restricted and/or obstructed diffusion in at least two spatial domains. This is consistent with the water in the cell suspensions occupying both the intra- and extracellular spaces. Because water exchanges rapidly across the cell membranes there is a blurring of the effects of restriction of motion in one compartment by that in the other. The water outside the cells moved with a larger apparent diffusion coefficient than that inside, which was restricted by the cell membranes (*1*). Nevertheless, the extracellular diffusion is obstructed by the outside of the cell membranes and so the apparent diffusion coefficient is dependent on the packing density (hematocrit) of the suspension; as such it is a parameter that is readily under experimental control.

Correlation with Cell Diameter

The NMR signal that persisted at the higher values of the field-gradient would have been that from water that had the smallest apparent diffusion coefficient, namely water inside the cells. The second to eighth points, and the last eight points, of each data set were moderately well described by separate straight lines but the regression-fit was better for the first set. It is worth emphasizing that the subdivision of the points was arbitrary and was based simply on separating the data into the first and last half of each set.

From previous q-space analysis of erythrocyte suspensions (*1–3*) it is known that for larger values of the field gradients the signal that remains is primarily from the water inside the cells. In the previous q-space analysis of red cell suspensions the conclusion regarding alignment of the cells with their disc planes parallel to $\mathbf{B}_0$ was based on the consistency of the position of the first diffusion–diffraction minimum with a scalar distance that was equal to the known main diameter of the human red cell (*18*).

The area of the membrane of a human erythrocyte does not change significantly as it shrinks or swells (*19*); an increase in the volume only comes about by the biconcave disc becoming more spherical and hence taking a smaller main diameter. Therefore, the values of D_{33} for the cells of different sizes should be reflected in the relative magnitude of this parameter. Indeed, this was the case (see Table 2), with D_{33} being $(6.69 \pm 0.38) \times 10^{-10}\ m^2\ s^{-1}$ for the swollen cells with the smallest main diameter, $(7.27 \pm 0.30) \times 10^{-10}\ m^2\ s^{-1}$ for cells of normal volume, and $(8.14 \pm 0.27) \times 10^{-10}\ m^2\ s^{-1}$ for the cells that were flattened and therefore had the largest diameter.

Euler Angles

The fifth columns of Tables 1 and 2 show that after diagonalizing the experimentally determined $\mathbf{D}$ there was no statistically significant change in the values of the diagonal elements of the tensor. This implies that the sample frame of reference was aligned with that defined by the magnetic field-gradients.

The Appendix shows one example of a set of angles ($\theta = 91°$, $\phi = 30°$, and $\psi = 1°$) that were required to align the laboratory (gradient) frame of reference with the sample frame. This set relates to the second to eighth points from the isotonic sample referred to in Table 1. The *Mathematica* function SingularValues diagonalizes a matrix and then places the elements of the diagonal matrix in echelon form, from left to right down the leading diagonal. Thus the element D_{33} in the experimental tensor was moved to the position of D_{11} in the diagonal matrix. Since the original experimental tensor was almost diagonal the value of θ would be expected to be near 90°, as was the case. The fact that ϕ was not 0° or 90° was also evident with the other analyses, and this is consistent with the high

level of statistical noise in the off-diagonal terms of the experimental tensor. In other words, the similarity of the values of the elements on the leading diagonal in the experimental tensor with those of its diagonalized form (Tables 1 and 2) showed that, within experimental error, the cells were aligned with their disc planes parallel to the direction of $\mathbf{g}_z$ and $\mathbf{B}_0$.

Statistics

A final comment on the statistical analysis is warranted. The output from the *Mathematica* program (see Appendix) contains valuable information in addition to the values of the elements of the diffusion tensor. These items include the standard errors (SE) of the parameter estimates, t statistic, and P value. The latter were minute ($\ll 0.01$) in all cases for the diagonal elements, indicating a high level of statistical significance of the estimated values and their consistency with the fitted quadratic form (Eq. [9]). A large change was noticed in the SEs estimated in the regression analysis of the first eight points, when the first point in each set was eliminated. This effect was traced to the fact that the first spectrum, acquired with a low value of field-gradient, was usually not of consistent intensity compared with the others in the series. Since the points lay at the extremes (beginning) of the series of fitted points it was deemed justified to eliminate them from the analysis.

Conclusions

The clinical significance of the alignment of erythrocytes in a magnetic field, as demonstrated here, is unknown as the cells were not flowing. The effect of flow on the alignment of erythrocytes *in vivo* is imperfectly understood; but it is conceivable that the microperfusion of tissues could be altered as a result of the different orientations of the perfusing blood vessels and the alignment of the erythrocytes in them (*1*). Since red cells become distorted when passing through capillaries, such effects would presumably only be manifest in the larger arterioles and venules that feed and drain the capillary beds, respectively.

The physical basis of the alignment of the discocytes in $\mathbf{B}_0$ is primarily the diamagnetic anisotropy of the phospholipids in the membranes, with some opposing contribution from the differences between the bulk magnetic susceptibility across the cell membrane (*3, 20*).

A systematic approach to estimating the diffusion tensor from PGSE data was developed using functions available in *Mathematica*. This provided a compact and rapid analytical strategy for evaluating the Euler rotation matrix and defining the relationship between the laboratory and sample Cartesian-reference frames. While quantitative determinations of the values of the elements of the diffusion tensor are generally not sought in MRI, these values are required for a precise description of the rate of solvent and solute diffusion in biophysical studies of tissues and cells. Thus a suspension of carbonmonoxygenated human erythrocytes may serve as a well-characterized diffusion-tensor phantom for calibrating an MRI instrument for quantitative biophysical studies.

APPENDIX

The *Mathematica* program was used with PGSE NMR data to calculate: (1) the diffusion tensor in the laboratory frame of reference; (2) the diagonalized form of the tensor and hence the tensor in the frame of reference of the sample; and (3) the Euler rotation matrix that specifies the frame of reference of the sample relative to the laboratory frame. The Input commands are given in boldface and the Input comments and Output statements are in plain text. The input and output values/numbers are from the actual experiment whose data are given in Fig. 2. The fit was to the 2nd to the 8th points in each set of 16 4-tuples. The blanking off of the primary data was done with the bracket–asterisk comment declarer.

(*Diffusion tensor calculation from PGSE data*)

In[1]:=

Needs["Statistics‘LinearRegression‘"]

gam = 2.67 × 10⁸; (*γ radians s^{-1}, magnetogyric ratio of protons*)

lildel = 0.002; (*δ seconds, duration of field-gradient pulse*)

bigdel = 0.02; (*Δ seconds, time interval between field-gradient pulses*)

stejTan = gam∧2 lildel∧2 (bigdel − lildel/3); (*Stejskal–Tanner variable*)

(*data consist of the 4-tuples { gx, gy, gz, signal} where the signal has been normalized, in *uxnmr,* with respect to that in the first spectrum for which the gradient has the least value*)

data =

{(*{0.01, 0.0, 0.0, 1.0},*) (*1st 4-tuple, first gx value, gy, gz = 0; signal = 1.0*)

                              (*blanking off the 1st 4-tuple improves quality of fit*)

{0.043, 0.0, 0.0, 0.9780},

●
● (*blanking off the 9th to the 16th 4-tuple to fit first linear section*)
●

{0.5, 0.0, 0.0, 0.09408},*) (*16th 4-tuple, last gx value, gy, gz = 0*)

(***{0.0, 0.01, 0.0, 1.0},***)(*1st 4-tuple, first gy value, gx, gz = 0; signal = 1.0*)
(*blanking off the 1st 4-tuple improves quality of fit*)
　　{0.0, 0.043, 0.0, 0.9749},

●
●(*blanking off the 9th to the 16th 4-tuple to fit first linear section*)
●

　　{0.0, 0.5.0, 0.0, 0.09605), *) (*16th 4-tuple, last gy value, gx, gz = 0*)

●
●
●

●　　(*16 × 4-tuples, only gz applied*)
●　　(*16 × 4-tuples, gx and gy applied*)
●　　(*16 × 4-tuples, gx and gz applied*)
●　　(*16 × 4-tuples, gy and gz applied*)
●　　(*16 × 4-tuples, gx, gy, and gz applied*)
　　　};

(*transform the data so that the 4th element in the 4-tuple is divided by the Stejskal–Tanner parameter that includes the maximum gradient squared (according to Eq. [8] in the text), and the field-gradient elements are normalized by dividing by the length of the gradient vector, namely the square root of the sum of the squares of the magnitudes of the three constituent basis gradients*)

trans[x_,y_]:= −Log[x]/(stejTan*y^2)
transdat = Partition[Flatten[Map[{{Part[#,1],Part[#,2],Part[#,3]}/
　　(Sqrt[Part[#,1]^2+Part[#,2]^2+Part[#,3]^2),trans[Part[#,4],
　　Sqrt[Part[#,1]^2+Part[#,2]^2+Part[#,3]^2]]}&,data]], 4];

(*the quadratic form of Eq. [9], described by the gradient basis functions, is fitted onto the data*)

fitr = Resgress[transdata, {x∧2, y∧2, z∧2, 2 x y, 2 x z, 2 y z}, {x, y, z},
　　　　IncludeConstant→False]

Out[2]=
　{ParameterTable→

	Estimate	SE	TStat	PValue
x^2	6.89×10^{-10}	1.72×10^{-11}	40.0093	0.
y^2	7.07×10^{-10}	1.72×10^{-11}	41.0547	0.
z^2	1.02×10^{-9}	1.72×10^{-11}	59.4686	0.　　,
2 x y	-3.12×10^{-11}	1.87×10^{-10}	−1.65917	0.104358
2 x z	1.59×10^{-11}	1.86×10^{-10}	0.858712	0.395261
2 y z	-8.82×10^{-11}	1.86×10^{-10}	−0.0047507	0.996231

RSquared → 0.982403, AdjustedRSquared → 0.980291,
EstimatedVariance → 7.68077 × 10^{-21}, ANOVATable →

	DF	SumOfSq	MeanSq	FRatio	PValue
Model	6	3.24×10^{-17}	5.39×10^{-18}	2498.09	0.
Error	43	9.28×10^{-20}	2.16×10^{-21}		}
U Total	49	3.25×10^{-17}			

(*repeat fit and extract diffusion tensor from Output Table*)
In[3]=
fitr = Regress[transdata, {x^2, y^2, z^2, 2 x y, 2 x z, 2 y z}, {x, y, z},
     IncludeConstant→False, RegressionReport →
     {ParameterConfidenceRegion}];
resf = ParameterConfidenceRegion/.fitr[[1]];
dt = resf[[1]];

diffTens = {{dt[[1]], 0.5 dt[[4]], 0.5 dt[[5]]},
          {0.5 dt[[4]], dt[[2]], 0.5 dt[[6]]},
          {0.5 dt[[5]], 0.5 dt[[6]], dt[[3]]}};
{u, md, v} = SingularValues[diffTens]
MatrixForm[DiagonalMatrix[md]]

Out[4]=
{{{0.024, −0.0013, 0.100}, {−0.498, 0.867, 0.013}, {0.867, 0.498, −0.020}}, {1.02 × 10⁻⁹, 7.16 × 10⁻¹⁰, 6.79 × 10⁻¹⁰},
{0.024, −0.0013, 0.100}, {−0.498, 0.867, 0.013}, {0.867, 0.498, −0.020}}}

Out[5]=

$$
\begin{bmatrix}
1.02041 \times 10^{-9} & 0 & 0 \\
0 & 7.15563 \times 10^{-10} & 0 \\
0 & 0 & 6.79495 \times 10^{-10}
\end{bmatrix}
$$

In[6]=

(*the Euler matrix is as follows:
rotMat:={{Cos[fi]Cos[th]Cos[psi]−Sin[fi]Sin[psi],Sin[fi]Cos[th]Cos[psi]+
Cos[fi]Sin[psi],−Sin[th]Cos[psi]},{−Cos[fi]Cos[th]Sin[psi]−
Sin[fi]Cos[psi],−Sin[fi]Cos[th]Sin[psi]+Cos[fi]Cos[psi],
Sin[th]Sin[psi]},{Sin[th]Cos[fi],Sin[th]Sin[fi],Cos[th]}}.
To determine fi, theta, and psi, equate elements (3,3), (3,2), and (2,3)
with the corresponding terms of the Euler matrix and solve for each angle*)

In[7]=
theta = ArcCos[ut[[3,3]]]*180/Pi//N
phi = ArcSin[ut[[3,2]]/Sin[ArcCos[ut[[3,3]]]]*180/Pi//N
psi = ArcSin[ut[[2,3]]/Sin[ArcCos[ut[[3,3]]]]*180/Pi//N

Out[8]= 91.1586

Out[9]= 29.8692

Out[10]= 0.753636

ACKNOWLEDGMENTS

REFERENCES

1. P. W. Kuchel, A. Coy, and P. Stilbs, NMR "diffusion–diffraction" of water revealing alignment of erythrocytes in a magnetic field and their dimensions and membrane transport characteristics, *Magn. Reson. Med.* **37,** 637–643 (1997).

2. A. M. Torres, R. J. Michniewicz, B. E. Chapman, G. A. R. Young, and P. W. Kuchel, Characterisation of erythrocyte shapes and sizes by NMR diffusion–diffraction of water: Correlation with electron micrographs, *Magn. Reson. Imaging* **16,** 423–434 (1998).

3. A. M. Torres, A. T. Taurins, D. G. Regan, B. E. Chapman, and P. W. Kuchel, Assignment of coherence features in NMR *q*-space plots to particular diffusion modes in erythrocyte suspensions, *J. Magn. Reson.* **138,** 135–143 (1999).

4. P. J. Basser, J. Mattiello, and D. LeBihan, Estimation of the effective self-diffusion tensor from the NMR spin echo. *J. Magn. Reson. B* **103,** 247–254 (1994).

5. P. J. Basser and C. Pierpaoli, Microstructural and physiological features of tissues elucidated by quantitative-diffusion-tensor MRI. *J. Magn. Reson. B* **111,** 209–219 (1996).

6. A. M. Ulug and P. C. M. van Zijl, Orientation-independent diffusion imaging without tensor diagonalisation: Anisotropy definitions based on physical attributes of the diffusion ellipsoid. *J. Magn. Reson. Imaging* **9,** 804–813 (1999).

7. W-Y. I. Tseng, T. G. Reese, R. M. Weisskoff, and V. J. Weeden, Cardiac diffusion tensor MRI without in vivo strain correction. *Magn. Reson. Med.* **42,** 393–403 (1999).

8. D. K. Jones, M. A. Horsfield, and A. Simmons, Optimal strategies for measuring diffusion in anisotropic systems by magnetic resonance imaging. *Magn. Reson. Med.* **42,** 515–525 (1999).

9. S. Pajevic and C. Pierpaoli, Color schemes to represent the orientation of anisotropic tissues from diffusion tensor data: Application to white matter fiber tract mapping in the human brain. *Magn. Reson. Med.* **42,** 526–540 (1999).

10. P. van Gelderen, D. DesPres, P. C. M. van Zijl, and C. T. Moonen, Evaluation of restricted diffusion in cylinders. Phosphocreatine in rabbit leg muscle, *J. Magn. Reson. B* **103,** 255–260 (1994).

11. S. Wolfram, "The Mathematica Book," Cambridge Univ. Press, Cambridge (1999).

12. E. O. Stejskal and J. E. Tanner, Spin diffusion measurements: Spin-echoes in the presence of a time-dependent field gradient. *J. Chem. Phys.* **42,** 288–292 (1965).

13. H. Goldstein, "Classical Mechanics," Second ed., Addison–Wesley, Reading (1980).

14. B. T. Bulliman, P. W. Kuchel, and B. E. Chapman, "Overdetermined" one dimensional NMR exchange analysis: A 1-D counterpart of the 2-D EXSY experiment. *J. Magn. Reson.* **82,** 377–384 (1989).

15. M. L. Abell, J. P. Braselton, and J. A. Rafter, "Statistics with Mathematica," Version 3, Academic Press, San Diego (1999).

16. R. Mills, Self-diffusion in normal and heavy water in the range 1–45°. *J. Phys. Chem.* **77,** 685–688 (1973).

17. Z. H. Endre, B. E. Chapman, and P. W. Kuchel, Cell volume dependence of ^{1}H spin echo NMR signals in human erythrocyte suspensions: The influence of in situ field gradients. *Biochim. Biophys. Acta* **803,** 137–144 (1984).

18. J. V. Dacie and S. M. Lewis, "Practical Haematology," Churchill Livingstone, Edinburgh (1975).

19. A. J. Grimes, "Human Red Cell Metabolism," Blackwell Sci., Oxford (1980).

20. T. Higashi, A. Yamagishi, T. Takeuchi, N. Kawaguchi, S. Sagawa, S. Onishi, and M. Date, Orientation of erythrocytes in a strong magnetic field. *Blood* **82,** 1328–1334 (1993).

PAPER IV

Thermodynamic and Hydrodynamic Properties of Human Tropoelastin

ANALYTICAL ULTRACENTRIFUGE AND PULSED FIELD-GRADIENT SPIN-ECHO NMR STUDIES*

Prachumporn Toonkool‡§, David G. Regan‡¶, Philip W. Kuchel‡, Michael B. Morris‖, and Anthony S. Weiss‡**

From the ‡Department of Biochemistry and the ‖Faculty of Pharmacy, University of Sydney, New South Wales 2006, Australia

Tropoelastin is the soluble precursor of elastin that bestows tissue elasticity in vertebrates. Tropoelastin is soluble at 20 °C in phosphate-buffered saline, pH 7.4, but at 37 °C equilibrium is established between soluble protein and insoluble coacervate. Sedimentation equilibrium studies performed before (20 °C) and after (37 °C) coacervation showed that the soluble component was strictly monomeric. Sedimentation velocity experiments revealed that at both temperatures soluble tropoelastin exists as two independently sedimenting monomeric species present in approximately equal concentrations. Species 1 had a frictional ratio at both temperatures of ~2.2, suggesting a very highly expanded or asymmetric protein. Species 2 displayed a frictional ratio at 20 °C of 1.4 that increased to 1.7 at 37 °C, indicating a compact and symmetrical conformation that expanded or became asymmetric at the higher temperature. The slow interconversion of the two monomeric species contrasts with the rapid and reversible process of coacervation suggesting both efficiently incorporate into the coacervate. A hydrated protein of equivalent molecular weight modeled as a sphere and a flexible chain was predicted to have a frictional ratio of 1.2 and 1.6, respectively. Tropoelastin appeared as a single species when studied by pulsed field-gradient spin-echo NMR, but computer modeling showed that the method was insensitive to the presence of two species of equal concentration having similar diffusion coefficients. Scintillation proximity assays using radiolabeled tropoelastin and sedimentation analysis showed that the coacervation at 37 °C was a highly cooperative monomer-*n*-mer self-association. A critical concentration of 3.4 g/liter was obtained when the coacervate was modeled as a helical polymer formed from the monomers via oligomeric intermediates.

Elastin forms a highly insoluble cross-linked extracellular matrix that is predominantly responsible for the elasticity of vertebrate tissue. The precursor of elastin, tropoelastin, is devoid of cross-links. Following secretion from the cell surface, tropoelastin undergoes coacervation, which is a process of self-association characterized by an inverse temperature transition (1). Tropoelastin is soluble in aqueous solution at room temperature *in vitro*, but upon raising the temperature to 37 °C the solution becomes turbid as tropoelastin molecules associate to form large aggregates (2, 3). This process of coacervation results from multiple intermolecular interactions of the hydrophobic domains (3, 4). The tropoelastin coacervate is a thick viscoelastic phase that is not miscible with the overlying solution (5). On cooling to 20 °C, the aggregates dissociate reversibly, and the solution turns clear. Alternating between hydrophobic domains in the protein are short sequences of amino acid residues that form the cross-linking domains (6). Coacervation may concentrate and align tropoelastin molecules prior to elastin formation via lysyl oxidase-mediated cross-linkage of the lysine residues that leads to a growing elastic fiber (4, 7, 8).

Vrhovski *et al*. (1) demonstrated that maximal coacervation of recombinant human tropoelastin occurs under the physiologically relevant conditions of 37 °C, 150 mM NaCl, and pH 7–8. Through coacervation, tropoelastin molecules were thought to be converted from molecules largely lacking secondary and tertiary structure to a more ordered state (2, 7, 9, 10). Electron micrographs show parallel arrays of 5-nm-wide filaments of tropoelastin coacervates that are similar to the fibrous structure of mature elastin (3, 4, 11). The importance of coacervation in the formation of lysine cross-links has been shown in smooth muscle cells where culturing at temperatures below 37 °C hampers elastin formation (12, 13).

In the work described here, analytical ultracentrifugation, pulsed field-gradient spin-echo (PGSE)[1] nuclear magnetic resonance spectroscopy, and scintillation proximity assays were employed, in conjunction with computer modeling studies, to characterize the thermodynamic and hydrodynamic properties of recombinant tropoelastin before (20 °C) and after (37 °C) coacervation. We show that at both temperatures soluble tropoelastin exists as at least two monomeric forms that have the capacity to coacervate in a manner similar to a classical critical concentration model of polymerization.

MATERIALS AND METHODS

Preparation of Tropoelastin SHELΔ26A—Tropoelastin SHELΔ26A (M_r = 60,140) was expressed and extracted from a culture of *Escherichia coli* BL21(DE3) as described previously (1, 14). SHELΔ26A is a recombinant human tropoelastin lacking the hydrophilic domain encoded by exon 26A and is identical to a naturally occurring isoform of

[1] The abbreviations used are: PGSE, pulsed field-gradient spin-echo; PBS, phosphate-buffered saline; T, tesla.

human tropoelastin found in connective tissue. Sodium dodecyl sulfate-polyacrylamide gel electrophoresis was performed to check the purity of protein samples (15). Concentrations of acrylamide for the resolving gel and the stacking gel were 10 and 4%, respectively. For coacervation, full-length tropoelastin was dissolved in phosphate-buffered saline (PBS) containing 10 mM phosphate buffer, pH 7.4, and 150 mM NaCl, which mimics the ionic conditions found to be optimal for coacervation (1).

Sedimentation Equilibrium—Sedimentation equilibrium of tropoelastin was performed in a Beckman XL-A analytical ultracentrifuge at different initial loading concentrations ranging from 0.3 to 4.0 g/liter. The protein solution was dialyzed extensively against PBS at 4 °C and spun in a benchtop centrifuge at room temperature at ~12,000 × g for 30 min prior to the ultracentrifuge experiments. 120-μl aliquots of tropoelastin were loaded into the sample channels of Yphantis 6-channel, 12-mm centerpieces, and 125 μl of diffusate into the corresponding reference channels. Centrifugation was conducted in an AnTi-60 rotor at 15,000 rpm to sedimentation equilibrium at 20 and 37 °C. Radial absorbance scans were collected in continuous scan mode at 280 and 250 nm every 4 h with 10 replicates and a step size of 0.001 cm. A base-line scan at 360 nm was taken to correct for optical imperfections. Sedimentation equilibrium was considered to have been achieved when there was an overlap between two consecutive scans.

The Ω function was used to test for sample homogeneity and attainment of chemical equilibrium (16, 17).[2] Ω is defined (16) as indicated in Equation 1,

$$\Omega = c(r)\exp[\phi_1 M_1(r_F{}^2 - r^2)]/c(r_F)$$
$$= a_1(r_F)c(r)/a_1(r)c(r_F) \qquad (Eq.\ 1)$$

where $c(r)$ is the total protein concentration at radial distance r; $c(r_F)$ is the total protein concentration at reference radial distance r_F; $a_1(r)$ is the thermodynamic activity of the protomer at radial distance r; $a_1(r_F)$ is the thermodynamic activity of the protomer at reference radial distance r_F; and M_1 is the molar weight of the protomer. $\phi_1 = (1 - \bar{v}\ \rho)\omega^2/2RT$, where $\bar{v}$ is the partial specific volume (ml/g) of tropoelastin at the absolute temperature T; ρ is the density of the solvent (g/ml) at the experimental temperature; ω is the angular velocity of the rotor; and R is the universal gas constant.

Protein concentrations were determined using the calculated extinction coefficient value of 0.322 liters/g/cm at 280 nm (GCG version 8.0-UNIX Peptidesort) and 0.154 liters/g/cm at 250 nm. The $\bar{v}$ of SHELΔ26A was calculated from the amino acid composition to be 0.7574, 0.7595, and 0.7646 ml/g at 20, 25, and 37 °C, respectively (Sednterp version 1.01; retrieved from the RASMB server; 18). The ρ of PBS was calculated to be 1.0057 and 1.0008 g/ml at 20 and 37 °C, respectively (Sednterp version 1.01).

The WinNonlin version 1.035 software package (19) was used to fit plots of $c(r)$ *versus* $r^2/2$ obtained from three different loading concentrations of tropoelastin centrifuged to chemical equilibrium. The program returned values of the molar weight and the second virial coefficient, B, together with values representing the 95% confidence intervals of the parameter values. B is a measure of the nonideality of the solute, which principally arises from the size and shape of the solute and its effective charge in the buffer conditions employed (19).

Values of apparent weight average molar weight, M_w^{app}, were obtained by a sliding 19-point linear regression of plots of $\ln c(r)$ *versus* r^2. Regression of the plots and smoothing were performed with the Om-menu series of programs.[2] M_w^{app} is defined in Equation 2 (20),

$$M_w^{app} = [d\ln c(r)/dr^2]/\phi_1$$
$$= M_w/[1 + BM_wc(r)] \qquad (Eq.\ 2)$$

where M_w is the ideal weight average molar weight.

Sedimentation Velocity—Sedimentation velocity was performed in the Beckman XL-A analytical ultracentrifuge at initial loading concentrations ranging from 0.4 to 5.0 g/liter. 400-μl aliquots of tropoelastin were loaded into the sample channels of double-sector, 12-mm centerpieces and 450 μl of buffer into the corresponding reference channels. Centrifugation was conducted in an AnTi-60 rotor at 48,000 rpm for 5 h at either 20 or 37 °C. Radial absorbance scans were collected in contin-

uous scan mode at either 280 or 250 nm every 4 min with two replicates and a step size of 0.005 cm.

Data analysis was performed by directly fitting plots of $dc(r)/dt$ *versus* s^* using the DCDT+ package. s^* is the apparent sedimentation coefficient defined in Equation 3 (21),

$$s^* = \ln(r/r_m)/\omega^2 t \qquad (Eq.\ 3)$$

where r_m is the radial distance of the solution meniscus, and t is the equivalent time of sedimentation. The data were best fit by a model describing two independently sedimenting species, and the program returned values of the sedimentation and diffusion coefficients (s and D, respectively) for each species along with their standard errors (22).

Values of s and D were corrected to the equivalent values in water at 20 °C ($s_{20,w}$ and $D_{20,w}$, respectively) using values for the viscosity, η, of PBS of 1.0192 and 0.70346 centipoise at 20 and 37 °C, respectively (Sednterp version 1.01), and density values as given above. Plots of $s_{20,w}$ and $D_{20,w}$ *versus* initial loading concentration were extrapolated to zero concentration by linear regression to give the $s_{20,w}^0$ and $D_{20,w}^0$ values.

The molar weight, M, of each species was then calculated from the relationship (23) shown in Equation 4,

$$M = s_{20,w}^0 RT/D_{20,w}^0(1 - \bar{v}\rho_{20,w}) \qquad (Eq.\ 4)$$

where $\rho_{20,w}$ is the density of water at 20 °C.

Sedimentation data were used to calculate the frictional ratio $f_{20,w}^0/f_0$ of tropoelastin. $f_{20,w}^0$ is defined in Equation 5 (23),

$$f_{20,w}^0 = M(1 - \bar{v}\rho_{20,w})/Ns_{20,w}^0 \qquad (Eq.\ 5)$$

where N is Avogadro's number. f_0 is the frictional coefficient of a hard, unhydrated spherical particle and is defined in Equation 6 and as follows (23),

$$f_o = 6\pi\eta R_e \qquad (Eq.\ 6)$$

$$R_e = (3M\bar{v}/4\pi N)^{1/3} \qquad (Eq.\ 7)$$

where η is the viscosity of water at 20 °C and R_e is the radius of the sphere of the particle with molar weight of SHELΔ26A at 20 °C.

By using values of $f_{20,w}^0$ calculated from Equation 5, R_e for sedimenting species of tropoelastin was calculated using an equation analogous to Equation 6. The value of $f_{20,w}^0/f_0$ was used to obtain an axial ratio, a/d, for a prolate spheroid of revolution (where a represents the major axis and d represents the minor axis) (23).

Nuclear Magnetic Resonance Spectroscopy—Tropoelastin was dissolved in both PBS and pure water, and the solutions were brought to concentrations ranging from 0.5 to 10 g/liter. Samples were loaded in 5-mm outer diameter NMR tubes (Shigemi) to a height of 1 cm.

PGSE experiments were conducted on a Bruker DRX-400 spectrometer (Karlsruhe, Germany) with an Oxford Instruments 9.4 T vertical wide bore magnet (Oxford, UK), using a Bruker 10 T/m z axis gradient probe. PGSE experiments conducted at 20 °C used a pulse sequence as described previously (24). Experiments conducted at 37 °C used a double spin-echo pulse sequence to compensate for convection in the sample (25). The pulse sequence parameters for all experiments are as follows: duration of field-gradient pulses, $\delta = 2$ ms; time interval between field-gradient pulses, $\Delta = 20$ ms; 90° R_F pulse, 18–20 μs; total spin-echo time, TE = 40 ms; between 128 transients per spectrum for the highest concentration sample (10 g/liter) and 4096 transients per spectrum for the lowest concentration sample (0.5 g/liter) were acquired; maximum field-gradient, $g_{max} = 3.75$ T/m. The water signal was suppressed during the relaxation delay to allow the use of higher receiver gain. Routinely, 16 spectra were acquired with a sequential increase in the value of g.

The gradients were calibrated using the known diffusion coefficient of water in an isotropic and unbounded region (26). A single experiment was conducted for each concentration of sample at 20 °C. At 37 °C duplicate experiments were conducted on a 10 g/liter sample of tropoelastin in water only. Tropoelastin forms a coacervate in PBS at 37 °C yielding a sedimenting phase in the sample tube (1), thus precluding this type of sample for diffusion measurements at 37 °C.

In each spectrum the signal intensity was measured as the integral of the tropoelastin resonance envelope in the aliphatic region (~5.5–2.5 ppm) after manual phase and base-line correction. Signal intensities were normalized with respect to the signal intensity in the first spectrum, corresponding to the smallest field gradient. The natural logarithm of the signal intensity was plotted as a function of the Stejskal-Tanner parameter, b, which is proportional to the square of the applied field gradient (27). The Origin software package (Microcal) was used to

Properties of Human Tropoelastin

fit a straight line to the plotted data, and the slope of this line provided an estimate of the diffusion coefficient. Diffusion coefficients for tropoelastin in water and in PBS at 20 °C were then plotted as a function of concentration, and linear regression was used again to extrapolate the line to zero concentration thus yielding values for D^0. D^0 for tropoelastin in PBS was then corrected for the viscosity of water to yield $D^0_{20,w}$. A weight average $D_{37,w}$ was calculated from the duplicate diffusion coefficients estimated for tropoelastin in water at 37 °C; the weighting factor was the inverse of the variance of each value.

Computer Modeling—Computer modeling was used to address two questions arising from the ultracentrifuge data. First, is the resolution of the PGSE NMR diffusion data adequate to suggest the existence of more than one species? Second, does a system in which one species is modeled as a compact sphere and the other species as a flexible chain or rigid rod molecule account for the observed hydrodynamic properties?

To answer the first question, a computer model (model I) was written in Maple (Waterloo Software Inc., Canada). Signal intensities for a PGSE NMR diffusion experiment were calculated for a series of gradient values using the same parameters as those used in the actual experiment. The model assumed two independent non-interacting species of equal concentration having $D^0_{20,w}$ of 4.0 and 6.0×10^{-11} m²/s (comparable to those determined by sedimentation velocity experiments at 20 °C, see "Results"). The following formula, shown in Equation 8, was used for the calculation,

$$E = C_1 e^{-D_1 b} + C_2 e^{-D_2 b} \qquad \text{(Eq. 8)}$$

where E is signal intensity; C_1 and C_2 are the concentrations of the two species; D_1 and D_2 are the diffusion coefficients of the two species; and b is the Stejskal-Tanner parameter (27).

The signal-to-noise ratio and its standard deviation were calculated from the actual PGSE NMR experiment. Random noise, whose amplitude had a standard deviation equal to that of the experimental data, was then superimposed on the calculated signal intensities. The natural logarithm of the calculated signal intensity with its associated noise was then plotted as a function of the Stejskal-Tanner parameter b. Linear regression was used to fit a straight line to the simulated PGSE NMR data in order to determine whether there was any statistically discernible deviation from linearity.

To answer the second question, a model (Model II) was written in Matlab (MathWorks) and was used to predict $D^0_{20,w}$ for a tropoelastin monomer, when it was modeled as follows: 1) a hard unhydrated sphere; 2) a hard hydrated sphere; 3) a hydrated flexible chain; and 4) a rigid rod. Note that the aim of the simulation was not to calculate accurate values of $D^0_{20,w}$ for possible conformations of the protein but rather to determine whether the difference in the experimental values could be explained in terms of these conformations. For this reason, the model assumed an ideal solution in which the diffusing molecules do not interact or give rise to excluded volume effects. The amino acid residues, which constitute the monomers in the flexible chain and rigid rod models, were assumed to be identical hard spherical units and to have the same partial specific volume (0.7574 ml/g) as was determined for the protein from its amino acid sequence (see "Materials and Methods").

The Stokes equation and the Einstein equation (also referred to as the Einstein-Smoluchowski equation (see Ref. 28)) were used to calculate values of $f^0_{20,w}$ and $D^0_{20,w}$, respectively, of the amino acid residues in the flexible chain and rigid rod models, and of the unhydrated and hydrated spheres. The hydrodynamic parameters for the flexible chain were calculated using Equations 36 and 37 of Kirkwood and Riseman (29) and for the rigid rod using Equations 22 and 23 of Riseman and Kirkwood (30). A weighted average specific volume for the hydrated molecules was calculated to account for the associated water molecules. For a typical protein, each gram of its dry weight contains between 0.3 and 0.6 g of associated water, whose properties are significantly different to those of the bulk water (31). This corresponds to limits of ∼1.4 and ∼2.8 water molecules per amino acid residue for tropoelastin monomers, and thus hydrodynamic parameters were calculated for all models on the basis of these two values. The values of $f^0_{20,w}/f_0$ for the hydrated sphere, flexible chain, and rigid rod were calculated as the ratio of the molecule's $f^0_{20,w}$ to that of the hard unhydrated sphere.

Scintillation Proximity Assays—[125]I-Labeled tropoelastin was prepared by incubating 1 mg of tropoelastin (in 0.5 ml of PBS) with 5 µl of [125]I (supplied as sodium iodide by Amersham Pharmacia Biotech) for 10 min at room temperature in a microcentrifuge tube coated with 20 ng of IODO-GEN. ^{125}I-Tropoelastin was separated from the unincorporated ^{125}I by passing the solution through a 9-ml column of Sephadex G-25 beads (Amersham Pharmacia Biotech), and 0.5-ml fractions were collected. The scintillation proximity assays were carried out in Flash-
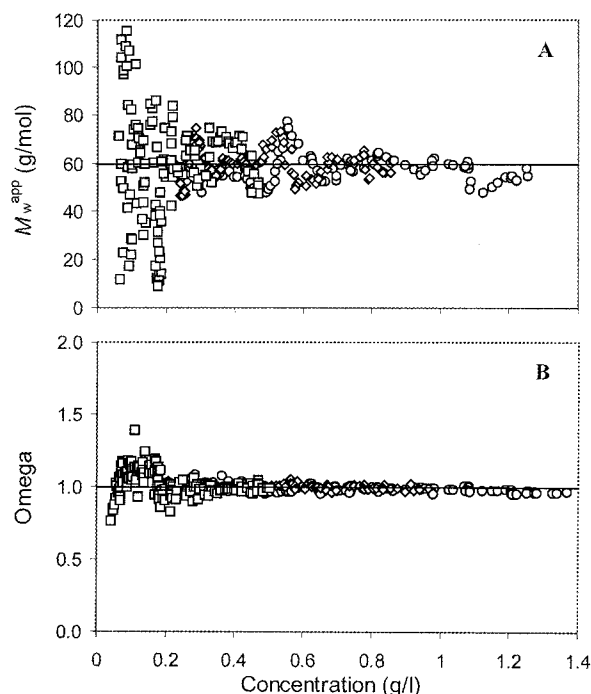

FIG. 1. **Distribution of apparent weight average molar weight (A) and the Ω function (B) for soluble tropoelastin at 37 °C in PBS, pH 7.4, at sedimentation equilibrium.** Coacervate rapidly sedimented to the base of the solution column and remained undetected. The overlap of the data from the three separate loading concentrations (□, ◇, and ○) shows that the protein is homogeneous.

Plates (Canberra Packard Co.). ^{125}I-Labeled tropoelastin was dissolved in PBS at 10 g/liter, and 100 µl of serially diluted solution was placed into duplicate wells. The plate was loaded into a Packard TopCount microplate scintillation and luminescence counter (Canberra Packard Co.) and allowed to equilibrate for 1 h at 20 and 35 °C prior to counting. 35 °C is the highest functional temperature. Association of ^{125}I-labeled tropoelastin by coacervation brought the radioactive signals in close proximity to excite the scintillant, whereas signals from the uncoacervated material remaining in solution very poorly excite scintillant. γ-Counts were determined for 1 min per well in the low energy range and normal efficiency mode. Cross-talk reduction was applied to reduce signals from neighboring wells. For each set of assays, the duplicate data were averaged. The data at 20 °C were subtracted from those at 35 °C to correct for passive coating of the wells by the protein. The corrected counts at 10 g/liter were normalized to 100%. A plot of the normalized counts *versus* the total concentration of tropoelastin was then produced from three independent sets of data.

RESULTS

Sedimentation Equilibrium—Fig. 1 shows representative results from sedimentation equilibrium experiments performed at 15,000 rpm on tropoelastin in PBS before (20 °C) and after (37 °C) coacervation. Any insoluble coacervate was rapidly sedimented to the base of the solution column and was not detected. At both temperatures, the plots of apparent weight average molar weight, M^{app}_w, *versus* concentration, $c(r)$, from three different loading concentrations of protein indicated that the soluble protein was monomeric (*e.g.* Fig. 1A). Plots of the Ω function *versus* $c(r)$ (*e.g.* Fig. 1B) from the different loading concentrations overlapped closely, indicating that both chemical and sedimentation equilibrium had been attained. Thus, the samples were homogeneous, and there were no significant concentrations of incompetent species such as irreversibly formed aggregates or truncated species (16, 17).

Plots of $c(r)$ *versus* $r^2/2$ were fit with a model describing a single nonideal species using nonlinear least squares techniques (*e.g.* Fig. 2A). Values were returned for both the molar weight, M_w, of the species and its nonideality as measured by
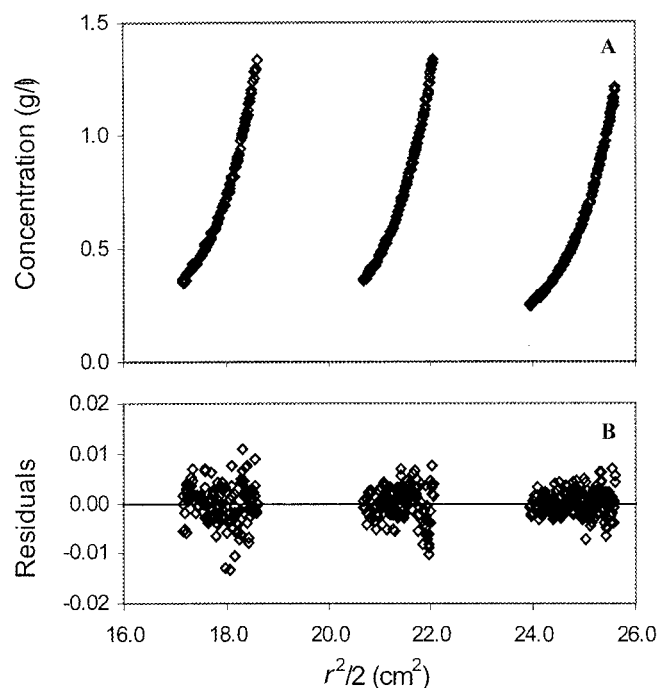
FIG. 2. **Sedimentation equilibrium of three different loading concentrations of tropoelastin at 37 °C in PBS, pH 7.4.** *A,* the plots of concentration *versus* $r^2/2$ were fit to a single species model using simultaneous nonlinear least squares regression (19). The residuals to the fit are shown in *B* and the returned values of molar weight and second virial coefficient, *B,* are shown in Table I.

the second virial coefficient, *B* (Table I). This model adequately fitted the data obtained at both 20 and 37 °C as judged by the random distribution of residuals (*e.g.* Fig. 2*B*). Returned estimates of the molar weight were consistent with that of the monomer of tropoelastin. The value of *B* increased with temperature (Table I) indicating molecular expansion and/or asymmetry. A monomer-dimer model equation fit to the data did not significantly improve the fit as judged by a lack of improvement in the sums of squares of the residuals.

Sedimentation Velocity—Sedimentation velocity experiments were performed on tropoelastin in PBS at 20 and 37 °C. At 48,000 rpm, coacervate was rapidly sedimented to the base of the solution column. Plots of $dc(r)/dt$ *versus* s^* at both temperatures for the remaining soluble component contained a single peak that was either asymmetric or broadened, suggesting the presence of more than one species (Fig. 3). When the data were fit to a single species model (Equation 4), the returned estimates of the molar mass at both temperatures were approximately half of the expected value for tropoelastin monomer of 60.14 kDa, also suggesting the presence of more than one species. Although more than one soluble species was present, each appeared to be monomeric since (i) the sedimentation equilibrium experiments showed that soluble tropoelastin was strictly monomeric (Table I), and (ii) the values of weight average $s_{20,w}$ decreased linearly with the increasing loading concentration indicating no concentration-dependent self-association of the protein (Fig. 4*A*). Therefore, the sedimentation velocity data at both temperatures were fit to a non-interacting two-species model where the molar mass of both species was either fixed at 60.14 kDa or allowed to float (Fig. 3). This model fit all plots of $dc(r)/dt$ *versus* s^* as well as or better than the single species model, as judged by the distribution and sums of squares of the residuals. Where the molar mass of the two species was allowed to float, the returned values for both species ranged from 54 to 60 kDa. Plots of $s_{20,w}$ and $D_{20,w}$ *versus* loading concentration for each of the two species at both 20 and

37 °C were extrapolated to zero concentration to obtain the values of $s_{20,w}^0$ and $D_{20,w}^0$ (Fig. 4). By using Equation 4 and the values of $s_{20,w}^0$ and $D_{20,w}^0$, the calculated molar mass of tropoelastin for both species at both 20 and 37 °C was similar to that for tropoelastin monomer (Table II).

The data were also fit with a "whole boundary" approach using the program Svedberg version 3.16 (32) and confirmed the results obtained from fitting plots of $dc(r)/dt$ *versus* s^*. Claverie simulations (33) of the sedimenting boundaries for two species using similar values of $s_{20,w}^0$ and $D_{20,w}^0$ to those obtained from fits to the experimental data were also performed. With noise added, the simulated boundaries were fit with a two-species model, and the values of the returned parameters were, within error, the same as the values used to generate the boundaries.

Pulsed Field-gradient Spin-Echo NMR Experiments—PGSE NMR experiments were conducted on samples of tropoelastin dissolved in either PBS or pure water. A concentration dependence study (Fig. 5) at 20 °C yielded $D_{20,w}^0$ values for the protein in PBS and in water of $(3.59 \pm 0.01) \times 10^{-11}$ m²/s and $(2.29 \pm 0.03) \times 10^{-11}$ m²/s, respectively.

In the presence of salt at 37 °C, tropoelastin at concentrations above ~1.5 g/liter formed a coacervate that settled to the bottom of the NMR sample tube. For this reason, and because concentrations below ~1.5 g/liter necessitated much longer spectral acquisition times, a concentration dependence study was not conducted in PBS at this temperature. Duplicate experiments were conducted to measure the *D* of tropoelastin at 10 g/liter in water at 37 °C, and the weight average $D_{37,w}$ was calculated to be $(3.11 \pm 0.06) \times 10^{-11}$ m²/s.

Computer Modeling—When the signal intensities from Model I (see "Materials and Methods") were plotted as a function of *b* without the addition of noise, a slight systematic deviation from linearity was visually discernible. Once noise was added to the simulated data it became impossible to determine whether or not there was any systematic deviation from linearity even after the regression line was superimposed on the plot. The gradient of the regression line, which corresponded to the diffusion coefficient in a one-species system, was ~4.6×10^{-11} m²/s.

The data generated by Model II (see "Materials and Methods") are summarized in Table III. They predicted that the values of $s_{20,w}^0$ and $D_{20,w}^0$ for a hydrated sphere of tropoelastin monomer would decrease by ~30 and 90% when it was modeled as flexible chain and a rigid rod, respectively. An inverse relationship of the same order applied to the values of $f_{20,w}^0$ and $f_{20,w}^0/f_0$. It is notable that the effect of change in the degree of hydration was more significant for the hydrated sphere model than for the other two models.

Determination of the Critical Concentration of Coacervation—By using the scintillation proximity assay, the equilibrium established between the soluble species of tropoelastin and the coacervate was not disturbed and was quantifiable. Fig. 6*A* shows the normalized values of radioactivity (representing tropoelastin in close proximity to the scintillant) plotted against the total concentration of tropoelastin. The data show two approximately linear components with a discontinuity at ~2 g/liter. The data above 2 g/liter were fitted by linear regression. Simple extrapolation of the fit to the abscissa represents an estimate of the critical concentration, c_c, for coacervation of ~2.4 g/liter.

In sedimentation studies performed at 2,000 rpm, the absorbance at 280 nm of the tropoelastin sample at 20 °C was recorded. This absorbance represents the total concentration of tropoelastin since significant coacervation does not occur at this temperature. Upon raising the temperature from 20 to

TABLE I

Summary of thermodynamic parameters of tropoelastin in PBS, pH 7.4, as determined from sedimentation equilibrium experiments at 20 and 37 °C

Parameter	Estimated value	20 °C[a]	37 °C[a]
M_w (g/mol)	$60,140^b$	60,636 (58,610, 62,662)	60,258 (59,304, 61,212)
B (10^{-7} l mol/g^2)	4.27 (2.17, 7.39)^c	5.05 (3.00, 7.15)	25 (20, 30)

[a] Values of the parameters obtained by nonlinear regression of plots of $c(r)$ *versus* $r^2/2$ (*e.g.* Fig. 2). The values in parentheses represent the 95% confidence intervals.

[b] Calculated from the protein sequence.

[c] Calculated on the basis that $B = B_E + B_C$, where B_E represents the excluded volume component and B_C the charge component of the nonideality (48, 49). A charge of +37.6 was estimated for tropoelastin at pH 7.4 based on its amino acid sequence and using standard pK_a values for the residues. Counterion binding is expected to reduce the net charge by 50 ± 20% (50) resulting in a value for $B_C = 3.26$ (1.16, 6.38) × 10^{-7} l mol/g^2. Assuming that the molecule is a hard, smooth sphere, the volume occupied by one molecule of tropoelastin was calculated to be 7.59×10^{-23} l per molecule based on its partial specific volume at 25 °C, resulting in a value for $B_E = 1.01 \times 10^{-7}$ l mol/g^2.
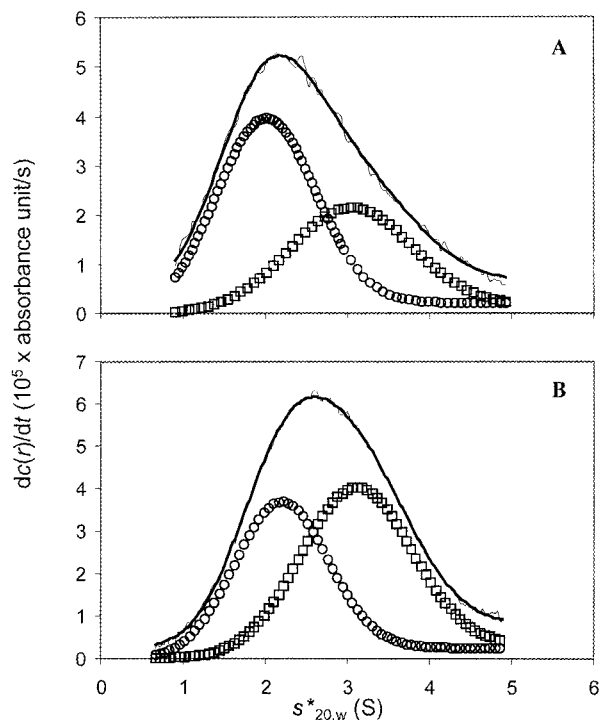
FIG. 3. **Plots of d$c(r)$/dt *versus* apparent sedimentation coefficient corrected to water at 20 °C, $s^*_{20,w}$, for tropoelastin in PBS, pH 7.4, at 20 °C (*A*) and 37 °C (*B*).** The plots were fit using the program DCDT+ with a model representing two independently sedimenting species. The returned values of the parameters from the fitting process are shown in Table II. The *thin line* represents the experimental data, and the *thick line* represents the best fit and is the sum of the contribution to the sedimenting boundary from Species 1 (○) and Species 2 (□).

FIG. 4. **Concentration dependence of $s_{20,w}$ (*A*) and $D_{20,w}$ (*B*) of tropoelastin in PBS, pH 7.4, at 37 °C.** The values for Species 1 (○) and Species 2 (□) were obtained from fitting plots of $s^*_{20,w}$ *versus* d$c(r)$/dt with a model representing two independently sedimenting species (*e.g.* Fig. 3). Weight average $s_{20,w}$ values are represented by ▲. The *straight lines* represent linear regression of the data, with the *ordinate* intercept representing the values of $s^0_{20,w}$ and $D^0_{20,w}$ (see Table II).

37 °C, the absorbance at 360 nm increased due to light scattering caused by aggregation of tropoelastin molecules in the solution column. These aggregates sedimented rapidly to the base of the solution column. When the temperature stabilized at 37 °C, the absorbance at 280 nm decreased from its original value at 20 °C and was again recorded. This absorbance represents the concentration of soluble tropoelastin following coacervation. Fig. 6B shows the plot of soluble tropoelastin *versus* the total concentration of protein. The plot was fitted with a model equation representing the cooperative polymerization of a monomer to a large helical *n*-mer via a trimeric nucleating species, a situation that approximates that for actin (34, 35), see Equations 9 and 10,

$$C_o = C_1 + \sigma C_1/(1 - K_h C_1)^2 \qquad \text{(Eq. 9)}$$

$$\sigma = \gamma K^2/K_h^2 \qquad \text{(Eq. 10)}$$

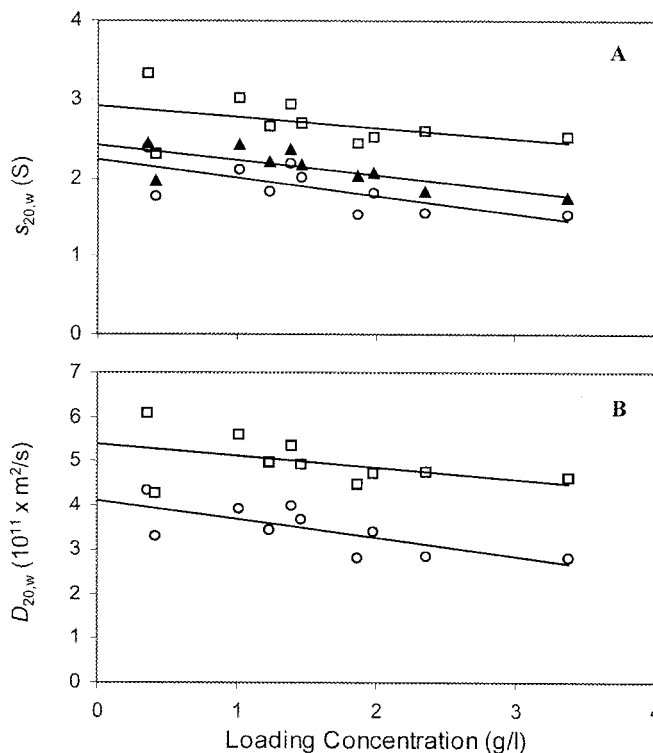where $\sigma \ll 1$, $K < K_h$, C_o, and C_1 are the total concentration

and monomer concentration in units of mol/solvent mol, respectively; γ is the excess free energy required to deform the linear trimer to give curvature to the helical polymer; K_h is the binding constant for the addition of a monomer to the end of the helical polymer; and K is the binding constant for the addition of a monomer to a simple linear polymer. For this model, the critical concentration equals $1/K_h$. This model fit the data well (*solid line,* Fig. 6B) and returned a value for the critical concentration of 3.4 ± 0.1 g/liter.

DISCUSSION

Sedimentation Equilibrium—Our sedimentation equilibrium results showed that the recombinant tropoelastin used in this study could be centrifuged to simultaneous sedimentation and chemical equilibrium at both 20 and 37 °C. The excellent overlap of the plots of the Ω function *versus* $c(r)$ from three different loading concentrations of protein (*e.g.* Fig. 1B) showed that the recombinant protein was free of soluble, irreversibly

TABLE II
Summary of hydrodynamic parameters of tropoelastin in PBS, pH 7.4, as determined from sedimentation velocity experiments at 20 and 37 °C

Parameter	20 °C		37 °C	
	Species 1	Species 2	Species 1	Species 2
$s^0_{20,w}$ (S)[a]	2.3 ± 0.2	3.5 ± 0.4	2.2 ± 0.2	2.9 ± 0.2
$D^0_{20,w}$ (10^{-11} m²/s)[a]	4.0 ± 0.3	6.2 ± 0.7	4.1 ± 0.3	5.4 ± 0.3
M (kDa)[a,b]	57 ± 6	57 ± 9	54 ± 5	54 ± 5
$f^0_{20,w}$ (10^{-7} g/s)[c,d]	1.1 (1.0, 1.2)	0.7 (0.6, 0.8)	1.1 (1.0, 1.2)	0.8 (0.8, 0.9)
$f^0_{20,w}/f_o$[d,e]	2.2 (2.0, 2.3)	1.4 (1.3, 1.6)	2.2 (2.1, 2.4)	1.7 (1.6, 1.8)
R_e (nm)[d,f]	5.6 (5.2, 6.1)	3.7 (3.3, 4.1)	5.8 (5.4, 6.2)	4.4 (4.2, 4.7)
Axial ratio[d,g]	>20	5–10	>20	11–15

[a] Errors represent the standard deviation.
[b] Calculated using Equation 4.
[c] Calculated using Equation 5.
[d] Values in parentheses represent the range of values based on the standard deviation in $s^0_{20,w}$.
[e] Calculated using Equations 5–7. The value of f_o, was calculated to be 4.91×10^{-8} g/s.
[f] Calculated from Equation 6 after substituting $f^0_{20,w}$ for f_o.
[g] Based on $f^0_{20,w}/f_o$ values and modeling the protein as a prolate ellipsoid of revolution with axial ratio a/d, where a represents the major axis and d the minor axis (23).
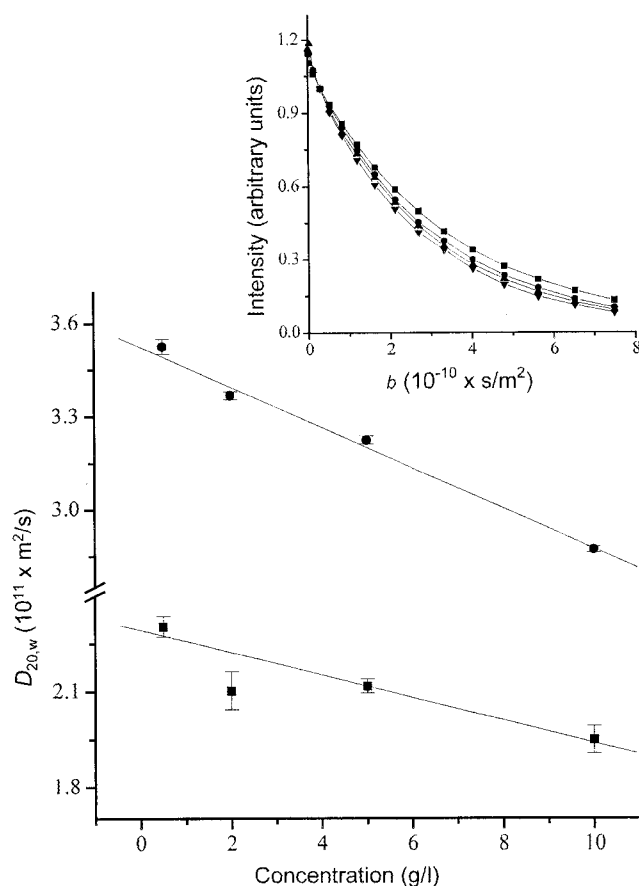
FIG. 5. **The PGSE NMR analysis of diffusion of tropoelastin.** The *main graph* shows the dependence of D on concentration in PBS (●) and in pure water (■) at 20 °C. The intercepts of the two lines with the *ordinate* give the diffusion coefficient in the respective medium at zero concentration, $D^0_{20,w}$. The *inset* shows the dependence of the signal intensity on the Stejskal-Tanner parameter, b, for tropoelastin in PBS at 20 °C for each of the following concentrations: 10 g/liter (■); 5 g/liter (●); 2 g/liter (▲); and 0.5 g/liter (▼). The linearized data were fit to estimate the diffusion coefficient for each concentration. The *error bars* denote ± 1 S.D.

formed polymers and of proteolyzed protein. Plots of $c(r)$ *versus* $r^2/2$ fit by nonlinear regression with a model describing a single nonideal species showed that the soluble tropoelastin was monomeric up to the highest concentrations we recorded: ~3 g/liter at 20 °C and ~1.5 g/liter at 37 °C (*e.g.* Fig. 2). The returned value of the molar weight of the protein was consistent with that expected for the recombinant protein (Table I). Coacervation of tropoelastin at 37 °C is a highly cooperative process (1),

and from the above results we conclude that the protomer for this association process is the monomer. Sedimentation equilibrium is also sensitive to the presence of a small percentage of larger oligomers in equilibrium with monomer. Thus, if a larger soluble species were present, such as a nucleating species for the coacervation, it was at concentrations too small to be detected under the solution and sedimentation conditions used.

We estimated a value of the second virial coefficient, B, for tropoelastin using an estimate of its net charge and based on it being a hard incompressible sphere (Table I). This value (4.27×10^{-7} l mol/g²) is similar to the experimentally determined value obtained at 20 °C (Table I), indicating that at this temperature tropoelastin molecules are, on average, relatively compact and globular. At 37 °C, however, the experimentally determined value of B increased significantly (Table I). Assuming that the nonideality due to charge was constant with temperature, these results represent an equivalent spherical radius, R_e, of 3.2 and 7.3 nm at 20 and 37 °C, respectively, in contrast to an R_e of 2.6 nm for a smooth, compact, spherical particle of tropoelastin (Equation 7). This suggests that, on average, tropoelastin molecules are more expanded or asymmetric at the higher temperature.

Sedimentation Velocity—The results from sedimentation equilibrium experiments are consistent with those from sedimentation velocity experiments. Only monomer was observed at both 20 and 37 °C in the sedimenting boundary. Furthermore, at each temperature, two different forms of tropoelastin monomer, Species 1 and 2, existed (Figs. 3 and 4; Table II). The two species were present at approximately equal concentration at both temperatures (data not shown) and did not appear to interconvert significantly over the time scale of these experiments (up to 5 h). If the species interconverted rapidly, then a single symmetrical sedimenting boundary would have been observed that could have been fitted with a single species model returning a molar weight equivalent to the monomer weight of tropoelastin.

The value of the frictional ratio, $f^0_{20,w}/f_0$, represents the degree of deviation, due to hydration, rugosity, asymmetry, and expansion of the molecule, from the minimum possible value of 1.0 for a hard, incompressible, unhydrated sphere. Compact globular proteins often yield a frictional ratio of about 1.2, the number being greater than 1.0 principally due to hydration. For tropoelastin, Species 1 represents a population of expanded or asymmetric molecules at both 20 and 37 °C; that is, the value of $f^0_{20,w}/f_0$ is large at ~2 (Table II). In contrast, Species 2 which is quite compact and symmetrical at 20 °C becomes somewhat more expanded/asymmetric when the temperature is raised to 37 °C (Table II). This expansion/asymmetry in Species 2 at the higher temperature is consistent with the

Properties of Human Tropoelastin

TABLE III

Modeling of the hydrodynamic parameters of tropoelastin in water

See Model II under "Materials and Methods" for details.

Parameter	Hard hydrated sphere		Flexible chain		Rigid rod	
	2.8[a]	1.4	2.8	1.4	2.8	1.4
$s_{20,w}^0$ (S)	4.05	4.40	3.09	3.10	0.40	0.40
$D_{20,w}^0$ (10^{-11} m^2/s)	6.72	7.30	5.13	5.14	0.66	0.67
$f_{20,w}^0$ (10^{-7} g/s)	0.60	0.55	0.79	0.79	6.13	6.06
$f_{20,w}^0/f_o$	1.22	1.12	1.59	1.59	12.4	12.2

[a] Hydration in H_2O molecules/residue.
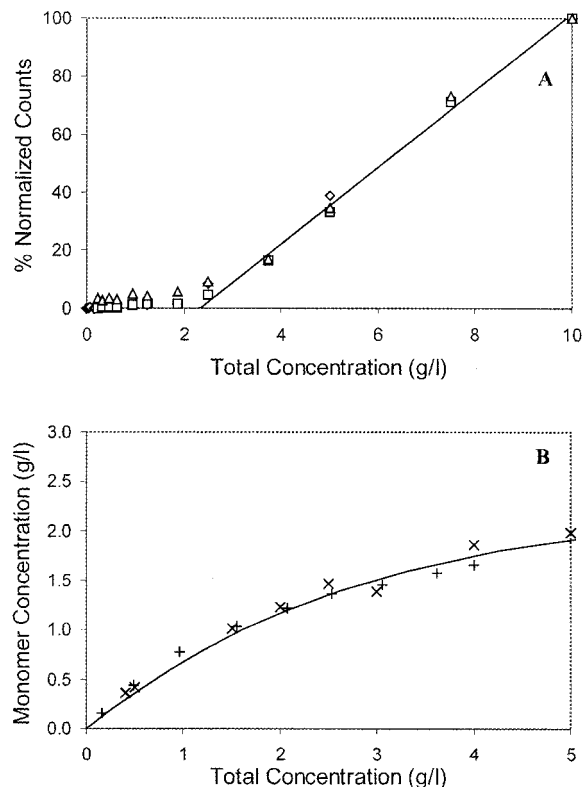
FIG. 6. **Determination of the critical concentration of coacervation.** *A,* plot of normalized counts *versus* total concentration determined from three independent scintillation proximity assays at 35 °C (△, □, and ◇). The *straight line* represents the linear regression of the data above 2 g/liter which, when extrapolated to the *abscissa*, represents an estimate of the critical concentration for coacervation (2.4 g/liter). *B,* plot of monomer concentration *versus* total concentration determined from sedimentation experiments at 37 °C (+ and ×). The *black line* represents the best fit to the data for a model representing the helical polymerization of a monomer to an *n*-mer via a nucleating trimer. The returned value of the critical concentration for this model was 3.4 ± 0.1 g/liter.

temperature-dependent increase in nonideality of tropoelastin as measured in sedimentation equilibrium experiments (Table I).

To support the interpretation of the hydrodynamic parameters determined from the sedimentation velocity experiments, a series of molecular modeling studies was performed to predict hydrodynamic properties of the protein (Table III). A hard sphere of tropoelastin hydrated at 2.8 molecules of water per amino acid residue has the "expected" frictional ratio of ~1.2. This increases modestly to 1.6 upon changing to a flexible chain, whereas a dramatic increase results from a change to a rigid rod conformation (Table III). Therefore, we propose an explanation for the sedimentation data; there exist two species of tropoelastin monomer in solution, one of which, Species 2, displays properties between that of a globular protein and a flexible coil, whereas Species 1 has a more expanded/asymmetric form.

Sedimentation velocity data alone cannot distinguish between expansion and asymmetry associated with a large frictional ratio (36), and additional experimental information is required to unequivocally determine the hydrodynamic properties of tropoelastin. Typically, the concentration dependence of the sedimentation coefficient, k_s, can be used together with the intrinsic viscosity of the protein, $[\eta]$, to determine the molecular shape, regardless of its size (37). A $k_s/[\eta]$ value close to 1.6 combined with a large frictional ratio indicates an expanded spherical molecule as, for example, occurs for the tetramer of spectrin (38). Smaller values of $k_s/[\eta]$ combined with a large frictional ratio suggest greater molecular asymmetry as occurs for myosin ($k_s/[\eta] = 0.3$; see Ref. 37). However, in our sedimentation velocity experiments, each species would have sedimented more slowly in the presence of the other than it would alone (23), thus resulting in abnormally large values of k_s. If Species 1 and 2 could be separately purified, then it may be possible to distinguish the degree to which the individual species are either expanded or asymmetric through measurement of $k_s/[\eta]$.

Other techniques such as small angle X-ray scattering and electron microscopy could be used to determine the shape of human tropoelastin (36, 39). In electron micrographs, purified bovine and chick tropoelastin appeared spherical with a diameter of 5–7 nm (4, 40). Chick tropoelastin was interpreted as existing as a random coil with an $s_{20,w}$ of 2.1 S as determined by sucrose density gradient centrifugation (41). This value is similar to the $s_{20,w}^0$ of Species 1 at both 20 and 37 °C and together with electron micrographs of chick tropoelastin (4) suggest that Species 1 may adopt an expanded spherical form in solution.

PGSE NMR—Through PGSE NMR studies, the diffusion coefficient of tropoelastin in water at 20° C was significantly smaller than in the same medium at 37° C, as was expected. However, the diffusion coefficient in water at 20° C was also significantly less than in PBS at the same temperature. This is likely to be due to conformational differences in tropoelastin in the two media. There could also have been a diminution in the extent of monomer-monomer interactions due to the absence of electrostatic shielding in water resulting in surface charge repulsion. The low signal-to-noise ratio in the ${}^1H$ NMR spectra of tropoelastin in PBS at 37 °C was due to coacervation of tropoelastin, consistent with the notion that coacervation is predominantly the result of hydrophobic interactions (3, 4).

Estimates of the diffusion coefficient, D, of tropoelastin obtained from sedimentation velocity and PGSE NMR data constitute a novel comparison of data from each method. The hydrodynamic parameters estimated from the sedimentation velocity experiments were biased toward those of the monomeric species since high molecular weight aggregates rapidly sedimented to the base of the centrifuge cell in the presence of a high centrifugal field. On the other hand, the NMR method yielded a tracer, or weight average self-diffusion coefficient (42), and included species of all molecular weights as the gravitational field in the NMR experiment was only at unit gravity. The error bars on the concentration dependence for the PGSE NMR data (Fig. 5) represent intra-experimental uncertainty

estimated by linear regression analysis. However, the inter-experimental variation was likely to be such that a deviation of the straight-line fit from the data would not be statistically significant.

In contrast to the sedimentation velocity data, the PGSE NMR data did not provide evidence of two non-interacting species. Computer modeling (see Model I under "Materials and Methods" for details) showed that for a system of two non-interacting species with diffusion coefficients of ~4 and ~6 × 10^{-11} m^2/s, the resolution of the data from a PGSE NMR experiment would be insufficient to discern a deviation in linearity of the Stejskal-Tanner plot. Additionally, when the concentrations of the two species were set as equal in the computer modeling, the apparent diffusion coefficient calculated by linear regression favored the slower species. This was due to the more rapid attenuation of the signal from the faster diffusing species as the field gradient was increased, such that its overall relative contribution to the signal intensity was reduced.

A Model for Coacervation—There was no evidence to suggest that either Species 1 or 2 was incompetent. On the basis of their individual concentrations before and after coacervation, as measured in the sedimentation velocity experiments, they both participated in the coacervation process (data not shown). Furthermore, coacervation is a rapidly reversible process (of the order of minutes), but the two species interconvert only very slowly (hours or longer). This suggests the coacervate consists of a mixture of the two species rather than a conversion of one species to the other which then forms the coacervate. Further work is required to determine the stoichiometry of the two species in the coacervate with good accuracy and precision.

The process of coacervation was further examined by scintillation proximity assays. The biphasic plot obtained at 35 °C (Fig. 6*A*) is typical of the helical polymerization of macromolecules as diverse as actin, insulin, fibrin, and tropocollagen (43). Helical polymerization occurs above the critical concentration because of the presence of unstable, slow forming nuclei that act as seeds for the rapid production of filaments. The system reaches equilibrium or a steady state when the monomer concentration falls to the critical concentration (35). We could not detect nuclei under the sedimentation velocity conditions used, but time course measurements of tropoelastin coacervation have demonstrated an initial lag phase prior to a sigmoidal rise in turbidity (1, 14), consistent with the nucleated condensation mechanism of helical polymerization (44).

Turbidity measurements may not provide additional information about the coacervation process since turbidity is not proportional to the mass of coacervated tropoelastin.[3] Indeed, the increase in turbidity is due to the formation of microscopic oil-like droplets, or microcoacervates, as the solution is heated (45). However, on the basis of model fitting to absorbance measurements for soluble tropoelastin (Fig. 6*B*), trimeric tropoelastin may be a nucleating species for coacervation although the true situation, as with actin, is likely to be more complex (35).

In summary, we have shown that monomers are the predominant form of soluble tropoelastin before and during coacervation. These monomers appear to exist in solution in more than one conformation. Coacervation of tropoelastin proceeds via the cooperative association of tropoelastin monomers to form large aggregates, in a process that is the same as or similar to the formation of helical polymer. It would be useful to demonstrate directly the presence of oligomeric intermediates under conditions different from those used in the present experiments. Although we have not separated the two species of tropoelastin

that co-existed in solution, conversion to the more compact Species 2 should be favored in the presence of "crowding" agents (46), whereas the presence of denaturants should favor conversion to the more expanded/asymmetric Species 1. The conformational conversion and the possible existence of folding intermediates could be monitored via ultraviolet absorption spectroscopy or circular dichroism (47). The information obtained will further shed light on the secondary and tertiary structures of tropoelastin in solution. In addition, the way in which the two monomeric species interact during coacervation will help refine the association model for tropoelastin self-assembly. This will be valuable for a more complete understanding of the biological mechanism in the assembly of elastin in the extracellular matrix and the underlying mechanism of elasticity.

REFERENCES

1. Vrhovski, B., Jensen, S., and Weiss, A. S. (1997) *Eur. J. Biochem.* **250,** 92–98
2. Urry, D. W., Starcher, B., and Partridge, S. M. (1969) *Nature* **222,** 795–796
3. Cox, B. A., Starcher, B. C., and Urry, D. W. (1974) *J. Biol. Chem.* **249,** 997–998
4. Bressan, G. M., Pasquali-Ronchetti, I., Fornieri, C., Mattioli, F., Castellani, I., and Volpin, D. (1986) *J. Ultrastruct. Mol. Struct. Res.* **94,** 209–216
5. Urry, D. W. (1988) *J. Protein Chem.* **7,** 1–34
6. Vrhovski, B., and Weiss, A. S. (1998) *Eur. J. Biochem.* **258,** 1–8
7. Starcher, B. C., Saccomani, G., and Urry, D. W. (1973) *Biochim. Biophys. Acta* **310,** 481–486
8. Urry, D. W. (1978) *Perspect. Biol. Med.* **21,** 265–295
9. Cox, B. A., Starcher, B. C., and Urry, D. W. (1973) *Biochim. Biophys. Acta* **317,** 209–213
10. Urry, D. W., and Long, M. M. (1976) *CRC Crit. Rev. Biochem.* **4,** 1–45
11. Bressan, G. M., Castellani, I., Giro, M. G., Volpin, D., Fornieri, C., and Ronchetti, P. (1983) *J. Ultrastruct. Res.* **82,** 335–340
12. Narayanan, A. S., Page, R. C., Kuzan, F., and Cooper, C. G. (1978) *Biochem. J.* **173,** 857–862
13. Prosser, I. W., and Mecham, R. P. (1988) in *Self-assembling Architecture* (Varner, J. E., ed) pp. 1–23, Alan R. Liss, Inc., New York
14. Wu, W. J., Vrhovski, B., and Weiss, A. S. (1999) *J. Biol. Chem.* **274,** 21719–21724
15. Laemmli, U. K. (1970) *Nature* **222,** 680–685
16. Milthorpe, B. K., Jeffrey, P. D., and Nichol, L. W. (1975) *Biophys. Chem.* **3,** 169–176
17. Ralston, G. B., and Morris, M. B. (1992) in *Analytical Ultracentrifugation in Biochemistry and Polymer Science* (Harding, S. E., Rowe, A. J., and Horton, J. C., eds) pp. 253–274, The Royal Society of Chemistry, Cambridge, UK
18. Laue, T. M., Shah, B. D., Ridgeway, T. M., and Pelletier, S. L. (1992) in *Analytical Ultracentrifugation in Biochemistry and Polymer Science* (Harding, S. E., Rowe, A. J., and Horton, J. C., eds) pp. 90–125, The Royal Society of Chemistry, Cambridge, UK
19. Johnson, M. L., Correia, J. J., Yphantis, D. A., and Halvorson, H. R. (1981) *Biophys. J.* **36,** 575–588
20. Teller, D. C. (1973) *Methods Enzymol.* **27,** 346–441
21. Stafford, W. F., III. (1994) in *Modern Analytical Ultracentrifugation* (Schuster, T. M., and Laue, T. M., eds) pp. 119–137, Birkhauser Boston, Inc., Cambridge, MA
22. Philo, J. S. (1996) *Biophys. J.* **72,** 435–444
23. van Holde, K. S. (1971) *Physical Biochemistry,* pp. 79–121, Prentice-Hall, Englewood Cliffs, NJ
24. Torres, A. M., Taurins, A. T., Regan, D. G., Chapman, B. E., and Kuchel, P. W. (1998) *J. Magn. Reson.* **138,** 135–143
25. Sørland, G. H., Seland, J. G., Krane, J., and Anthonsen, H. W. (2000) *J. Magn. Reson.* **142,** 132–135
26. Mills, R. (1973) *J. Phys. Chem.* **77,** 685–688
27. Stejskal, E. O., and Tanner, J. E. (1965) *J. Chem. Phys.* **42,** 288–292
28. Tyrrell, H. J. V., and Harris, K. R. (1984) *Diffusion in Liquids: A Theoretical and Experimental Study,* Butterworths, London
29. Kirkwood, J. G., and Riseman, J. (1967) in *Macromolecules* (Auer, P. L., ed) pp. 67–80, Gordon and Breach Science Publishers, Inc., New York
30. Riseman, J., and Kirkwood, J. G. (1967) in *Macromolecules* (Auer, P. L., ed) pp. 96–106, Gordon and Breach Science Publishers, Inc., New York
31. Cooke, R., and Kuntz, I. D. (1974) *Annu. Rev. Biophys. Bioeng.* **3,** 95–126
32. Philo, J. S. (1994) in *Modern Analytical Ultracentrifugation* (Schuster, T. M., and Laue, T. M., eds) pp. 156–170, Birkhauser Boston, Inc., Cambridge, MA
33. Claverie, J.-M., Dreux, H., and Cohen, R. (1975) *Biopolymers* **14,** 1685–1700
34. Oosawa, F., and Asakura, S. (1975) *Thermodynamics of the Polymerization of Protein,* pp. 25–40, Academic Press, London
35. Attri, A. K., Lewis, M. S., and Korn, E. D. (1991) *J. Biol. Chem.* **266,** 6815–6824
36. Morris, M. B., and Ralston, G. B. (1994) in *Subcellular Biochemistry* (Hilderson, H. J., and Ralston, G. B., eds) Vol. 23, pp. 25–82, Plenum Publishing Corp., New York
37. Creeth, J. M., and Knight, C. G. (1965) *Biochim. Biophys. Acta* **102,** 549–558
38. Ralston, G. B. (1976) *Biochim. Biophys. Acta* **455,** 163–172

---

[3] S. A. Jensen and A. S. Weiss, unpublished data.

39. Kumosinski, T. F., and Pessen, H. (1985) *Methods Enzymol.* **117,** 154–182
40. Mecham, R. P., and Heuser, J. E. (1991) in *Cell Biology of Extracellular Matrix* (Hay, E. D., ed) 2nd Ed., pp. 79–109, Plenum Publishing Corp., New York
41. Schein, J., Carpousis, A., and Rosenbloom, J. (1977) *Adv. Exp. Med. Biol.* **79,** 727–740
42. Callaghan, P. T., and Pinder, D. N. (1983) *Macromolecules* **16,** 968–973
43. Oosawa, F., and Kasai, M. (1962) *J. Mol. Biol.* **4,** 10–21
44. Andreu, J. M., and Timasheff, S. N. (1986) *Methods Enzymol.* **130,** 47–59
45. Kaibara, K., Watanabe, T., and Miyakawa, K. (2000) *Biopolymers* **53,** 369–379
46. Ralston, G. B. (1990) *J. Chem. Educ.* **67,** 857–860
47. Parkinson, E. J., Morris, M. B., and Bastiras, S. (2000) *Biochemistry* **39,** 12345–12354
48. Johnson, M. L., and Yphantis, D. A. (1978) *Biochemistry* **17,** 1448–1455
49. Morris, M., and Ralston, G. B. (1989) *Biochemistry* **28,** 8561–8567
50. Tanford, C. (1961) *Physical Chemistry of Macromolecules,* pp. 526–586, Wiley, New York

PAPER V

Simulations of Molecular Diffusion in Lattices of Cells: Insights for NMR of Red Blood Cells

David G. Regan and Philip W. Kuchel

School of Molecular and Microbial Biosciences, University of Sydney, New South Wales 2006, Australia

ABSTRACT   The pulsed field-gradient spin-echo (PGSE) nuclear magnetic resonance (NMR) experiment, conducted on a suspension of red blood cells (RBC) in a strong magnetic field yields a q-space plot consisting of a series of maxima and minima. This is mathematically analogous to a classical optical diffraction pattern. The method provides a noninvasive and novel means of characterizing cell suspensions that is sensitive to changes in cell shape and packing density. The positions of the features in a q-space plot characterize the rate of exchange across the membrane, cell dimensions, and packing density. A diffusion tensor, containing information regarding the diffusion anisotropy of the system, can also be derived from the PGSE NMR data. In this study, we carried out Monte Carlo simulations of diffusion in suspensions of "virtual" cells that had either biconcave disc (as in RBC) or oblate spheroid geometry. The simulations were performed in a PGSE NMR context thus enabling predictions of q-space and diffusion tensor data. The simulated data were compared with those from real PGSE NMR diffusion experiments on RBC suspensions that had a range of hematocrit values. Methods that facilitate the processing of q-space data were also developed.

INTRODUCTION

Pulsed magnetic field-gradients can be used in nuclear magnetic resonance (NMR) experiments to encode spatial information in spin-magnetization to measure positional displacement. The analogy of the resulting spatial coherences seen in NMR data to optical diffraction was first pointed out by Mansfield and Grannell (1973). Cory and Garroway (1990) showed that pulsed field-gradient spin-echo (PGSE) NMR diffusion measurements in heterogeneous systems can be used to obtain a displacement profile of molecules in a liquid, allowing the delineation of features of compartments too small to be observed using conventional NMR imaging. Callaghan et al. (1991) demonstrated interference-like effects in PGSE NMR diffusion studies of fluids in porous media and recently reviewed the spatial coherence phenomena arising from these experiments (Callaghan et al., 1999). We have conducted PGSE NMR diffusion studies of red blood cell (RBC) suspensions and showed that diffusion–diffraction and diffusion–interference of water occurs; this was used to show the alignment of RBC in the static magnetic field of the spectrometer and to estimate cell dimensions, detect shape changes with time, and to estimate membrane transport characteristics (Kuchel et al., 1997, 2000; Torres et al., 1998, 1999). It has been independently demonstrated that RBC align in a strong magnetic field with their disc planes parallel to the magnetic field (Higashi et al., 1993) so this was important in the design of the diffusion-simulation models used herein (see Materials and Methods).

Diffraction-like effects from PGSE NMR diffusion experiments can be visualized by plotting the relative signal intensities as a function of the spatial wave vector $\mathbf{q}$, where $\mathbf{q} = (2\pi)^{-1}\gamma\mathbf{g}\delta$, and where γ is the magnetogyric ratio of the observed nucleus, $\mathbf{g}$ is the magnetic field gradient, and δ is the duration of each of the magnetic field-gradient pulses used in the experiment. The resulting graph (q-space plot), from an RBC suspension consists of a series of maxima and minima whose positions in q space can be related to average cell dimensions and the average spacing of the extracellular cavities or "pores" (Torres et al., 1998, 1999). The positions of these features may also change when there is a change in the rate of exchange of diffusant across the cell membrane (Kuchel et al., 1997).

We have previously used simulations of diffusion in an RBC suspension, in the PGSE NMR context, to aid in the assignment of q-space features to particular modes of diffusion (Torres et al., 1999). Here we extend this work and demonstrate that these simulations provide further insights that are useful for the interpretation of q-space and diffusion tensor data from RBC suspensions. Specifically, we show that the q-space and diffusion tensor data contain information relating to the packing density of the cells in a suspension and the mean cell geometry. This study, therefore, extends the methodology and concepts used in interpreting data from PGSE NMR diffusion experiments on RBC suspensions and potentially in analogous cellular systems.

MATERIALS AND METHODS

Simulations

Individual computer models were developed to simulate diffusion in a suspension of biconcave discs (Program I), and to simulate diffusion in a suspension of oblate spheroids (Program II). (All programs described in this report may be obtained from DGR at d.regan@mmb.usyd.edu.au.) These models enable the simulation of diffusion during a standard PGSE
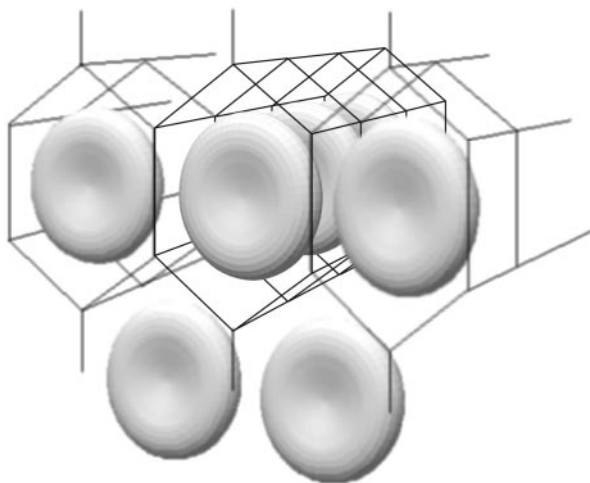

FIGURE 1 Hexagonal lattice of virtual cells. The figure illustrates the arrangement of cells (shown here as biconcave discs) used in the simulations of diffusion in the 3D infinite tessellation. The latter was effectively generated by the application of periodic boundary conditions to a unit cell.
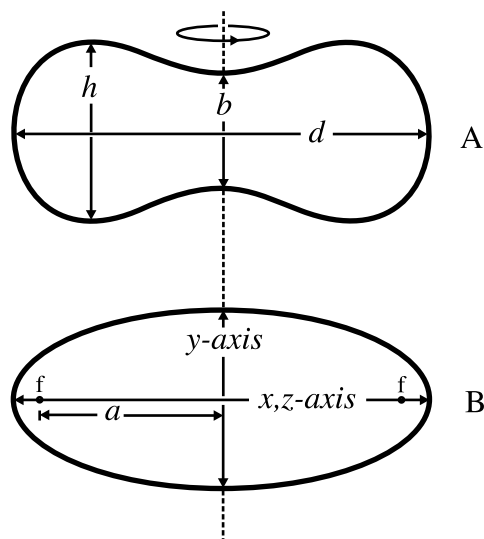

FIGURE 2 Cell geometry. (A) Two-dimensional representation of a biconcave disc whose shape and dimensions are defined by the parameters b, d, and h approximating those of a human red blood cell. (B) Two-dimensional representation of an oblate spheroid whose shape is defined by the parameters a (the distance from the foci, f, to the center of the oblate spheroid) and η (not shown) whose values are calculated as a function of the x-, y-, and z-semi-axis values using Eq. 2 and Eq. 3. Rotation around the axis indicated by the dotted line generates the 3D cell shapes used in the simulations.

NMR experiment (Kuchel et al., 1997; Torres et al., 1998) and produce an array of signal intensities corresponding to the respective field gradient strengths specified for a simulated experiment.

The programs use a Monte Carlo technique to simulate diffusion in a three-dimensional (3D) hexagonal lattice of "virtual" cells (see Fig. 1) as described previously (Lennon and Kuchel, 1994a,b; Torres et al., 1998). The uniform arrangement of virtual cells in a hexagonal lattice, having an order parameter of unity, is justified on the basis that real RBC align in the magnetic field, and that it was the intention to design a canonical pure system to form the basis of the interpretation of experimental q-space data (see Discussion).

Simulations were performed for ensembles of up to 10^8 noninteracting point molecules on a 64 processor SGI Origin 2400 supercomputer (APAC National Facility, Australian National Univ., Canberra, Australia). The intrinsic ensemble nature of the calculations allowed ensembles to be split into smaller "packets" of ~200,000 point-molecule trajectories, which could be distributed across multiple processors. In this way the parallel capability of the supercomputer was used. When the full complement of trajectories was completed, the results were summed and averaged.

The simulations were of diffusion in a 3D hexagonal lattice of cells having either biconcave disc (Fig. 2 A) or oblate spheroid (Fig. 2 B) geometry. The analysis was expedited by invoking a "unit cell," consisting of a regular hexagonal prism containing a cell, centered on the Cartesian origin, and applying periodic boundary conditions, thereby simulating an infinite tessellation. (In all simulations and experiments discussed in this report, a Cartesian coordinate system was used such that the z axis was aligned with the static magnetic field, $\mathbf{B}_0$, of the NMR spectrometer.) A random number generator and a random binary-digit generator were used to determine a random starting position for the trajectory of each point molecule (Regan and Kuchel, 2000). The same random number and random binary-digit generators were used to test for membrane transition and to choose random jump directions, respectively.

The biconcave disc in Program I was represented by a degree-4 equation in Cartesian coordinates (Kuchel and Fackerell, 1999). The shape of the biconcave disc (Fig. 2 A) was defined by the three parameters: b, thickness in the dimpled region; h, maximum thickness; and d, main diameter, whose respective values of 1.0×10^{-6} m, 2.12×10^{-6} m, and 8.0×10^{-6} m were assigned to closely approach the shape of human RBC and to yield the known mean volume of human RBC of 8.6×10^{-17} m^3 (Dacie and Lewis, 1975). The points of intersection of point-molecule trajectories with the

biconcave disc were calculated using a Newton–Raphson algorithm (Regan and Kuchel, 2000).

The oblate spheroid used in Program II is described by the function

$$\frac{x^2}{a^2\cosh^2\eta} + \frac{y^2}{a^2\cosh^2\eta} + \frac{z^2}{a^2\sinh^2\eta} = 1, \qquad (1)$$

where, a is the distance of the foci from the center of the oblate spheroid (Fig. 2 B), and the oblate spheroidal coordinate η is a constant (Moon and Spencer, 1988). The values of a and η were calculated, as functions of the specified values for the oblate spheroid semi-axes, using the formulae

$$\eta = \frac{\ln((1 + r)/(1 - r))}{2} \qquad r = \frac{x}{y}; \qquad (2)$$

$$a = y/\sinh \eta, \qquad (3)$$

where x, y, and z are the values of the oblate spheroid semi-axes (Fig. 2 B) for the body centered at the origin of a Cartesian coordinate system. The x, y, and z semi-axes were assigned values of 8.0×10^{-6} m, 2.0×10^{-6} m, and 8.0×10^{-6} m, respectively. These values were chosen to match the overall dimensions of the biconcave disc but yielded a smaller volume of 6.7×10^{-17} m^3.

Another characteristic of a virtual cell that is useful for interpreting PGSE NMR data is the mean barrier separation in the cell. This value was calculated for both cell types in the x, z, and y directions. The calculation was performed by assigning a random coordinate inside the cell and calculating the length of the chord, in the relevant direction (x, z, or y), that intersected this point. This process was repeated for 10^7 random coordinates and the average chord length calculated. The mean barrier separation in the x, z, and y directions for the biconcave disc and the oblate spheroid were 5.8×10^{-6} m, 5.8×10^{-6} m, and 1.8×10^{-6} m, and 6.0×10^{-6} m, 6.0×10^{-6} m, and 1.5×10^{-6} m, respectively.

For each cell type, the following simulations were performed: diffusant (water) confined by an impermeable membrane to the intracellular space; diffusant confined by an impermeable membrane to the extracellular space, and packing density or hematocrit (Ht, the volume fraction of the unit cell that is occupied by a cell) set to either 0.3, 0.4, or 0.5; and diffusant in both the intracellular and extracellular spaces and able to exchange through a semi-permeable membrane, with hematocrits (Ht) set to 0.3, 0.4, or 0.5.

Intracellular (D_{in}) and extracellular (D_{out}) diffusion coefficients were assigned values of 1.6×10^{-9} m^{2}s^{-1} and 8.0×10^{-10} m^{2}s^{-1}, respectively, in accordance with preliminary estimates we have obtained experimentally (using standard PGSE NMR methods) for water in human RBC suspensions. The length of a jump, s, was calculated using the Einstein diffusion equation (Tanford, 1961),

$$\langle s^2 \rangle = 2D_{in/out}t, \qquad (4)$$

where D is the diffusion coefficient in the relevant compartment (i.e., D_{in} or D_{out}), and t is the duration of a single jump (as determined from the assignment of other simulation parameters). For simulations in which the membrane was semi-permeable, the permeability (P_d) was assigned a value of 6.1×10^{-5} m s^{-1} as has been determined experimentally for human RBC (Benga et al., 1990). For simulations in which the membrane was required to be impermeable, P_d was set to zero.

We have previously demonstrated that the probability of transition across the membrane (tp) when the membrane is intersected by a point-molecule trajectory, in the context of the simulations described here, is related to s (jump length) and P_d by (Regan and Kuchel, 2000)

$$tp = P_d s / D_{in/out}. \qquad (5)$$

The value of tp, therefore, depends on whether transition across the membrane is from the intra- or extracellular space.

The parameter values for the simulations were chosen to be identical to those used for the PGSE NMR experiments on RBC suspensions described in the Results. The PGSE NMR parameters for all simulations were as follows: field-gradient pulse duration, $\delta = 2$ ms; time interval separating field-gradient pulses, $\Delta = 20$ ms; the magnitude of the field-gradient, g, was sequentially incremented in 96 steps from 0.0 to 9.9 T m^{-1}; proton magnetogyric ratio, $\gamma = 2.675 \times 10^8$ radian T^{-1}. The phase shifts accumulated during the total diffusion time ($\delta + \Delta$) for all point-molecule trajectories were summed and averaged, and the signal intensity calculated for each value of g.

It has been shown that magnetic susceptibility differences between the interior and exterior of oxygenated or carbonmonoxygenated RBC in a suspension are negligible (Endre et al., 1984). Hence the model did not incorporate differences in PGSE signal intensity that might ordinarily be expected to occur in a system that is heterogeneous in magnetic susceptibility and hence magnetic field.

PGSE NMR experiments

PGSE NMR diffusion experiments were conducted on RBC suspensions having HT values of 0.2, 0.3, 0.4, 0.5, and 0.6. The general methods (pulse sequences, etc.) used for conducting these experiments and for preparing RBC suspensions were as described previously (Kuchel et al., 1997; Torres et al., 1998, 1999).

The experiments were conducted at 298 K on a Bruker AMX400 spectrometer (Karlsruhe, Germany) with an Oxford Instruments 9.4 T vertical wide-bore magnet (Oxford, UK), using a Bruker 10 T m^{-1}, z-axis gradient-diffusion probe. Identical pulse-sequence parameters were used for all experiments as follows: field-gradient pulse duration, $\delta = 2$ ms; time interval separating gradient pulses, $\Delta = 20$ ms; 32 transients per spectrum. The magnitude of the field-gradient was incremented from 0.001 to 9.9 T m^{-1} in 32 equal steps. (Unless the first spectrum [corresponding to the smallest field gradient] was acquired with a small nonzero gradient, its phase was substantially different from the rest in the series; therefore a

value close to zero (0.01 T m^{-1}) was used.) The gradients were calibrated using the known diffusion coefficient of water in an isotropic and unbounded region (Mills, 1973).

The signal intensity was measured as the integral of the water resonance after automatic phase and baseline correction. Signal intensities were normalized with respect to that of the first spectrum before q-space analysis (see Data Analysis).

Data Analysis

q-Space analysis

q-Space plots were generated using both Origin (Microcal Software, Northampton, MA) and MATLAB (The Mathworks, Natick, MA) from simulated or experimental PGSE NMR data by plotting the normalized signal intensities as a function of the magnitude of **q**. A semi-logarithmic scale (logarithmic in the ordinate) was used to improve visualization of the features (maxima and minima) of the plots. Further enhancement was achieved by either applying a cubic spline to the data, or fitting a polynomial and interpolating points to increase their number from 96 to 1000. Simulated data invariably contained negative values at the extreme minimal intensities (see Discussion for an explanation of this phenomenon); these points could not be plotted on a logarithmic scale and thus resulted in gaps in the plots (see Figs. 3–6).

A combination of methods was used to determine, as precisely as possible, the positions of maxima and minima in q-space plots (the reciprocals of which correspond to mean dynamic displacements). Maxima and minima were determined, to a first approximation, by reading the values directly from the plot using the tools available in the respective plotting programs (Origin or MATLAB). This was not possible when data points were missing in semi-logarithmic plots due to negative signal intensities. This problem was obviated by replotting the absolute values of the signal intensities, again on a semi-logarithmic scale, so that regions containing negative values appeared as inverted peaks with q values that could be readily determined. Maximum and minimum values were then more closely pinpointed by aligning the putative values with maxima and minima in the plots of the first and second derivatives of the data (generated in MATLAB). In most cases, it was possible to determine accurately the positions of at least the first two maxima and minima (see Error Analysis). This method can be applied in the analysis of q-space data for diffusion along any axis but was carried out here for diffusion in the z direction only.

Diffusion tensor calculations

A program was written in MATLAB to calculate the terms of the diffusion tensor from PGSE NMR data (either real or simulated) according to the method of Kuchel et al. (2000). The program takes the normalized signal intensities and their corresponding gradient values (in each of the x, y, z, xy, xz, yz, and xyz directions) as inputs. Linear regression calculates initial estimates of the terms of the diffusion tensor, which are then used to calculate the final values and confidence intervals by nonlinear regression. In all cases, five signal intensities were included in the analysis (the q-space plot is approximately a single exponential over this range of gradient strengths), starting at the second value (i.e., points 2–6; the first point was eliminated because it corresponded to $g = 0$ and resulted in "divide by zero"). The diagonal terms of the resulting diffusion tensor provided estimates of the apparent diffusion coefficients (D_{app}) in the x, y, and z directions. Diffusion tensor calculations were only performed for simulated data because the experimental data were limited to diffusion in the z direction only.

Fourier transform analysis

The Fourier transform of q-space data is, in most cases, approximately Gaussian (see Discussion) and thus yields an approximation of the trans-

lational displacement probability (Cory and Garroway, 1990). The width-at-half-height, $\Delta w_{1/2}$, of the peak in the Fourier transform plot can therefore be related to the effective root mean square displacement (RMSD), σ, by (Bailey, 1995)

$$\sigma = \frac{\Delta w_{1/2}}{2[2 \ln 2]^{1/2}} . \qquad (6)$$

Plotting the Fourier transform, and calculation of the width-at-half-height, was achieved by means of a program written in MATLAB. The program displays a plot of the transformed data, that have been zero-filled where necessary to ensure that the number of data points is a power of two, and allows the height of the peak to be read directly from the plot. This step improves the efficiency of the fast Fourier transform algorithm. The width-at-half-height is calculated using a cubic interpolation function that returns the value of the abscissa at half the height measured in the previous step. This value is then doubled (since only positive displacements are plotted) to yield the effective RMSD.

Error analysis

Both linear and nonlinear regression analyses were conducted in Origin and MATLAB. Error analysis of q-space plots, as it affects the estimation of critical values of q and their uncertainty, is influenced by two factors: the intrinsic signal-to-noise of the NMR spectra, and the resolution in q that is determined by the interval between q values, that are under experimental control. This matter has been discussed previously (Torres et al., 1999) and elaborated upon recently (Benga et al., 2000). It is important to note that, under the experimental conditions used in the present work, the uncertainty in the estimates was dominated by the resolution in q; in other words, the constant differences in consecutive q values that were specified in each experiment determined the spatial resolution of the imaging method.

RESULTS

General

In this study, we conducted simulations of diffusion in lattices of virtual cells having either biconcave disc or oblate spheroidal geometry. Simulations were conducted under two conditions: water confined to the intra- and extracellular spaces in the absence of exchange, and water exchanging between the intra- and extracellular regions at a rate that was determined by $P_{d} = 6.1 \times 10^{-5}$ m s^{-1}. In all cases, except where water was confined to the intracellular region, simulations were conducted at Ht values of 0.3, 0.4, and 0.5. In addition, a series of PGSE NMR experiments were conducted on real RBC suspensions at Ht values of 0.2, 0.3, 0.4, 0.5, and 0.6, at 298 K. To facilitate comparisons with real data sets, the simulation parameters were chosen to be identical to those used in the real experiments.

Simulations: exchange off

Intracellular diffusion

The q-space plots for simulation of diffusion of water inside biconcave discs and oblate spheroids (no exchange across the membrane) are shown in Fig. 3. Signal intensities at given values of q were initially higher for the oblate spher-
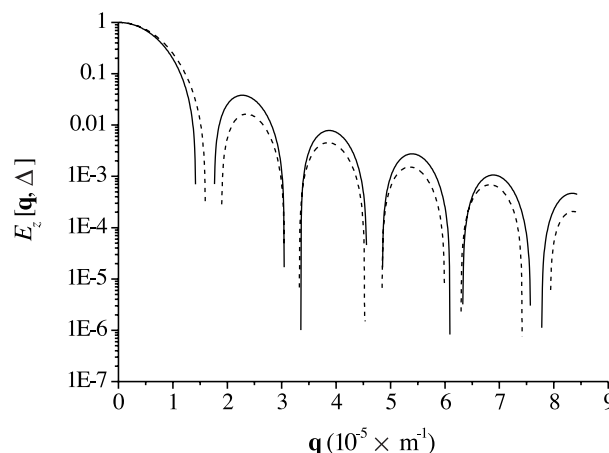

FIGURE 3 Simulation of diffusion in the intracellular spaces. q-Space plots derived from simulations of water diffusion inside biconcave discs (*solid line*) and oblate spheroids (*dashed line*). Point molecules were confined to the intracellular space by starting all trajectories inside the cell and setting P_{d} to zero.

oid but were lower for the second and subsequent peaks. The apparent diffusion coefficients (D_{app}), estimated from diffusion tensor analysis (see Table 1), were smaller for the oblate spheroid than for the biconcave disc in each of the respective x, y, and z directions. For each cell type individually, however, the apparent diffusion coefficients measured in the x and z directions were identical within the stated error range. A similar trend was observed for the RMSD calculated from the Fourier transform of the q-space data (see Table 2): RMSD values were smaller for the oblate spheroid than for the biconcave disc in their respective directions and, in each case, had virtually identical values in the x, z, and xz directions as anticipated. The smallest values of D_{app} and RMSD for both cell types were observed in the y direction. The critical values in q space are given in Table 3. Although the relevant values in this case are the minima, which we have previously shown can be related to mean cell dimensions (Benga et al., 2000; Torres et al., 1998), both maxima and minima are given for completeness. The q value of the first minimum was smaller for the biconcave disc than for the oblate spheroid, corresponding to a larger dynamic displacement (q^{-1}), but there was no significant difference in the positions of the second minimum.

Extracellular diffusion

Figure 4 shows the q-space plots for diffusion of water in the extracellular region of suspensions of oblate spheroids (*A*) and biconcave discs (*B*) at Ht values of 0.3, 0.4, and 0.5. The figure illustrates two important features: a shift in the positions of the peaks to higher q values as Ht was increased and, with respect to the first peak, higher signal intensities as Ht was increased. Table 3 confirms the shift to higher q values (smaller dynamic displacements) as Ht is increased;

TABLE 1 Apparent diffusion coefficients of water, from simulated data, as a function of packing density of the cells and the direction of the applied magnetic field gradient

Exchange*	Ht	Biconcave Disc D_{app} ($10^9 \times$ m² s⁻¹)			Oblate Spheroid D_{app} ($10^9 \times$ m² s⁻¹)		
		D_{xx}	D_{yy}	D_{zz}	D_{xx}	D_{yy}	D_{zz}
On	0.3	1.81 ± 0.14	0.95 ± 0.07	1.81 ± 0.14	1.82 ± 0.12	0.84 ± 0.05	1.82 ± 0.12
	0.4	1.52 ± 0.12	0.73 ± 0.06	1.52 ± 0.12	1.56 ± 0.10	0.62 ± 0.05	1.56 ± 0.10
	0.5	1.28 ± 0.10	0.56 ± 0.05	1.28 ± 0.10	1.33 ± 0.08	0.46 ± 0.04	1.33 ± 0.08
Off$_{extra}$	0.3	2.73 ± 0.07	1.43 ± 0.03	2.74 ± 0.07	2.70 ± 0.06	1.22 ± 0.02	2.70 ± 0.06
	0.4	2.61 ± 0.06	1.26 ± 0.03	2.62 ± 0.06	2.63 ± 0.06	1.03 ± 0.02	2.64 ± 0.06
	0.5	2.53 ± 0.06	1.15 ± 0.02	2.54 ± 0.06	2.58 ± 0.06	0.88 ± 0.02	2.59 ± 0.06
Off$_{intra}$		0.18 ± 0.0009	0.0047 ± 0.0007	0.18 ± 0.0009	0.16 ± 0.0006	0.0026 ± 0.0005	0.16 ± 0.0006

Values were obtained using diffusion tensor analysis.

*In this and subsequent tables: exchange "off" refers to simulations in which the diffusant was confined to either the intra- or extracellular region as indicated by the subscript; exchange "on" refers to simulations where exchange was allowed to occur between the two regions; and "endogenous" (Tables 2 and 3 only) refers to real PGSE NMR experiments on RBC suspensions in which exchange was occurring naturally at a rate determined by $P_d = 6.1 \times 10^{-5}$ m s⁻¹. Note also that a Ht value is not relevant for simulations where diffusion was confined to the intracellular space, where it is independent of the packing density, hence no value is given. The errors associated with the estimates of D correspond to ± one standard deviation.

in this case, the relevant values are the positions of the maxima because we have shown these to be related to the mean spacing of cells in the suspension (Torres et al., 1999). At all three Ht values, the corresponding dynamic displacements (q^{-1}) were higher for the biconcave discs than for the oblate spheroids. The apparent diffusion coefficients (Table 1) decreased as Ht was increased and, although of similar magnitude for both cell types in the x and z directions (when associated errors were considered), they were larger for the biconcave discs in the y direction. RMSD values (Table 2) were similarly decreased with increasing Ht and were of generally larger magnitude for the biconcave discs.

Simulations: exchange on

The results of simulations in which water was diffusing in both the intra- and extracellular regions and exchanging across the membrane are shown in Fig. 5. Signal intensities at given q values became larger as Ht was increased, and the pore-hopping shoulder (in the region of $q = 0.75 \times 10^5$ m⁻¹) shifted to higher q values and became less pronounced.

q-Space plots for the two cell types when the diffusion was measured in the x, y, and z directions are compared in Fig. 6. Points to note are: 1) the overall increase in signal

TABLE 2 Root mean square displacements estimated from Fourier transform analysis of q-space plots from simulated and experimental data

System	Exchange	Ht	RMSD ($10^6 \times$ m)						
			x	y	z	xy	xz	yz	xyz
Oblate Spheroid									
	On	0.3	13.74	6.04	13.54	11.18	13.63	11.11	11.92
		0.4	12.34	4.44	12.16	9.72	11.27	9.66	10.63
		0.5	11.13	3.63	11.74	8.56	11.08	8.50	9.43
	Off$_{extra}$	0.3	18.65	4.41	18.69	15.57	18.70	15.61	16.61
		0.4	18.33	3.18	18.46	15.09	18.47	15.14	16.32
		0.5	18.17	0.76	18.14	14.73	18.24	14.73	16.01
	Off$_{intra}$		4.95	0.39	4.95	3.49	4.95	3.49	4.06
Biconcave Disc									
	On	0.3	13.37	4.89	13.49	11.00	13.42	10.97	11.82
		0.4	11.89	3.59	11.78	9.40	11.89	9.42	10.30
		0.5	10.54	1.20	10.17	8.22	10.55	8.17	9.01
	Off$_{extra}$	0.3	18.56	5.21	18.98	16.08	18.98	16.08	17.01
		0.4	17.87	3.22	18.34	15.56	18.54	15.51	16.50
		0.5	17.12	1.73	17.98	15.14	18.13	15.10	16.17
	Off$_{intra}$		5.25	0.70	5.25	3.73	5.25	3.72	4.30
RBC Suspension									
	Endogenous	0.2			14.51				
		0.3			13.40				
		0.4			12.43				
		0.5			11.13				
		0.6			9.67				

TABLE 3 q-Values and dynamic displacements measured in the z direction from q-space plots of simulated and experimental data*

| | | | $q_{1,min}$ | | $q_{2,min}$ | | $q_{1,max}$ | | $q_{2,max}$ | |
System	Exchange	Ht	q	q^{-1}	q	q^{-1}	q	q^{-1}	q	q^{-1}
Oblate Spheroid										
	On	0.3	1.75	5.70	3.12	3.21	0.72	13.95	2.20	4.54
		0.4	1.77	5.65	3.24	3.09	0.75	13.31	2.31	4.34
		0.5	1.51	6.62	3.22	3.10	0.79	12.72	2.39	4.18
	Off$_{extra}$	0.3	0.96	10.43	2.20	4.54	1.32	7.57	2.57	3.90
		0.4	1.01	9.90	2.31	4.34	1.39	7.19	2.70	3.70
		0.5	1.05	9.57	2.43	4.12	1.43	7.02	2.82	3.54
	Off$_{intra}$		1.75	5.70	3.19	3.14	2.36	4.24	3.86	2.59
Biconcave Disc										
	On	0.3	1.62	6.19	3.34	2.99	0.68	14.66	2.10	4.76
		0.4	1.62	6.19	3.17	3.15	0.73	13.62	2.19	4.58
		0.5	1.46	6.85	3.17	3.15	0.77	13.01	2.27	4.40
	Off$_{extra}$	0.3	0.89	11.24	2.05	4.89	1.27	7.88	2.44	4.09
		0.4	0.96	10.4	2.19	4.58	1.34	7.47	2.57	3.90
		0.5	1.01	9.90	2.27	4.40	1.39	7.19	2.69	3.72
	Off$_{intra}$		1.58	6.33	3.18	3.14	2.27	4.40	3.88	2.58
RBC Suspension										
	Endogenous	0.2	1.88	5.31			0.96	10.40	2.29	4.37
		0.3	1.87	5.36			0.97	10.35	2.25	4.44
		0.4	1.83	5.47			0.97	10.29	2.21	4.53
		0.5	1.83	5.47			0.97	10.29	2.24	4.47
		0.6	1.82	5.50			0.95	10.56	2.24	4.47

q-values (q; $10^{-5} \times m^{-1}$) and corresponding dynamic displacements (q^{-1}; $10^6 \times m$)

*Because q^{-1} was rounded to two decimal places from its original calculated value (i.e., not from the rounded value of q), two table entries may have the same value of q and slightly different values of q^{-1}.

attenuation at given q values for the oblate spheroid relative to the biconcave disc; 2) a shift in the positions of coherence maxima to higher q values for the oblate spheroid; 3) a much lesser degree of signal attenuation, for a given q value, in the y direction than in the x and z directions for both cell types; and 4) the appearance of some additional critical points (Fig. 6 A, $q = 2.3 \times 10^5$ m^{-1} and 4.2×10^5 m^{-1}, and relative to Fig. 6 C) in the plots for the x direction, which were otherwise very similar to those for the z direction for both cell types.

The apparent diffusion coefficients estimated from the diffusion tensor analysis (Table 1) decreased with increasing Ht. In the x and z directions, D_{app} values were virtually identical for both cell types but were larger for the biconcave disc in the y direction. In contrast, RMSD values (Table 2) were higher for the oblate spheroid than for the biconcave disc at equivalent Ht values. However, the same trend of decreasing RMSD with increasing Ht was observed for both cell types. Although no clear trend was evident in the positions of the first two diffraction minima ($q_{1,min}$ and $q_{2,min}$) for either cell type, the positions of the pore-hopping shoulder ($q_{1,max}$) corresponded to smaller dynamic displacements as Ht was increased and the respective values were smaller for the biconcave disc than for the oblate spheroid.

PGSE NMR experiments

The q-space plots of the PGSE NMR data obtained from real RBC suspensions are shown in Fig. 7. These plots illustrate two very clear results: signal intensities decreased at a given q value with decreasing Ht, and the point of inflection discernible at $q = \sim 1.0 \times 10^5$ m^{-1} was more pronounced at lower Ht.

Note that the high-power diffusion probe used in these experiments only allowed for the application of the magnetic field gradient coaxially with the static field (i.e., in the z direction). This limitation precluded the calculation of a diffusion tensor because this requires the gradient to be applied in at least six directions. In addition, the gradient values used in the experiment were restricted to a range over which it was possible to obtain sufficient signal-to-noise. Although it was possible to observe higher-order coherences with higher gradients, estimation of displacements from the data became increasingly error prone.

Fourier transform analysis of these data (Table 2) clearly showed that as Ht was increased the values of RMSD decreased. The relationship between RMSD and Ht was remarkably linear as evidenced by linear regression onto the data, which yielded the expression RMSD = $(1.70 \pm 0.02) \times 10^7 - ((1.20 \pm 0.05) \times$ Ht$)$, with a correlation
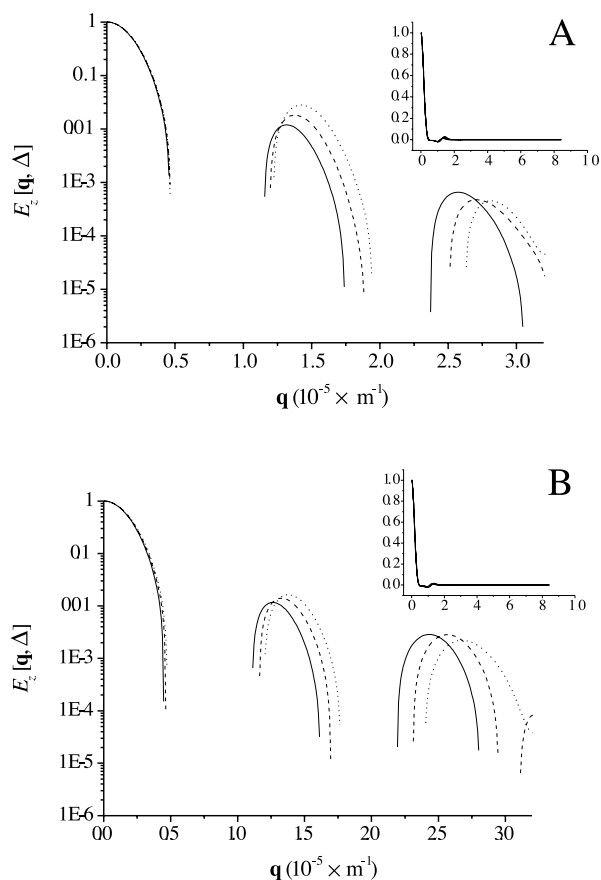
FIGURE 4   Simulation of diffusion in the extracellular spaces. *q*-Space plots derived from simulations of water diffusion in the extracellular region measured in the *z* direction in (*A*) a lattice of oblate spheroids, and (*B*) a lattice of biconcave discs. The main graphs were plotted on a semilogarithmic scale and were discontinuous in the regions containing (minutely) negative signal intensities. The insets were plotted on normal axes to show that the data were continuous over the entire range of **q**. The simulations were performed using a range of packing densities: Ht = 0.3 (*solid line*); Ht = 0.4 (*dashed line*); and Ht = 0.5 (*dotted line*). Molecules studied were confined to the extracellular space by starting all trajectories outside the cell and setting P_d to zero.

FIGURE 5   Simulations of diffusion in both the intra- and extracellular regions in (*A*) a lattice of oblate spheroids, and (*B*) a lattice of biconcave discs. The *q*-space plots were derived using measurements of diffusion of water in the *z* direction, and the exchange across the membrane occurred at a rate that was determined by $P_d = 6.1 \times 10^{-5}$ m s^{-1}. The simulations were performed using a range of packing densities: Ht = 0.3 (*solid line*); Ht = 0.4 (*dashed line*); and Ht = 0.5 (*dotted line*).

coefficient of -0.99. However, dynamic displacements calculated from *q*-space data were difficult to determine using the analytical methods that have been developed so far, and no clear trends were apparent in the values estimated. Although the dynamic displacements corresponding to $q_{1,\text{min}}$, $q_{1,\text{max}}$, and $q_{2,\text{max}}$ were smaller than the corresponding values for the simulated data from biconcave discs and oblate spheroids, they were of comparable magnitude.

DISCUSSION

Simulations: exchange off

We have considered two cases of simulation in which exchange across the membrane was prevented by setting P_d to zero. The first case was where the diffusant (water) inside

the cells alone was studied. The second case was where the diffusant in the extracellular region alone was studied. In the latter case, simulations were conducted at three Ht values, 0.3, 0.4, and 0.5.

Intracellular diffusion

Figure 3 illustrates that overall signal attenuation (for diffusion in the *z* direction) for the oblate spheroid was greater than for the biconcave disc despite having a smaller volume, identical main-axis dimensions, and larger mean barrier separation in this direction. This seemingly counterintuitive result can be explained in terms of the shape of the biconcave disc. It has inward protrusions at its center that have a closest approach of 1×10^{-6} m constituting a kind of bottleneck restriction to diffusion in the *z* direction. In the initial part of the *q*-space curve in Fig. 3, the signal intensity
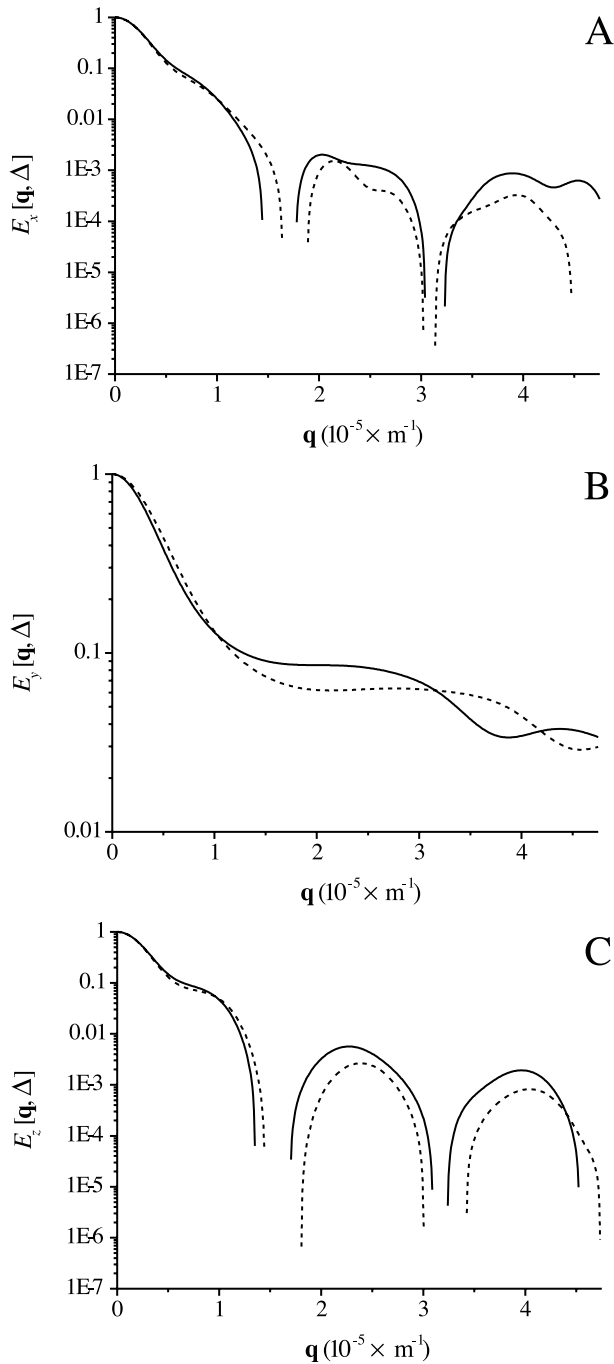
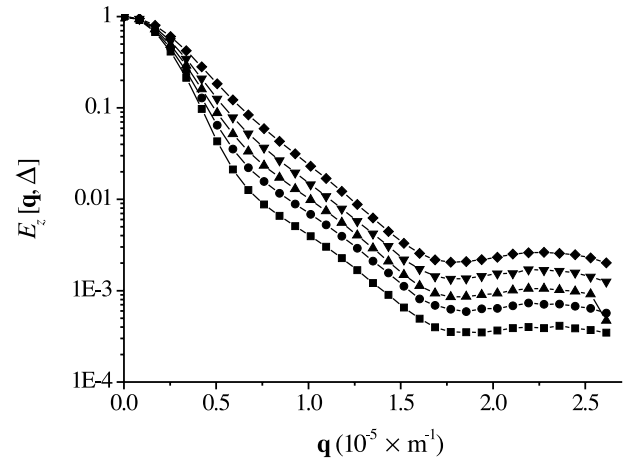FIGURE 7 Experimental q-space data from PGSE NMR experiments on RBC suspensions having Ht = 0.2 (*square*), 0.3 (*circle*), 0.4 (*triangle*), 0.5 (*inverted triangle*), and 0.6 (*diamond*). Features of particular interest are $q_{1,max}$ at $\sim 1 \times 10^5$ m^{-1} and $q_{1,min}$ at $\sim 1.75 \times 10^5$ m^{-1}.

the D_{app} values are smaller for the oblate spheroid than for the biconcave disc. For both cell types individually, these values were the same in the x and z directions, reflecting the fact that, in these directions, their dimensions are identical, and much lower in the y direction, which is the direction in which diffusion was most restricted. The smaller volume occupied by the oblate spheroid is reflected in the smaller RMSD values (Table 2) with identical values recorded for both cell types individually in the x, z, and xz directions, in which the dimensions were identical. The critical q values (Table 3) in this case are the minima ($q_{1,min}$ and $q_{2,min}$) which are related to cell dimensions. Although both cell types had identical dimensions in the z direction, and the positions of $q_{2,min}$ did indeed yield identical estimates of the dynamic displacements, the positions of $q_{1,min}$ were not identical and suggest a smaller effective mean dimension in the z direction for the oblate spheroid than for the biconcave disc. These and the RMSD values reflect the fact that, although both cell types had identical main dimensions in x and z directions, their shapes and hence their mean dimensions along these axes were not identical.

FIGURE 6 Simulated q-space plots derived for water diffusion in suspensions of biconcave discs (*solid lines*) and oblate spheroids (*dashed lines*) measured in (*A*) the x direction, (*B*) the y direction, and (*C*) the z direction. The transmembrane exchange rate was determined by $P_d = 6.1 \times 10^5$ m s^{-1} and Ht was 0.5.

is higher for the oblate spheroid than for the biconcave disc; and it was this region of the curve that was used for diffusion tensor analysis. Consequently, the apparent diffusion coefficients calculated using this method (Table 1) appear to be inconsistent with the result just described, i.e.,

Extracellular diffusion

The greater degree of signal attenuation that accompanied a decrease in Ht (see Fig. 4) was consistent with the notion that, as the compartment bounding the diffusant becomes less confining, the apparent diffusion coefficient will become larger, resulting in a more rapid attenuation of the signal in the PGSE NMR experiment. Table 1 shows that, as Ht was lowered, the apparent diffusion coefficient in the x, y, and z directions (as estimated by diffusion tensor analysis), increased for both cell types. Predictably, a decrease in Ht, and hence an increase in D_{app}, gave rise to an increase

in the RMSD calculated from the Fourier transform of the corresponding q-space plots (Table 2). Slightly higher values of RMSD estimated for the biconcave disc in most directions highlights the fact that, at equivalent Ht values, there was a greater volume available to the diffusant in this suspension because the volume of each biconcave disc was greater. The few exceptions to this observation, revealed by careful comparison of the data, are attributed to differences in the cell shapes that, in turn, give rise to differently shaped pores in the extracellular region.

The observation that, for both biconcave discs and oblate spheroids, the signal intensity at a given q value in the second peak of the q-space plot increased as Ht was decreased (i.e., opposite to the anticipated result that is observed for the first peak) is explained as follows. The position of the second peak results from a second-order effect i.e., displacement of molecules between next-nearest neighboring pores. At lower Ht values, the RMSD is larger so there is a higher probability of displacement occurring into these pores (in the observation time of the experiment) than for a higher Ht. The number of spins giving rise to this signal at low Ht will consequently be larger than the number at a higher Ht. Thus, the resulting signal intensity will be relatively higher (i.e., relative to that at higher Ht) than for diffusion between the first coordination layer of cells.

The data in Tables 1 and 2 indicate that, for the oblate spheroids, the effect of changing Ht is more dramatic for diffusion measured in the y direction than in other directions (particularly those not containing a y component). The y direction is orthogonal to the disc planes of the virtual cell and is therefore the most confining for the diffusant. Therefore, it is anticipated that relaxing the impediment to diffusion in this direction (by reducing Ht) will have a dramatic effect on the estimated apparent diffusion coefficient and thus the RMSD. This effect is less dramatic for the biconcave disc, and the reason for this can be understood as follows: The dimpled regions of the biconcave disc result in diffusion orthogonal to the disc planes being, on average, less restricted than for oblate spheroids. Hence, the effect on the RMSD of increasing the distance between the discs is less dramatic with biconcave discs.

We noted above that the critical values in the q-space plots, in this case, the pore-hopping maxima $q_{1,max}$ and $q_{2,max}$, are related to the spacing of the major extracellular pores in the array. As Ht was increased, the q values of these critical points would be expected to become larger (and their reciprocal values, the dynamic displacements, become smaller), and this was indeed the case (Table 3). A larger q value corresponds to a smaller dynamic displacement, and, as Ht was increased (i.e., the hexagonal prism containing the unit cell was made smaller), the distance between the centers of adjacent pores became smaller. The hexagonal prism enclosing the biconcave disc was larger than that for the oblate spheroid because the volume of the cell was larger. This explains the slightly larger dynamic displacements

observed for the biconcave disc. For the oblate spheroid, the scaling factors relating the position of $q_{1,max}^{-1}$ and $q_{2,max}^{-1}$ to the cell diameter were: 1.06 and 2.05 for Ht = 0.3; 1.11 and 2.16 for Ht = 0.4; and 1.14 and 2.26 for Ht = 0.5. For the biconcave disc, the scaling factors were: 1.02 and 1.96 for Ht = 0.3; 1.07 and 2.05 for Ht = 0.4; and 1.11 and 2.15 for Ht = 0.5. For the latter of these relationships, i.e., for the biconcave disc at Ht = 0.5, we previously reported scaling factors of 1.063 and 2.146; these are in close agreement with those values obtained here.

Simulations: exchange on

The simulations of diffusion involved identical systems to those described in the section above, but they were conducted with exchange occurring between the intra- and extracellular regions. Molecules were assigned initial coordinates either inside or outside the virtual cell in a random manner, with a distribution (inside or outside) that was determined by the Ht. One measure of the robustness, or reproducibility, of these simulations was that, at a given Ht, the final distribution of point molecules between the intra- and extracellular spaces did not change to a statistically significant extent from the initial distribution.

Relative to the simulations of diffusion in which exchange was absent, decreasing the Ht resulted in a greater degree of signal attenuation with increasing q value (Fig. 5). Again, this is attributable to the diffusant in the extracellular region being less restricted as the spacing between the cells was increased. This observation is reinforced by the estimates of the D_{app} and RMSD values, which, without exception, increased with decreasing Ht (Tables 1 and 2). It is also notable that the pore-hopping shoulder was more pronounced at lower Ht values as a result of the proportionally increased contribution to the signal from the extracellular water. The additional critical points observed in Fig. 6 A arise from the fundamentally different topological arrangement of pores and cells in a hexagonal array when projected in the x and z directions.

The data in Table 2 show that RMSD values were slightly smaller for the biconcave disc than for the oblate spheroid. This result is opposite from that obtained for either intra- or extracellular diffusion in the absence of exchange. Thus the estimate of the apparent diffusion coefficient (directly related to the RMSD) in a two-compartment system with exchange is a nonlinear weighted sum of the apparent values in each compartment.

PGSE NMR experiments

The simulations described above were conducted to improve our interpretation of data obtained from PGSE NMR experiments on real cellular systems. It was shown that the

biconcave disc simulations did indeed give rise to features that were seen in q-space plots from RBC suspensions.

However, as seen from (Fig. 7) and previous reports (Benga et al., 2000; Kuchel et al., 1997; Torres et al., 1998, 1999), the various features and critical points of the q-space plots were less pronounced than for the simulated canonical data. This is readily interpreted as being due to real RBC suspensions having a distribution of cell sizes and, to a lesser extent, shapes. In addition, the cells in a real suspension in the NMR spectrometer, although virtually completely aligned in the z direction, will not be so aligned in the x and y directions. Also, they move slightly during each NMR pulse sequence and therefore will be arranged in a continuously changing and random manner. The simulations were conducted on systems in which all cells were identical both in size and shape, and their orientations were exactly specified with their packing arrangement fixed and regular. Further work could entail building in random fluctuations in cell orientation and this would lead to a blurring of the features of q-space plots.

It is also clear from the experimental data (Fig. 7) that the extent of signal attenuation was increased at all values of q as Ht was decreased, as occurred with the simulated data. The pore-hopping shoulder was more pronounced at lower values of Ht, and this is attributed to the greater volume of water in the extracellular region resulting in its greater contribution to the overall water signal. However, had the Ht been further decreased, it is anticipated that, at some value, this feature would have become less pronounced and eventually disappeared altogether as the extracellular pores would have become ill-defined.

Also in Fig. 7, a decrease in Ht was accompanied by an increase in RMSD, reflecting the diminished restriction to diffusion in the extracellular region afforded by the lower volume occupied by the RBC. Once again, this result was observed in the simulations. The relationship between Ht and RMSD was very linear (see Results), thus suggesting a method for estimating the Ht of a sample simply by measuring the width-at-half-height of the Fourier transform of the q-space plot. The RMSD at Ht = 0.5 was considerably higher than that for the biconcave discs at the same Ht, and was closer to that for the oblate spheroids. The reason for the discrepancy lies in the values chosen for the intra- and extracellular diffusion coefficients for which only preliminary experimental values were used in the simulations.

The features of the q-space plots in Fig. 7 are not highly resolved, and, consequently, determination of the critical q-values was more difficult than for the simulated data. Nevertheless, the relationships between critical values and characteristics of the cells in the suspension at Ht = 0.5 are comparable with the simulated data at Ht = 0.5.

General points

It has been pointed out above that, in a real RBC suspension, the cells are not of identical size and are not motionless

in a regular lattice. The models used in this study, in contrast, were based on an ideal and hence simplified system. The intention in the work was not merely to provide a simplification but rather to develop a canonical system that would reveal features that would be difficult to discern in a more realistic system due to the blurring effect of randomization of cell orientation.

The degree of signal attenuation in the PGSE NMR experiments on real RBC suspensions extended to greater than 10^3. Despite this high level of attenuation, we are able to ignore the contaminating signals from other cellular metabolites or components. The concentration of water protons in the cell is 70–80 M and close to 100 M in the extracellular fluid. The concentration of nonexchangeable glycyl protons from glutathione, the most abundant metabolite inside the cells, is just 4 mM, a factor of 10^5 lower than water. The hemoglobin concentration, although significantly higher, has a short T_2 relaxation time, so, in PGSE NMR experiments with an echo time of greater than 20 ms, the hemoglobin makes no significant contribution to the signal in the region of the water resonance (Kuchel and Chapman, 1991).

A complicating factor in the analysis of simulation data has been the appearance of negative signal values at the minima. The magnitude of these negative echoes was, on average, of the order of 10^{-5} of the initial signal intensity. Although methods have been developed to overcome this difficulty (see Materials and Methods), considerable thought was given to the origin of this phenomenon. At the much less than Avogadro's number of trajectories performed for any single simulation, there will always be an excess of displacements in the ensemble in either the positive or negative direction along any axis. Any excess, however small, will constitute a degree of apparent flow and will give rise to negative spin-echo signal intensities (Callaghan et al., 1999).

q-Space data from real or simulated cell suspensions is clearly not Gaussian, and, consequently, the propagator obtained from the Fourier transform of the data is also not Gaussian. However, fitting a Gaussian to a typical q-space data set yielded a width-at-half-height of $(2.27 \pm 0.01) \times 10^4$ m with a correlation coefficient of 0.99. Therefore, on the basis that the propagator is approximately Gaussian, we contend that the width-at-half-height of the Fourier transform of q-space data is related to the effective RMSD (see Eq. 6).

CONCLUSIONS

We used random walk simulations of diffusion to study the relationship between the features of NMR q-space data and the shapes of the cells in the sample. Different cell geometries gave rise to differences in features in the q-space plots, so this finding will be useful in detecting pathological changes in cells and in the identification of cell types

(Torres et al., 1998). We have pointed out the differences that exist between the simulated and real-cell suspensions. The ideality of the simulated systems has, in fact, allowed us to identify features in q-space plots that appear with lower resolution in such plots from real RBC suspensions. Thus, we could assign these features of q-space plots to particular modes of diffusion in an ideal setting. Two methods for facilitating the analysis were described: first- and second-derivative analysis of q-space plots for the determination of q values of critical points in q-space plots, and Fourier transform analysis for calculating apparent RMSD values. The latter method provides a quick and simple means of determining the Ht of cell suspensions. Finally, we used diffusion tensor analysis to estimate the apparent diffusion coefficients and to show their dependence on direction of movement of the diffusant in a heterogeneous system, such as a suspension of cells with only one axis of symmetry.

REFERENCES

Bailey, N. T. J. 1995. Statistical Methods in Biology. Cambridge University Press, Cambridge, UK.

Benga, G., P. W. Kuchel, B. E. Chapman, G. C. Cox, I. Ghiran, and C. H. Gallagher. 2000. Comparative cell shape and diffusional water permeability of red blood cells from Indian elephant (*Elephas maximus*) and Man (*Homo sapiens*). *Compar. Haematol. Int.* 10:1–8.

Benga, G., V. I. Pop, O. Popescu, and V. Borza. 1990. On measuring the diffusional water permeability of human red blood cells and ghosts by nuclear magnetic resonance. *J. Biochem. Biophys. Methods.* 21:87–102.

Callaghan, P. T., S. L. Codd, and J. D. Seymour. 1999. Spatial coherence phenomena arising from translational spin motion in gradient spin echo experiments. *Concepts Magn. Reson.* 11:181–202.

Callaghan, P. T., A. Coy, D. MacGowan, K. J. Packer, and F. O. Zelaya. 1991. Diffraction-like effects in NMR diffusion studies of fluids in porous solids. *Nature.* 351:467–469.

Cory, D. G., and A. N. Garroway. 1990. Measurement of translational displacement probabilities by NMR: an indicator of compartmentation. *Magn. Reson. Med.* 14:435–444.

Dacie, J. V., and S. M. Lewis. 1975. Practical Haematology. Churchill Livingstone, London.

Endre, Z. H., B. E. Chapman, and P. W. Kuchel. 1984. Cell volume dependence of ^1H spin-echo signals in human erythrocytes suspensions: the influence of in situ field gradients. *Biochim. Biophys. Acta.* 803: 137–144.

Higashi, T., A. Yamagishi, T. Takeuchi, N. Kawaguchi, S. Sagawa, S. Onishi, and M. Date. 1993. Orientation of erythrocytes in a strong static magnetic field. *Blood.* 82:1328–1334.

Kuchel, P. W., and B. E. Chapman. 1991. Translational diffusion of hemoglobin in human erythrocytes and hemolysates. *J. Magn. Reson.* 94:574–580.

Kuchel, P. W., A. Coy, and P. Stilbs. 1997. NMR "diffusion-diffraction" of water revealing alignment of erythrocytes in a magnetic field and their dimensions and membrane transport characteristics. *Magn. Reson. Med.* 37:637–643.

Kuchel, P. W., C. J. Durrant, B. E. Chapman, P. S. Jarrett, and D. G. Regan. 2000. Evidence of red cell alignment in the magnetic field of an NMR spectrometer based on the diffusion tensor of water. *J. Magn. Reson.* 145:291–301.

Kuchel, P. W., and E. D. Fackerell. 1999. Parametric-equation representation of biconcave erythrocytes. *Bull. Math. Biol.* 61:209–220.

Lennon, A. J., and P. W. Kuchel. 1994a. Enhancement of the "diffraction-like" effect in NMR diffusion experiments. *J. Magn. Reson. A.* 111: 208–211.

Lennon, A. J., and P. W. Kuchel. 1994b. Neural networks used to interpret pulsed-gradient restricted-diffusion data. *J. Magn. Reson. A.* 107: 229–235.

Mansfield, P., and P. K. Grannell. 1973. NMR 'diffraction' in solids? *J. Phys. C: Solid State Phys.* 6:L422–L426.

Mills, R. 1973. Self-diffusion in normal and heavy water in the range 1–45°. *J. Phys. Chem.* 77:685–688.

Moon, P., and D. E. Spencer. 1988. Field Theory Handbook. Including Coordinate Systems, Differential Equations and Their Solutions. Springer-Verlag, Berlin.

Regan, D. G., and P. W. Kuchel. 2000. Mean residence time of molecules diffusing in a cell bounded by a semi-permeable membrane: Monte Carlo simulations and an expression relating membrane transition probability to permeability. *Eur. Biophys. J.* 29:221–227.

Tanford, C. 1961. Physical Chemistry of Macromolecules. John Wiley and Sons, New York.

Torres, A. M., R. J. Michniewicz, B. E. Chapman, G. A. R. Young, and P. W. Kuchel. 1998. Characterisation of erythrocyte shapes and sizes by NMR diffusion-diffraction of water: correlations with electron micrographs. *Magn. Reson. Imaging.* 16:423–434.

Torres, A. M., A. T. Taurins, D. G. Regan, B. E. Chapman, and P. W. Kuchel. 1999. Assignment of coherence features in NMR q-space plots to particular diffusion modes in erythrocyte suspensions. *J. Magn. Reson.* 138:135–143.

PAPER VI

ARTICLE

David G. Regan · Philip W. Kuchel

Simulations of NMR-detected diffusion in suspensions of red cells: the "signatures" in *q*-space plots of various lattice arrangements

Abstract Coherence effects from pulsed field-gradient spin-echo (PGSE) nuclear magnetic resonance diffusion experiments have been observed and characterized for diffusants in many heterogeneous systems, ranging from porous materials to cell suspensions. The resulting coherence patterns appear in plots of the normalized PGSE signal intensities as a function of the spatial wave vector **q** in a so-called *q*-space plot. The origin of these phenomena and their mathematical and physical underpinnings are now well established. We have conducted a number of studies of diffusion-coherence phenomena in suspensions of red blood cells and have made extensive use of computer simulations of molecular diffusion in virtual lattices of cells to aid in the interpretation and analysis of experimental data. In the current work we extended the canonical model used in these studies to investigate the effect that varying the packing arrangement of cells in the suspension has on the coherence patterns, as seen in *q*-space plots. We show that changes in the packing arrangement of cells are reflected in the *q*-space plots and in the results of diffusion tensor analysis and thus we speculate upon the possible clinical importance of these findings.

Keywords Diffusion tensor · Monte Carlo · Erythrocyte · Pulsed field-gradient spin-echo · *q*-Space plot

Abbreviations *DWI*: diffusion-weighted imaging · *Ht*: haematocrit · *MRI*: magnetic resonance imaging · *PGSE*: pulsed field-gradient spin-echo · *RBC*: red blood cell · *RBDG*: random binary digit generator · *RFPNG*: random floating point number generator · *RNG*: random number generator

D.G. Regan · P.W. Kuchel (✉)
School of Molecular and Microbial Biosciences,
University of Sydney, NSW 2006, Australia
E-mail: p.kuchel@mmb.usyd.edu.au
Fax: +61-2-93514726

Introduction

Pulsed field-gradient spin-echo (PGSE) nuclear magnetic resonance (NMR) is an expeditious and accurate method for measuring molecular diffusion in isotropic solution (Kärger et al. 1988). The method is based on the encoding of spatial information in the phase of spin magnetization, by the imposition of a magnetic field gradient on the sample, in order to measure positional displacement. Magnetic resonance imaging (MRI) also makes use of magnetic field gradients but in this case the spatial information is usually encoded in water spin density rather than the magnetization phase (Talagala and Lowe 1991). Increasingly, diffusion-weighted imaging (DWI) is being used clinically as a methodology but uses relative diffusion rates of water in the imaging of tissues.

In heterogeneous systems, PGSE NMR can yield diffraction and interference-like effects that arise as a result of spatial coherences in the magnetization phase in the sample (Mansfield and Grannell 1973). NMR diffusion-interference has been used to study the structure of porous media at a resolution inaccessible to conventional MRI (Callaghan et al. 1991) and we have shown that the PGSE method may also be used to study transport processes, cell morphology, and compartmentation in suspensions of red blood cells (RBCs) (Kuchel et al. 1997; Torres et al. 1998, 1999; Regan and Kuchel 2002).

These diffraction and interference-like effects, which are termed diffusion-coherence, can be visualized graphically by plotting the relative signal intensities from the PGSE NMR experiment as a function of the spatial wave vector **q** (units, m^{-1}):

$$\mathbf{q} = (2\pi)^{-1}\gamma\delta\mathbf{g} \tag{1}$$

where γ is the nuclear magnetogyric ratio, δ is the duration of each magnetic field-gradient pulse and **g** is the applied magnetic field-gradient vector. The *q*-space plot for a suspension of RBCs (which are aligned in the static

field, $\mathbf{B}_0$) (Kuchel et al. 1997, 2000) consists of a pore-hopping shoulder, which is due to water diffusing between the extracellular cavities (diffusion-interference), followed by a series of coherence peaks which are due to the restricted diffusion of water inside the cells (diffusion-diffraction) (Torres et al. 1999). The position of the pore-hopping shoulder in q-space plots is inversely related to the spacing of cells in the suspension, while the positions of the diffraction minima are inversely related to the average projected dimension of the cells in the direction in which the field-gradient has been imposed.

We have recently shown that the diffusion tensor of water in an RBC suspension, obtained from PGSE NMR diffusion measurements, provides information regarding the diffusion anisotropy of the sample and yields additional evidence of cell alignment in the magnetic field of the spectrometer (Kuchel et al. 2000). Diffusion tensor and q-space analysis are now being combined with conventional MRI (Basser et al. 1994; Basser 2002) to map fibre tracts in tissues such as the central nervous system (Basser and Pierpaoli 1996; Assaf and Cohen 1999; Pajevic and Pierpaoli 1999; Xue et al. 1999; Assaf and Cohen 2000).

In the present work we used computer simulations of diffusion, and combined diffusion tensor and q-space analysis of the theoretical data in a spectroscopic rather than imaging context. We set out to provide insights into q-space plots that would enable solution of the "inverse problem", whereby, from a q-space plot and minimal other information, the packing arrangement of uniform cells could be reconstructed.

The great advantage of both NMR imaging and spectroscopic methods for studying tissue structure and other properties is that they are non-invasive. Here we present an alternative and potentially useful technique for detecting changes in tissue structure using NMR and one that is capable of higher spatial resolution than conventional NMR imaging techniques.

Theory of methods

General

The work involved the computer simulation of molecular diffusion in three-dimensional lattices of cells. The method used a Monte Carlo random walk technique in the context of a PGSE NMR experiment. The output from the simulations was a set of calculated signal intensity values corresponding to the respective field-gradient strengths used in the simulation. The cells were assigned a biconcave disc shape (Fig. 1F) that closely approximates that of a human RBC. A "unit cell" consisted of a regular hexagonal prism containing a single RBC (Fig. 1F), both centered on the Cartesian origin. The unit cell was extended to a three-dimensional hexagonal lattice of unit cells (Fig. 1A) by the application of periodic boundary conditions. Layers of unit cells were offset with respect to one another in the x- and z-directions (Fig. 1A–C).

Random walks and random number generators

The Monte Carlo methods are so-named because of their utilization of sequences of uncorrelated random numbers. A Monte Carlo random walk simulates random molecular motion (viz., diffusion), and this representation is useful in exploring a binary tree, where it is necessary to emulate the random branching of a trajectory. Each step of a random walk involves executing a displacement (e.g., for diffusion, the displacement is of a particle in space and may be executed in one, two, or three dimensions) along a path whose direction is determined randomly by the generation of a random number.

Diffusion is brought about by the random motion of particles (molecules) due to thermally driven collisions. In an isotropic solution the mean-square distance traveled by molecules in an ensemble, in the time t, is given by the Einstein diffusion equation (Tanford 1961):

$$\langle r^2 \rangle = 6Dt \tag{2}$$

where r is the distance traveled by a single molecule and D is the diffusion coefficient. However, the exact analytical description of diffusion is difficult or impossible in a complex system such as a cell suspension which is compartmentalized (intra- and extracellular compartments) and in which the diffusant is exchanging between compartments, as has recently been reaffirmed by Jiang et al. (2001). The value of the apparent diffusion coefficient in a system such as this may vary as a function of its compartmental location. The difficulty of deriving an analytical solution, and the intrinsically stochastic nature of diffusion, make the Monte Carlo random walk an ideal method for exploring problems of this type.

The main element of the random walk simulation is a random number generator (RNG); the design of this algorithm is crucial to ensuring the absence of systematic bias in the final solution (Park and Miller 1988; Press and Teukolsky 1992; Knuth 1998). Any computer-generated sequence of numbers will be *pseudo-random* because no matter how large the period (i.e., the number of values generated in the sequence before the sequence repeats itself) the sequence will be predictable. An operational definition of randomness in the context of computer-generated sequences of numbers was suggested by Press et al. (1996): "the deterministic program that produces a random sequence should be different from and – in all measurable respects – uncorrelated with the computer program that uses its output". This implies that if any two different RNGs produce statistically different results when used in a particular program, then at least one of them is not a good generator.

Two RNGs were used in the present work: a random binary digit (or bit) generator (RBDG), whose output
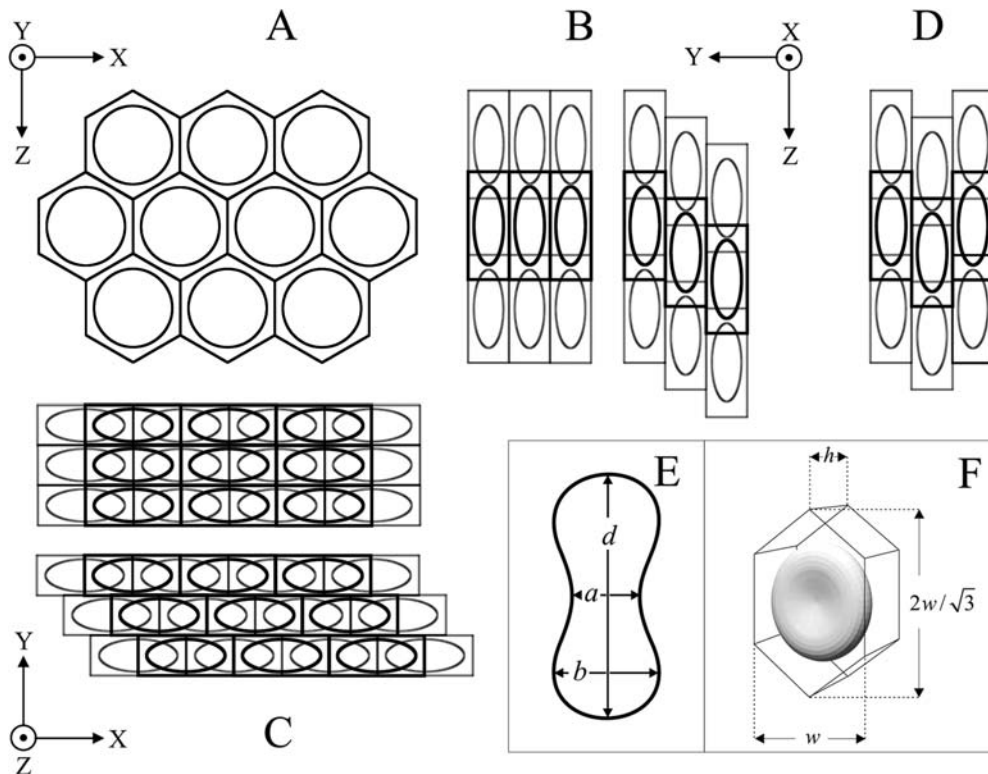
Fig. 1A–F Arrangement of virtual cells in the 3-D hexagonal lattice, the manner in which layers of unit cells are offset with respect to one another, and the geometry of the biconcave disc-shaped cell and the unit cell. The point of view of observation in **A**, **B**, **C**, and **D** in a Cartesian axis system is indicated by the *dot in a circle* (denoting a direction perpendicularly out of the page) and *arrow symbols*. **A** shows the arrangement of cells in a single layer of the hexagonal lattice. **B** and **C** show the manner in which adjacent layers of cells are offset with respect to one another in the *z*- and *x*-directions, respectively. **D** shows an alternative scheme for offsetting the layers; this scheme is not used in the work described in this paper. **E** is a schematic illustration of a cross-section of a biconcave disc through the axis of symmetry perpendicular to the disc planes; *a* is the minimum thickness of the disc in the dimpled region, *b* is the maximum thickness, and *d* is the main diameter. **F** shows the composition of the unit cell consisting of a hexagonal prism containing a biconcave disc-shaped RBC; *w* is the width of the prism and *h* is its depth

was either +1 or –1, and a random floating-point number generator (RFPNG), whose output was a double-precision floating point number between 0.0 and 1.0. Random binary digits were generated using a shift register generator (Knuth 1998), so named because the main step involves extracting the low-order bit of a *k*-bit word, where $k = 32$. This RBDG has been extensively tested by Tausworthe (1965), so is often referred to as a Tausworthe generator. The principal reasons for choosing this generator were computational speed and demonstrated statistical randomness. The RFPNG was used in the simulations for assigning random starting coordinates for random walk "trajectories" and for testing the condition for transition across the cell membrane. The algorithm was taken from Numerical Recipes in C (Press et al. 1996) and combines two different sequences obtained using a multiplicative

congruential algorithm for maximum period (L'ecuyer 1988) with a Bays-Durham shuffle algorithm (Knuth 1998) for removing low-order serial correlations. To the best of our knowledge, these are the most robust and appropriate methods for the computer generation of random numbers for simulations of the type described here. While there is no perfect method[1], there were no systematic anomalies in the present model that were attributable to the RNGs.

Virtual cell

The model of the cell used in the simulations was a degree-four (quartic) surface (or cyclide; Fig. 1E and F), which closely approximates the shape of a human RBC (Kuchel and Fackerell 1999). This biconcave disc-shaped cell was chosen because NMR diffusion-coherence phenomena are reproducibly obtained from suspensions of these cells (Kuchel et al. 1997; Torres et al. 1998, 1999).

In Cartesian coordinates the surface is (Moon and Spencer 1988):

$$(x^2 + y^2 + z^2) - 2E(x^2 + z^2) - 2Fy^2 + G = 0 \qquad (3)$$

where the parameters *E*, *F*, and *G* are constants whose values are related to the shape in terms of its diameter *d*,

---

[1]The authors of this RNG contend that it provides perfect random numbers "within the limits of its floating point precision" and have offered $1000 to the designer of a statistical test that the generator fails in a "non-trivial way"

maximum thickness b, and minimum thickness a (Fig. 1E), such that (Kuchel and Fackerell 1999):

$$E = \frac{d^2}{4} - \frac{a^2}{4}\left(\frac{d^2}{b^2} - 1\right)\left[1 - \sqrt{1 - \frac{b^2}{a^2}}\right] \qquad (4)$$

$$F = \frac{d^2}{b^2}E - \frac{b^2}{8}\left(\frac{d^4}{b^4} - 1\right) \qquad (5)$$

$$G = d^2E - d^4/8 \qquad (6)$$

The volume (V_{cell}) was calculated numerically using *Mathematica* (Wolfram Research, Champaign, Ill., USA). It involved evaluating the volume terms of the sum of the areas of slices taken parallel to the disc planes of the cell from its center to the beginning of the dimpled region and from the beginning of the dimpled region to the extremity of the disc. Thus:

$$V_1 = 2\pi \int_0^{b/2} \left(\sqrt{\left[(2y^2 - 2E)^2 - 4(y^4 - 2Fy^2 + G)\right]} \right.$$
$$\left. - (2y^2 - 2E) \right)/2 \, dy \qquad (7)$$

$$V_2 = 2\pi \int_{b/2}^{a/2} \sqrt{\left[(2y^2 - 2E)^2 - 4(y^4 - 2Fy^2 + G)\right]} \, dy \qquad (8)$$

$$V_{cell} = V_1 + V_2 \qquad (9)$$

Spatial location

Following every step in the random walk it was necessary to determine whether the new coordinates denoted a position inside or outside the RBC. For a point molecule that has moved from P (x_1, y_1, z_1) to Q (x_2, y_2, z_2) in relation to a biconcave disc centered on O (0, 0, 0), a point A (x, y, z) is defined as the point of intersection between the displacement vector $\overrightarrow{OQ}$ and the surface of the cell:

$$\overrightarrow{OA} = \frac{t(x_2\mathbf{i} + y_2\mathbf{j} + z_2\mathbf{k})}{m} \qquad (10)$$

where m and t denote the magnitude of $\overrightarrow{OQ}$ and the relative position of A along $\overrightarrow{OQ}$, respectively. Substituting the Cartesian coordinates of the point A (i.e., tx_2/m, ty_2/m, and tz_2/m) into Eq. (3) yields a quadratic in t^2:

$$\frac{t^4\left[x^4 + y^4 + z^4 + 2x^2y^2 + 2x^2z^2 + 2y^2z^2\right]}{m^4}$$
$$- \frac{t^2\left[2E(x^2 + y^2) + 2Fy^2\right]}{m^2} + G = 0 \qquad (11)$$

If $|t|t \geq m$, then the point Q lies inside the RBC, otherwise Q lies outside the RBC. In this latter case it was necessary to calculate the point of intersection between $\overrightarrow{PQ}$ and the surface of the RBC. An analytical solution exists to this problem but involves the solution of a quartic expression yielding four solutions, which are tested to determine the physically correct one. For reasons of computational speed we used a numerical method to solve for the roots in this problem. The algorithm used a combination of the Newton-Raphson and bisection methods (Faires and Burden 1998). This method is particularly well suited to this problem since the solution is known to be bracketed in the small interval defined by $\overrightarrow{PQ}$. Mathematica was used to generate the necessary expressions[2], which owing to their length and complexity are not given here[3]. The computation converged rapidly (within a few iterations) to a solution of the specified accuracy.

Permeability and membrane transition

In the context of the Monte Carlo simulations of diffusion in cell suspensions, membrane permeability (P_d) is related to the probability of transition across the membrane, tp, by (Regan and Kuchel 2000):

$$tp = P_d s/D \qquad (12)$$

where P_d (units, m s^{-1}) is the permeability of the membrane, s is the length of a single step in the random walk, and D is the intra- or extracellular diffusion coefficient. In order to test the condition for membrane transition, a random number was generated with the RFPNG and compared with the calculated value of tp; transition across the membrane was allowed if the generated number was less than tp.

Unit cell

The primary unit cell consisted of a regular hexagonal prism containing a virtual RBC (see Fig. 1E). For convenience, both objects were centered at the origin of a Cartesian coordinate system. The primary unit cell, and the application of periodic boundary conditions (described below), provided the basis for simulating diffusion in a three-dimensional lattice of RBC (a two-dimensional representation is given in Fig. 1A). The hexagonal prism was invoked in the simulations by specifying its boundaries in the xz- and yz-planes: $|x| \leq w/2$, $|y| \leq h/2$, and $|z| \leq (w - |x|)/\sqrt{3}$, where w is the distance separating the parallel sides of the prism in

---

[2] Two expressions were necessary for the Newton-Raphson algorithm: (1) an expression that equated the equation for the biconcave disc with the line segment defined by **PQ**; and (2) the first derivative of the former expression

[3] The code listings for these and all other algorithms described here are available on request from the authors

the x-direction, and h is the distance separating the hexagonal faces of the prism in the y-direction (see Fig. 1F).

The dimensions of the hexagonal prism were subjected to two constraints: (1) the volume, which is given by:

$$V_{prism} = 4w^2 h \sin(\pi/3) \tag{13}$$

conforms to:

$$V_{prism} = V_{RBC}/Ht, \tag{14}$$

ensuring that the desired haematocrit of the suspension is maintained for any value of cell volume; and (2) the distance separating the extremities of the disc planes and the edges of the disc from the surface of the prism are equal, viz.:

$$h - a = w - d \tag{15}$$

The analytical simultaneous solution of Eqs. (13, 14, 15) in *Mathematica* yielded formulae for calculating the values of w and h.

Diffusion tensor

In aqueous suspensions, human RBCs become aligned in a strong magnetic field with their disc planes parallel to the direction of the field (Higashi et al. 1993, 1996). The first evidence of alignment in the $\mathbf{B}_0$ field of an NMR spectrometer was obtained by using both q-space analysis (Kuchel et al. 1997) and subsequently by diffusion tensor analysis (Kuchel et al. 2000). The latter is based on the diffusion anisotropy that occurs as a result of the alignment of the disc-like cells.

The diffusion tensor, $\mathbf{D}$, is second-rank with nine elements:

$$\mathbf{D} = \begin{pmatrix} D_{11} & D_{12} & D_{13} \\ D_{21} & D_{22} & D_{23} \\ D_{31} & D_{32} & D_{33} \end{pmatrix} \tag{16}$$

In order to determine the values of the elements in $\mathbf{D}$, diffusion must be measured in at least six different directions, which in the case of the PGSE NMR method requires that the magnetic field gradients be applied in at least six different directions; this is readily achieved by using a modern triple-axis gradient probe which allows any combination of x-, y-, and z-gradients to be applied. Multivariate regression analysis is used to evaluate $\mathbf{D}$ (Kuchel et al. 2000) and the elements (D_{11}, D_{22}, D_{33}) of the diagonalized tensor are the estimates of the apparent diffusion coefficients in the x-, y-, and z-directions.

These estimates are generally dominated by the value for the intracellular water whose diffusion is severely restricted by the cell membrane. This results in a spin-echo signal that is attenuated less rapidly than the signal from the extracellular water. On the other hand, the extracellular water does contribute to the signal so the diffusion tensor should reflect differences in the way in which cells are arranged with respect to one another. In the simulations described here, layers of cells were offset in the x- and z-directions; hence it was anticipated that this would give rise to measurable differences in the diagonal elements of the respective diffusion tensors.

Methods

General

Molecular diffusion in lattices of RBCs was simulated as described above. Random walk trajectories for ensembles of point molecules in a three-dimensional lattice were used. Periodic boundary conditions were applied to a unit cell to simulate an infinite array, as described above (see Theory of methods: Unit cell). In addition to calculating the positional displacement of a point molecule at each step of the random walk, the phase[4] (ϕ) of the magnetic dipole moment vector (MDMV) was also calculated in the context of a PGSE NMR experiment. Various geometrical arrangements of the RBC were considered; layers of cells in the lattice were offset by different amounts with respect to each other in the x- and y- directions (Fig. 1A–C). The resulting list of relative signal intensities from each simulation was plotted as a function of the magnitude of $\mathbf{q}$, in a q-space plot.

Monte Carlo simulations

The RFPNG was used to assign each random walk trajectory in an ensemble with a random starting position in the unit cell[5]. The ratio of trajectories with starting positions inside the biconcave disc to those with starting positions outside it (but inside the hexagonal prism) was therefore determined by the chosen value of Ht. The size (s) of each step (in a particular compartment, i.e., intra- or extracellular) in the random walk was identical and was calculated as a fraction (f) of either the smallest dimension of the cell (i.e., a) or the minimum distance separating cells (i.e., $w–d$), whichever was smaller. Previous work had shown that, for simulations of diffusion between perfectly reflecting parallel planes, the distance separating the planes must be at least $5s$ (Piton et al. 1993) for results to match the analytical solution (Tanner and Stejskal 1968). Using this as a guideline, f was assigned a value of 0.1. The duration of a single step was calculated using Eq. (2). For each step in the random walk the RBDG was used to assign a random direction in each of the x-, y-, and z-directions. The point molecule was thus displaced in these directions by a distance corresponding to the product of the output from the RBDG (± 1) and s.

Upon execution of each step of the random walk, it is necessary to determine whether the molecule is located inside or outside the biconcave disc and, in the case where it is outside the disc prior to the last jump, whether it has exited the hexagonal prism[6]. If the point molecule has moved from inside to outside the biconcave disc, or vice versa, the membrane transition condition is tested, and the point molecule either reflected back off the surface or allowed to cross the surface, depending on the outcome of the test. If the

---

[4] This phase relates to the angle between the projection of the magnetic dipole moment vector onto the xy-plane and the y-axis in the rotating frame of reference

[5] While in the work described here trajectories were assigned starting positions anywhere in the unit cell, the program also allows the user to specify whether to start all trajectories either inside or outside the biconcave disc. Point molecules can therefore be confined to either compartment by turning off membrane exchange

[6] The constraints on step size precluded a point molecule moving from inside the biconcave disc to a position outside the hexagonal prism, or vice versa, in a single step

568

point molecule has exited the hexagonal prism, the periodic boundary conditions are applied to place it back inside the prism, in the position it would have occupied in the adjacent prism, while keeping track of its real displacement (p). If the point molecule has exited the hexagonal prism in the y-direction (i.e., has moved into a unit cell in the adjacent layer; $|y| > h/2$), the user-specified offsets are applied in the x- and z-directions by moving the point molecule, with respect to the prism, by the amount of the offset. The offset in x is specified as a fraction of the width (w) of the prism and the offset in z as a fraction of its height ($2w/\sqrt{3}$). Figure 2 is a schematic illustration (for two adjacent layers) of the different offset arrangements used in the simulations, while Fig. 3 shows the result of one such arrangement for a real simulation.

The change in MDMV phase accumulated as a result of the overall displacement of the point molecule during its trajectory is calculated (for all values of magnetic field-gradient strength, g) by incrementing the phase change that occurs as a result of each step executed during the first gradient pulse of the PGSE sequence and decrementing those executed during the second refocusing pulse:

$$\phi(g) = \gamma g t p \tag{17}$$

These values are summed and averaged for the entire ensemble and the signal intensity (E) is calculated for all values of g, as the projection of the bulk magnetization vector onto the y-axis. This is given by:

$$E(g) = \cos \phi(g) \tag{18}$$

Parameter values

Simulation parameters

All simulations were for ensembles of 10^8 non-interacting point-molecule trajectories. The values of the intracellular and extracellular diffusion coefficients were 8×10^{-10} m^2 s^{-1} and 1.6×10^{-9} m^2 s^{-1}, respectively[7] The dimensions of the biconcave disc, a, b, and d, were 1.0×10^{-6}, 2.12×10^{-6}, and 8.0×10^{-6} m, respectively, yielding a volume of 8.6×10^{-17} m^3, in accordance with the measured value for human RBCs (Dacie and Lewis 1975). Membrane permeability was 6.1×10^{-5} m s^{-1}, as determined experimentally for human RBCs (Benga et al. 1990), and Ht was 0.5. The tolerance for the Newton-Raphson routine (see Theory of methods: Virtual cell) was calculated as $10^{-4}\times a$, which yielded 10^{-10} for all simulations described here. Layers of cells were offset in the x- and z-directions by a factor of 0.0, 0.2, 0.25, or 0.5 times the width and height of the hexagonal prism, respectively (see Fig. 2).

PGSE parameters

The values of the PGSE parameters used in the simulations were in accordance with those used when conducting experiments on real RBC suspensions (Kuchel et al. 1997; Torres et al. 1998, 1999; Regan and Kuchel 2002) using a 400 MHz (proton frequency)
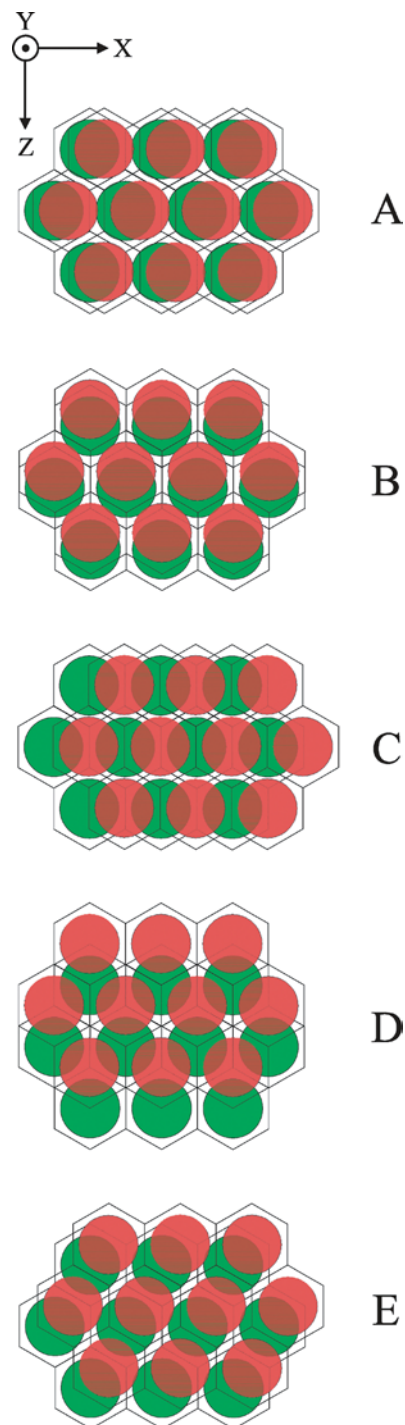

Fig. 2A–E Two-layer representations of the offset arrangements of layers of cells in the lattice used in the simulations. A offset of 0.2 in the x-direction; B offset of 0.2 in the z-direction; C offset of 0.5 in the x-direction; D offset of 0.5 in the z-direction; and E offset of 0.25 in both the x- and z-directions. No diagram is given for the arrangement in which the layers are not offset in either direction

spectrometer and the standard PGSE pulse train: delay-90°-τ-180°-τ-acquire (Kärger et al. 1988). The duration of the magnetic field-gradient pulses (δ) was 2 ms, and the time interval separating the pulses (Δ) was 20 ms, giving a total "diffusion time" of 22 ms. A set of 96 values, linearly spaced between 0 and 9.9 T m^{-1}, constituted
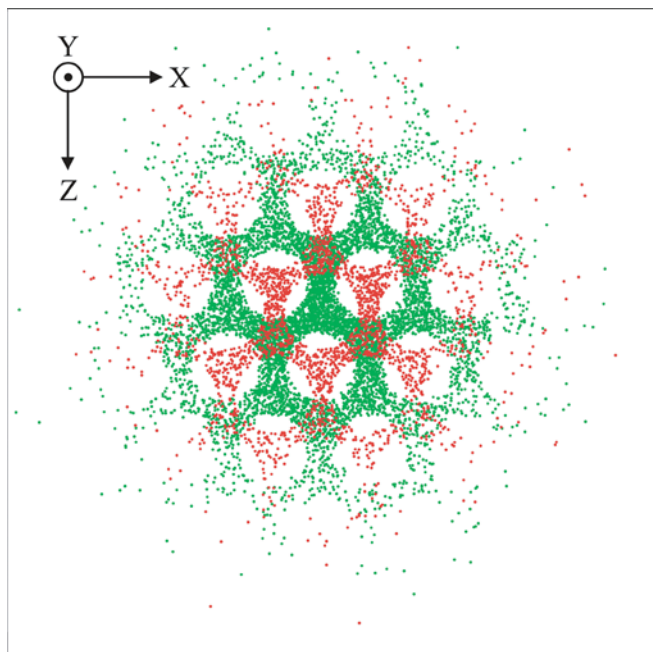
Fig. 3 Actual mapping of final coordinates from a simulation in which point molecules were confined to the extracellular space of the cell lattice (membrane permeability turned off and trajectories started outside the virtual cell) and layers were offset by 0.25 in both the x- and z-directions. The figure was generated using a program written in Matlab, which displayed final coordinates in thin slices through the centers of two adjacent layers parallel to the disc planes

the field-gradient strengths. The proton magnetogyric ratio was 2.675×10^8 rad s^{-1} T^{-1}.

Data analysis

Data from the simulations consisted of a set of signal intensities and a corresponding list of q-values. Matlab (Mathworks, Mass., USA) was used to apply a cubic spline to the data, which were then interpolated to increase the resolution from 96 to 1000 points[8]. q-Space plots were then generated from the interpolated data by using Origin (Microcal Software, Mass., USA) to plot the normalized signal intensities as a function of the magnitude of q. A logarithmic ordinate scale was used to improve visualization of coherence features, which are otherwise difficult to discern as they occur at attenuation levels of 10^2 and greater (with the exception of the pore-hopping peak which occurs at lower levels of attenuation).

  Matlab was used to calculate the elements of the diffusion tensor (from the raw data rather than from the interpolated data) using the method of Kuchel et al. (2000). Linear regression provided rough estimates of the terms of the tensor, which were then used as the initial estimates for calculating the final values, and confidence intervals by non-linear regression. The first five or six points only, lying in the region in which the data are of approximately single-exponential form, were included in the analysis.

---

[8]While very little overhead would be incurred by increasing the number of data points in the simulation from 96 to 1000 (i.e., the number of gradient values), this is not the case for the real PGSE NMR experiment in which a separate experiment is required for each data point. This method of improving data resolution, however, can be applied to both experimental and simulated data

Results

Simulations were conducted of diffusion of water in a three-dimensional hexagonal lattice of biconcave disc-shaped RBCs. Layers of cells were offset with respect to one another, as illustrated in Fig. 1A–C and Fig. 2. Figure 1D illustrates an alternative method for the off-setting of adjacent layers of cells but one that we did not employ. For all simulations, point molecules moved between the intra- and extracellular regions at the rate that we had determined experimentally for human RBC suspensions (see Methods: Parameter values). q-Space plots of diffusion in the x-, y-, and z-directions for all datasets (i.e., all alternative lattice arrangements) are shown in Fig. 4. A diffusion tensor was calculated for each dataset and the values of their diagonal elements are shown graphically in Fig. 5; these elements constitute estimates of the apparent diffusion coefficients in the x-, y-, and z-directions.

  It is useful to introduce some specific notation to facilitate discussion of the results: the various lattice arrangements illustrated in Fig. 2 and described in Methods are referred to as follows: xO_xzO_z, where O_x and O_z are the fraction of the width or height of the unit cell, by which the layers of cells are offset in the x- and z-directions, respectively. For example $x0.25z0.25$ refers to an offset in the x-direction of 0.25 times the width of the hexagonal prism and an offset in the z-direction of 0.25 times its height.

  Primarily for the purpose of discussing the results, simulations were also conducted for an $x0.0z0.2$ layer arrangement in which exchange was turned off (by setting the membrane permeability to 0.0 m s^{-1}); in other words, transition across the membrane could not occur. Three such simulations were conducted as follows: (1) diffusant in both the intra- and extracellular regions; (2) diffusant in the intracellular region only; and (3) diffusant in the extracellular region only. The q-space plots for these simulations, as well as for a previously published result (Regan and Kuchel 2002), in which there was no offsetting of layers (Fig. 6C, inset), are shown in Fig. 6.

Exchange on

x-Direction

The distinctive features of the q-space plots for diffusion measured in the x-direction (Fig. 4B) are as follows: (1) in the region of the pore-hopping shoulder (centered at $q = \sim 0.9 \times 10^5$ m^{-1}) the curves were superimposed to a large extent, although it is possible to discern that the higher the offset values the flatter the shoulder, with the $x0.5z0.0$ and $x0.0z0.5$ curves being the flattest, and the $x0.0z0.0$ case having the most pronounced shoulder (see left inset of Fig. 4B); (2) the curves in the region of the first coherence peak (centered at $q = \sim 2.3 \times 10^5$ m^{-1})
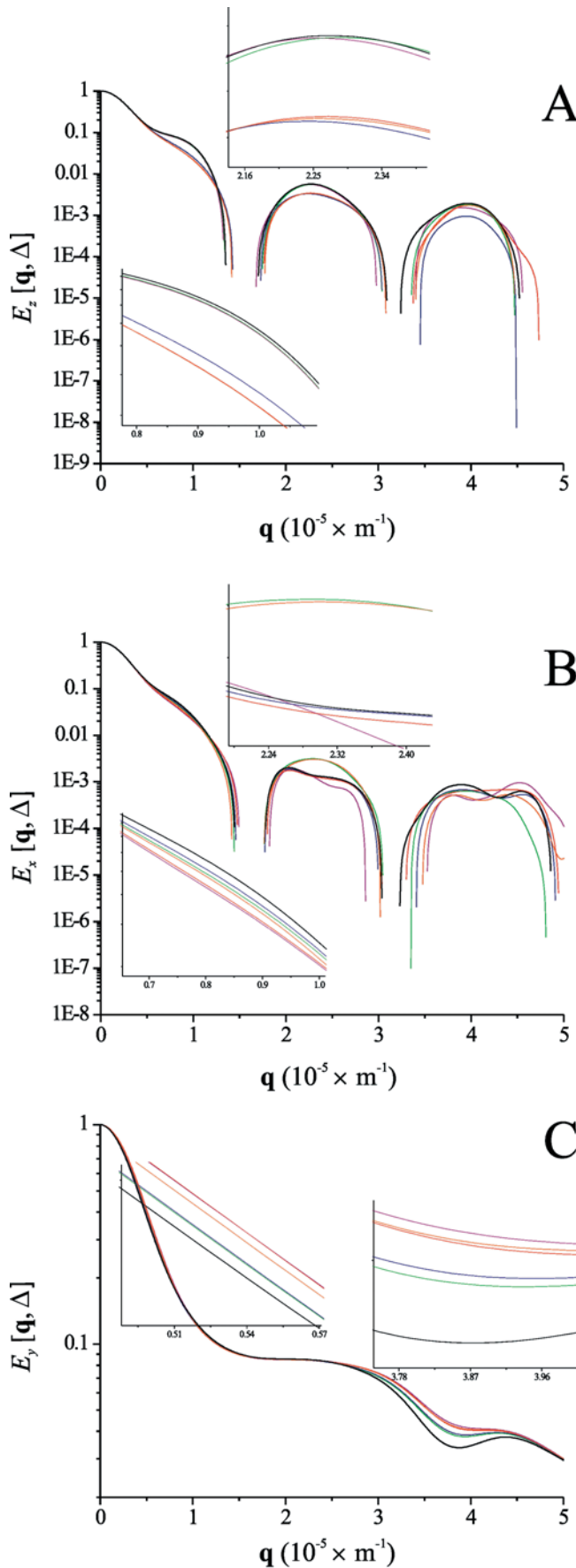
Fig. 4A–C *q*-Space plots from simulations of diffusion of water in suspensions of cells in which the layers of cells in a three-dimensional lattice were offset with respect to one another in the *x*- and *z*-directions. **A** diffusion measured in the *z*-direction; **B** diffusion measured in the *x*-direction; and **C** diffusion measured in the *y*-direction. In each of **A**, **B**, and **C** the *left inset* is a magnification of the region encompassing the center of the pore-hopping shoulder, and the *right inset* is a magnification of the region encompassing the center of the first coherence peak. *Key* (the notation used to represent the arrangement of layers is explained in Results): *black*, x0.0z0.0; *green*, x0.2z0.0; *blue*, x0.0z0.2; *orange*, x0.25z0.25; *crimson*, x0.5z0.0; *red*, x0.0z0.5
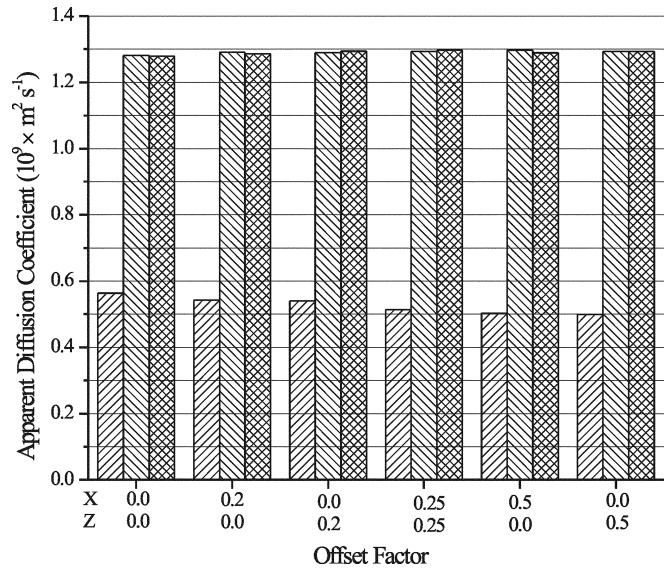
Fig. 5 Apparent diffusion coefficients measured in the *x*-, *y*-, and *z*-directions for simulations of diffusion of water in cell suspensions having different lattice arrangements. The values were obtained by calculating a diffusion tensor, as described in Theory of methods, and taking the diagonal terms. Each triplet of bars therefore represents the diagonal terms of the diffusion tensor for a particular offset arrangement, as indicated by the labeling beneath the abscissa. *Key*: *diagonally hatched, ascending from left to right*: diffusion measured in the *y*-direction; *diagonally hatched, descending from left to right*: diffusion measured in the *x*-direction; *cross-hatched*: diffusion measured in the *z*-direction

are almost superimposed for the pair x0.2z0.0 and x0.25z0.25 and for the triplet x0.0z0.0, x0.0z0.2, and x0.0z0.5, with x0.5z0.0 conforming more closely to the latter than the former (see right inset of Fig. 4B); (3) the previous grouping was also distinguished by a single peak for the pair (x0.2z0.0 and x0.25z0.25) and fine structure in the form of a double peak for the others (x0.0z0.0, x0.0z0.2, x0.0z0.5, and x0.5z0.0); and (4) the curves in the region of the second coherence peak (centered at $q = \sim 4.2 \times 10^5$ m^{-1}) all exhibit a degree of fine structure, although for x0.0z0.5 and x0.2z0.0 the peaks are more flattened than undulating.

Diffusion tensor analysis (see Fig. 5) revealed only small differences in the apparent diffusion coefficient in the *x*-direction for the different lattice arrangements. The lowest apparent diffusion coefficient was for

◄
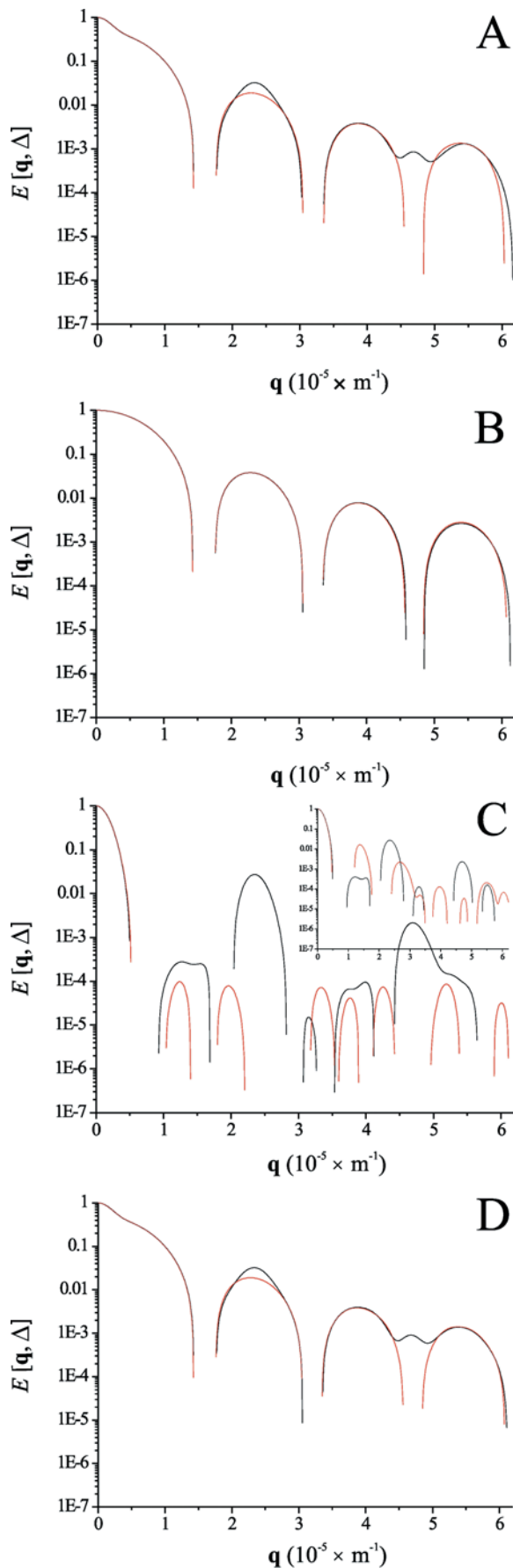
Fig. 6A–D *q*-Space plots for simulations of diffusion of water in an *x*0.0*z*0.2 lattice arrangement of cells in which exchange of water across the membrane was disabled by setting the permeability of the membrane to zero. *Key*: *black*, diffusion measured in the *x*-direction; *red*, diffusion measured in the *z*-direction. **A** water in both the intra- and extracellular regions; **B** water in the intracellular region only; **C** water in the extracellular region only; **C** *inset*: water in the extracellular region only and no offsetting of layers (i.e., *x*0.0*z*0.0); **D** the result of the superposition of **B** and **C**

*x*0.0*z*0.0 and the highest was for *x*0.5*z*0.0. In general, there was an increase in apparent diffusion coefficient as the amount of the offset was increased.

y-Direction

The *q*-space plots for diffusion in the *y*-direction (Fig. 4C) were distinct from those for diffusion in the *x*- and *z*-directions, which had similar graphical attributes. The curves for all datasets are almost indistinguishable except in the region of the minimum centered at $q = \sim 3.8 \times 10^5$ m^{-1}. In this region the curves are vertically separated into three clear groupings: *x*0.5*z*0.0, *x*0.0*z*0.5, and *x*0.25*z*0.25 are the least attenuated (*x*0.5*z*0.0, *x*0.0*z*0.5 are not distinguishable); *x*0.2*z*0.0 and *x*0.0*z*0.2 are attenuated to an intermediate extent; and *x*0.0*z*0.0 alone is attenuated to the greatest extent (see right inset of Fig. 4C). A similar separation can be discerned in the initial region of the curves centered at $q = \sim 0.5 \times 10^5$ m^{-1} (see left inset of Fig. 4C).

A clear trend is evident in the values of the apparent diffusion coefficients obtained from diffusion tensor analysis (Fig. 5). As the offset was increased the apparent diffusion coefficient in the *y*-direction became smaller. The extent of this decrease in the value of the apparent diffusion coefficient was higher for offsets in the *z*-direction than for equivalent offsets in the *x*-direction.

z-Direction

The *q*-space plots for diffusion in the *z*-direction (Fig. 4A) show a very clear grouping in both the region of the pore-hopping peak (at $q = \sim 0.9 \times 10^5$ m^{-1}; see left inset of Fig. 4A) and in the region of the first coherence peak (at $q = \sim 2.3 \times 10^5$ m^{-1}; see right inset of Fig. 4A). In these regions there is a significant vertical separation between the curves for the *x*0.0*z*0.0, *x*0.5*z*0.0, and *x*0.2*z*0.0 lattice arrangements and those for *x*0.0*z*0.2, *x*0.25*z*0.25, and *x*0.0*z*0.5. Within each grouping there is very little separation between the curves. In contrast to the curves for diffusion in the *x*-direction, there is no significant fine structure (double peaks) in the regions of the first or second coherence peak (centered at $q = \sim 4.0 \times 10^5$ m^{-1}).

As for diffusion in the *x*-direction, the apparent diffusion coefficients in the *z*-direction obtained from

diffusion tensor analysis show only small differences for the various lattice arrangements (Fig. 5). The smallest value of apparent diffusion coefficient occurred for $x0.0z0.0$, as was the case for diffusion in the x-direction; however, the highest value occurred for $x0.25z0.5$, whereas the highest value in the x-direction was for $x0.5z0.0$.

Exchange off

Figure 6 shows the q-space plots for three simulations, in an $x0.0z0.2$ lattice arrangement, in which exchange across the membrane was disabled by making the membrane impermeable. The figure illustrates that when the signal is obtained exclusively from the intracellular water (Fig. 6B), the q-space plots for the x- and z-directions are virtually indistinguishable. However, when the signal is obtained exclusively from the extracellular water (Fig. 6C), substantial differences in the q-space plots emerge in the form of fine structure in the coherence peaks for the x-direction, coupled with greatly varying levels of signal intensity. The inset of Fig. 6C shows the result of an earlier analogous simulation in which exchange was disabled but in which no offsetting of layers was implemented (i.e., an $x0.0z0.0$ lattice arrangement). Figure 6A shows the q-space plot for water diffusing in both the intra- and extracellular spaces simultaneously with exchange disabled, and although the signal is clearly dominated by the signal from the intracellular water, differences in the form of fine structure for diffusion in the x-direction are observed. Figure 6D was generated by combining the signals from the simulations in which water was confined to either the intra- or extracellular region. As expected, it is identical to the q-space plot for water diffusing in both regions simultaneously (Fig. 6A). It is important to note that the simulations used to generate Fig. 6A–C were entirely independent simulations, whereas Fig. 1D was generated by combining the results of the simulations that were used to generate Fig. 6B and C (i.e., it is not the result of an independent simulation). It is also noteworthy that Fig. 6A was generated from a simulation in which 10^8 point-molecule trajectories were recorded, while Fig. 6D was effectively generated from two such simulations so it was the result of 2×10^8 point-molecule trajectories.

Discussion

A number of general comments can be made regarding the results of the diffusion tensor and q-space analysis. First, the differences in apparent diffusion coefficients obtained from diffusion tensor analysis for the various lattice arrangements are very small. This is particularly true for the x- and z-directions, and although definite trends can be discerned, these are not likely to be discernible in real experimental data; the differences for the y-direction, however, are larger and the trend more ap-

parent. Second, very clear differences are observed in the q-space plots for the various lattice arrangements and this in itself is significant as it suggests an alternative non-invasive method for detecting or monitoring changes in tissues that are of an intrinsically ordered nature. Third, while the q-space plots for all lattice arrangements are separately resolved, a loose grouping is apparent which may be explained on the basis of the topology of the extracellular region (see below). Fourth, the q-space plots for diffusion in the x-direction are discernibly different from those for diffusion in the z-direction and this can also be explained in terms of differences in the extracellular topology. A more detailed examination of these observations follows.

Exchange off

It is useful at this point to discuss the results obtained for diffusion in the absence of exchange, as illustrated in Fig. 6. These results show first and most importantly that differences in the q-space plots for diffusion in the x- and z-directions arise as a result of signals obtained from the extracellular water (Fig. 6C); no differences are observed for simulations in which water is diffusing in the intracellular region only (Fig. 6B). While the intracellular water experiences identical topology, regardless of its x- and z-components of diffusional direction, this is not the case for the extracellular water. As is illustrated in Fig. 7, water moving from one pore to another nearest-neighbor pore experiences two fundamentally different topologies: (1) the topology illustrated by the yellow and red shaded regions (which are symmetrically identical) implies an overall displacement having both x-and z-components of direction; and (2) the topology illustrated by the green shaded region which implies an
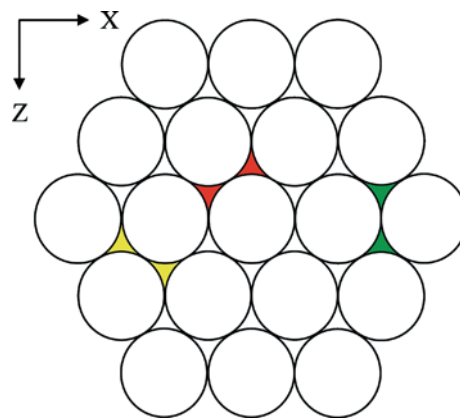
Fig. 7 Illustration of the different nearest-neighbor pore structures. The *red and yellow shaded regions* are symmetrically equivalent pore structures while the *green shaded region* is unique in its orientation. Transitions between nearest-neighbor pores in the x-direction are limited to transitions between pores of a single shape (those illustrated by the equivalent *red and yellow shaded regions*), while measured in the z-direction transitions can also occur between nearest-neighbor pores of the shape illustrated by the *green shaded region*

overall displacement in the z-direction only. It is therefore to be expected that the signal arising from the extracellular water will be different when measured in the x-direction than when measured in the z-direction.

The fact that Fig. 6D (obtained by superimposing the data from the separate simulations of intra- and extracellular water) is identical to Fig. 6A (simultaneous simulation of intra- and extracellular water in the absence of exchange) demonstrates that in the absence of exchange the overall signal is simply a superposition of the signals from the intra- and extracellular water; the composition of the overall signal is far more complex when exchange is introduced. This outcome is also predicted by the approximate analysis of Jiang et al. (2001).

Figure 6 also illustrates two other important points: (1) the overall signal is dominated by the signal from the intracellular water – this is because diffusion inside the cell is more restricted, resulting in a smaller apparent diffusion coefficient and the signal is consequently attenuated to a lesser degree than its extracellular counterpart for a given q-value; and (2) as illustrated by the inset of Fig. 6C (extracellular water, $x0.0z0.0$ lattice arrangement), different lattice arrangements give rise to q-space plots that are clearly different (although they contain similar gross features) and this can be attributed to the differences in the extracellular topology.

Exchange on

When exchange is introduced to the system, the PGSE signal is no longer the simple superposition of the intra- and extracellular signals but contains information relating to the rate at which the exchange is occurring. Additionally, while the topology of the extracellular region is fundamentally the same as described above for the non-exchanging system (and similarly is altered by changing the lattice arrangement), the boundaries of this topology are "blurred" by the exchange process. It is in accordance with expectation, therefore, that the q-space plots for the exchanging system are quite different from those of the non-exchanging one. The non-exchanging system, however, serves to identify the source of the fine structure observed in the exchanging one.

The complex nature of the exchanging system, combined with the complex topologies of the extracellular regions associated with each of the different lattice arrangements, makes it difficult to quantitatively interpret the different groupings and the fine structure described in Results. However, we can declare that the differences in the groupings are attributable to general differences in the three-dimensional topology of the extracellular region, while the fine structure observed in q-space plots for diffusion in the x-direction, but absent from those for diffusion in the z-direction, is due to the specific differences in the topology in those directions as described above (Discussion: Exchange off) and illustrated in Fig. 7.

The groupings observed for diffusion in the y-direction are more amenable to physical interpretation because, with reference to Fig. 2, we can more easily visualize the effect that offsetting the layers has on water diffusing in that direction. As the layers of cells are offset, part of the lattice that had a clear unimpeded path to diffusion for extracellular water in the y-direction becomes (partially) occluded by cells. Clearly, the $x0.0z0.0$ lattice arrangement (not shown in Fig. 2 but implied in Fig. 1A) provides the least impeded path to diffusion in the y-direction and therefore the highest attenuation of the PGSE signal. The lattice arrangements that offer the greatest impediment to diffusion in the y-direction are the $x0.5z0.0$, $x0.0z0.5$, and $x0.25z0.25$ arrangements and consequently the attenuation of the signal was the lowest in the q-space plots for these simulations. The $x0.2z0.0$ and $x0.0z0.2$ arrangements offer a similar and intermediate impediment to diffusion in the y-direction and this is reflected in an intermediate degree of signal attenuation.

The estimates of the apparent diffusion coefficients obtained from the diffusion tensors for the different lattice arrangements (see Fig. 5) are coarse because they constitute an average value that is weighted according to the relative contributions of the intra- and extracellular water signals. Although the Ht of the suspension was 0.5, the overall signal was dominated by the intracellular water whose intrinsic diffusion coefficient was smaller (to reflect the more viscous intracellular environment) and whose diffusion was more restricted (by the confinement of the cell membrane); the signal from the extracellular water was therefore attenuated to a greater extent at all given q-values as a result of its overall faster diffusion. It is therefore expected that it would be difficult to discern large differences in the apparent diffusion coefficients because changes in the lattice arrangement only affects the extracellular water. It is also not surprising that the most significant differences were observed for diffusion in the y-direction, because as the layers are moved relative to each other, the path an extracellular water molecule takes will be most changed in that direction. The trend that is observed for the y-direction, namely a reduced apparent diffusion coefficient as the offset is increased and a greater reduction for offsets in the z-direction, can be understood by referring to Fig. 2: the degree to which diffusion is restricted in the y-direction correlates very closely with the amount of white space, which constitutes the degree to which water is free to move in that direction. As the layers are moved with respect to one another the cells in each layer occlude, or eclipse, the path in the y-direction to some extent and this is reflected in the apparent diffusion coefficient.

Conclusions

We have shown that differences in the arrangement of layers in the simulated RBC lattice are reflected in the form of the respective q-space plots and in the values of

the apparent diffusion coefficients obtained from diffusion tensor analysis; hence the notion of "signatures" of cellular arrangements in the q-space plots. For diffusion in the x- and z-directions, these differences are primarily attributable to changes in the three-dimensional topology of the extracellular region. For diffusion in the y-direction, the differences are attributable mainly to the varying degree to which diffusion is impeded by offsetting the layers of cells. Future work will involve refining the analysis of the fine details and features present in the q-space plots and in obtaining more precise diffusion tensor data for the x- and z-directions. The computational methods and insights described here, however, constitute a means of understanding this novel and non-invasive NMR-based approach. It has potential applications in monitoring changes in the morphology of cells in suspensions and in solid tissues that normally display a degree of order in the arrangement of their layers of cells.

References

Assaf Y, Cohen Y (1999) Structural information in neuronal tissue as revealed by q-space diffusion NMR spectroscopy of metabolites in bovine optic nerve. NMR Biomed 12:335–344

Assaf Y, Cohen Y (2000) Assignment of the water slow-diffusing component in the central nervous system using q-space diffusion MRS: implications for fiber tract imaging. Magn Reson Med 43:191–199

Basser PJ (2002) Relationships between diffusion tensor and q-space MRI. Magn Reson Med 47:392–397

Basser PJ, Pierpaoli C (1996) Microstructural and physiological features of tissues elucidated by quantitative-diffusion-tensor MRI. J Magn Reson B 111:209–219

Basser PJ, Mattiello J, LeBihan D (1994) MR diffusion tensor spectroscopy and imaging. Biophys J 66:259–267

Benga G, Pop VI, Popescu O, Borza V (1990) On measuring the diffusional water permeability of human red blood cells and ghosts by nuclear magnetic resonance. J Biochem Biophys Methods 21:87–102

Callaghan PT, Coy A, MacGowan D, Packer KJ, Zelaya FO (1991) Diffraction-like effects in NMR diffusion studies of fluids in porous solids. Nature 351:467–469

Dacie JV, Lewis SM (1975) Practical haematology, 5th edn. Churchill Livingstone, London

Faires JD, Burden R (1998) Numerical methods, 2nd edn. Brooks/Cole, Pacific Grove, Calif

Higashi T, Yamagishi A, Takeuchi T, Kawaguchi N, Sagawa S, Onishi S, Date M (1993) Orientation of erythrocytes in a strong static magnetic field. Blood 82:1328–1334

Higashi T, Sagawa S, Ashida N, Takeuchi T (1996) Orientation of gluteraldehyde-fixed erythrocytes in strong static magnetic fields. Bioelectromagnetics 17:335–338

Jiang P-C, Yu T-Y, Perng W-C, Hwang L-P (2001) Pore-to-pore hopping model for the interpretation of the pulsed gradient spin echo attenuation of water diffusion in cell suspension systems. Biophys J 80:2493–2504

Kärger J, Pfeifer H, Heink W (1988) Principles and application of self-diffusion measurements by nuclear magnetic resonance. Adv Magn Reson 12:1–89

Knuth DE (1998) Seminumerical algorithms The art of computer programming, vol 2. Addison-Wesley-Longman, Reading, Mass., pp 1–193

Kuchel PW, Fackerell ED (1999) Parametric-equation representation of biconcave erythrocytes. Bull Math Biol 61:209–220

Kuchel PW, Coy A, Stilbs P (1997) NMR "diffusion-diffraction" of water revealing alignment of erythrocytes in a magnetic field and their dimensions and membrane transport characteristics. Magn Reson Med 37:637–643

Kuchel PW, Durrant CJ, Chapman BE, Jarrett PS, Regan DG (2000) Evidence of red cell alignment in the magnetic field of an NMR spectrometer based on the diffusion tensor of water. J Magn Reson 145:291–301

L'ecuyer P (1988) Efficient and portable combined random number generators. Commun ACM 31:742–751

Mansfield P, Grannell PK (1973) NMR 'diffraction' in solids? J Phys C Solid State Phys 6:L422–L426

Moon P, Spencer DE (1988) Field theory handbook, including coordinate systems, differential equations and their solutions. Springer, Berlin Heidelberg New York

Pajevic S, Pierpaoli C (1999) Color schemes to represent the orientation of anisotropic tissues from diffusion tensor data: application to white matter fiber tract mapping in the human brain. Magn Reson Med 42:526–540

Park SK, Miller KW (1988) Random number generators: good ones are hard to find. Commun ACM 31:1192–1201

Piton MC, Gilbert RG, Chapman BE, Kuchel PW (1993) Diffusion of oligomeric species in polymer solutions. Macromolecules 26:4472–4477

Press WH, Teukolsky SA (1992) Portable random number generators. Comput Phys 6:522–524

Press WH, Teukolsky SA, Vetterling WT, Flannery BP (1996) Numerical recipes in C, 2nd edn. Cambridge University Press, Cambridge

Regan DG, Kuchel PW (2000) Mean residence time of molecules diffusing in a cell bounded by a semi-permeable membrane: Monte Carlo simulations and an expression relating membrane transition probability to permeability. Eur Biophys J 29:221–227

Regan DG, Kuchel PW (2002) Simulations of molecular diffusion in lattices of cells: insights for NMR of red blood cells. Biophys J 83:161–171

Talagala SL, Lowe IJ (1991) Introduction to magnetic resonance imaging. Concepts Magn Reson 3:145–159

Tanford C (1961) Physical chemistry of macromolecules. Wiley, New York

Tanner JE, Stejskal EO (1968) Restricted self-diffusion of protons in colloidal systems by the pulsed-gradient, spin-echo method. J Chem Phys 49:1768–1777

Tausworthe RC (1965) Random numbers generated by linear recurrence modulo two. Math Comput 19:201–205

Torres AM, Michniewicz RJ, Chapman BE, Young GAR, Kuchel PW (1998) Characterisation of erythrocyte shapes and sizes by NMR diffusion-diffraction of water: correlations with electron micrographs. Magn Reson Imaging 16:423–434

Torres AM, Taurins AT, Regan DG, Chapman BE, Kuchel PW (1999) Assignment of coherence features in NMR q-space plots to particular diffusion modes in erythrocyte suspensions. J Magn Reson 138:135–143

Xue R, van Zijl PCM, Crain BJ, Solaiyappan M, Mori S (1999) In vivo three-dimensional reconstruction of rat brain axonal projections by diffusion tensor imaging. Magn Reson Med 42:1123–1127

PAPER VII

MRC

PGSE NMR diffusion study of the self-association of *N*-methylacetamide in carbon tetrachloride

David G. Regan, Bogdan E. Chapman and Philip W. Kuchel*

School of Molecular and Microbial Biosciences, University of Sydney, NSW 2006, Australia

N-**Methylacetamide (NMA) is known to self-associate in solution through the formation of hydrogen bonds. This behavior, and the presence in the molecule of an amide bond, make this an interesting model for study since the oligomer can be considered to be a protein analogue. The aims of the present study were to estimate the thermodynamic parameters of the self-association process, through the measurement of the diffusion coefficient of NMA in carbon tetrachloride (CCl₄), and to predict the population distribution of oligomers as a function of the concentration of NMA. Diffusion coefficients were measured using pulsed field gradient spin-echo (PGSE) NMR spectroscopy. A computer model based on the Kirkwood–Riseman theory of macromolecular diffusion and an attenuative model of self-association were used to fit the experimental data and to derive estimates of the thermodynamic association constants and bond length, and these values were, in turn, used to estimate the oligomer distribution. In addition, the temperature dependence of the diffusion coefficient was measured at three different concentrations in order to calculate the apparent Arrhenius activation energies so as to provide additional insight into the self-association process. Finally, the concentration dependence of the viscosity of NMA in CCl₄ was measured to characterize further the hydrodynamic behavior of the polydisperse system. Copyright © 2002 John Wiley & Sons, Ltd.**

KEYWORDS: NMR; ¹H NMR; *N*-methylacetamide; pulsed field gradient spin-echo; self-association; isodesmic; attenuative; polydisperse; Arrhenius; activation energy

INTRODUCTION

N-methylacetamide (NMA) is a small planar molecule (see Fig. 1) of fundamental significance as a model of a self-assembling oligomeric system, similar to some biological macromolecules. The peptide bond is the basic structural unit of the peptide chains in proteins, and NMA is one of the smallest molecules also to contain such a bond. NMA is known to self-associate, both in its pure liquid form and as a solute in solution, through the formation of hydrogen bonds. These properties make it an ideal model for studying many aspects of the behavior of macromolecules in solution.

Indeed, a large number of studies have been conducted which investigated the self-associating behavior of NMA and the properties of the hydrogen bonds through which this process occurs. Methods used to study this system have included infrared (IR)[1–5] and near-infrared (NIR)[6–8] spectroscopy, equilibrium ultracentrifugation,[9,10] calorimetry,[11] x-ray diffraction[12,13] and nuclear magnetic resonance (NMR).[1,2,14–22] The structural simplicity of this system has also lent itself to *ab initio* calculations of binding energies, geometries and spectroscopic properties.[23–26]

Most NMR studies of NMA have investigated its hydrogen bonding properties (either to itself or to other hydrogen bonding compounds) in a variety of solvents (e.g. H₂O, CCl₄, CHCl₃, benzene) using the amide proton chemical shift[1,2,15–19,21] and relaxation data[14,22] as a probe of the average extent of hydrogen bonding. Diffusion measurements should also provide an indication of the extent of association and while such studies have been conducted for NMA,[20,27] they have neglected to address the issue of polydispersity, and they have not suggested a model by which the self-association process occurs.

The aim of the present work, therefore, was to measure the diffusion coefficient of NMA in a non-interacting solvent, over a range of concentrations, and to use the values obtained to test various models of self-association. Once a suitable model was found it was possible to estimate the association constants and bond lengths and these allowed us to predict the distribution of the polydisperse solutions of oligomers as a function of concentration. The chosen solvent was carbon tetrachloride (CCl₄), which has been used in a number of other studies and which does not disrupt the hydrogen bonding of the NMA. Diffusion coefficients were measured using contemporary refinements of the pulsed field gradient spin-echo (PGSE) NMR method.

Two early sedimentation equilibrium studies by Albers *et al.*[10] and Howlett *et al.*[9] formed the basis of this study; both studies demonstrated that the extent of self-association

*Correspondence to: Philip W. Kuchel, School of Molecular and Microbial Biosciences, University of Sydney, NSW 2006, Australia.
E-mail: p.kuchel@biochem.usyd.edu.au

was concentration dependent, and that an indefinite self-association model could be successfully used to estimate equilibrium constants for the association. In addition, we used the seminal work of Kirkwood and Riseman[28–30] as the theoretical basis for calculating the diffusion coefficients of NMA oligomers in solution, for the purpose of computer modeling the polydispersity.

In order to gain some mechanistic insight into the self-association process, we measured the viscosity of NMA–CCl$_4$ solutions as a function of NMA concentration. We also conducted a study of diffusion as a function of temperature at three concentrations, thus enabling us to estimate the apparent activation energies of diffusion from Arrhenius plots.

We show here that PGSE NMR measurements of diffusion in a polydisperse self-associating system can be used, in conjunction with computer modeling techniques and non-linear least-squares fitting procedures, to estimate the equilibrium constants of association and to predict the population distribution of oligomers as a function of solute concentration. The prerequisites for the success of this approach are suitable models to describe the diffusional behavior of the solute and the mode of self-association.

THEORY OF METHODS

The work described here relies upon some fundamental theories, of which a brief explanation is warranted. The first of these is the aforementioned Kirkwood–Riseman theory, which provides a formulation for calculating the friction and diffusion coefficients for macromolecules in solution, and the second is the theory which describes the various models for indefinite self-association. The formulation for the latter is provided by a review of such models by Martin.[31]

The theory developed by Kirkwood and Riseman refers to flexible and rigid rod-like molecules. For the present work we tested models in which NMA oligomers were treated as flexible chains or rigid rod-like molecules according to this theory, or as hard spheres in which the frictional coefficients and diffusion coefficients can easily be calculated using the Einstein–Smoluchowski and Stokes equations.[32] As is described more fully in the Results section, the model of best fit to the experimental data was the rigid rod-like model, so it is this model which we outline here.

According to the rigid rod model of macromolecular diffusion,[30] the macromolecule consists of a rigid chain of identical monomeric subunits separated by rigid bonds. In the present case the monomers were single NMA molecules connected by hydrogen bonds. We treated the monomeric NMA subunit as a hard sphere whose frictional coefficient was calculated using the Stokes equation. The frictional scaling factor (λ) and diffusion coefficient (D) of the oligomer were then calculated according to the following equations:

$$\lambda = \frac{\zeta}{6\pi\eta_0 b_l} \tag{1}$$

$$D = \frac{kT}{Z\zeta} 2\lambda\{\log Z - [1 - (1/2\lambda)]\} \tag{2}$$

where ζ is the frictional coefficient of the monomeric subunit, η_0 is the viscosity of the solvent, b_l is the bond length, k is the

Boltzmann constant, T is the absolute temperature and Z is the effective number of subunits in the oligomer (the order of oligomerization).

A number of studies have shown that NMA self-associates in solution to a high order of oligomerization.[4,9,10] This has prompted the adoption, with some degree of success, of indefinite association models in attempts to estimate the association constants. In the present work we tested three models of indefinite self-association: an isodesmic model in which the association constant for the formation of dimers (K_{dimer}) is equal to that for the formation of higher order oligomers (K_{oligo}); a semi-isodesmic model in which K_{oligo} is not equal to K_{dimer}; and a model in which successive equilibrium constants for self-association are attenuated according to the prescription $K_n = K_{oligo}/n$, where n is the order of oligomerization. Each model of association was tested in conjunction with each of the diffusional models (flexible, rigid rod and sphere as described above). The model which provided the best fit with the experimental data was the attenuative model hence this is the one that is outlined below.

According to this model, $K_{dimer} = K_{oligo}/2$, $K_3 = K_{oligo}/3$, $K_4 = K_{oligo}/4$, etc. For convenience we define the dimensionless variables $x = K_{oligo}[A]$ and $L = K_{oligo}C_T$, where [A] is the concentration of unassociated monomer and C_T is the total molar concentration of solute in all its forms (i.e. $C_T = [A] + 2[A_2] + 3[A_3] + \ldots$. The ratio $\tau = 2K_{dimer}/K_{oligo}$ is also defined (such that $K_{dimer} = \tau K_{oligo}/2$, $K_3 = K_{oligo}/3$, $K_4 = K_{oligo}/4$, etc.) to allow for the equilibrium constant for dimerization not to follow the pattern described above unless $\tau = 1$. Dimerization is favored when τ is assigned a value greater than 2/3. The formulation yields the following two results for the mole fraction of monomer (α) and the mole fraction of the nth species (i.e. the oligomer of order n):

$$\alpha = x/L = 1/[1 + \tau(e^x - 1)] \tag{3}$$

$$\alpha_n = \tau\alpha x^{n-1}/(n-1)! = \tau\alpha^n L^{n-1}/(n-1)! \quad \text{with } n \geq 1 \tag{4}$$

Equation (3) must be solved numerically and then by combining the models of diffusion and self-association, and supplying the appropriate parameter values, a weight-average diffusion coefficient (D_w) can be calculated from the calculated distribution of oligomeric species. It is this value, D_w, that is measured in a PGSE NMR[33] diffusion experiment. Of course, for the theory to be valid in the case of a polydisperse sample, such as the one described here, the equilibrium must be dynamic (fast) on the NMR time-scale.

EXPERIMENTAL

Reagent-grade NMA (Aldrich, Wilwankee, WI, USA) was distilled to remove impurities and water was removed using a molecular sieve (4 Å, 8–12 mesh; Nika Seiko, Japan). Samples were made up in dry (using the same molecular sieve) NMR-grade CCl$_4$ (Merck, Darmstadt, Germany) to concentrations calculated to be 0.14, 0.21, 0.34, 0.41, 0.75, 1.09, 1.71, 2.60 and 3.97 mol l^{-1} by serial dilution of a standard solution of 6.07 mol l^{-1} which constituted the 10th sample.

PGSE NMR experiments were conducted using a DRX-400 spectrometer (Bruker, Karlsruhe, Germany), a 9.4 T

vertical wide bore magnet (Oxford Instruments, Oxford, UK) and a Bruker 10 T m^{-1} z-axis gradient probe. All experiments conducted at 25 °C employed the standard PGSE pulse train: delay$-\tau-180°-\tau-$acquire (the symbol τ used in this context should not be confused with the same symbol used in the formulation of the attenuative self-association model).[34] Experiments conducted at higher temperatures employed a double spin-echo sequence to compensate for convection in the sample.[35] For experiments conducted at temperatures above 20 °C an ethylene glycol capillary was incorporated in the sample to allow accurate temperature calibration, and a methanol capillary was used at temperatures below 20 °C. The magnetic field gradient was calibrated such that measuring the diffusion coefficient of pure water at 25 °C yielded a value of 2.3×10^{-9} m^2 s^{-1}.[36] Experimental parameters were as follows: field-gradient pulse duration, $\delta = 2$ ms; time interval separating gradient pulses, $\Delta = 10$ ms; 16 transients per spectrum. The magnitude of the field-gradient, g, was incremented from 0.01 T m^{-1} to between 0.65 T m^{-1} (lowest concentration sample) and 1.5 T m^{-1} (highest concentration sample) in 16 equal steps. The signal intensity was measured as the integral of the acetyl methyl proton resonance (see Fig. 1) after automatic phase and baseline correction. Signal intensities were normalized with respect to that of the first spectrum.

Diffusion coefficients were calculated by plotting the logarithm of the normalized signal intensities as a function of the Stejskal–Tanner parameter [$b = \gamma^2 g^2 \delta^2 (\Delta - \delta/3)$, where γ is the proton magnetogyric ratio] and calculating the slope of the regression line.[37] Plotting and linear regression were performed using Origin (Microcal, Northampton MA, USA); this program was used to generate the graphs in Figs 2–5 and to perform the linear regression for Fig. 5.

The measurement of viscosity was a two-stage process: transit times were measured for all samples at 25 °C using an Ostwald viscometer (custom made, University of Sydney),[38] and sample densities were measured at 25 °C using an Anton Paar (Graz, Austria) DMA 601 density measuring cell and DMA60 digital density processing unit. Viscosities were calculated as a function of the transit times and densities, relative to CCl$_4$ at 25 °C.[39]

Computer modeling of diffusion of NMA in CCl$_4$ was performed using a combination of Matlab (The MathWorks, Natick, MA, USA) and Maple (Waterloo Maple, ON, Canada). Matlab was used to fit the experimental data and to extract estimates for the values of K_{dimer}, K_{oligo} and b_l (bond length). Input to this program included the experimentally measured diffusion coefficients and their associated concentrations, initial estimates of K_{dimer}, K_{oligo} (based on values cited in the literature) and b_l (the monomer Stokes radius provided a convenient initial estimate for this parameter) and physical parameters and constants such as temperature, solvent viscosity, solute partial specific volume and Boltzmann and universal gas constants. The experimental data were fitted, using the non-linear least-squares fitting routine nlinfit from the Matlab Statistics package, in the context of a model combining the attenuative self-association and rigid rod formulations described in Theory of Methods, since this combination provided the best fit to the data. The solution to Eqn (3) was obtained numerically using the standard Matlab function fzero. The resulting estimates of the parameters were then used as input to a program written in Maple which calculated the distribution of oligomeric species as a function of solution concentration and the polydispersity factor[32] (given by the ratio of the weight-average molecular weight, M_w, and the number-average molecular weight, M_n, i.e. M_w/M_n), which provides a measure of the 'spread' in the distribution (a monodisperse solution will have a polydispersity factor of 1).

RESULTS

PGSE NMR
The results of a typical PGSE NMR diffusion experiment on NMA are shown in Fig. 1; the 16 resonance intensities correspond to a range of increasing g values, from left to right. Each resonance in the series is from the acetyl methyl protons in the chemical shift range 1.96–2.04 ppm. In addition, Fig. 1 shows a single one-dimensional ^{1}H spectrum of the same sample, plus its structural assignments. The spectrum was calibrated to place the acetyl methyl protons at the known chemical shift of 2.000 ppm with respect to TMS at 0.000 ppm.[40] The estimates of the value of D were made for a series of 10 different NMA concentrations.

Concentration dependence of D
The measured diffusion coefficients (D) for NMA in CCl$_4$, at 25 °C, are shown in Fig. 2 as a function of sample concentration. It should be pointed out that the Stejskal–Tanner plots (not shown; see Experimental) used to calculate the diffusion coefficients from the experimental concentrations were highly linear (correlation coefficient $R > 0.99$) at all concentrations. The value of D decreased from a maximum of 8.00×10^{-10} m^2 s^{-1} at the lowest concentration of NMA to a minimum of 3.09×10^{-10} m^2 s^{-1} at the highest concentration. Figure 2 also shows the fitted data obtained using the computer model as described in Theory of Methods and Experimental. The fitted value of D decreased from a maximum of $(7.65 \pm 0.22) \times 10^{-10}$ m^2 s^{-1} at the lowest concentration to a minimum of $(3.18 \pm 0.19) \times 10^{-10}$ m^2 s^{-1} at the highest concentration The error bars on the fitted data represent the 95% confidence intervals that were calculated on the basis of the error associated with the fitted parameters. The values returned for the fitted parameters were $K_{dimer} = 0.025 \pm 0.033$ M^{-1}, $K_{oligo} = 14.46 \pm 5.46$ M^{-1} and $b_l = (2.82 \pm 0.45) \times 10^{-10}$ m. The Stokes radius of the monomer, calculated according to the hard sphere model, was 3.12×10^{-10} m.

Oligomer distribution
From the estimated values of the bond length and equilibrium association constants, the oligomer distribution was calculated for each concentration used in the experiments. The results are presented in Fig. 3. For illustrative purposes the mole fractions plotted here were only to an oligomerization order (n) of 20 (even though the model accounts for an indefinite self-association), since beyond this point the mole fractions became exceedingly small. The figure illustrates
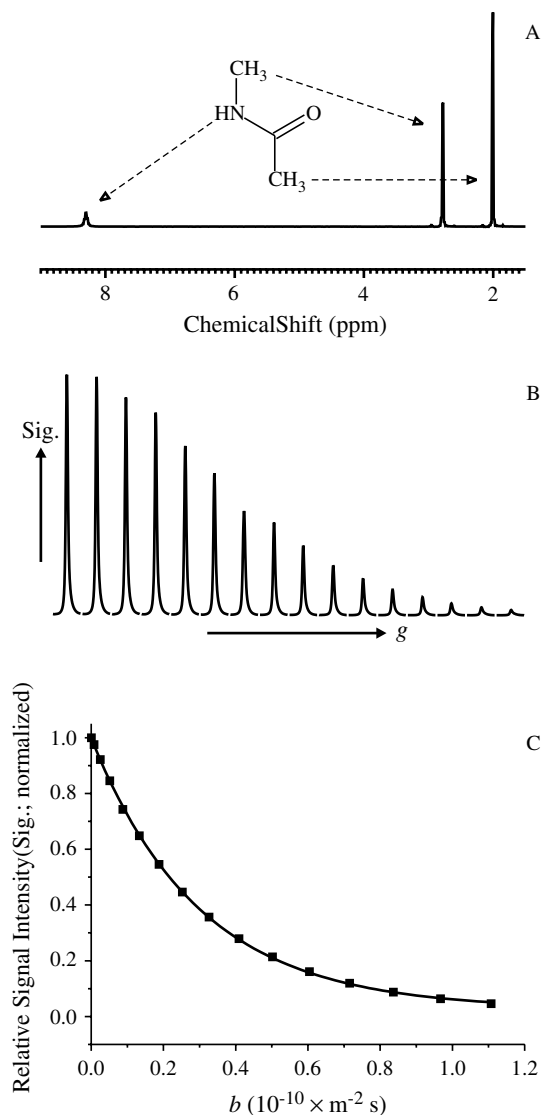
Figure 1. Resonances and data analysis from an illustrative PGSE NMR diffusion experiment conducted on a solution of NMA in CCl_4 ($\sim$6.1 mol l^{-1}). (A) The ^{1}H spectrum for the sample and the proton resonance assignments. (B) The relative signal intensities for a series of 16 experiments in which the magnetic field gradient was incremented in 16 equal steps from a minimum of 0.01 T m^{-1} (first peak from left) to a maximum of 0.50 T m^{-1} (last peak from left). Each individual peak represents the acetyl methyl proton resonance in the chemical shift range 2.04–1.96 ppm with respect to TMS at 0.000 ppm. (C) Graph of relative signal intensity as a function of the Stejskal–Tanner parameter b (see Experimental) fitted with a single exponential of the form Signal = Signal$_{offset}$ + Ae^{-Db}, and in this particular case Signal$_{offset}$ = 0.027 $\pm$ 0.003, A = 0.971 $\pm$ 0.003 and D = (3.32 $\pm$ 0.03) $\times$ 10^{-10} m^2 s^{-1}.

that as the concentration of NMA in the sample increases, so does the value of n for the predominant oligomer, the concentration of the predominant oligomer increases, and oligomers of higher order are present at detectable concentrations. Figure 3 also shows that the monomer concentration is higher than the dimer concentration at all sample concentrations, that it steadily decreases as sample concentration
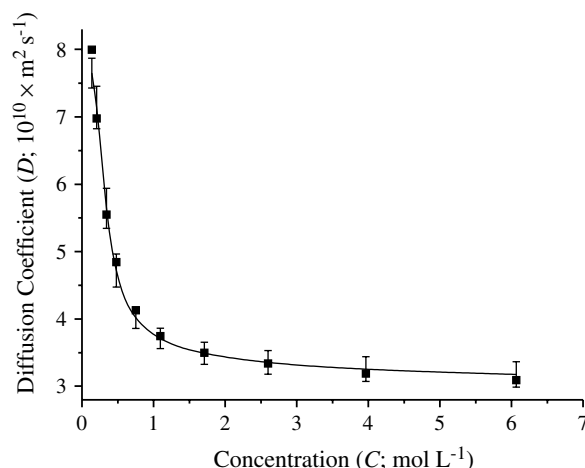

Figure 2. Experimental values of the diffusion coefficient (■) of NMA in CCl_4 as a function of NMA concentration as measured by PGSE NMR (see Experimental section for experimental parameters). The solid line (generated by applying a cubic spline to the fitted data points, and serving as a guide to the eye) represents the fitted values obtained using the attenuative indefinite self-association scheme[31] and a model of NMA diffusion in which the oligomeric species are treated as rigid rods according to the Kirkwood–Riseman[30] formulation of macromolecular diffusion. The error bars represent the 95% confidence intervals on the fitted values. This model yielded estimates for the dimerization association constant (K_{dimer}) of 0.025 $\pm$ 0.033, for the higher order association constant (K_{oligo}) of 14.46 $\pm$ 5.46 and for the average bond-length (b_l) of (2.82 $\pm$ 0.45) $\times$ 10^{-10} m.
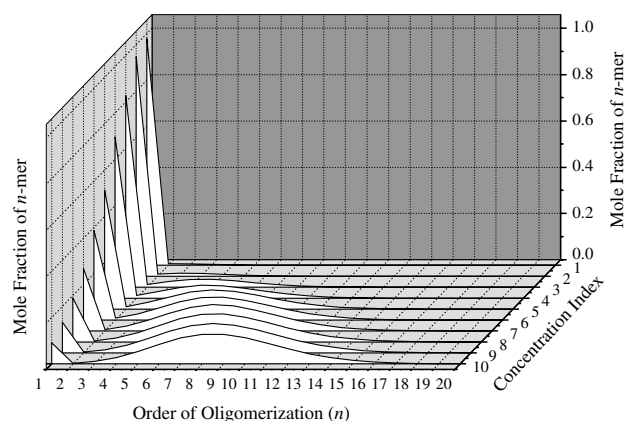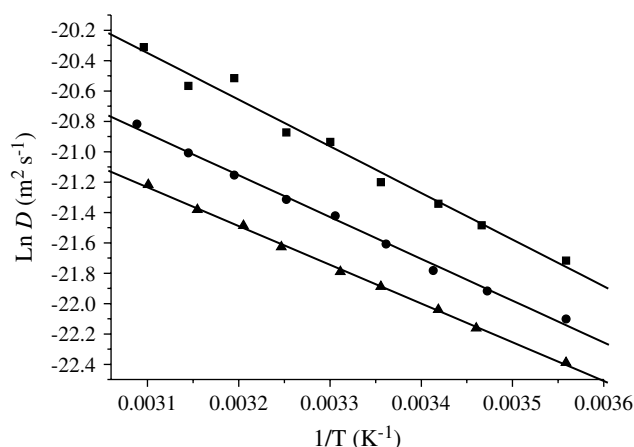

Figure 3. Distribution of NMA oligomers in solution as a function of concentration. The concentration index runs from 1, the lowest concentration of NMA in CCl_4 ($\sim$0.14 mol l^{-1}), to 10, the highest concentration ($\sim$6.1 mol l^{-1}). The order of oligomerization (n; abscissa) represents the length of NMA oligomers in number of NMA monomer units and the mole fraction for each value of n, at each of the experimental concentrations, is plotted on the ordinate. The distributions were generated on the basis of the estimated values of the equilibrium constants for an attenuative model of self-association.

increases and that the dimer concentration constitutes a local minimum in the distribution.
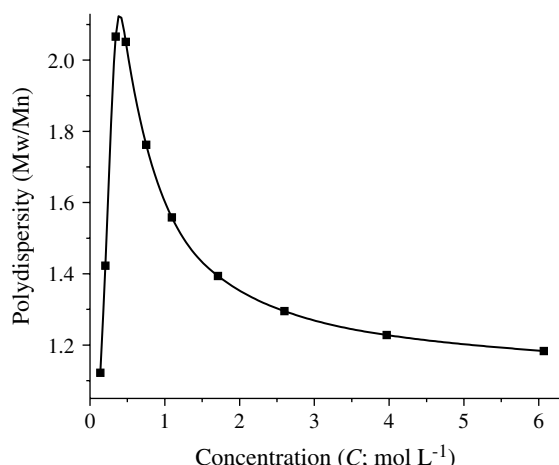
Figure 4. Polydispersity of NMA oligomeric species in solution as a function of concentration. The polydispersity factor is defined as the ratio of the weight-average molecular weight (M_w) and the number-average molecular weight (M_n). It is a measure of the spread of the oligomer distribution. The polydispersity values plotted here were calculated on the basis of the oligomer distributions (see Fig. 3) for the attenuative model of self-association. The solid line through the data is a cubic spline that serves to guide the eye. A maximum value of ~2.13 is indicated at an NMA concentration of 0.4 mol l^{-1}.

Table 1. Relative (to CCl$_4$) and specific viscosity (η_r and η_{sp}, respectively) values for NMA in CCl$_4$ at 20 °C as a function of concentration (C) calculated using an Ostwald viscometer and an Anton Paar digital density meter to measure sample densities (ρ) (see Experimental)

C (mol l^{-1})	ρ (g mL^{-1})[a]	η_r[b]	η_{sp}[c]
0.137	1.578	1.034 ± 0.009	0.034
0.205	1.575	1.099 ± 0.011	0.099
0.342	1.569	1.127 ± 0.008	0.127
0.479	1.565	1.216 ± 0.012	0.216
0.752	1.548	1.417 ± 0.015	0.417
1.094	1.528	1.591 ± 0.017	0.591
1.710	1.496	1.929 ± 0.016	0.929
2.599	1.462	2.401 ± 0.024	1.401
3.967	1.399	2.920 ± 0.025	1.920
6.068	1.293	3.684 ± 0.037	2.684

[a] The errors associated with this measurement (made using an Anton Paar digital density meter) were insignificant (coefficient of variation <0.1%) in comparison with other errors and are not quoted.
[b] The errors associated with the η_r values indicate ±1SD.
[c] The errors associated with the η_{sp} values are the same as for η_r because $\eta_{sp} = \eta_r - 1$.

Arrhenius plots of D

Figure 5 shows the Arrhenius plots for NMA diffusion as a function of temperature at three different concentrations. The measurements were made for samples of 0.14, 0.48 and 6.07 mol l^{-1} over a temperature range 8–50 K. Apparent activation energies were calculated from the slopes yielding estimates of (25.53 ± 0.24) kJ mol^{-1} for the low concentration, (22.88 ± 0.04) kJ mol^{-1} for the intermediate concentration and (21.20 ± 0.01) kJ mol^{-1} for the high concentration, where the errors indicate ±1 SD.

Concentration dependence of viscosity

Table 1 contains the results of the viscosity measurements. The viscosities are relative to the viscosity of CCl$_4$ measured using the same method (see Experimental); the density measurement for CCl$_4$ at 25 °C was 1.584 g ml^{-1} (the value is quoted in the literature[41] as 1.589 g ml^{-1}). The table shows an approximately linear dependence of viscosity (both relative and specific) on the concentration of NMA, although the best fit to the data was achieved by fitting a degree-2 polynomial (not shown). When a degree-2 polynomial was fitted to the specific viscosity data, and extrapolated to zero concentration, an intrinsic viscosity of −0.05 was obtained, relative to CCl$_4$.

Figure 5. Arrhenius plot consisting of the logarithm of diffusion coefficient (ln$D$) of NMA in CCl$_4$ as a function of the reciprocal of the absolute temperature (T) at 0.14 (■), 0.48 (●) and 6.07 mol l^{-1} (▲). Apparent activation energies were calculated from these plots yielding values of 25.53 ± 0.24 kJ mol^{-1} for the low concentration, 22.88 ± 0.04 kJ mol^{-1} for the intermediate concentration and 21.20 ± 0.01 kJ mol^{-1} for the high concentration (the quoted errors indicate ±1SD).

Measure of polydispersity

The dependence of the polydispersity factor as a function of sample concentration is shown in Fig. 4. The data were fitted with a cubic spline as a visual aid and the curve shows that the degree of spread in the oligomer distribution increases sharply from a value of 1.12 at the lowest NMA concentration to a value of ~2.13 (by interpolation) at 0.4 mol l^{-1}, and then decreases, approximately exponentially, to a value of 1.18 at the highest concentration.

DISCUSSION

PGSE NMR

In a solution in which the solute does not associate it is expected that, ignoring effects due to solution non-ideality, the diffusion coefficient will be independent of the concentration. As can be seen from Fig. 2, this is not the case for NMA in CCl$_4$. In fact, the dependence of

D_{NMA} in this system decays approximately exponentially (second order, fit not shown) with concentration. This relationship suggests that increases in concentration at low NMA concentration, less than about 0.5 mol l^{-1} according to Fig. 2, result in relatively large changes in M_w whereas at higher concentrations the change is less dramatic, and indeed by extrapolation we can predict that at concentrations much higher than 6.0 mol l^{-1} the concentration-rate of change will be close to zero. When the first derivative of a cubic spline fitted to the data is plotted (not shown) resulting in a graph of the concentration-rate of change of the diffusion coefficient (and hence M_w) as a function of concentration, this can be clearly visualized.

Values of binding constants

The estimated values of the equilibrium constants, particularly K_{dimer}, have large uncertainties associated with them. These errors, however, do not suggest a difference in the relative values of K_{dimer} and K_{oligo}, there being a 1000-fold difference in favor of K_{oligo}. Despite the magnitude of the uncertainty, the experimental data, with the exception of the first data point, fall within the 95% confidence intervals of the fitted values. The values of the equilibrium constants yield a τ-value ($2K_{dimer}/K_{oligo}$, see Theory of Methods) of ~0.003, indicating that dimerization is highly thermodynamically unfavorable and clearly the limiting step in the association process, if the attenuative model of indefinite association is accepted as an accurate representation of the real system. This result is reflected in the oligomer population distributions (Fig. 3), which show that the concentration of dimers is very low at all concentrations relative to that of monomer. It is of little merit to compare the values obtained here for the equilibrium constants with those published in the literature because there is so much variation in those results and none of them are based on an attenuative model of indefinite self-association.

Interpretation of the model

In addition to illustrating the role of dimerization in the attenuative self-association process, Fig. 3 shows that at low concentration the solution contains predominantly monomers and that this situation pertains at all but the very highest concentrations. This is due, of course, to the low value of K_{dimer}, which is counterbalanced by the initial concentration of monomer at high concentration. The low concentration of dimer at all concentrations indicates that once the dimer is formed it readily associates to form higher order oligomers, as anticipated from the relatively high value of K_{oligo}. As the concentration of the solution is increased, more monomer associates to form dimer and thence more dimer to higher order oligomers, resulting in an increase in the concentration of the predominant oligomer (the local maximum in the distribution plots) and an increase in the breadth of the distribution of oligomers.

As illustrated in Fig. 4, the polydispersity, which provides a measure of the spread in the oligomer distribution, increases rapidly with concentration, to have a maximum value when the concentration is ~0.4 mol l^{-1}, and it decreases approximately exponentially (second order) to a value close

to that for the lowest concentration. That this is so is not immediately apparent from the population distribution plots (Fig. 3), but can be understood as follows: at the lowest concentration the distribution is dominated by monomer which is present at a mole fraction close to 1 (0.98) while at the highest concentration the distribution is dominated by oligomers comprising eight or nine subunits; the degree of spread in the distribution is greater therefore at the intermediate concentrations where the monomer fraction is reduced and the oligomer distribution is fairly flat.

Interpretation of activation energy data

Activation energies in the context of diffusion rates (as opposed to reaction rates where they have their traditional interpretation) have been interpreted as the sum of the energy needed to create a void into which the diffusing molecule can move and the energy required to transfer it from the force field associated with its neighbors into the void.[42] Because the experimental activation energies for diffusion have generally been inconsistent with energies of most chemical reactions, these values should be treated as apparent activation energies and should not be given too much physical significance. Nevertheless, the comparative values do provide us with some insight to the nature of the system. As is illustrated in Fig. 5, there is a decrease in the apparent activation energy as the concentration is increased and this can be explained as follows: an increase in the order of oligomerization which accompanies an increase in concentration also results in a lower surface area to volume ratio for the individual oligomer and consequently the force field acting on the molecule, per unit surface area, will also be smaller and less energy will be required to transfer it into a void.

Bond length

The value obtained for the length of the hydrogen bond (b_l) involved in the self-association process was slightly less than the calculated value of the Stokes radius for an NMA molecule modeled as a hard sphere; by taking the uncertainty in the results it is realistic to claim that the two values are comparable. Hence this result suggests that the NMA monomer is not spherical since the minimum distance separating two adjacent spheres is twice the radius. However, the Stokes radius constitutes a hydrodynamic radius and contains little information regarding the steric properties of the molecule that will determine the geometry of hydrogen bonding. It is also noted that while the Kirkwood–Riseman theory is based on a stick regime for the boundary conditions which specify the frictional coefficient of the polymer, other models[43] may also represent the NMA–CCl$_4$ system and may lead to alternative estimates of the length of the hydrogen bonds.

Solvent and contaminants

The linearity of the Stejskal–Tanner plots which were used to calculate the diffusion coefficients (which are not shown here) is evidence that the self-association process is a dynamic one, at least on the time-scale of the NMR experiment. Further evidence of this is given by the viscosity measurements

(Table 1), that show only a slight deviation from linear dependence on concentration, despite the self-association process that leads to oligomers of higher order as the concentration of NMA is increased (Fig. 3). This suggests that non-ideality of the higher concentration solutions, due to crowding, will be of lesser importance than would be the case for a less dynamic system.

The authors of one study claimed that there was evidence of an interaction between CCl$_4$ and NMA via hydrogen bonding and that this must be taken into account.[1] However, other studies have failed to show this interaction. We have assumed a lack of interaction, since none was manifest in our NMR studies, and have disregarded any solution non-ideality that would arise from such an interaction and which would potentially affect the self-association process. We have conducted preliminary studies (data not presented here) which show that the introduction of even small amounts of hydrogen bonding compounds (e.g. water, ethanol) has a significant effect on the concentration dependence of the diffusion and hence on the self-association process. It is highly likely that the interactions alluded to above were from such contaminants.

Non-ideality

Non-ideality of the sample solutions, particularly those of high concentration, is not accounted for in the model used here. However, for the reasons given above, we expect these effects to be minor. In addition, it can be shown that when activity coefficients are applied to the equilibria in the formulation of the indefinite self-association, they cancel, so that the concentration constants remain numerically unchanged.[31] The implication of this is that while the activity coefficient will be reflected in the experimental results, it will only be reflected in the results of the modeling in the estimated values of the equilibrium constants.

CONCLUSION

Diffusion coefficients for NMA in CCl$_4$ were measured as a function of NMA concentration using the PGSE NMR method. Computer models which account for the self-associative and hydrodynamic properties of this system were developed and tested. The model which gave the most satisfactory fit to the experimental data was one in which self-association occurs according to an indefinite self association-attenuative scheme and in which the NMA oligomer is treated as a rigid rod-like molecule; the theory is according to Kirkwood and Riseman.[30] This model enabled us to estimate values for the equilibrium association constants and the average length of the hydrogen bonds in the associated oligomers, and to predict the population distribution of oligomers as a function of the NMA concentration. The temperature dependence of the diffusion coefficient in this system was also measured, permitting the calculation of apparent activation energies, and this provided some additional insight into the process of self-association. The methodology used in this work demonstrates that diffusion measurements made using PGSE NMR for polydisperse samples can be used, in conjunction with computer modeling, to estimate the values of both thermodynamic and hydrodynamic parameters and to predict the population distribution of oligomeric species.

REFERENCES

1. Akiyama M, Torii H. *Spectrochim. Acta, Part A* 1999; **56**: 137.
2. Akiyama M, Ohtani T. *Spectrochim. Acta, Part A* 1994; **50**: 317.
3. Kuznetsova LM, Furer VL, Maklakov LI. *J. Mol. Struct.* 1996; **380**: 23.
4. Klotz IM, Franzen JS. *J. Am. Chem. Soc.* 1962; **84**: 3461.
5. Hummel H, Bonnart R. *Makromol. Chem.* 1985; **186**: 2049.
6. Liu Y, Ozaki Y. *J. Phys. Chem.* 1996; **100**: 7326.
7. Liu Y, Czarnecki MA, Ozaki Y. *Appl. Spectrosc.* 1994; **9**: 1095.
8. Krikorian SE. *J. Phys. Chem.* 1982; **86**: 1875.
9. Howlett GJ, Nichol LW, Andrews PR. *J. Phys. Chem.* 1973; **77**: 2907.
10. Albers RJ, Swanson AB, Kreshek GC. *J. Am. Chem. Soc.* 1971; **93**: 7075.
11. Kreshek GC, Klotz IM. *Biochemistry* 1969; **8**: 8.
12. Katz JL, Post B. *Acta Crystallogr.* 1960; **13**: 624.
13. Hamzaoui F, Baert F. *Acta Crystallogr., Sect. C* 1994; **50**: 757.
14. Bagno A, Gerard S, Kevelam J, Menna E, Scorrano G. *Chem. Eur. Phys.* 2000; **6**: 2915.
15. Takahashi F, Li NC. *J. Phys. Chem.* 1965; **69**: 2950.
16. LaPlanche LA, Thompson HB, Rogers MT. *J. Phys. Chem.* 1965; **69**: 1482.
17. Graham LL, Chang CY. *J. Phys. Chem.* 1971; **75**: 784.
18. Hinton JF, Amis ES. *Z. Phys. Chem* 1968; **60**: 159.
19. Mathur R, Wang SM, Li NC. *J. Phys. Chem.* 1964; **68**: 2140.
20. Chen L, Gross T, Lüdemann H-D. *Z. Phys. Chem* 1999; **214**: 239.
21. Graham LL, Chang CY. *J. Phys. Chem.* 1971; **75**: 776.
22. Seipelt CG, Zeidler MD. *Ber. Bunsen-Ges. Phys. Chem.* 1997; **101**: 1501.
23. Bagno A. *Chem. Eur. Phys.* 2000; **6**: 2925.
24. Czernek J, Fiala R, Sklenar V. *J. Magn. Reson.* 2000; **145**: 142.
25. Ludwig R. *J. Mol. Liq.* 2000; **84**: 65.
26. Imamura A, Ohsaku M. *Polymer* 1983; **24**: 1639.
27. Longsworth LG. *J. Colloid Interface Sci.* 1966; **22**: 3.
28. Kirkwood JG. *J. Polym. Sci.* 1954; **12**: 1.
29. Kirkwood JG, Riseman J. *J. Chem. Phys.* 1948; **16**: 565.
30. Riseman J, Kirkwood JG. *J. Chem. Phys.* 1951; **18**: 512.
31. Martin RB. *Chem. Rev.* 1996; **96**: 3043.
32. Tanford C. *Physical Chemistry of Macromolecules*. Wiley: New York, 1961.
33. Callaghan PT, Pinder DN. *Macromolecules* 1983; **16**: 968.
34. Kärger J, Pfeifer H, Heink W. *Adv. Magn. Reson.* 1988; **12**: 1.
35. Sørland GH, Seland JG, Krane J, Anthonsen HW. *J. Magn. Reson.* 2000; **142**: 323.
36. Mills R. *J. Phys. Chem.* 1973; **77**: 685.
37. Stejskal EO, Tanner JE. *J. Chem. Phys.* 1965; **42**: 288.
38. McKie JE, Brandts JF. *Methods Enzymol.* 1972; **26(Pt. C)**: 257.
39. Sheldon D. *Physical Biochemistry*. Wiley: New York, 2000.
40. Pouchert CJ, Campbell JR (eds). *The Aldrich Library of NMR Spectra*, vol. III. Aldrich: Milwaukee, WI, 1974.
41. O'Neil MJ (ed). *The Merck Index* (13th edn). Merck Research Laboratories: Whitehouse Station, NJ, 2001.
42. Tyrrell HJV, Harris KR. *Diffusion in Liquids*. Butterworths: London, 1984.
43. Boeré RT, Kidd RG. *Annu. Rep. NMR Spectrosc.* 1982; **13**: 319.